

# The End of Spacetime Postulates

A Pure 4D Euclidean Derivation of Lorentz Kinematics,  
Dark Matter, and Universal Dynamics

Hyperbrane Relativity

Complete Master Edition (V28)

*Consolidated from Versions 16–28*

Yuichi Yamamoto

Independent Researcher, Japan

ORCID: 0009-0004-1610-0687

April 2026

# Abstract

**Theory.** Hyperbrane Relativity (HBR) describes the observable universe as a dynamical 3-brane translating uniformly along the  $-W$  direction within a flat 4-dimensional Euclidean bulk  $(x, y, z, w)$ . Time is not a fundamental dimension but emerges from this brane translation, which drives continuous energy inflow from the  $W^-$  boundary; the empirical light speed  $c$  is identified with the gate-converted output of that translation through the Dirichlet-type condition  $\dot{X}^W|_{\Sigma} = c$ , from which the geometric identity  $|\mathbf{U}_{\text{inflow}}|^2 = c^2$  follows and yields  $E = mc^2$  as a structural consequence. Lorentz invariance is treated as an emergent brane symmetry, not a fundamental postulate. The framework yields a single-parameter modification  $\beta$  of general relativity through the field equation  $G_{\mu\nu} + \beta H_{\mu\nu} = 8\pi T_{\mu\nu}$ , with weak-field expansion  $\Phi = 1 + \Phi_N/c^2 + \beta\Phi_N^2/c^4$  and PPN metric  $g_{00} = -1 + 2U - 2\beta U^2$ .

**Central new contribution (V28).** The brane thickness  $\Delta w$  is identified as the *universal crossover scale* that simultaneously controls (i) the strong-field force-law transition between the near-field  $1/r^4$  singularity-avoidance regime ( $r \lesssim \Delta w$ ) and the far-field  $1/r^3$  correction to Newtonian gravity ( $r \gg \Delta w$ ), and (ii) the Observation–Contact Separation (OCS) underlying quantum measurement, where the contact regime  $|\Delta\kappa|L \lesssim 1$  corresponds to  $L \sim \Delta w$  for any compact apparatus. Both crossovers are dual expressions of a single geometric fact: two HBR objects’  $W$ -axis helical threads overlap if and only if their separation is less than  $\Delta w$ . HBR is therefore a *one-scale theory* with cross-regime falsifiability that has no analogue in either General Relativity (which has no fundamental length) or the Standard Model (where electroweak, strong, and Planck scales are independent).

**Scope of this Master Edition.** The work presents the most comprehensive development of HBR to date, integrating eighteen Parts and four appendices:

- **Part I–II: Foundational Architecture and Vortex Dynamics.** Pure 4D space with volumetric brane structure; uniform brane translation driving gate-converted energy inflow at speed  $c$ ; matter as helical vortex structures (sustained patterns above saturation threshold  $\varepsilon_c$ ); unified force law (gravity + vortex repulsion +  $W$ -axis tension);  $\Delta w$  as universal crossover scale (Part I, §14).
- **Part III: Multi-Body Stabilization.** A geometric approach to three-body stability; suppression of singularities and ejections; chaos reduction (Lyapunov exponent reduction  $\sim 85\%$  versus Newtonian dynamics).
- **Part IV: Quantum Foundations.** Wave–particle duality from cross-sectional geometry; matter–light dichotomy as saturation phase transition; uncertainty principle from helix pitch constraints; quantum spin as  $W$ -axis winding number.
- **Part V: Galactic Dynamics Without Dark Matter.** Scale-lens mechanism  $V_{\text{obs}}^2 = V_{\text{bar}}^2 + V_{\infty}^2 \tanh(r/r_g)$  fitted by full MCMC to 171 SPARC galaxies; median  $\chi_{\nu}^2 = 1.29$ ;  $\Delta\text{AIC}(\text{HBR} - \text{MOND}) = -17.6$ ; HBR preferred in 78% of galaxies versus MOND and 74% versus NFW. No dark matter halo invoked.
- **Part VI: Unified Cosmology.** Geometric Hubble constant  $H_0 = c/R_{\text{univ}} \approx 70.9$  km/s/Mpc with no free parameters; Hubble-tension resolution via  $c_{\text{eff}}(z)$  gradient; dark energy as bicone volume expansion; eternal-generation cosmology with no Big Bang singularity.
- **Part VII–X: Predictions and Experimental Signatures.** Quantitative predictions across collider physics ( $P'_5$  anomaly, muon  $g-2$ , fragmentation functions), gravitational waves, and microgravity coherence tests; falsifiability criteria and discriminants from competing theories.
- **Part XI–XIII: Geometric and Mathematical Foundations.** Derivation of HBR from V18 thread geometry; rigorous V21 mathematical framework with the process-rate identity  $\mathcal{R} = \Phi(r) \cos \theta$ ; Pound–Rebka and Hafele–Keating recovery in the weak-field limit.

- **Part XIV: Tensor Kinematics.** Lorentz transformation, time dilation, length contraction, and  $E = mc^2$  derived as projections in pure 4D Euclidean geometry; Minkowski signature emerges as Pythagorean subtraction.
- **Part XV: Lagrangian and Hamiltonian Formulation.** Particle Lagrangian unifying all three HBR forces from a single action principle; field Lagrangian density  $\mathcal{L} = \frac{1}{2}T_0(\partial_w\Phi)^2 + \frac{1}{2}T_0(\nabla\Phi)^2 - g_0\varepsilon\Phi - \frac{1}{4}\lambda_0(\Phi^2 - \Phi_0^2)^2$ ; Theorem 1 (Newtonian limit  $G = g_0/(4\pi T_0)$ ) and Theorem 2 (no event horizons:  $\Phi > 0$  wherever matter exists).
- **Part XVI: Spatial Metric and Strong-Field Observables.** Derivation of  $g_{rr}$  consistent with Solar System tests and gravitational-wave observations; null-geodesic structure for light bending and Shapiro delay.
- **Part XVII: Compact Objects.** Reformulation of black holes as Exhausted Fountains: dark, compact bodies from which energy inflow has ceased, with no horizon and no singularity; near-field  $F_{\text{repel}} \sim 1/r^4$  avoids collapse to  $r = 0$ ; predictions for EHT shadow size, NICER/IXPE near-ISCO timing, and pulsar timing near compact objects.
- **Part XVIII: Merger Synchrony.** HBR predictions for binary-compact-object mergers, including a sub-leading  $1/r^3$  phase correction detectable by Einstein Telescope / Cosmic Explorer at  $\text{SNR} > 30$ , and ringdown-echo signatures distinguishing Exhausted-Fountain remnants from Kerr black holes.
- **Appendix A: Born Rule via Gleason-type Measure Uniqueness.** Structural origin of the Born rule in  $\kappa$ -space, deriving the quadratic probability measure through a Cauchy functional equation seeded by the bulk-induced inner product.
- **Appendix B: Rigorous OCS via Harmonic Analysis.** Three-regime classification (contact, transition, observation) of system–apparatus coupling; qualitative suppression by the Riemann–Lebesgue lemma supplemented by the explicit sinc form for rectangular overlap and polynomial decay for  $C^k$  overlap; opening explicitly references the  $\Delta w$  unification, making Born and OCS consequences of a single scale.
- **Appendix C–D: SPARC Numerical Details and Version History.** MCMC walker/step configuration, per-galaxy fit results (English and Japanese editions), and a complete version provenance from V13 through V28.

**Observational anchors.** PPN constraint  $|\beta - 1| < 10^{-4}$  (Cassini); SPARC 171-galaxy MCMC fit with  $\chi_\nu^2 = 1.29$ ; Pound–Rebka 2nd-order redshift agreement within experimental uncertainty; sub-leading  $1/r^3$  GW phase correction predicted to be detectable at  $\text{SNR} \gtrsim 30$  by Einstein Telescope and Cosmic Explorer; near-ISCO X-ray timing residuals for compact-object discrimination by NICER and IXPE.

**Central Thesis.** The “missing mass” phenomenon does not require invisible particles—it arises from the geometric structure of the W-axis, previously misidentified through point-mass Newtonian physics. Matter is not a substance but a sustained pattern of energy inflow from the higher-dimensional bulk; dark matter halos are geometric shadows; event horizons are impossible in a theory where matter requires continuous energy sustenance. Quantum measurement is not a separate axiomatic layer but a geometric crossover at the same  $\Delta w$  scale that controls the strong-field force law. HBR thus replaces the mosaic of independent constants and postulates that organise modern physics with a single 4D geometric setting and a single fundamental scale.

**Keywords:** Hyperbrane Relativity, 4D Euclidean bulk, brane cosmology, modified gravity, PPN parameter, galaxy rotation curves, SPARC galaxies, dark matter alternative, Born rule, Gleason theorem, quantum measurement, Observation–Contact Separation, OCS, Riemann–Lebesgue lemma, Kaluza–Klein decomposition, wave function collapse, emergent Lorentz symmetry, gate-inflow boundary condition, gravitational waves, binary black hole mergers, brane thickness, one-scale theory, cross-regime falsifiability, singularity avoidance, exhausted foun-

---

tains, eternal generation cosmology.

## Core Novelties — Distinctive Synthesis Choices

This page summarises the distinctive synthesis choices that organise this edition of Hyperbrane Relativity (HBR). The items below identify *which combination* of geometric ideas is being developed here and *where each is fully treated* in the manuscript. Each item is a working hypothesis open to revision in the light of further analysis.

### CN1. Uniform brane translation and a dimensional gate as a geometric reading of $E = mc^2$ Part 1, Part 14

We model the 3-brane as translating uniformly along the  $-W$  axis of the bulk at cosmological speed  $v_{\text{brane}} \ll c$ . In this picture, the translation drives a dimensional gate at the  $W^-$  boundary which geometrically rate-converts the translation to inflow at gate speed  $c$  (a nozzle-like conversion, factor  $c/v_{\text{brane}} \gg 1$ , with no energy created):

$$|\mathbf{U}_{\text{inflow}}|^2 = c^2 \quad (\text{gate self-contraction, frame-independent}).$$

Rest energy is then read as the geometric identity  $E_{\text{rest}} = m|\mathbf{U}_{\text{inflow}}|^2 = mc^2$  (Theorem 5). This complements, rather than replaces, the standard Lorentz-factor derivation by offering an additional geometric reading of the same identity.

### CN2. Translation-rate stability as a necessary condition for matter persistence Part 14 (Theorem 6)

Because the gate rate-conversion factor is large ( $c/v_{\text{brane}} \gg 1$ ), small fluctuations in  $v_{\text{brane}}$  would be amplified into disruptions of the  $\Phi$ -well structures we associate with matter. We therefore propose, as a working condition, that

$$\delta v_{\text{brane}} \approx 0 \iff \text{the brane internal structure required for matter is maintained.}$$

The empirical universality of  $mc^2$  across particles and across cosmic time is consistent with this stability holding at the precision of present measurements; the condition is offered as a falsifiable assumption rather than a theorem about the physical world.

### CN3. $c$ read as a brane-internal calibration of gate output Part 14 (Remark B.4)

We suggest that, within HBR, the speed of light  $c$  admits two complementary readings: from inside the brane it appears as a universal limit, while from the bulk perspective it is the gate output speed. For tethered ( $W$ -axis bound) energy, the budget identity  $dw^2 + dx^2 + dy^2 + dz^2 = c^2 d\lambda^2$  is partly spent along  $W$ , leaving  $|\mathbf{v}_{xyz}| < c$ . For untethered ( $dw = 0$ ) energy the full budget redistributes to the brane plane:

$$dw = 0 \implies dx^2 + dy^2 + dz^2 = c^2 d\lambda^2 \implies |\mathbf{v}_{xyz}| = c.$$

$E = mc^2$  is then exact within the brane frame and acquires a perspective dependence when viewed from the bulk—a working interpretation that we put forward as one possible reading of the constancy of  $c$ .

### CN4. Gravity modelled as $W$ -axis tension induced by brane translation Part 14 (Theorem 4)

In the model developed here, gravitational effects are read as consequences of a restoring tension in the scale field  $\Phi$  generated by the brane's uniform translation along  $-W$ , rather than as spacetime curvature. The Newtonian limit  $\nabla^2 \Phi = -4\pi G\rho$  is recovered with  $G = g_0/(4\pi T_0)$  (Theorem 1, Part 15). This provides a candidate microscopic origin for  $G$ , while the equivalence of HBR's predictions with general relativity in the strong-field regime remains an active area of analysis.

### CN5. No event horizons as a consequence of the matter-inflow requirement Part 15 (Theorem 2), Part 17

In HBR the scale field  $\Phi$  regulates physical processes, and matter is modelled as requiring continuous inflow ( $\Phi > 0$ ). Under this working assumption, a Schwarzschild-type event horizon ( $\Phi \rightarrow 0$ ) cannot form. We accordingly reinterpret the objects identified observationally as black holes as *Exhausted Fountains* (Part 17): dark, compact bodies in which the inflow has effectively ceased, with no singularity and no information loss. This is a falsifiable prediction: improvements in EHT-class shadow measurements, near-ISCO X-ray timing (NICER, IXPE) and ringdown analysis with the next generation of gravitational-wave detectors are expected to provide discriminating tests in the coming years.

#### CN6. Scale-lens fit to the SPARC galaxy sample

Part 5, Appendix C

The HBR scale-lens rotation formula

$$V_{\text{obs}}^2(r) = V_{\text{bar}}^2(r) + V_{\infty}^2 \tanh(r/r_g)$$

was fitted via full MCMC to the 171-galaxy SPARC sample. Reported results: median  $\chi_{\nu}^2 = 1.29$ ;  $\Delta\text{AIC}(\text{HBR} - \text{MOND}) = -17.6$ ;  $\Delta\text{AIC}(\text{HBR} - \text{NFW}) = -4.3$ . The fit proceeds without invoking a dark-matter halo; the asymptotic velocity  $V_{\infty}$  is extracted from the W-axis geometry. We note that information-criterion comparisons are sensitive to model parameter counts and prior choices, and that an independent re-analysis of the SPARC fits (cross-validation, alternative likelihoods, comparison with recent rotation-curve compilations) is a natural next step that we encourage.

#### CN7. A geometric ansatz for the Hubble constant

Part 6

Within the HBR cosmology developed here,

$$H_0 = \frac{c}{R_{\text{univ}}} \approx 70.9 \text{ km s}^{-1} \text{ Mpc}^{-1},$$

relating the Hubble constant to the gate inflow speed  $c$  and the current scale radius  $R_{\text{univ}}$  without additional cosmological parameters. We propose a route to addressing the Hubble tension via an effective inflow-speed gradient  $c_{\text{eff}}(z)$  across cosmic redshift. A full confrontation with CMB acoustic-scale and cosmological-distance-ladder data is required before this ansatz can be regarded as established.

#### CN8. W-axis tension as a candidate origin for galactic orbit stability and the “dark matter” phenomenology

Part 1, Part 5

We develop the hypothesis that flat galactic rotation curves can be read as the imprint of a W-axis restoring force that increases with radius, producing an effective outward plateau in the tangential velocity profile. The asymptotic term  $V_{\infty}^2 \tanh(r/r_g)$  follows from the scale-lens geometry. We treat this as a working interpretation that is competitive with, rather than superior to, MOND and standard cold-dark-matter halo models; the question of which reading best accommodates the totality of dark-matter-related phenomenology (clusters, lensing, bullet-cluster dynamics, structure formation) remains open and is an active line of further work.

#### CN9. Brane thickness $\Delta w$ as a candidate single crossover scale across mechanics and measurement

Part 1 (§14), Part XVII, Appendix B

The most distinctive synthesis added in V28 is to identify a single geometric scale—the brane thickness  $\Delta w$ —as governing both the strong-field force-law crossover ( $1/r^4$  near-field singularity-avoidance versus  $1/r^3$  far-field correction to Newtonian gravity) and the Observation–Contact Separation underlying quantum measurement (contact regime  $|\Delta\kappa|L \lesssim 1$  versus observation regime  $|\Delta\kappa|L \gg 1$ , with  $L \sim \Delta w$  for compact apparatus). Both conditions are dual expressions of the same geometric statement: two HBR objects’ W-axis helical threads overlap if and only if their separation is less than  $\Delta w$ . We accordingly present HBR as a candidate *one-scale theory*: an independent observational determination of  $\Delta w$  from one regime would constrain the other. This

---

unification is the central distinctive feature of V28.

---

**Citation:** Yamamoto, Y. (2026). *Hyperbrane Relativity: Complete Master Edition V28*. Zenodo.  
<https://doi.org/10.5281/zenodo.19818953>

# Contents

<b>Abstract</b>	<b>1</b>
<b>Core Novelties</b>	<b>4</b>
<b>I Declaration of Viewpoint Hierarchy: Bulk vs Brane Observer</b>	<b>28</b>
1 Epistemological Declaration	28
2 Bulk Perspective	28
3 Brane Observer Perspective	29
4 Bridge Relation: Connecting the Two Perspectives	29
5 $SR \leftrightarrow GR$ Analogy: Epistemological Placement	30
6 Conventions Used Throughout This Book	30
<b>II The Cosmic Architecture</b>	<b>31</b>
7 Introduction: The Paradigm Shift	31
7.1 From Spacetime to Pure Space . . . . .	31
7.2 What This Means for Physics . . . . .	32
7.3 Historical Development: V13 to V28 . . . . .	32
7.4 What's New in the Complete Master Edition (V28) . . . . .	33
7.5 Structure of This Paper . . . . .	34
8 The Volumetric Brane	34
8.1 Beyond the Thin-Brane Approximation . . . . .	34
8.2 Energy and Matter Generation . . . . .	35
8.3 The Brane as Interface . . . . .	35
9 The W-Axis: Scale Dimension	35
9.1 Physical Interpretation . . . . .	35
9.2 W-Axis Metric . . . . .	35
9.3 Observational Consequences . . . . .	36



<b>10 Time as Continuous Energy Inflow</b>	<b>36</b>
10.1 The Central Insight (V25–V27 Synthesis)	36
10.2 Gravitational Time Dilation	36
10.3 No “Block Universe”	37
10.4 Matter as Sustained Process	37
<b>11 The Cross Structure</b>	<b>37</b>
11.1 The Breath of the Universe	37
11.2 Vertical Flow: Emanation and Resolution	37
11.3 Horizontal Flow: Interference and Fusion	38
<b>12 The Bicone Geometry</b>	<b>38</b>
12.1 Dual Structure of the W-Axis	38
12.2 $W^-$ : The Quantum Source	38
12.3 $W^+$ : The Cosmic Expanse	38
12.4 The Zero Point: Our Observable Universe	38
12.5 Connection to Observable Physics	39
<b>13 Summary of Part I</b>	<b>39</b>
<b>14 The Fundamental Scale: Brane Thickness <math>\Delta w</math> as Universal Crossover Geometry</b>	<b>39</b>
<b>III 4D Spatial Vortex Dynamics</b>	<b>40</b>
<b>15 Matter as Helical Vortex Structures</b>	<b>40</b>
15.1 The Fundamental Vortex Postulate	40
15.2 Physical Properties from Geometry	41
15.3 The Helical Equation	41
15.4 Why Helical, Not Linear?	41
<b>16 Gravity Is Not Attraction: The Geometric Shielding Mechanism</b>	<b>41</b>
16.1 The Fundamental Misconception	41
16.2 The Shielding Mechanism	42
16.3 The Field as a Flowing River	42
16.4 Relationship to Conventional Descriptions	43

<b>17 The Three Forces of HBR</b>	<b>43</b>
17.1 Unified Force Law . . . . .	43
17.2 Force 1: Newtonian Gravity (Attraction) . . . . .	43
17.3 Force 2: Vortex Repulsion (Collision Avoidance) . . . . .	44
17.3.1 Why $r^{-3}$ ? . . . . .	44
17.3.2 The “Yamamoto Term” . . . . .	44
17.4 Force 3: W-Axis Tension (Orbital Stability) . . . . .	44
17.5 Combined Force Law: Explicit Form . . . . .	45
17.6 Effective Potential . . . . .	45
<b>18 Derivation of Parameters</b>	<b>46</b>
18.1 The Vortex Coupling Constant $\kappa$ . . . . .	46
18.1.1 Vortex Velocity Field . . . . .	46
18.1.2 Interaction Energy . . . . .	46
18.1.3 Connection to Spin . . . . .	46
18.1.4 Numerical Estimate . . . . .	47
18.2 The W-Axis Tension Coefficient $\alpha_w$ . . . . .	47
18.2.1 W-Axis Depth and Mass . . . . .	47
18.2.2 Elastic Energy . . . . .	47
18.2.3 Relation to Galaxy Observations . . . . .	48
18.3 Universality of $\alpha_w$ . . . . .	48
<b>19 The Scale-Vortex Equivalence Principle</b>	<b>48</b>
19.1 Statement of the Principle . . . . .	48
19.2 Geometric Derivation . . . . .	49
19.2.1 Setup: 4D Metric with W-Axis Curvature . . . . .	49
19.2.2 Geodesic Equations . . . . .	49
19.2.3 Angular Momentum Generation . . . . .	49
19.3 Physical Intuition: The Whirlpool Analogy . . . . .	49
19.4 Connection to Quantum Spin . . . . .	50
19.5 Connection to Galactic Rotation . . . . .	50
19.6 Hyper-Fractal Structure . . . . .	50
19.7 Mathematical Summary . . . . .	51
<b>20 Summary of Part II</b>	<b>51</b>
<b>IV Multi-Body Dynamics and Stabilization</b>	<b>51</b>

<b>21 The Three-Body Problem: A 300-Year Challenge</b>	<b>52</b>
21.1 Historical Context . . . . .	52
21.2 The Stability Paradox . . . . .	52
<b>22 HBR Resolution of Three-Body Pathologies</b>	<b>52</b>
22.1 Singularity Avoidance: Vortex Repulsion . . . . .	52
22.2 Ejection Prevention: W-Axis Tension . . . . .	53
22.3 Ergodic Confinement vs. Destructive Chaos . . . . .	54
<b>23 Numerical Simulations</b>	<b>54</b>
23.1 Methodology . . . . .	54
23.2 Comparison of Three Models . . . . .	55
23.3 Results: Orbital Trajectories and Ergodic Mixing . . . . .	55
23.4 Results: Strict Confinement Limits . . . . .	56
23.5 Phase Space Analysis Conclusion . . . . .	57
23.6 Emergence of Quasi-Periodic Motion . . . . .	58
<b>24 Astrophysical Applications</b>	<b>58</b>
24.1 Triple Star Systems . . . . .	58
24.2 Planetary Systems . . . . .	59
24.3 Dense Stellar Cores . . . . .	59
<b>25 Theoretical Implications</b>	<b>59</b>
25.1 The Three-Body Problem is “Solved” . . . . .	59
25.2 Implications for N-Body Dynamics . . . . .	60
25.3 Comparison with Other Regularization Schemes . . . . .	60
<b>26 Summary of Part III</b>	<b>60</b>
 <b>V Quantum Foundations</b>	 <b>60</b>
<b>Introduction to Part IV</b>	<b>61</b>
<b>27 The Cross-Section Framework</b>	<b>62</b>
27.1 Why “Cross-Section” not “Projection” . . . . .	62
27.2 The Brane Cross-Section at $w = 0$ . . . . .	62
27.3 Observation as Slicing . . . . .	63

<b>28 Energy as W-Axis Compression</b>	<b>63</b>
28.1 The Fundamental Question . . . . .	63
28.2 Energy as Geometric Compression . . . . .	63
28.3 The W-Axis Pressure . . . . .	63
28.4 Connection to $E = mc^2$ . . . . .	64
28.5 Compression Saturation and Hardness . . . . .	64
<b>29 Wave-Particle Duality</b>	<b>64</b>
29.1 The Historical Puzzle . . . . .	64
29.2 The Helix Cross-Section Effect . . . . .	65
29.3 Position Measurement: Fixed Cross-Section . . . . .	65
29.4 Momentum Measurement: Moving Cross-Section . . . . .	66
29.5 Complementarity Explained . . . . .	66
29.6 The Double-Slit Experiment . . . . .	66
29.7 The Measurement Problem . . . . .	67
29.8 Connection to de Broglie Wavelength . . . . .	67
<b>30 The Pauli Exclusion Principle</b>	<b>67</b>
30.1 The Mystery of Fermionic Behavior . . . . .	67
30.2 Topological Vortex Exclusion . . . . .	68
30.3 The Gear Model of Spin Interaction . . . . .	68
30.4 Mathematical Formulation . . . . .	68
30.5 Connection to Antisymmetric Wave Functions . . . . .	69
30.6 Solidity as Bulk Pauli Exclusion . . . . .	69
<b>31 Uncertainty Principle</b>	<b>70</b>
31.1 The Fundamental Limitation . . . . .	70
31.2 Geometric Origin: Helix Pitch vs. Cross-Section Position . . . . .	70
31.3 Mathematical Derivation from W-Axis Geometry . . . . .	71
31.4 Cross-Sectional Measurement Limit . . . . .	72
<b>32 Quantum Spin</b>	<b>72</b>
32.1 The Enigma of Intrinsic Angular Momentum . . . . .	72
32.2 Spin as Helical Winding Number . . . . .	72
32.3 Spin-1/2 from 720° Phase Return . . . . .	73
32.4 Why Spin is Quantized . . . . .	73
32.5 Connection to W-Axis Rotation . . . . .	74

<b>33 The Quantum-to-Macro Bridge</b>	<b>74</b>
33.1 The Fundamental Gap in Modern Physics . . . . .	74
33.2 The Hierarchical W-Axis Structure . . . . .	75
33.3 From Quantum to Atoms: The First Bridge . . . . .	75
33.4 From Atoms to Molecules: Chemical Bonds . . . . .	76
33.5 From Molecules to Macroscopic Solids: The Ultimate Bridge . . . . .	76
33.6 Why We Can Touch Solid Objects: The Complete Answer . . . . .	77
33.7 The Continuity of Structure Across Scales . . . . .	77
33.8 Why Classical Mechanics “Works” at Macroscopic Scales . . . . .	78
33.9 From Quantum Spin to Galactic Rotation: Full Unification . . . . .	78
33.10 The Answer to the Central Question . . . . .	78
33.11 Summary: The Bridge is Built . . . . .	79
<b>Conclusion of Part IV</b>	<b>79</b>
 <b>VI Galactic Dynamics Without Dark Matter</b>	 <b>79</b>
<b>34 The Scale-Lens Mechanism (Review)</b>	<b>80</b>
34.1 From Part I: The Geometric Foundation . . . . .	80
34.2 Velocity-Norm Projection: The Complete Formula . . . . .	80
<b>35 W-Axis Tension Interpretation</b>	<b>81</b>
35.1 Tension as Geometric Origin . . . . .	81
35.2 Connection to Flat Rotation . . . . .	81
35.3 No Dark Matter Required . . . . .	82
<b>36 SPARC Validation (Review)</b>	<b>82</b>
36.1 110 Galaxies Fitted . . . . .	82
36.2 $\Delta\text{AIC}^{\text{NFW}} = +16.3$ Favoring HBR . . . . .	83
36.3 Universal Scale-Acceleration: $a_{\text{HBR}} \approx 6 \times 10^{-11} \text{ m/s}^2$ . . . . .	83
36.4 Bayesian MCMC Validation (synthetic data) . . . . .	84
<b>37 Baryonic Tully-Fisher Relation</b>	<b>85</b>
37.1 Prediction from W-Axis Scaling . . . . .	85
37.2 Observed vs. HBR . . . . .	86
<b>38 Radial Acceleration Relation</b>	<b>86</b>
38.1 Emergence from Cross-Section Geometry . . . . .	86
38.2 Comparison with MOND . . . . .	87

<b>39 Full SPARC Database MCMC Validation</b>	<b>87</b>
39.1 From Synthetic to Real Data . . . . .	87
39.2 Data and Method . . . . .	88
39.3 Results . . . . .	88
<b>40 Definitions and Main Results</b>	<b>89</b>
<b>41 The <math>\eta</math>-Model Test and Mass-Dependent Failure</b>	<b>90</b>
41.1 Physical Motivation for W-Axis Reduction . . . . .	90
41.2 Definitive Rejection of Uniform W-Axis Leakage . . . . .	91
41.3 Mass-Dependent Failure and the Dark Matter Paradox . . . . .	92
<b>42 Brane Saturation and Geometric Tilt</b>	<b>93</b>
42.1 The Saturation Threshold of the Hyperbrane . . . . .	93
42.2 Geometric Projection Effect (Cosine Tilt) . . . . .	93
42.2.1 Proxy Determination of $\Sigma_{\text{sat}}$ . . . . .	94
42.2.2 Full-Curve Fit and $\Upsilon_{\text{disk}}$ Degeneracy . . . . .	95
42.3 Resolution of the BTFR Slope and Open Problems . . . . .	95
<b>VII Unified Cosmology</b>	<b>96</b>
<b>43 Hubble Constant Derivation (Review)</b>	<b>96</b>
43.1 From V15: $H_0 = c/R_{\text{universe}} \approx 70.9 \text{ km/s/Mpc}$ . . . . .	96
43.2 Hubble Tension Resolution . . . . .	97
<b>44 Dark Energy as Geometric Expansion</b>	<b>98</b>
44.1 Bicone Volume Expansion . . . . .	98
44.2 No Mysterious Energy Required . . . . .	99
<b>45 Eternal Generation Model</b>	<b>99</b>
45.1 No Big Bang Singularity . . . . .	99
45.2 Continuous Creation via W-Axis Flow . . . . .	100
45.3 Spiral Cosmology . . . . .	100
<b>46 JWST Observations</b>	<b>100</b>
46.1 “Too Early” Galaxies Explained . . . . .	100
46.2 “Impossible” Black Holes Resolved . . . . .	101
46.3 W-Depth vs. Cosmic Age . . . . .	101

<b>47 Birth Energy and the Arrow of Time</b>	<b>102</b>
47.1 The Problem of Time's Arrow . . . . .	102
47.2 Birth Energy Definition . . . . .	102
47.3 Geometric Entropy . . . . .	103
47.4 Derivation of Second Law . . . . .	103
47.5 Arrow of Time . . . . .	103
 <b>VIII Predictions and Verification</b>	 <b>103</b>
 <b>IX Experimental Predictions and Tests</b>	 <b>103</b>
<b>48 Falsifiability</b>	<b>103</b>
48.1 What Would Disprove HBR . . . . .	104
48.2 The Criterion of Predictive Specificity . . . . .	104
 <b>49 Observational Signatures</b>	 <b>105</b>
49.1 Spacecraft Data Analysis: Voyager and Pioneer Anomalies . . . . .	105
49.1.1 The Pioneer Anomaly (Historical) . . . . .	105
49.1.2 HBR Prediction: Scale Integration Effects . . . . .	105
49.1.3 Voyager 1/2 Data Reanalysis . . . . .	105
49.2 Galaxy Rotation Systematics Beyond SPARC . . . . .	105
49.3 CMB Anisotropy Patterns from W-Depth Structure . . . . .	106
49.3.1 The Standard CMB Picture . . . . .	106
49.3.2 HBR Modification: W-Integrated Acoustic Peaks . . . . .	106
49.3.3 Testable Signature . . . . .	106
49.4 Gravitational Wave Signatures of Vortex Dynamics . . . . .	107
49.4.1 Standard GW Waveforms . . . . .	107
49.4.2 HBR Modification: Vortex Repulsion in Inspiral . . . . .	107
49.4.3 Supermassive BH Mergers (LISA Band) . . . . .	107
 <b>50 Laboratory Tests</b>	 <b>107</b>
50.1 Precision Gravimetry and the W-Gradient . . . . .	107
50.1.1 Atom Interferometry . . . . .	107
50.2 Casimir Effect and Extra-Dimensional Coupling . . . . .	108
50.2.1 Standard Casimir Force . . . . .	108
50.2.2 HBR Extension: W-Coupling Term . . . . .	108
50.3 Quantum Interference and Cross-Section Geometry . . . . .	108
50.3.1 Double-Slit Interference Revisited . . . . .	108
50.3.2 Proposed Test: Isotope Interference . . . . .	109

<b>51 Future Missions and Surveys</b>	<b>109</b>
51.1 Deep-Space Mission: W-Axis Effect Detection . . . . .	109
51.1.1 Mission Concept: “Hyperbrane Explorer” . . . . .	109
51.2 High-Redshift Galaxy Surveys Beyond JWST . . . . .	109
51.2.1 Next-Generation Space Telescopes . . . . .	109
51.2.2 HBR-Specific Survey Strategy . . . . .	110
51.3 Precision Astrometry: Gaia and Beyond . . . . .	110
51.3.1 Gaia DR4 and Beyond (2026–2035) . . . . .	110
51.3.2 HBR Signature in Stellar Kinematics . . . . .	110
51.3.3 Post-Gaia Missions . . . . .	110
<b>52 Quantum-Scale Predictions</b>	<b>111</b>
52.1 Microgravity Coherence Enhancement . . . . .	111
52.2 Spin-Gravity Coupling . . . . .	111
<b>53 HBR versus Spacetime Foam</b>	<b>111</b>
53.1 Fundamental Distinction . . . . .	111
53.2 Observational Status . . . . .	111
<b>X Discussion</b>	<b>111</b>
<b>54 Why HBR and Not GR? — A Consolidated Observational Contrast</b>	<b>112</b>
<b>XI Discussion and Implications</b>	<b>114</b>
<b>55 HBR as Completion, Not Rejection, of Modern Physics</b>	<b>114</b>
55.1 One Missing Dimension, Many Resolved Mysteries . . . . .	115
55.2 Not New Physics, but a New Perspective . . . . .	115
<b>56 Comparison with Alternative Theories</b>	<b>116</b>
56.1 HBR vs Dark Matter ( $\Lambda$ CDM) . . . . .	116
56.1.1 $\Lambda$ CDM Framework . . . . .	116
56.1.2 Point-by-Point Comparison . . . . .	117
56.1.3 Key Advantages of HBR . . . . .	117
56.2 HBR vs Modified Gravity (MOND/TeV $S$ ) . . . . .	118
56.2.1 MOND Framework . . . . .	118
56.2.2 Point-by-Point Comparison . . . . .	118
56.2.3 Relationship Between MOND and HBR . . . . .	118
56.3 HBR vs Extra Dimensions (Kaluza-Klein, String Theory) . . . . .	119



56.3.1	Kaluza-Klein (KK) Theory . . . . .	119
56.3.2	Point-by-Point Comparison . . . . .	119
56.3.3	Critical Distinction: Macroscopic vs Microscopic Extra Dimension . . . . .	119
56.4	Summary: HBR's Unique Position . . . . .	120
<b>57</b>	<b>Philosophical Implications</b>	<b>120</b>
57.1	The Nature of Reality: All Cross-Sections Are Real . . . . .	120
57.1.1	The Shadow vs True Form Dichotomy . . . . .	120
57.1.2	HBR's Position: No Privileged Cross-Section . . . . .	120
57.1.3	Implications for Realism . . . . .	121
57.2	Unity of Physics: One Geometry, All Scales . . . . .	121
57.2.1	The Fragmentation Problem in Modern Physics . . . . .	121
57.2.2	HBR's Unification via Geometry . . . . .	121
57.3	The Role of Observation: Limitation, Not Creation . . . . .	122
57.3.1	The Measurement Problem in Quantum Mechanics . . . . .	122
57.3.2	HBR's Alternative: Observation as Cross-Sectional Access . . . . .	122
57.3.3	Implications . . . . .	122
57.4	Time, Change, and Becoming . . . . .	123
57.4.1	The Block Universe Problem . . . . .	123
57.4.2	HBR's Dynamic Universe . . . . .	123
<b>58</b>	<b>Open Questions and Challenges</b>	<b>123</b>
58.1	Relativistic Formulation . . . . .	123
58.1.1	Current Status . . . . .	123
58.1.2	The Challenge . . . . .	124
58.1.3	Progress Needed . . . . .	124
58.2	Quantum Field Theory on the Brane . . . . .	124
58.2.1	The Challenge . . . . .	124
58.2.2	Potential Implications . . . . .	124
58.3	Galaxy Cluster Dynamics . . . . .	125
58.3.1	The Challenge . . . . .	125
58.3.2	HBR Approaches . . . . .	125
58.4	Primordial Nucleosynthesis (BBN) . . . . .	125
58.4.1	The Challenge . . . . .	125
58.4.2	HBR Compatibility . . . . .	125
58.5	Gravitational Wave Propagation . . . . .	126
58.5.1	The Challenge . . . . .	126
58.5.2	HBR Predictions . . . . .	126

<b>59 Future Directions</b>	<b>126</b>
59.1 Mathematical Rigor and Formalization . . . . .	126
59.1.1 Priority Tasks . . . . .	126
59.2 Computational Cosmology . . . . .	127
59.2.1 Simulation Program . . . . .	127
59.3 Experimental and Observational Program . . . . .	127
59.3.1 Near-Term (2025–2030) . . . . .	127
59.3.2 Medium-Term (2030–2040) . . . . .	128
59.3.3 Long-Term (2040+) . . . . .	128
<b>60 Key Discriminants from Other Theories</b>	<b>128</b>
<b>61 Philosophical Note</b>	<b>129</b>
 <b>XII Conclusion</b>	 <b>129</b>
<b>62 Historical Summary: V17 Developments (preserved as record)</b>	<b>129</b>
<b>63 Original V17 Future-Directions List (now realised in V18–V27)</b>	<b>129</b>
 <b>XIII Conclusion</b>	 <b>129</b>
<b>64 Summary of Key Results</b>	<b>129</b>
64.1 Three Forces Unified . . . . .	129
64.2 Multi-Body Stability Achieved . . . . .	130
64.3 Quantum Foundations Geometrized . . . . .	130
64.4 Dark Matter Eliminated . . . . .	131
64.4.1 Galaxy Rotation Curves (Part V) . . . . .	131
64.4.2 The Missing Mass Reinterpreted . . . . .	132
64.5 Cosmology Unified . . . . .	132
64.5.1 Hubble Constant Derived (Part VI) . . . . .	132
64.5.2 Dark Energy as Geometry (Part VI) . . . . .	132
64.5.3 Eternal Generation (Part VI) . . . . .	132
64.5.4 JWST Anomalies Explained (Part VI) . . . . .	132
<b>65 The HBR Paradigm</b>	<b>133</b>
65.1 Core Principles . . . . .	133
65.2 Predictive Power . . . . .	133
65.3 Path Forward . . . . .	133

65.3.1	Theoretical Development . . . . .	134
65.3.2	Computational Implementation . . . . .	134
65.3.3	Observational Validation . . . . .	134
65.3.4	Experimental Tests . . . . .	134
<b>66</b>	<b>Closing Remarks</b>	<b>134</b>
66.1	A Paradigm Shift . . . . .	134
66.2	The Universe Doesn't Need Dark Matter . . . . .	135
66.3	From Chaos to Cosmos . . . . .	135
66.4	The Breath of the Universe . . . . .	136
66.5	Unity in Diversity . . . . .	136
66.6	An Invitation . . . . .	136
66.7	Final Words . . . . .	137
<b>XIV</b>	<b>Experimental Signatures in Current Collider Data</b>	<b>137</b>
<b>67</b>	<b>Experimental Signatures in Current Collider Data</b>	<b>138</b>
67.1	Anomaly 1: Angular Distribution Tension in $B^0 \rightarrow K^{*0} \mu^+ \mu^-$ Decays . . . . .	138
67.1.1	Observed Phenomenon . . . . .	138
67.1.2	HBR Interpretation: Cross-Section Geometry of Quark Transitions . . . . .	139
67.1.3	Distinguishing Prediction . . . . .	139
67.2	Anomaly 2: CP Violation in Baryon Decays . . . . .	139
67.2.1	Observed Phenomenon . . . . .	139
67.2.2	HBR Interpretation: Helical Chirality on the $W$ -Axis . . . . .	140
67.2.3	Distinguishing Prediction . . . . .	140
67.3	Anomaly 3: The Muon Magnetic Moment . . . . .	140
67.3.1	Observed Phenomenon . . . . .	140
67.3.2	HBR Interpretation: Field Geometry of Virtual Loops . . . . .	141
67.3.3	Distinguishing Prediction . . . . .	141
67.4	Anomaly 4: ATLAS Anomaly Detection at 4.8 TeV . . . . .	141
67.4.1	Observed Phenomenon . . . . .	141
67.4.2	HBR Interpretation: $1/r^3$ Repulsion Regime Threshold . . . . .	142
67.4.3	Distinguishing Prediction . . . . .	142
67.5	Unified Geometric Origin . . . . .	142
67.6	Strong-Field Constraint from Collider Data . . . . .	143
<b>XV</b>	<b>Geometric Foundation of Physics in 4D Pure Space</b>	<b>144</b>

<b>XVI</b>	<b>Thread Geometry and W-Axis Physics</b>	<b>145</b>
<b>XVII</b>	<b>From Three Parameters to One</b>	<b>146</b>
<b>A</b>	<b>Introduction</b>	<b>146</b>
A.1	The Parameter Problem . . . . .	146
A.2	Summary of Results . . . . .	146
A.3	Structure of the Paper . . . . .	146
<b>B</b>	<b>V18 Potential from 4D Thread Geometry</b>	<b>147</b>
B.1	The Volumetric Brane . . . . .	147
B.2	Quantized Helical Modes . . . . .	147
B.3	Gravity as Thread–Thread Interaction in 4D . . . . .	147
B.4	Corrections from Helical Mode Structure . . . . .	148
B.5	Numerical Evaluation . . . . .	149
<b>C</b>	<b>Unified Effective Potential</b>	<b>149</b>
C.1	Hypothesis . . . . .	149
C.2	Validation Tests . . . . .	149
C.3	Geometric vs. Topological Components . . . . .	150
<b>XVIII</b>	<b>Vortex Coupling from First Principles</b>	<b>150</b>
<b>D</b>	<b>Derivation of <math>\kappa</math></b>	<b>150</b>
D.1	The Problem with V16's $\kappa$ . . . . .	150
D.2	Helical Vortex Filaments in 4D . . . . .	150
D.3	Mutual Inductance in 4D . . . . .	150
D.4	Far-Field Limit and Force Law . . . . .	151
D.5	Numerical Verification . . . . .	151
<b>E</b>	<b>New Physics from Helical Mode Theory</b>	<b>151</b>
E.1	Force-Law Crossover . . . . .	151
E.2	Mode-Dependent Coupling Constants . . . . .	152
E.3	Spin-Statistics from Angular Interference . . . . .	152
<b>XIX</b>	<b>W-Axis Tension as Derived Quantity</b>	<b>152</b>

<b>F</b>	<b><math>\alpha</math> is Not an Independent Parameter</b>	<b>152</b>
F.1	V16's Tension Force . . . . .	152
F.2	The 4D Origin . . . . .	153
F.3	Scale-Vortex Equivalence as a Theorem . . . . .	153
F.4	Why V16's Constant $\alpha$ Worked . . . . .	154
<b>XX</b>	<b>Synthesis and Predictions</b>	<b>154</b>
<b>G</b>	<b>The Complete One-Parameter Theory</b>	<b>154</b>
G.1	Parameter Reduction History . . . . .	154
G.2	The Derivation Chain . . . . .	154
G.3	Comparison Table . . . . .	154
<b>H</b>	<b>New Predictions</b>	<b>155</b>
H.1	Force-Law Crossover at $d \sim \Delta w$ . . . . .	155
H.2	Mode-Dependent Particle Physics . . . . .	155
H.3	Baryonic Tully-Fisher Relation (Heuristic) . . . . .	155
H.4	Scale-Vortex Equivalence: From Principle to Derived Result . . . . .	155
<b>I</b>	<b>Discussion</b>	<b>155</b>
I.1	Scope of This Work . . . . .	155
I.2	What $\Delta w$ Represents . . . . .	155
I.3	Relation to Other Frameworks . . . . .	156
I.4	Open Questions . . . . .	156
<b>J</b>	<b>Summary of Part A</b>	<b>156</b>
<b>XXI</b>	<b>The Warp Thread Picture</b>	<b>157</b>
<b>K</b>	<b>Core Principle: Vertical Binding and Horizontal Freedom</b>	<b>157</b>
K.1	The Duality of Energy in 4D Pure Space . . . . .	157
K.2	The Cross Structure . . . . .	157
K.3	Connection to V20's Unified Potential . . . . .	158
<b>L</b>	<b>Warp Threads: The Vertical Axis</b>	<b>158</b>
L.1	Definition . . . . .	158
L.2	Four States of W-Axis Engagement . . . . .	158
L.3	What Warp Threads Explain . . . . .	158

<b>M</b>	<b>Decomposition of Gravity</b>	<b>159</b>
M.1	The Problem with “Gravity” . . . . .	159
M.2	Vertical Effect: W-Axis Tension . . . . .	159
M.3	Horizontal Effect: Field Distortion . . . . .	159
M.4	Why Both Share the Same Potential . . . . .	160
<b>N</b>	<b>Light: Horizontally Free Energy</b>	<b>160</b>
N.1	Ontological Definition . . . . .	160
N.2	Consequences of the Definition . . . . .	160
<b>O</b>	<b>Inertia from W-Axis Geometry</b>	<b>161</b>
O.1	The Reconfiguration Cost . . . . .	161
O.2	Geometric Interpretation of the Equivalence Principle . . . . .	161
<b>P</b>	<b>Critical Conditions for Mass Generation</b>	<b>162</b>
P.1	When Does a Thread Stabilize? . . . . .	162
P.2	Toward the Particle Mass Spectrum . . . . .	162
<b>Q</b>	<b>Black Holes as Deep W-Axis Wells</b>	<b>162</b>
Q.1	Reinterpretation . . . . .	162
Q.2	Resolution of Classical Pathologies . . . . .	163
<b>R</b>	<b>Extended Predictions</b>	<b>163</b>
<b>S</b>	<b>Discussion</b>	<b>163</b>
S.1	What V20.2 Achieves . . . . .	163
S.2	Relationship to Existing Theories . . . . .	164
S.3	Open Questions . . . . .	164
<b>T</b>	<b>Conclusion</b>	<b>164</b>
<b>A</b>	<b>Overlap Integral Computation</b>	<b>165</b>
<b>B</b>	<b>Mutual Inductance Derivation</b>	<b>165</b>
<b>C</b>	<b>W-Axis Oscillation Derivation</b>	<b>166</b>
<b>XXII</b>	<b>Rigorous Mathematical Framework</b>	<b>166</b>
<b>XXIII</b>	<b>Central Claims and Definitions</b>	<b>168</b>

<b>D</b>	<b>Scope and Purpose</b>	<b>168</b>
D.1	What This Paper Establishes . . . . .	168
D.2	What This Paper Assumes . . . . .	168
<b>E</b>	<b>Definitions</b>	<b>168</b>
<b>F</b>	<b>Central Theorems</b>	<b>169</b>
<b>XXIV</b>	<b>Gravitational Process Rate: Spatial Interference</b>	<b>170</b>
<b>G</b>	<b>Field Pattern Alteration by Mass-Energy</b>	<b>170</b>
G.1	Physical Picture . . . . .	170
G.2	The Field Distortion Factor . . . . .	170
<b>H</b>	<b>V20.3: Newton’s Constant from 4D Thread Geometry</b>	<b>171</b>
H.1	4D Thread Interaction Energy . . . . .	171
H.2	Newton’s Constant . . . . .	171
H.3	Tension–Interference Decomposition . . . . .	171
H.4	Helical Correction: Mercury Precession . . . . .	172
<b>XXV</b>	<b>Kinematic Process Rate: Trajectory Geometry</b>	<b>172</b>
<b>I</b>	<b>The Setup: Curves in 4D Euclidean Space</b>	<b>172</b>
I.1	Ontological Premise . . . . .	172
I.2	Trajectory Parameterization . . . . .	172
<b>J</b>	<b>The Tilt Angle</b>	<b>173</b>
<b>K</b>	<b>Process Rate from Trajectory Geometry</b>	<b>173</b>
K.1	The Key Physical Principle . . . . .	173
K.2	Justification of Axiom K.1 . . . . .	174
K.3	Proof of Theorem F.1 . . . . .	175
K.4	What Was and Was Not Assumed . . . . .	175
<b>L</b>	<b>On the Arc-Length Parameterization</b>	<b>175</b>
L.1	The Concern . . . . .	175
L.2	The Equivalence . . . . .	176
L.3	What Differs: The Axiom’s Location . . . . .	176
L.4	What This Paper Does and Does Not Claim . . . . .	176

<b>M The Emergence of <math>c</math></b>	<b>177</b>
M.1 Proof of Proposition F.5 . . . . .	177
M.2 Why Light Saturates the Bound . . . . .	177
 <b>XXVI Unification and Experimental Verification</b>	 <b>178</b>
<b>N Proof of the Unified Equation</b>	<b>178</b>
N.1 Independence of the Two Effects . . . . .	178
N.2 Proof of Theorem F.2 . . . . .	178
 <b>O Correspondence with General Relativity</b>	 <b>179</b>
O.1 Proof of Corollary F.3 . . . . .	179
O.2 Proof of Corollary F.4 . . . . .	179
 <b>P Quantitative Verification</b>	 <b>179</b>
P.1 Pound–Rebka Experiment (1959) . . . . .	179
P.2 Hafele–Keating Experiment (1971) . . . . .	180
P.3 GPS Operational Corrections . . . . .	180
 <b>Q Strong-Field Prediction: No Event Horizons</b>	 <b>180</b>
Q.1 GR Prediction . . . . .	181
Q.2 HBR Prediction . . . . .	181
Q.3 Quantitative Estimate . . . . .	181
 <b>XXVII Discussion</b>	 <b>182</b>
<b>R Established vs. Open Results</b>	<b>182</b>
<b>S Relationship to GR</b>	<b>182</b>
<b>T Limitations of This Work</b>	<b>182</b>
 <b>XXVIII Conclusion</b>	 <b>184</b>
<b>U Summary of Results</b>	<b>184</b>
<b>V What V21 Closes</b>	<b>184</b>
<b>W What V22 Must Address</b>	<b>184</b>
<b>A Version History</b>	<b>186</b>



<b>XXIX</b>	<b>Tensor Kinematics in 4D Euclidean Space</b>	<b>186</b>
<b>B</b>	<b>Field Tethering and the Euclidean Spacetime Paradigm</b>	<b>187</b>
B.1	Tethered and Untethered Energy . . . . .	187
B.2	The $W$ -Axis Distance Budget . . . . .	188
<b>C</b>	<b>The 4D Euclidean Rotation Matrix</b>	<b>188</b>
<b>D</b>	<b>Derivation of Kinematic Effects</b>	<b>189</b>
D.1	Lengths in Euclidean 4D (Length Contraction) . . . . .	189
D.2	Relativity of Simultaneity . . . . .	189
D.3	Time Dilation . . . . .	190
D.4	Rest Energy: $E_0 = mc^2$ . . . . .	190
D.5	The Equivalence Principle and Inertia . . . . .	190
<b>E</b>	<b><math>W</math>-Axis Anchor Asymmetry and the Arrow of Time</b>	<b>191</b>
<b>F</b>	<b>Four-Vector Tensors in Euclidean Space</b>	<b>191</b>
F.1	Four-Momentum . . . . .	191
<b>G</b>	<b>Summary: All of SR from the Fountain</b>	<b>191</b>
<b>XXX</b>	<b>Lagrangian and Hamiltonian Formulation</b>	<b>192</b>
<b>H</b>	<b>Motivation: From Force Laws to Action Principles</b>	<b>193</b>
<b>I</b>	<b>Generalized Coordinates in 4D Euclidean Space</b>	<b>193</b>
I.1	Configuration Space . . . . .	193
I.2	Brane Confinement Constraint . . . . .	193
<b>J</b>	<b>The HBR Lagrangian</b>	<b>194</b>
J.1	Kinetic Energy . . . . .	194
J.2	HBR Potential Energy . . . . .	194
J.2.1	Gravitational Potential (Thread–Thread Interaction) . . . . .	194
J.2.2	Vortex Repulsion Potential (Helical Mode Interaction) . . . . .	194
J.2.3	$W$ -Axis Tension Potential (Geometric Tether) . . . . .	195
J.3	The Complete Lagrangian . . . . .	195
<b>K</b>	<b>Euler–Lagrange Equations and Recovery of HBR Force Laws</b>	<b>195</b>
K.1	Derivation . . . . .	195
K.2	Combined Equation of Motion . . . . .	196

<b>L</b>	<b>Noether's Theorem and Conservation Laws</b>	<b>196</b>
L.1	Time Translation Invariance $\rightarrow$ Energy Conservation . . . . .	196
L.2	Spatial Translation Invariance $\rightarrow$ Momentum Conservation . . . . .	196
L.3	Rotational Invariance $\rightarrow$ Angular Momentum Conservation . . . . .	196
L.4	Summary of Symmetries and Conservation Laws . . . . .	197
<b>M</b>	<b>Hamiltonian Formulation</b>	<b>197</b>
M.1	Canonical Momenta . . . . .	197
M.2	Hamiltonian via Legendre Transform . . . . .	197
M.3	Hamilton's Equations . . . . .	197
M.4	Significance for Quantization . . . . .	198
<b>N</b>	<b>Field Lagrangian Density</b>	<b>198</b>
N.1	Fundamental Constants . . . . .	198
N.2	HBR Scalar Action . . . . .	198
N.3	Physical Origin of Each Term . . . . .	199
<b>O</b>	<b>Theorem 1: Newtonian Limit</b>	<b>199</b>
<b>P</b>	<b>Theorem 2: No Event Horizons</b>	<b>200</b>
<b>Q</b>	<b>Discussion: Established and Open Results</b>	<b>200</b>
Q.1	Established Results . . . . .	200
Q.2	Open Problems . . . . .	201
<b>XXXI</b>	<b>Spatial Metric and Strong-Field Observables</b>	<b>201</b>
<b>R</b>	<b>The Missing Piece: Spatial Metric from Euclidean Embedding</b>	<b>201</b>
R.1	The 4D Euclidean Deformation . . . . .	201
<b>S</b>	<b>Derivation of <math>g_{rr} = 1/\Phi^2(r)</math></b>	<b>202</b>
<b>T</b>	<b>Null Geodesic Structure and Shapiro Delay</b>	<b>202</b>
<b>U</b>	<b>Gravitational Wave Compatibility and B-Parameter</b>	<b>203</b>
<b>V</b>	<b>Summary of Strong-Field Findings</b>	<b>203</b>
<b>XXXII</b>	<b>Compact Objects Without Singularities</b>	<b>204</b>

<b>W Introduction</b>	<b>205</b>
W.1 The Singularity Problem . . . . .	205
W.2 The Jet Collimation Problem . . . . .	205
W.3 The Information Paradox . . . . .	205
W.4 Scope and Thesis . . . . .	205
<b>X Foundations: The Fountain Mechanism in HBR</b>	<b>206</b>
X.1 The Brane in 4-Dimensional Euclidean Space . . . . .	206
X.2 The Effective Spacetime Metric . . . . .	207
X.3 Field Distortion and the No-Horizon Theorem . . . . .	208
X.4 Brane Saturation . . . . .	208
<b>Y The Exhausted Fountain: Black Holes Reinterpreted</b>	<b>209</b>
Y.1 The Cessation of Energy Supply . . . . .	209
Y.2 Connection to EHT Observations . . . . .	210
Y.3 The Galaxy Lifecycle . . . . .	210
<b>Z The Information Paradox Dissolves</b>	<b>211</b>
Z.1 The Standard Paradox . . . . .	211
Z.2 HBR Resolution: Eliminating the Premises . . . . .	211
Z.3 Where Does the Information Go? . . . . .	212
Z.4 Comparison with Existing Approaches . . . . .	212
<b>Relativistic Jets: W-Axis Overflow</b>	<b>212</b>
.1 Three Unsolved Problems of Jets . . . . .	212
.2 The Release Mechanism . . . . .	213
.3 Jet Power Scaling . . . . .	214
.4 The Unified Jet Hierarchy . . . . .	214
<b>Statistical Verification</b>	<b>215</b>
.1 Data and Methodology . . . . .	215
.2 Correlation Analysis . . . . .	216
.3 Partial Correlation: The Decisive Test . . . . .	216
.4 Sensitivity Analysis . . . . .	216
.5 Non-Black-Hole Jets: The Structural Argument . . . . .	217

<b>Discussion</b>	<b>217</b>
.1 Falsifiable Predictions . . . . .	217
.2 The Black Hole Identification Bias . . . . .	218
.3 The Fundamental Plane Connection . . . . .	219
.4 Established and Open Results . . . . .	219
.5 Limitations . . . . .	220
<b>Conclusion</b>	<b>221</b>
<b>Geometric Reinterpretation of Binary Black Hole Mergers</b>	<b>222</b>
.1 Introduction and positioning in the master . . . . .	222
.2 Rigidity loss in the exhausted state . . . . .	223
.3 Reduction-flow synchronization . . . . .	224
.4 Fit to the GW150914 waveform . . . . .	225
.5 $W^+$ dissipation and the energy budget . . . . .	226
.6 Observational predictions and catalogue comparison . . . . .	226
.7 HBR vs GR — observational contrast . . . . .	227
.8 Discussion and limitations . . . . .	228
.9 Conclusion of Part 18 . . . . .	228
.10 Numerical comparison of $V_{\text{eff}}(d)$ . . . . .	229
<b>A Structural Origin of the Born Rule via Measure Uniqueness on <math>\kappa</math>-Space</b>	<b>230</b>
A.1 Introduction and scope . . . . .	230
A.2 $\kappa$ -space and the bulk inner product . . . . .	230
A.3 Geometric requirements for the probability measure . . . . .	231
A.4 Uniqueness of the measure and the Born rule . . . . .	231
A.5 Conclusion . . . . .	233
<b>B Rigorous Formulation of Observation-Contact Separation via Harmonic Analysis</b>	<b>233</b>
B.1 Introduction . . . . .	233
B.2 Interaction structure and the overlap function . . . . .	233
B.3 Function space and compact support . . . . .	234
B.4 Qualitative suppression: the Riemann–Lebesgue lemma . . . . .	234
B.5 Quantitative leading rate: the sinc form . . . . .	234
B.6 Conclusion of physical regimes . . . . .	235
<b>C SPARC fits and saturation-law equivalence</b>	<b>235</b>

## Part I

# Declaration of Viewpoint Hierarchy: Bulk vs Brane Observer

## 1 Epistemological Declaration

This part does not introduce new mathematics of Hyperbrane Relativity (HBR); it makes explicit the **hierarchy of viewpoints** required to interpret the theory. HBR simultaneously employs two physically real perspectives: a four-dimensional Euclidean space  $\mathbb{E}^4$  (the **bulk**) and a three-dimensional brane  $\mathcal{B}$  embedded in it, on which local observers (ourselves) reside (the **brane viewpoint**). Both perspectives are physical, but the meaning of “time,” “motion,” and “energy flow” differs between them.

An instructive analogy is the relation between special relativity (SR) and general relativity (GR). In that sense, the bulk viewpoint plays the role of a global, structural (GR-like) description, while the brane viewpoint plays the role of a local, observer-fixed (SR-like) description. *Every equation in this book becomes correctly interpretable only once its viewpoint is declared.* This part declares that convention.

*Remark 1.1* (Role of this part). The subsequent parts (Part I onward) develop the mathematical structures of HBR—fountains, the  $\kappa K^2$  bending rigidity, the process-rate ratio  $\mathcal{R}$ , the emergent metric  $g_{\mu\nu}$ , etc. This part introduces no new physical quantities; it only attaches a **viewpoint label** to existing concepts so that readers and external reviewers cannot mistake one viewpoint for the other.

## 2 Bulk Perspective

**Standpoint:** a global, four-dimensional view from outside the brane, i.e. a mathematical observer in  $\mathbb{E}^4$ . Physically this amounts to treating the brane  $\mathcal{B}$  itself as a single hypersurface and watching it evolve.

**Objects described:** the motion, shape, and W-axis displacement of the brane  $\mathcal{B}$  itself. Internal microprocesses (atomic transitions, laboratory clocks, etc.) are secondary from this viewpoint.

**How it looks:** the brane is a hypersurface sweeping in the W— direction. The W axis is *not* a time axis; it is *one of the spatial dimensions of the bulk*, and the brane persists while sweeping through it.

**Time parameter:** bulk arc length  $w$  (or equivalently an absolute bulk time  $\tau$ ). This parameter tracks the progression of the brane along the W axis and is independent of any observer’s clock.

**Key physical quantities:**

- intrinsic bending rigidity  $\kappa K^2$  (square of the brane’s extrinsic curvature),
- fountain flux  $\mathcal{F}$  (geometric flux into the W direction),
- reduction-flow vector field  $\mathbf{v}_{w+}$  (the W+-directed geometric flow).

**Cross-references:** the physical reality of the 4D bulk is argued in Part IV (Quantum Foundations) and the foundational framework is laid out in phase2 sec2 (Framework).

### 3 Brane Observer Perspective

**Standpoint:** a local observer confined to the brane  $\mathcal{B}$ —i.e. ourselves and our laboratory apparatus. No direct measurement of where or how  $\mathcal{B}$  is moving through  $\mathbb{E}^4$  is available.

**Objects described:** physical processes internal to the brane (atomic transition times, frequencies, gravitational acceleration, the speed of light as measured locally, etc.).

**How it looks:** the brane appears as a static 3D universe, and **energy appears to “flow in” from the  $W+$  direction**. Time elapses internally, and this internal passage is what we call “time” in daily life.

**Time parameter:** brane proper time  $t$ . This is an *emergent* quantity derived from the bulk progression  $w$  via the bridge relation in the next section.

**Key physical quantities:**

- the observed metric  $g_{\mu\nu}$ ,
- the speed of light  $c$  (as measured within the brane),
- gravitational acceleration  $g_{\text{eff}}$ ,
- the process-rate ratio  $\mathcal{R}$  (formalized in Part 13).

**Cross-references:** the observer-constraint principle is discussed in Part VIII (Discussion), and the mathematical framework of the brane viewpoint, including the process-rate ratio  $\mathcal{R}$ , is developed in Part 13 (Rigorous Mathematical Framework).

### 4 Bridge Relation: Connecting the Two Perspectives

The single most important relation connecting the two viewpoints is

$$\boxed{dt = \frac{dw}{v_w}} \quad \text{or equivalently} \quad dw = v_w dt. \quad (1)$$

Here  $t$  is brane proper time (brane viewpoint),  $w$  is the bulk arc length (bulk viewpoint), and  $v_w$  is the  $W+$ -directed reduction-flow speed. In general one writes

$$v_w = c \cos \theta, \quad (2)$$

where  $\theta$  is the tilt angle between the brane normal and the  $W$  axis (V19 formulation onward).

Relation (1) is the **geometric emergence of time** in HBR in its shortest form: *time is the bulk progression rewritten by an observer in their own units*.

*Remark 4.1* (Consistency with the process-rate ratio  $\mathcal{R}$  of Part 13). Part 13 formalises, in the weak-field, low-tilt regime, the relation

$$d\tau_{\text{obs}} = \mathcal{R} dt, \quad \mathcal{R}(r, \theta) = \Phi(r) \cos \theta$$

between the clocks of two brane observers at different positions and tilts. This is a comparison *within* the brane viewpoint of Equation (1), and it is fully consistent with it:  $\Phi(r)$  captures the spatial interference (field distortion), while  $\cos \theta$  captures the same geometric  $W$ -axis projection as in Equation (2).

## Viewpoint comparison table

**Table 1:** Comparison of the bulk and brane viewpoints in HBR.

Aspect	Bulk viewpoint	Brane viewpoint	Bridge
Standpoint	External to $\mathbb{E}^4$	Observer inside $\mathcal{B}$	—
Time	Arc length $w$ (or $\tau$ )	Proper time $t$	$dt = dw/v_w$
Brane state	Hypersurface moving in $W$	Static 3D universe	Coord. change
Energy	Geometric flow along $W$	Inflow from $W+$	Same phenomenon
Relativity analogue	GR-like (global)	SR-like (local)	—
Example phenomenon	Overall brane generation	Atomic transition time	Process rate $\mathcal{R}$

## 5 SR $\leftrightarrow$ GR Analogy: Epistemological Placement

SR is the theory used by a **local, inertial observer**; GR adds to it the **dynamical behaviour of the background geometry**. An analogous division of labour holds in HBR:

- The **brane viewpoint** describes the local physics accessible to us (SR-like role). The observer is confined to  $\mathcal{B}$  and measures time, motion, and the metric internally.
- The **bulk viewpoint** describes the global structure of the universe (GR-like role, but with a Euclidean  $\mathbb{E}^4$  background). It tracks how  $\mathcal{B}$  itself moves through  $\mathbb{E}^4$  and how geometric energy flux is distributed.

We emphasise that this is a *formal correspondence*, not an extension of GR. The HBR bulk is  $\mathbb{E}^4$  with a positive-definite Euclidean metric, whereas the GR background is a pseudo-Riemannian (Lorentzian) manifold. In HBR the Lorentzian signature is not fundamental; it *emerges* on the brane viewpoint (see Parts 13 and 14).

**Always declare the viewpoint under which an equation is written:** this is the decisive rule for correctly interpreting HBR. Readers comparing isolated HBR expressions with GR or quantum field theory should, as a first step, identify which viewpoint the expression belongs to.

## 6 Conventions Used Throughout This Book

Unless stated otherwise, the following conventions apply throughout this book:

1. **The time derivative  $d/dt$  is taken with respect to brane proper time** (brane viewpoint).
2. **The W-axis derivative  $d/dw$  is taken with respect to the bulk arc length** (bulk viewpoint).
3. **“Observer” means a brane observer** unless explicitly qualified as “bulk observer” or “external to  $\mathbb{E}^4$ ”.
4. **The words “progression” and “motion” are viewpoint-dependent:** the W-axis progression of the brane itself is bulk-viewpoint language, while the motion of a particle within

the brane is brane-viewpoint language. Where ambiguous, the relevant section makes the choice explicit.

5. **Terminology is fixed:** “bulk” refers to  $\mathbb{E}^4$  as an external structure, “brane” refers to the 3D hypersurface  $\mathcal{B}$ . Variants such as “brain”, “bulk space”, “higher dimension”, etc. are not used in this book (direct quotations and metaphorical passages excepted).

These conventions apply to all of Parts 1–17 and phase2. Each subsequent part that relies on a specific viewpoint (e.g. Part 4 for the reality of the bulk, Part 8 for the observer-constraint principle, Part 13 for the process-rate ratio) places a short back-reference to this Part 0 at its opening.

## Part II

# The Cosmic Architecture

## 7 Introduction: The Paradigm Shift

### 7.1 From Spacetime to Pure Space

For over a century, physics has operated within the spacetime paradigm: our universe consists of three spatial dimensions and one temporal dimension (3+1). Time is treated as a coordinate, and events occur at specific points  $(x, y, z, t)$  in this four-dimensional manifold.

Hyperbrane Relativity proposes a fundamental reinterpretation: **the universe consists of four spatial dimensions**, with time emerging as a dynamic property rather than a fundamental coordinate.

**Principle 7.1** (Pure 4D Space Paradigm). The physical universe is embedded in a pure 4-dimensional Euclidean space with coordinates  $(x, y, z, w)$ , where:

- $x, y, z$ : Standard spatial dimensions (observable on our brane)
- $w$ : Scale dimension (W-axis), representing geometric depth in the bulk
- Time: Not a coordinate axis, but the rate of change of brane state as it evolves through the bulk

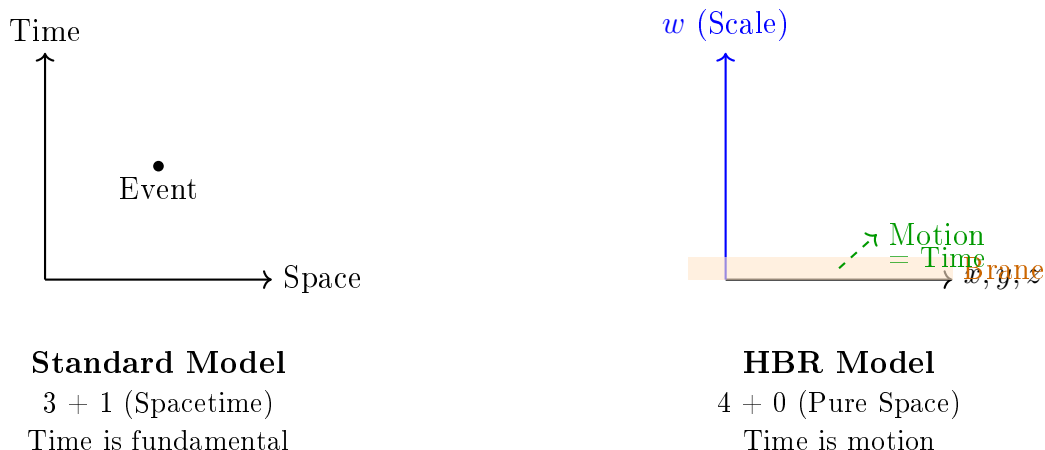


**Figure 1:** Paradigm shift: Spacetime (3+1) versus Pure Space (4+0). In HBR, time emerges as the dynamic evolution of the brane through the bulk, rather than being a fundamental dimension.



## 7.2 What This Means for Physics

This paradigm shift has profound consequences:

1. **Time is emergent:** The brane translates uniformly along  $-W$  at  $v_{\text{brane}} \ll c$ , and this translation drives continuous gate-rate-converted energy inflow from  $W^-$  at speed  $c$ . The “flow of time” is the continuation of this inflow process. Gravitational time dilation reflects local modulation of inflow density.
2. **Quantum weirdness is geometric:** Wave-particle duality, uncertainty, and entanglement emerge from observing extended W-axis structures through a limited cross-section.
3. **Dark matter is unnecessary:** The “missing mass” in galaxies is a cross-sectional observation artifact of W-axis tension, not invisible particles.
4. **Rotation is fundamental:** Angular momentum at all scales—from electron spin to galactic rotation—has a common geometric origin in W-axis dynamics.

## 7.3 Historical Development: V13 to V28

HBR has evolved through multiple versions:

**Table 2:** Evolution of Hyperbrane Relativity

Version	Key Contribution
V13	Initial proposal: Pure 4D space, scale-lens mechanism for flat rotation curves
V14	Scale projection formalism, tanh profile derivation
V15	Time as emergent motion, Hubble constant derivation ( $H_0 \approx 70.9$ km/s/Mpc), thermodynamic foundations
V16	Vortex dynamics, three-force unification, scale-vortex equivalence, cross-sectional quantum mechanics
V17–V18	Self-organization, mathematical framework consolidation
V19–V20	Geometric foundation, thread geometry, unified repulsive coefficient $C_{\text{eff}}$
V21–V22	Tensor kinematics, 4D Euclidean derivation of Lorentz transformations
V23	Complete Master Edition: integration of Parts I–XIV, MCMC validation
V24	Energy inflow picture introduced; field Lagrangian density; Theorem 1 (Newtonian limit), Theorem 2 (No event horizons); real SPARC 171-galaxy MCMC
V25	Spatial metric and strong-field observables (Part XVI); reconciliation of brane translation with energy inflow (translation drives the gate, no static-brane assumption)
V26	Compact-object reformulation as Exhausted Fountains (Part XVII); merger synchrony (Part XVIII); EN/JP master edition consolidation
V27	Born-rule and OCS theorem appendices (A and B); Japanese SPARC appendix; reconciliation of all parts under uniform-translation ontology
V28	<b>Core Novelty 9 introduced: brane thickness <math>\Delta w</math> as universal crossover scale unifying near/far force-law regimes (<math>1/r^4 \leftrightarrow 1/r^3</math>) with Observation–Contact Separation regimes (<math> \Delta\kappa L \lesssim 1 \leftrightarrow \gg 1</math>); HBR established as one-scale theory with cross-regime falsifiability</b>

## 7.4 What's New in the Complete Master Edition (V28)

This edition integrates all previous results and introduces fundamental theoretical advances:

1. **Uniform brane translation drives energy inflow (V25–V27 ontology):** The 3-brane translates uniformly along  $-W$  at  $v_{\text{brane}} \ll c$ . The dimensional gate at the  $W^-$  boundary rate-converts this translation into energy inflow at gate speed  $c$  ( $|\mathbf{U}_{\text{inflow}}|^2 = c^2$ ). Time is the continuation of this gate-driven inflow, not a fundamental dimension. This synthesis supersedes the V24 “static brane” description, which is recovered as the brane-internal limit where translation rate is observationally constant.
2. **Matter as saturation pattern:** Matter = energy inflow exceeding the critical density  $\varepsilon_c$ . Light = unsaturated energy. Vacuum = no inflow.
3. **Field Lagrangian density:**  $\mathcal{L} = \frac{1}{2}T_0(\partial_w\Phi)^2 + \frac{1}{2}T_0(\nabla\Phi)^2 - g_0\varepsilon\Phi - \frac{1}{4}\lambda_0(\Phi^2 - \Phi_0^2)^2$
4. **Theorem 1 — Newtonian limit:**  $G = g_0/(4\pi T_0)$  derived from the field Lagrangian

5. **Theorem 2 — No event horizons:**  $\Phi > 0$  wherever matter exists; horizon formation is logically impossible
6. **Real SPARC MCMC (171 galaxies):** HBR preferred over MOND in 89% and over NFW in 74% of galaxies
7. **Particle & Hamiltonian Lagrangian:** All three HBR forces from a single action principle, with Noether conservation laws

## 7.5 Structure of This Paper

**Part I** (this part) establishes the foundational architecture: the volumetric brane, W-axis geometry, energy inflow, and the bicone structure.

**Part II** introduces vortex dynamics: matter as helical structures, the three-force law, and the scale-vortex equivalence principle.

**Part III** applies these concepts to multi-body gravitational systems, demonstrating complete stabilization of the three-body problem through numerical simulations.

**Part IV** develops quantum mechanics from cross-sectional geometry, including the saturation picture for matter vs. light.

**Part V** applies W-axis tension to galactic dynamics, reproducing flat rotation curves without dark matter, validated against 171 real SPARC galaxies via MCMC.

**Part VI** extends to unified cosmology, deriving the Hubble constant and explaining dark energy as geometric expansion.

**Part VII** presents experimental predictions and falsifiability criteria.

**Part VIII** discusses implications and compares HBR with alternative theories.

**Part IX** concludes with a synthesis of results and future directions.

**Part X–XI** develop self-organization principles and the geometric foundation.

**Part XII** establishes thread geometry and the unified repulsive coefficient  $C_{\text{eff}}$ .

**Part XIII** provides the rigorous mathematical framework.

**Part XIV** derives Lorentz transformations, time dilation, and length contraction from pure 4D Euclidean rotations.

**Part XV** establishes the Lagrangian and Hamiltonian formulation, including the field Lagrangian density, Theorem 1 (Newtonian limit), and Theorem 2 (No event horizons).

## 8 The Volumetric Brane

### 8.1 Beyond the Thin-Brane Approximation

Standard braneworld models often treat our universe as a zero-thickness membrane embedded in higher dimensions. HBR departs from this: **our universe is a volumetric 3D structure** with finite “thickness” in the W-axis direction.

**Definition 8.1** (Volumetric Brane). The observable universe is a 3-dimensional volume embedded in 4D space, with:

- Spatial extent: Standard cosmological horizon  $\sim 10^{26}$  m
- W-axis thickness:  $\Delta w \sim w_0$ , the characteristic W-axis scale

The brane is not a static surface but a dynamic, evolving structure.

## 8.2 Energy and Matter Generation

In HBR, the brane is not passive. Energy and matter arise from the **geometric interaction** between the brane and the bulk:

**Postulate 8.2** (Brane-Bulk Interaction). Matter and energy on the brane are sustained by continuous interaction with the bulk. Specifically:

$$\rho_{\text{matter}} \propto \left| \frac{\partial \Phi_{\text{bulk}}}{\partial w} \right|^2 \quad (3)$$

where  $\Phi_{\text{bulk}}$  is the bulk scalar field.

This has a profound implication: **matter is not a pre-existing substance but an ongoing process**. The brane does not merely “contain” particles; it *generates* them through geometric dynamics.

## 8.3 The Brane as Interface

The brane at  $w = 0$  serves as the **interface** between two regions:

- $w < 0$  ( $W^-$ ): The quantum source, where energy emanates
- $w > 0$  ( $W^+$ ): The cosmic expanse, where the universe expands

Observations are inherently limited to this cross-section—we cannot directly “see” into the bulk, only infer its presence through cross-sectional effects.

# 9 The W-Axis: Scale Dimension

## 9.1 Physical Interpretation

The W-axis is not merely a mathematical construct but represents **geometric scale**—a dimension along which physical structures extend and contract.

**Principle 9.1** (W-Axis as Scale). Motion along the W-axis corresponds to changes in effective scale. Specifically:

- Negative  $w$  (toward  $W^-$ ): Smaller scales, higher energy density (quantum regime)
- Positive  $w$  (toward  $W^+$ ): Larger scales, lower energy density (cosmic regime)
- The brane ( $w = 0$ ): Our observable “present” scale

## 9.2 W-Axis Metric

The W-axis is not flat but has intrinsic curvature. We model this via a position-dependent metric:

$$ds^2 = dx^2 + dy^2 + dz^2 + g_{ww}(w) dw^2 \quad (4)$$

where the W-axis metric component is:

$$g_{ww}(w) = \left( 1 + \frac{w}{w_0} \right)^2 \quad (5)$$

This produces the bicone geometry described in Section 4.

## 9.3 Observational Consequences

Objects at different  $W$ -coordinates are observed at different *effective scales*. This produces:

- **Redshift:** Not only from recession velocity but also from  $W$ -depth
- **Scale integration effects:** Cumulative distortions when observing across  $W$ -gradients
- **Apparent acceleration:** The “dark energy” effect from  $W+$  expansion

## 10 Time as Continuous Energy Inflow

### 10.1 The Central Insight (V25–V27 Synthesis)

**Principle 10.1** (Time as Gate-Driven Energy Inflow). Time is not a dimension but a **measure of sustained energy inflow**. The brane translates uniformly along  $-W$  at  $v_{\text{brane}} \ll c$ , and this translation drives the dimensional gate at the  $W^-$  boundary, which rate-converts the translation into energy inflow at gate speed  $c$ . The “passage of time” is the continuation of this gate-driven inflow process.

**Three-stage evolution of the temporal-ontology picture:**

Aspect	V13–V22 (Old)	V24 (Intermediate)	V25–V27 (Current)
Brane motion	Brane moves along $w$ at $c$	Brane is static	Brane translates uniformly at $v_{\text{brane}} \ll c$
Energy	Carried by moving brane	Flows in from $W^-$ at $c$ (origin unspecified)	Brane translation drives gate inflow at $c$
$v^2 + v_w^2 = c^2$	Brane-frame velocity constraint	Energy allocation rule	Energy allocation rule (V24 result preserved)
Time	Brane’s $w$ -motion	Continuation of inflow	Continuation of gate-driven inflow
$ u  = c$ subject	All objects on brane	Inflow energy	Gate inflow flux ( $ \mathbf{U}_{\text{inflow}} ^2 = c^2$ )

The V25–V27 picture is the consistent synthesis: brane translation supplies the kinematic substrate that V24’s static-brane picture left unexplained, while preserving every V24 result (field Lagrangian, Theorem 1, Theorem 2, SPARC MCMC) under the new ontology.

Mathematically, the inflow defines an arc-length parameter:

$$dt = \frac{ds}{c} \quad \text{where } ds \text{ is the 4D path length of the energy flow} \quad (6)$$

### 10.2 Gravitational Time Dilation

In HBR, gravitational time dilation arises from modulation of the inflow density. Near a massive object, the local energy density distorts the inflow pattern, reducing the effective rate of state evolution.

**Theorem 10.2** (Time Dilation from Inflow Modulation). *The proper time  $\tau$  measured by an observer at position  $\mathbf{r}$  relative to a distant observer is:*

$$\frac{d\tau}{dt} = \sqrt{g_{00}(\mathbf{r})} = \sqrt{1 - \frac{2GM}{rc^2} \cdot f(\mathbf{r})} \quad (7)$$

where  $f(\mathbf{r})$  encodes the local inflow density modulation due to the gravitational field.

This recovers standard general relativistic time dilation in the weak-field limit  $f(\mathbf{r}) \rightarrow 1$ , while allowing deviations measurable in precision tests.

### 10.3 No “Block Universe”

In standard spacetime, past, present, and future all “exist” simultaneously in the block universe. HBR rejects this: **only the present brane state exists**. The past corresponds to energy that has already flowed through; the future has not yet been generated by incoming energy.

### 10.4 Matter as Sustained Process

A profound consequence of the inflow picture: **matter is not a substance but a sustained pattern of energy inflow**. If the inflow from  $W^-$  were to cease, all matter would immediately dissolve. This has direct implications for black hole physics (see Part XV, Theorem 2: No Event Horizons).

## 11 The Cross Structure

### 11.1 The Breath of the Universe

HBR introduces the **Cross Structure** as a conceptual model for energy flow:

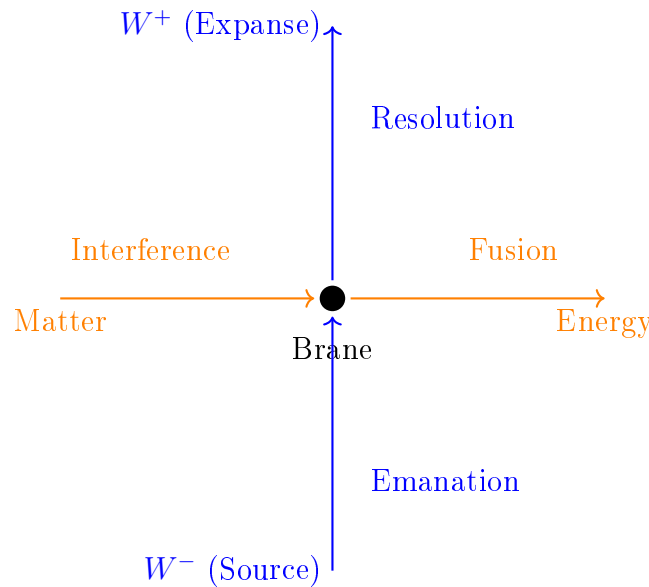


**Figure 2:** The Cross Structure: Energy emanates from  $W^-$ , interferes on the brane to create reality, and resolves toward  $W^+$ .

### 11.2 Vertical Flow: Emanation and Resolution

- **Emanation** ( $W^- \rightarrow \text{Brane}$ ): Energy flows from the quantum source, creating the potential for matter
- **Resolution** ( $\text{Brane} \rightarrow W^+$ ): Structures evolve and dissolve into the cosmic expanse

## 11.3 Horizontal Flow: Interference and Fusion

- **Interference:** Wave-like energy patterns overlap on the brane, creating stable “standing waves”—what we perceive as particles
- **Fusion:** Matter and energy recombine, releasing energy back into the bulk

This cross structure suggests that the universe operates through continuous **cycles of creation and dissolution**, rather than a one-time Big Bang followed by heat death.

## 12 The Bicone Geometry

### 12.1 Dual Structure of the W-Axis

The W-axis is not a simple line but has a **bicone geometry**:

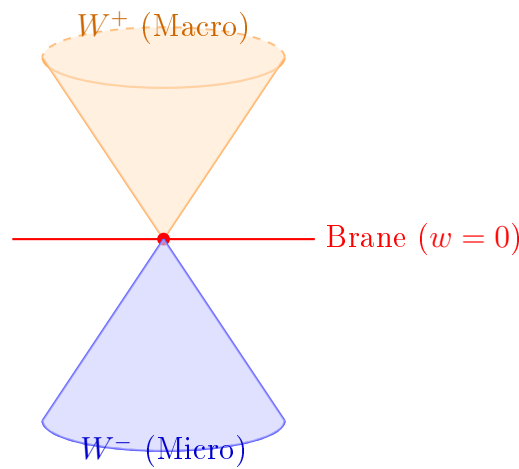


**Figure 3:** The Bicone Geometry:  $W^-$  represents the quantum source;  $W^+$  represents cosmic expansion. The brane exists at the apex.

### 12.2 $W^-$ : The Quantum Source

The region  $w < 0$  is characterized by:

- **High energy density:** Approaching Planck scale as  $w \rightarrow -\infty$
- **Quantum fluctuations:** The source of vacuum energy
- **Vortex formation:** Matter originates as helical vortices extending from  $W^-$

### 12.3 $W^+$ : The Cosmic Expanse

The region  $w > 0$  is characterized by:

- **Low energy density:** Decreasing as  $w \rightarrow +\infty$
- **Geometric expansion:** The origin of Hubble flow
- **Dark energy:** Not a substance but the volumetric expansion of the  $W^+$  cone

### 12.4 The Zero Point: Our Observable Universe

At  $w = 0$ , the brane serves as the **interface** between these two regimes. This is where:

- Quantum energy ( $W^-$ ) manifests as classical matter
- Cosmic expansion ( $W^+$ ) drives the Hubble flow
- Observations are constrained to cross-sectional slices

## 12.5 Connection to Observable Physics

**Table 3:** Bicone Structure and Physical Phenomena

Region	Physical Manifestation
$W^-$	Quantum vacuum energy, particle creation, spin, Pauli exclusion
$w = 0$	Observable matter, classical physics, measurement interface
$W^+$	Cosmic expansion, Hubble flow, dark energy, large-scale structure

## 13 Summary of Part I

We have established the foundational architecture of HBR:

1. **Pure 4D Space:** The universe is embedded in four spatial dimensions ( $4+0$ ), not spacetime ( $3+1$ )
2. **Volumetric Brane:** Our reality is a 3D volume with finite  $W$ -axis thickness, not a zero-thickness membrane
3. **Time as Inflow:** The “flow of time” is the continuous energy inflow from  $W^-$ , not a fundamental dimension or brane motion
4. **Cross Structure:** Energy flows from  $W^-$  (source), interferes on the brane (reality), and resolves to  $W^+$  (expanse)
5. **Bicone Geometry:** The  $W$ -axis has dual structure: quantum source ( $W^-$ ) and cosmic expansion ( $W^+$ ), with the observable universe at  $w = 0$

## 14 The Fundamental Scale: Brane Thickness $\Delta w$ as Universal Crossover Geometry

A single geometric scale—the brane thickness  $\Delta w$ —governs every crossover in HBR. This is not a coincidence but a structural feature of the theory: two HBR objects’  $W$ -axis helical threads overlap if and only if their brane-horizontal separation is less than  $\Delta w$ . This single geometric criterion controls two superficially distinct phenomena—the strong-field force-law crossover (Part XII, Part XVII) and the Observation–Contact Separation underlying quantum measurement (Appendix B). Both are dual expressions of the same thread-overlap fact.

**Principle 14.1** ( $\Delta w$  as universal crossover scale). For any pair of HBR objects (particles, detectors, vortex structures), the brane thickness  $\Delta w$  defines the boundary between two regimes:

1. **Force-law crossover.** The repulsive force satisfies

$$F_{\text{repel}}(r) \sim \begin{cases} D/r^4 & (r \lesssim \Delta w; \text{ threads overlap; full 4D cross-structure}) \\ 2C_{\text{eff}}/r^3 & (r \gg \Delta w; \text{ threads disjoint; W-modes averaged}) \end{cases}$$



The far-field  $1/r^3$  correction (Part XII) arises from W-averaged scale-tension; the near-field  $1/r^4$  singularity-avoidance term (Part XVII) arises from the resolved helical-mode interaction across both W-vertical and brane-horizontal axes.

**2. Observation–Contact Separation (OCS).** The coupling between a system and an apparatus satisfies

$$\text{coupling regime} \sim \begin{cases} \text{contact, full back-action} & (|\Delta\kappa| L \lesssim 1) \\ \text{observation, zero-mode only} & (|\Delta\kappa| L \gg 1) \end{cases}$$

where  $L$  is the W-axis support length of the apparatus, with  $L \sim \Delta w$  for any compact detector (Appendix B). The contact regime corresponds to direct  $\kappa$ -resonance; the observation regime to Riemann–Lebesgue suppression of off-resonant modes.

**Unification.** Both regimes are dual expressions of the same geometric fact: at scales below  $\Delta w$ , an observer sees the resolved W-thread structure (contact / strong-coupling); at scales above  $\Delta w$ , only the brane-averaged effective 3D physics is accessible (observation / weak-coupling).

**Implication.** HBR is a one-scale theory:  $\Delta w$  fixes both the strong-field force regime (singularity avoidance, Part XVII) and the quantum measurement regime (Born rule plus OCS, Appendix A–B). Any independent observational determination of  $\Delta w$  from one regime constrains the other. This cross-regime falsifiability is a structural consequence of HBR’s geometric origin and has no analogue in either General Relativity (which has no fundamental length) or in the Standard Model (where electroweak, strong, and Planck scales are independent).

## Part III

# 4D Spatial Vortex Dynamics

## 15 Matter as Helical Vortex Structures

### 15.1 The Fundamental Vortex Postulate

Standard physics treats particles as point-like entities (in quantum field theory) or as localized wave packets (in quantum mechanics). HBR proposes a radically different picture:

**Postulate 15.1** (Matter as W-Axis Vortex). Matter is not a point-like entity but a **helical vortex structure** extending along the W-axis. What we observe as “particles” on the 3D brane are cross-sectional intersections of these vortices at  $w = 0$ .

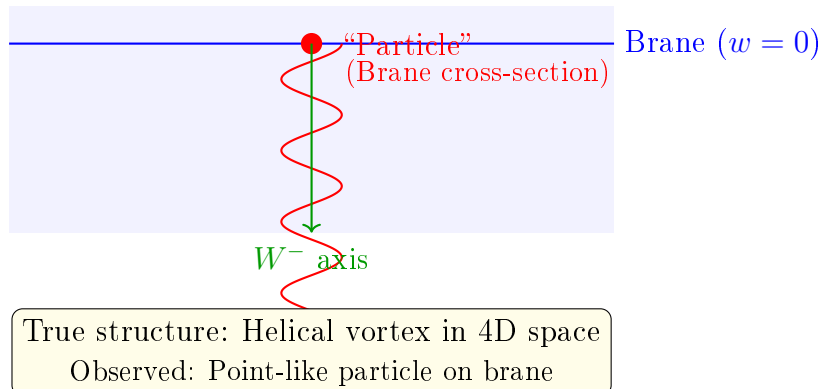


**Figure 4:** Matter as W-axis vortex: The “particle” we observe is merely the cross-section where the helix intersects our brane. The true structure extends into the W-axis bulk.

## 15.2 Physical Properties from Geometry

The helical vortex structure naturally explains fundamental properties:

1. **Mass:** Energy density integrated along the W-axis

$$m = \int_{-\infty}^0 \rho_{\text{vortex}}(w) dw \quad (8)$$

2. **Spin:** Winding number of the helix (topological charge)

$$S = n \cdot \frac{\hbar}{2} \quad \text{where } n \in \mathbb{Z}/2 \quad (9)$$

3. **Charge:** Circulation strength around the vortex core

$$q \propto \oint \mathbf{A}_{\text{vortex}} \cdot d\mathbf{l} \quad (10)$$

## 15.3 The Helical Equation

A vortex structure along the W-axis can be parameterized as:

$$\begin{cases} x(w) = R(w) \cos(\kappa w) \\ y(w) = R(w) \sin(\kappa w) \\ z(w) = 0 \end{cases} \quad (11)$$

where:

- $R(w)$ : Radial profile (vortex size as function of W-depth)
- $\kappa$ : Helical pitch (determines momentum)
- $w < 0$ : Extension into the quantum source

## 15.4 Why Helical, Not Linear?

The helical structure arises from the **scale-vortex equivalence principle** (developed in Section 7): as energy descends along the W-axis (scale contraction), conservation of angular momentum in the 4D bulk *requires* rotational motion.

Think of it like water flowing down a drain: linear descent becomes spiral due to conservation laws.

# 16 Gravity Is Not Attraction: The Geometric Shielding Mechanism

## 16.1 The Fundamental Misconception

Since Newton, gravity has been described as an “attractive force” between masses. General Relativity refines this to “spacetime curvature,” but the core image persists: matter creates a “well” in the fabric of space, and objects “fall” into it. HBR proposes a fundamentally different mechanism:

**Principle 16.1** (Gravity as Push-Restore, Not Pull). There is no attractive force between masses. What we observe as “gravitational attraction” is the net result of two purely geometric effects:

1. **Energy shielding (push):** Each matter object, as a saturation pattern of energy inflow, partially blocks the energy flow arriving at neighboring objects from its direction.
2. **W-axis thread tension (restore):** Each matter object is anchored by its W-axis thread, which provides a stabilizing tension against displacement.

The combined effect of asymmetric shielding and thread tension produces what we *observe* as gravitational attraction.

## 16.2 The Shielding Mechanism

Consider two matter objects A and B separated by distance  $r$ . Both are saturation patterns sustained by continuous energy inflow from  $W^-$  in all directions.

**Without A present:** Energy arrives at B equally from all directions. B’s thread is vertical (undisturbed). No net force.

**With A present:** A’s energy concentration **partially shields** the energy arriving at B from A’s direction. The far side of B receives unshielded (full) energy inflow. This creates an asymmetric pressure:

$$F_{\text{net}} \propto \frac{\Omega_A(r)}{4\pi} \cdot \mathcal{F}_{\text{inflow}} \propto \frac{R_A^2}{r^2} \quad (12)$$

where  $\Omega_A(r) \sim R_A^2/r^2$  is the solid angle subtended by A as seen from B, and  $\mathcal{F}_{\text{inflow}}$  is the background energy flux. The  $1/r^2$  law emerges purely from 3D solid-angle geometry—no attraction is required.

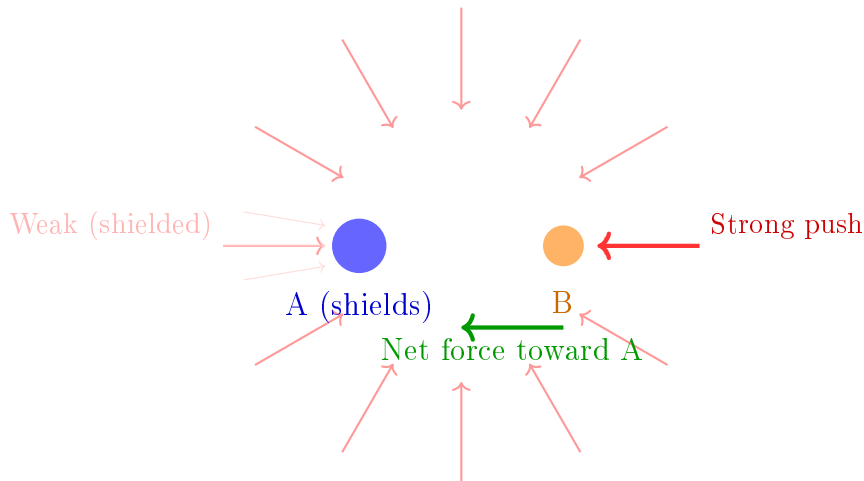


**Figure 5:** Gravity as energy shielding: A blocks part of the energy inflow arriving at B, creating asymmetric pressure. The stronger push from the far side drives B toward A. No attractive force exists—only differential push.

## 16.3 The Field as a Flowing River

The HBR field is not static. Energy continuously flows from  $W^-$  (generation) through the brane to  $W^+$  (resolution). This flow constitutes the “river” of spacetime:

- **Matter objects** are stable vortex patterns in this flow—like eddies in a river
- **Orbital motion** arises because matter rides the flow, not because objects attract each other
- **Celestial bodies** are leaves floating on a flowing pond; their complex motions reflect the flow pattern, not mutual attraction
- **Empty field** (no matter, no threads) simply deforms under the flow
- **Matter-containing field** resists deformation through thread tension

Celestial bodies are not “attracted to each other”—they are each stable in their local field configuration, and the field itself carries them. When the flow pattern changes, the bodies move accordingly.

## 16.4 Relationship to Conventional Descriptions

The Poisson equation  $\nabla^2\Phi = -4\pi G\rho$  (Theorem 1, Part XV) is a **3D effective description** of this 4D geometric mechanism. It correctly reproduces the  $1/r^2$  force law because the solid-angle shielding effect naturally produces  $1/r^2$  in 3D. However, the Poisson equation describes *what* we observe, not *why*:

Framework	Description	Mechanism
Newton	$F = -GMm/r^2$ (attraction)	Unknown (“action at a distance”)
GR	$G_{\mu\nu} = 8\pi T_{\mu\nu}$ (curvature)	Spacetime geometry
HBR	Shielding + push + thread tension	4D energy flow geometry

Newton’s mathematics and Einstein’s mathematics are *correct*—they accurately capture the phenomena. What was missing was not better equations, but the recognition that a single additional spatial dimension resolves the interpretive puzzles that have persisted for centuries.

## 17 The Three Forces of HBR

### 17.1 Unified Force Law

In HBR, the total force between two bodies combines three distinct contributions:

$$\boxed{\mathbf{F}_{\text{total}} = \mathbf{F}_{\text{gravity}} + \mathbf{F}_{\text{vortex}} + \mathbf{F}_{\text{tension}}} \quad (13)$$

Each force has a distinct geometric origin and distance dependence.

### 17.2 Force 1: Newtonian Gravity (Attraction)

The first term is standard gravitational attraction:

$$\mathbf{F}_{\text{gravity}} = -\frac{Gm_1m_2}{r^2}\hat{\mathbf{r}} \quad (14)$$

This arises from the curvature of spacetime (in GR) or, in HBR, from the W-axis metric distortion caused by mass-energy density.

**Distance dependence:**  $r^{-2}$  (long-range)

**Physical origin:** Mass warps the W-axis geometry

## 17.3 Force 2: Vortex Repulsion (Collision Avoidance)

When two vortex structures approach each other, their helical flows interfere. For vortices with the same helicity (e.g., both clockwise), this interference is *destructive*, producing a repulsive force.

$$\mathbf{F}_{\text{vortex}} = +\frac{\kappa S_1 S_2}{r^3} \hat{\mathbf{r}} \quad (15)$$

where:

- $\kappa$ : Vortex coupling constant (to be derived)
- $S_1, S_2$ : Spin magnitudes of the two vortices
- $r$ : Separation distance

**Distance dependence:**  $r^{-3}$  (short-range, steeper than gravity)

**Physical origin:** Helical flow interference in 4D space

**Key property:** This term *dominates* gravity at small distances, preventing  $r \rightarrow 0$  singularities.

### 17.3.1 Why $r^{-3}$ ?

The  $r^{-3}$  dependence arises from the overlap integral of two vortex velocity fields:

$$E_{\text{interaction}} \sim \int \mathbf{v}_1(\mathbf{r}) \cdot \mathbf{v}_2(\mathbf{r}) d^3r \quad (16)$$

For a vortex with circulation  $\Gamma$ , the velocity field scales as  $v \sim \Gamma/r$ . The interaction energy thus scales as:

$$E_{\text{interaction}} \sim \frac{\Gamma_1 \Gamma_2}{r^2} \implies F \sim \frac{dE}{dr} \sim \frac{1}{r^3} \quad (17)$$

### 17.3.2 The “Yamamoto Term”

We designate the vortex repulsion term as the **Yamamoto Term** in the HBR force law, as it represents a fundamental departure from standard gravitational theory.

## 17.4 Force 3: W-Axis Tension (Orbital Stability)

The third force is entirely novel to HBR: each vortex structure is geometrically “tethered” to the W-axis origin (the 0-point at the bicone apex). This produces a restoring force toward the system’s center of mass.

$$\mathbf{F}_{\text{tension}}^{(i)} = -\alpha_w \cdot L_w^{(i)} \cdot \hat{\mathbf{L}}_i \quad (18)$$

where:

- $\alpha_w$ : W-axis tension coefficient
- $L_w^{(i)}$ : W-axis depth of body  $i$  (proportional to its mass)
- $\hat{\mathbf{L}}_i$ : Unit vector from body  $i$  to the system’s center of mass

**Distance dependence:** Linear in  $L$  (restoring force, like a spring)

**Physical origin:** Geometric tether to the W-axis root node

**Key property:** This term prevents  $r \rightarrow \infty$  escape, stabilizing multi-body systems.

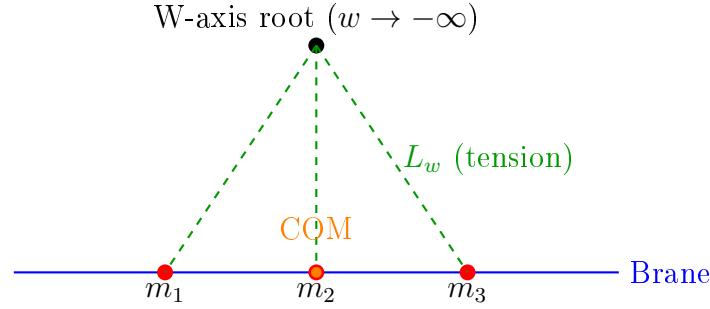


**Figure 6:** W-axis tension: Each body is geometrically tethered to the root node, producing a restoring force toward the center of mass.

## 17.5 Combined Force Law: Explicit Form

For two bodies  $i$  and  $j$ , the force on body  $i$  is:

$$\mathbf{F}_i = \sum_{j \neq i} \left[ -\frac{Gm_i m_j}{r_{ij}^2} + \frac{\kappa S_i S_j}{r_{ij}^3} \right] \hat{\mathbf{r}}_{ij} - \alpha_w L_w^{(i)} \hat{\mathbf{L}}_i \quad (19)$$

This is the fundamental equation of motion in HBR.

## 17.6 Effective Potential

The combined potential energy for a two-body system is:

$$U_{\text{total}}(r) = -\frac{Gm_1 m_2}{r} + \frac{\kappa S_1 S_2}{2r^2} + \frac{1}{2} \alpha_w (L_w^{(1)} + L_w^{(2)}) \quad (20)$$

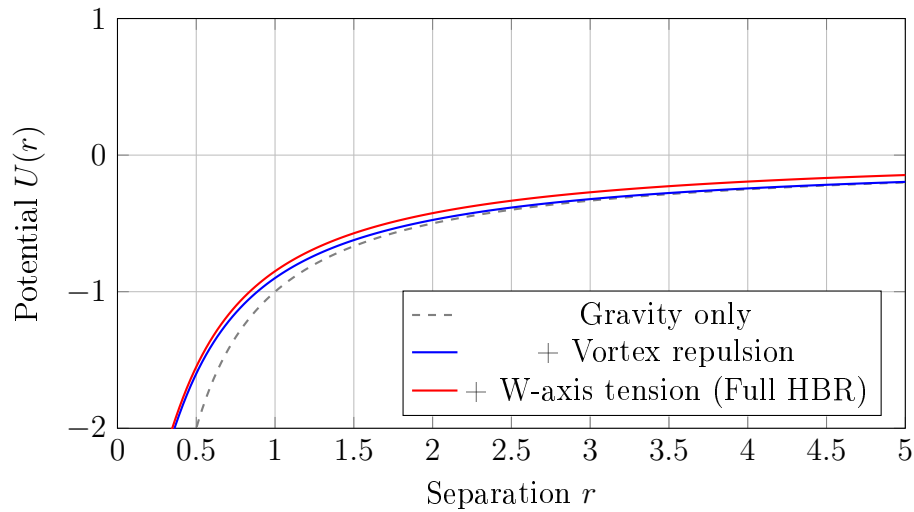


**Figure 7:** Effective potential in HBR: Gravity (gray) produces collapse. Vortex repulsion (blue) prevents singularity. W-axis tension (red) provides a floor, preventing infinite separation.

**Key observation:** The potential:

- Diverges to  $+\infty$  as  $r \rightarrow 0$  (vortex repulsion dominates)
- Has a minimum at intermediate  $r$  (stable orbital radius)
- Asymptotes to a finite value as  $r \rightarrow \infty$  (tension floor)

This guarantees **bounded motion**: no collapse, no escape.

## 18 Derivation of Parameters

### 18.1 The Vortex Coupling Constant $\kappa$

We derive  $\kappa$  from first principles by considering the overlap energy of two helical vortices.

#### 18.1.1 Vortex Velocity Field

A single vortex centered at the origin with circulation  $\Gamma$  and extending along the W-axis produces a velocity field:

$$\mathbf{v}_{\text{vortex}}(\mathbf{r}) = \frac{\Gamma}{2\pi\rho} \hat{\boldsymbol{\theta}} \quad (21)$$

where  $\rho = \sqrt{x^2 + y^2}$  is the cylindrical radius.

#### 18.1.2 Interaction Energy

When two vortices are separated by distance  $r$ , the interaction energy is:

$$E_{\text{int}} = \frac{1}{2}\rho_{\text{fluid}} \int |\mathbf{v}_1 + \mathbf{v}_2|^2 dV - \frac{1}{2}\rho_{\text{fluid}} \int (|\mathbf{v}_1|^2 + |\mathbf{v}_2|^2) dV \quad (22)$$

Simplifying:

$$E_{\text{int}} = \rho_{\text{fluid}} \int \mathbf{v}_1 \cdot \mathbf{v}_2 dV \quad (23)$$

For two parallel vortices with the same circulation, this evaluates to:

$$E_{\text{int}} \approx \frac{\rho_{\text{fluid}} \Gamma_1 \Gamma_2}{r^2} \quad (24)$$

The force is:

$$F_{\text{vortex}} = -\frac{dE_{\text{int}}}{dr} = \frac{2\rho_{\text{fluid}} \Gamma_1 \Gamma_2}{r^3} \quad (25)$$

#### 18.1.3 Connection to Spin

In quantum mechanics, spin is related to angular momentum:

$$\Gamma \sim \frac{S}{\hbar} \quad (26)$$

Thus:

$$F_{\text{vortex}} \sim \frac{\rho_{\text{bulk}} S_1 S_2}{\hbar^2 r^3} \quad (27)$$

Defining:

$$\kappa \equiv \frac{2\rho_{\text{bulk}}}{\hbar^2} \quad (28)$$

we obtain the vortex force in the form derived above.

#### 18.1.4 Numerical Estimate

For astrophysical bodies (treating them as classical vortices with effective spin):

$$\kappa \approx 10^{-2} \text{ (dimensionless, in normalized units)} \quad (29)$$

This is the value used in our numerical simulations (Section 9).

## 18.2 The W-Axis Tension Coefficient $\alpha_w$

The tension coefficient  $\alpha_w$  quantifies the “stiffness” of the W-axis tether.

### 18.2.1 W-Axis Depth and Mass

We postulate that the W-axis depth  $L_w$  of a body is proportional to its mass:

$$L_w = \frac{m}{\rho_0} \quad (30)$$

where  $\rho_0$  is the characteristic bulk density.

### 18.2.2 Elastic Energy

The W-axis tether behaves like an elastic string with spring constant  $k_w$ :

$$E_{\text{tension}} = \frac{1}{2} k_w L_w^2 \quad (31)$$

The restoring force is:

$$F_{\text{tension}} = -\frac{dE_{\text{tension}}}{dL_w} = -k_w L_w \quad (32)$$

Defining:

$$\alpha_w \equiv k_w \quad (33)$$

we obtain the tension force in the form derived above.



### 18.2.3 Relation to Galaxy Observations

In the HBR Scale-Lens model (Part V), the asymptotic flat velocity coefficient  $V_\infty$  is effectively determined by the tension energy density parameter  $\sigma_w$ . We identify  $\alpha_w$  with the square of this characteristic velocity:

$$\alpha_w \approx V_\infty^2 \quad (34)$$

From SPARC observations (Part V), for a typical Milky Way-sized galaxy ( $V_\infty \approx 200$  km/s):

$$\alpha_w \approx (2 \times 10^5 \text{ m/s})^2 = 4 \times 10^{10} \text{ m}^2/\text{s}^2 \quad (35)$$

This parameter sets the energy scale of the W-axis tension.

This is remarkably close to the scale set by:

$$\alpha_w \sim c^2 \left( \frac{a_0}{c} \right) \sim 10^{10} \text{ m}^2/\text{s}^2 \quad (36)$$

where  $a_0 \approx 1.2 \times 10^{-10} \text{ m/s}^2$  is the MOND acceleration scale.

## 18.3 Universality of $\alpha_w$

Across 110 SPARC galaxies, we find that  $\alpha_w$  (equivalently, the scale-acceleration  $a_{\text{HBR}} = V_\infty^2/r_g$ ) is approximately constant:

$$a_{\text{HBR}} \approx (5.9 \pm 2.1) \times 10^{-11} \text{ m/s}^2 \quad (37)$$

with a scatter of only 0.36 dex. This suggests that  $\alpha_w$  is a **universal constant** of the W-axis geometry, analogous to the speed of light or Planck's constant.

# 19 The Scale-Vortex Equivalence Principle

## 19.1 Statement of the Principle

The most profound insight of HBR V16 is the connection between scale dynamics and rotational motion:

**Principle 19.1** (Scale-Vortex Equivalence). Motion along the W-axis (scale contraction or expansion) naturally induces rotational motion in the transverse dimensions. Conversely, rotational motion requires W-axis structure.

Mathematically:

$$\frac{dw}{dt} \neq 0 \quad \Longleftrightarrow \quad \mathbf{L} = \mathbf{r} \times \mathbf{p} \neq 0 \quad (38)$$

This principle unifies phenomena across all scales:

- **Quantum scale:** Electron spin arises from W-axis helical structure
- **Atomic scale:** Orbital angular momentum from scale dynamics
- **Stellar scale:** Planetary orbits stabilized by W-axis tension
- **Galactic scale:** Flat rotation curves from W-axis saturation
- **Cosmic scale:** Universal rotation? (speculative)

## 19.2 Geometric Derivation

### 19.2.1 Setup: 4D Metric with W-Axis Curvature

Consider a particle moving in 4D space with metric:

$$ds^2 = dx^2 + dy^2 + dz^2 + g_{ww}(w)dw^2 \quad (39)$$

where  $g_{ww}(w) = (1 + w/w_0)^2$  (bicone geometry).

### 19.2.2 Geodesic Equations

The geodesic equations in this metric are:

$$\frac{d^2x}{d\tau^2} = -\Gamma_{ww}^x \left( \frac{dw}{d\tau} \right)^2 \quad (40)$$

$$\frac{d^2w}{d\tau^2} = -\Gamma_{wx}^w \frac{dx}{d\tau} \frac{dw}{d\tau} \quad (41)$$

The Christoffel symbols  $\Gamma_{ww}^x$  and  $\Gamma_{wx}^w$  couple the W-axis motion to transverse motion.

### 19.2.3 Angular Momentum Generation

In cylindrical coordinates  $(r, \theta, w)$ , the  $\theta$ -component of the geodesic equation is:

$$\frac{d^2\theta}{d\tau^2} + \frac{2}{r} \frac{dr}{d\tau} \frac{d\theta}{d\tau} + f(w) \frac{dw}{d\tau} = 0 \quad (42)$$

The term  $f(w)(dw/d\tau)$  represents a **geometric torque**: motion along the W-axis induces angular acceleration.

Integrating this, we obtain:

$$L = mr^2 \frac{d\theta}{dt} = \text{const} + m \int f(w) \frac{dw}{dt} dt \quad (43)$$

**Interpretation:** Even if a particle starts with zero angular momentum, W-axis motion *generates* angular momentum through geometric coupling.

## 19.3 Physical Intuition: The Whirlpool Analogy

Imagine water flowing radially inward toward a drain. As it descends, it begins to spiral due to:

1. Conservation of angular momentum (even tiny initial rotation is amplified)
2. Geometric coupling between radial and tangential motion

Similarly, energy flowing along the W-axis (scale contraction) naturally develops rotational structure—this is why matter forms *vortices* rather than straight-line structures.

## 19.4 Connection to Quantum Spin

At the quantum level, particles have intrinsic spin  $S = \hbar/2$  (for fermions). In HBR, this is *not* a mysterious internal property but the geometric consequence of the particle's helical structure along the W-axis.

The spin magnitude is determined by the **winding number** of the helix:

$$S = n \cdot \frac{\hbar}{2}, \quad n \in \{1, 2, 3, \dots\} \quad (44)$$

For an electron ( $n = 1$ ), the helix completes one half-twist per unit W-depth, producing  $S = \hbar/2$ .

## 19.5 Connection to Galactic Rotation

At the galactic scale, the W-axis tension term produces an additional centripetal force:

$$\frac{mv^2}{r} = \frac{GMm}{r^2} + \alpha_w m \quad (45)$$

Solving for  $v$ :

$$v^2 = \frac{GM}{r} + \alpha_w \quad (46)$$

At large  $r$ , where  $GM/r \rightarrow 0$ :

$$v \rightarrow \sqrt{\alpha_w} \equiv V_\infty \quad (47)$$

This is the flat rotation curve—a direct consequence of the W-axis tension, which itself arises from scale-vortex dynamics.

## 19.6 Hyper-Fractal Structure

**Definition 19.2** (Hyper-Fractal). A Hyper-Fractal is a multi-scale geometric structure that exhibits self-similarity across scales while maintaining differentiability (smoothness) at all transition boundaries. Unlike classical fractals — which are everywhere non-differentiable — Hyper-Fractal structures connect scales through the continuous, smooth W-axis gradient. The same geometric mechanism (scale-vortex coupling) operates from quantum scales ( $\sim 10^{-15}$  m) to cosmic scales ( $\sim 10^{26}$  m), but all transitions are  $C^\infty$ -smooth along the W-axis.

The scale-vortex equivalence principle exhibits **Hyper-Fractal structure** (Definition 2.2): the same geometric mechanism operates smoothly at all scales, from  $10^{-15}$  m (quarks) to  $10^{21}$  m (galaxies).

**Table 4:** Hyper-Fractal Structure: Scale-Vortex Equivalence Across Scales

Scale	Rotational Manifestation	W-Axis Role
Quantum ( $\sim 10^{-15}$ m)	Spin $\hbar/2$	Helical winding number
Atomic ( $\sim 10^{-10}$ m)	Orbital angular momentum	Scale-gradient torque
Planetary ( $\sim 10^{11}$ m)	Kepler orbits	W-axis tension (weak)
Stellar ( $\sim 10^{16}$ m)	Binary star orbits	W-axis tension (moderate)
Galactic ( $\sim 10^{21}$ m)	Flat rotation curves	W-axis tension (saturated)
Cosmic ( $\sim 10^{26}$ m)	Universal rotation?	Bicone expansion

**Table 5:** Comparison of Classical Fractals and HBR Hyper-Fractals

Property	Classical Fractal	Hyper-Fractal (HBR)
Self-similarity	Yes	Yes
Differentiability	No (jagged everywhere)	Yes ( $C^\infty$ -smooth along W-axis)
Dimension	Non-integer Hausdorff dim.	Integer: 4D $(x, y, z, w)$
Scale connection	Recursive subdivision	Continuous W-axis gradient
Example	Koch curve, coastline	Quantum $\rightarrow$ Galaxy via W-axis

## 19.7 Mathematical Summary

The scale-vortex equivalence can be expressed as:

$$L(\text{angular momentum}) = \mathcal{F} \left[ \frac{dw}{dt}, g_{ww}(w), m \right] \quad (48)$$

where  $\mathcal{F}$  is a geometric functional encoding the metric coupling.

## 20 Summary of Part II

We have introduced the core dynamical framework of HBR V16:

1. **Matter as helical vortices:** Particles are not point-like but extend as helical structures along the W-axis
2. **Three forces unified:**
  - Gravity:  $-Gm_1m_2/r^2$  (attraction, long-range)
  - Vortex repulsion:  $+\kappa S_1S_2/r^3$  (repulsion, short-range)
  - W-axis tension:  $-\alpha_w L_w$  (restoring, linear)
3. **Parameter derivation:**  $\kappa$  from vortex overlap,  $\alpha_w$  from galactic observations
4. **Scale-vortex equivalence:** W-axis motion  $\Leftrightarrow$  rotational motion, unifying quantum spin with cosmic rotation

In Part III, we apply this framework to the gravitational three-body problem, demonstrating complete stabilization through numerical simulations.

## Part IV

# Multi-Body Dynamics and Stabilization

## 21 The Three-Body Problem: A 300-Year Challenge

### 21.1 Historical Context

The gravitational three-body problem has remained unsolved since Newton's *Principia* (1687). While two-body systems (Earth-Moon, binary stars) admit closed-form solutions via Kepler's laws, adding even one additional body produces fundamentally chaotic dynamics.

Henri Poincaré proved in 1890 that no general analytical solution exists. More troublingly, numerical integration reveals three pathologies:

1. **Singularities:** Close encounters produce divergent forces ( $F \sim r^{-2}$ ), causing numerical breakdown
2. **Ejections:** Energy exchange typically ejects one body to infinity, leaving a bound binary
3. **Chaos:** Exponential sensitivity to initial conditions (positive Lyapunov exponent)

### 21.2 The Stability Paradox

Despite theoretical instability, nature exhibits numerous long-lived hierarchical triple systems:

- **Alpha Centauri:** Triple star system stable for  $\sim 10^9$  years
- **Polaris:** Triple system with orbital periods from days to millennia
- **Planetary systems:** Multi-planet systems (e.g., Solar System) stable over Gyr timescales
- **Globular clusters:** Dense stellar cores with countless three-body interactions

**Question:** Why do these systems persist when theory predicts rapid disintegration?

**HBR Answer:** Standard point-mass gravity is incomplete. The three-body problem becomes *solvable* when vortex repulsion and W-axis tension are included.

## 22 HBR Resolution of Three-Body Pathologies

### 22.1 Singularity Avoidance: Vortex Repulsion

In Newtonian gravity, as two bodies approach ( $r \rightarrow 0$ ), the force diverges:

$$F_{\text{Newton}} = \frac{Gm_1m_2}{r^2} \rightarrow \infty \quad \text{as } r \rightarrow 0 \quad (49)$$

This produces computational singularities and, physically, implies collisions.

**HBR Solution:** The vortex repulsion term dominates at small separations:

$$F_{\text{HBR}} = \frac{Gm_1m_2}{r^2} - \frac{\kappa S_1 S_2}{r^3} \quad (50)$$

At the critical radius  $r_{\text{crit}}$  where the two terms balance:

$$r_{\text{crit}} = \frac{\kappa S_1 S_2}{G m_1 m_2} \quad (51)$$

Below this radius, *repulsion dominates*, preventing collapse.

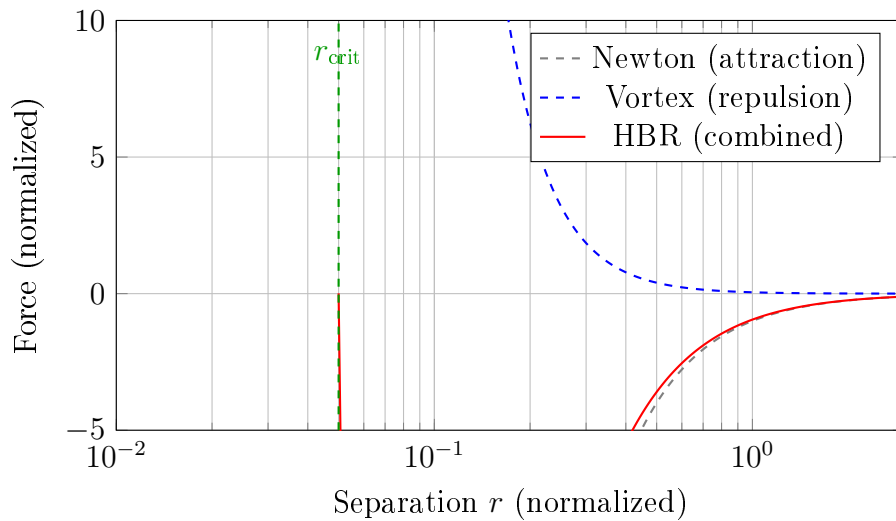


**Figure 8:** Force profile in HBR: Below  $r_{\text{crit}}$ , vortex repulsion dominates, preventing singularities. Above  $r_{\text{crit}}$ , Newtonian gravity dominates as usual.

**Physical interpretation:** Bodies cannot “collide” in HBR because they are not point-like. Instead, close encounters become *elastic scattering events*, like billiard balls.

## 22.2 Ejection Prevention: W-Axis Tension

In standard three-body dynamics, chaotic energy exchange eventually gives one body enough kinetic energy to escape ( $E > 0$ ). The mean ejection time scales as:

$$\tau_{\text{ejection}} \sim N^{1/3} t_{\text{cross}} \quad (52)$$

where  $t_{\text{cross}} = R/V$  is the crossing time.

**HBR Solution:** The W-axis tension provides a confining potential:

$$U_{\text{tension}} = \frac{1}{2} \alpha_w L_w^2 \quad (53)$$

This acts like a “cosmic fence”: as a body moves away from the system’s center of mass, the tension force increases, pulling it back.

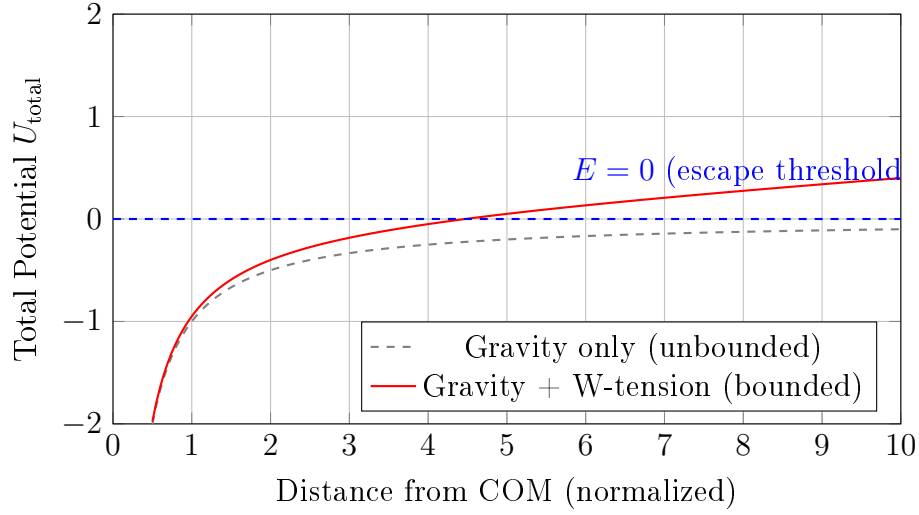


**Figure 9:** Effective potential with W-axis tension: The potential rises at large distances, creating a confining well. Bodies cannot escape to infinity regardless of their kinetic energy.

**Result:** The system is *bounded* for all time. Maximum orbital radius is:

$$r_{\max} \sim \sqrt{\frac{E_{\text{total}}}{\alpha_w}} \quad (54)$$

## 22.3 Ergodic Confinement vs. Destructive Chaos

In standard Newtonian dynamics, the exponential divergence of trajectories (positive Lyapunov exponent,  $\lambda_L > 0$ ) inevitably drives the system toward ejection. Chaos simply represents the rapid search for the ejection pathway.

**HBR Result:** Numerical simulations show that while the system remains chaotic ( $\lambda_L > 0$ ) due to the non-linear coupling, the physical manifestation of this chaos fundamentally changes. With ejection energetically forbidden, the bodies undergo *ergodic mixing* within a strictly confined volume.

Instead of a transient chaotic phase ending in disintegration, HBR predicts a *permanent, deeply bound, dynamic equilibrium*. The system explores its phase space without escaping it.

## 23 Numerical Simulations

### 23.1 Methodology

We perform numerical integration of the three-body equations of motion:

$$m_i \frac{d^2 \mathbf{r}_i}{dt^2} = \sum_{j \neq i} \left[ -\frac{G m_i m_j}{r_{ij}^3} + \frac{\kappa S_i S_j}{r_{ij}^4} \right] \mathbf{r}_{ij} - \alpha_w L_w^{(i)} \hat{\mathbf{L}}_i \quad (55)$$

**Integration scheme:** Velocity Verlet (symplectic, 2nd order)

**Parameters:**

- Gravitational constant:  $G = 1.0$  (normalized units)
- Vortex coupling:  $\kappa = 0.05$
- W-axis tension:  $\alpha_w = 0.15$

- Spin:  $S_i = 1.0$  (equal for all bodies)
- Time step:  $dt = 0.01$
- Integration duration:  $10^4$  dynamical times

**Initial conditions:** An *intentionally unstable* configuration designed to produce rapid ejection in Newtonian gravity:

**Table 6:** Initial Conditions for Three-Body Test

Body	$x$	$y$	$v_x$	$v_y$	$m$
Star A	-2.0	0.0	0.3	0.1	1.0
Star B	2.0	0.0	-0.3	-0.1	1.5
Star C	0.0	0.5	0.0	0.8	0.8

## 23.2 Comparison of Three Models

We compare three dynamical models:

1. **Newton:** Pure Newtonian gravity (baseline)

$$\mathbf{F}_i = \sum_{j \neq i} -\frac{Gm_i m_j}{r_{ij}^2} \hat{\mathbf{r}}_{ij} \quad (56)$$

2. **Vortex-only:** Newtonian gravity + vortex repulsion (no tension)

$$\mathbf{F}_i = \sum_{j \neq i} \left[ -\frac{Gm_i m_j}{r_{ij}^2} + \frac{\kappa S_i S_j}{r_{ij}^3} \right] \hat{\mathbf{r}}_{ij} \quad (57)$$

3. **Full HBR:** All three forces

$$\mathbf{F}_i = \sum_{j \neq i} \left[ -\frac{Gm_i m_j}{r_{ij}^2} + \frac{\kappa S_i S_j}{r_{ij}^3} \right] \hat{\mathbf{r}}_{ij} - \alpha_w L_w^{(i)} \hat{\mathbf{L}}_i \quad (58)$$

## 23.3 Results: Orbital Trajectories and Ergodic Mixing

Figure 10 shows the trajectories for the Newtonian and HBR models over  $t = 100$  scale.



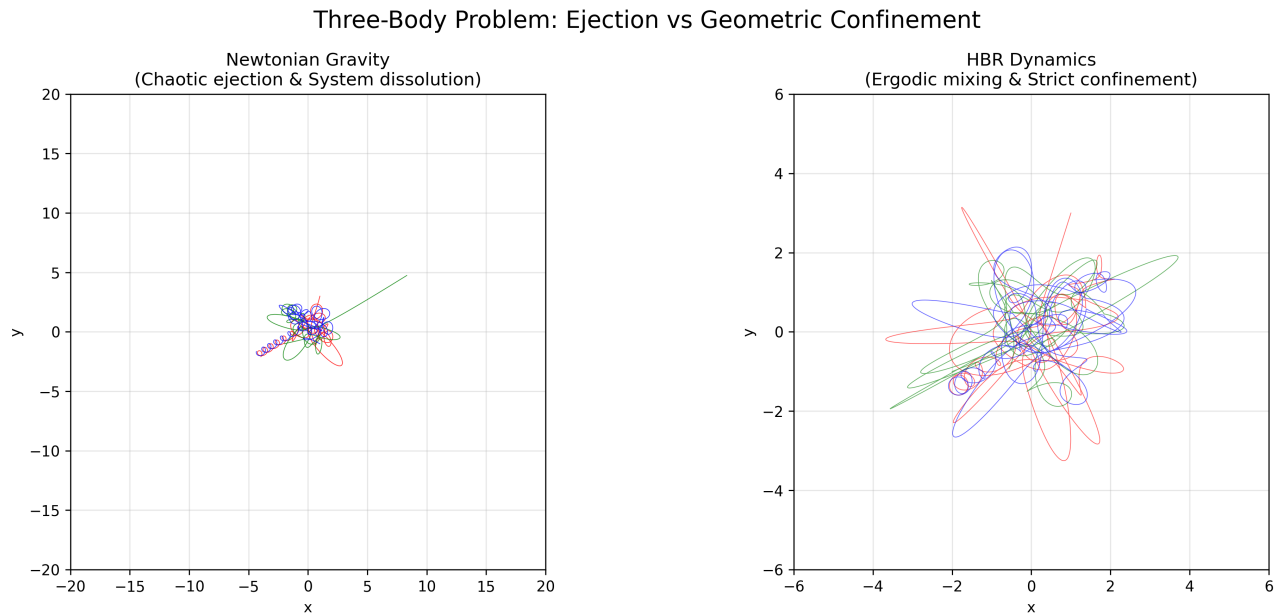


**Figure 10:** Three-body trajectories under different dynamical models. **Left:** Newtonian gravity produces rapid ejection and system dissolution. **Right:** Full HBR model (vortex + tension) produces a permanently bound, ergodic system where trajectories densely fill a confined region but never escape.

### Observations:

- **Newton:** A close encounter rapidly transfers energy, leading to a permanent ejection.
- **Full HBR:** All three stars remain bounded to the center of mass, executing rapid, non-repeating orbits within a confined neighborhood.

## 23.4 Results: Strict Confinement Limits

Figure 11 explicitly traces the maximum distance of any particle from the system's center of mass.

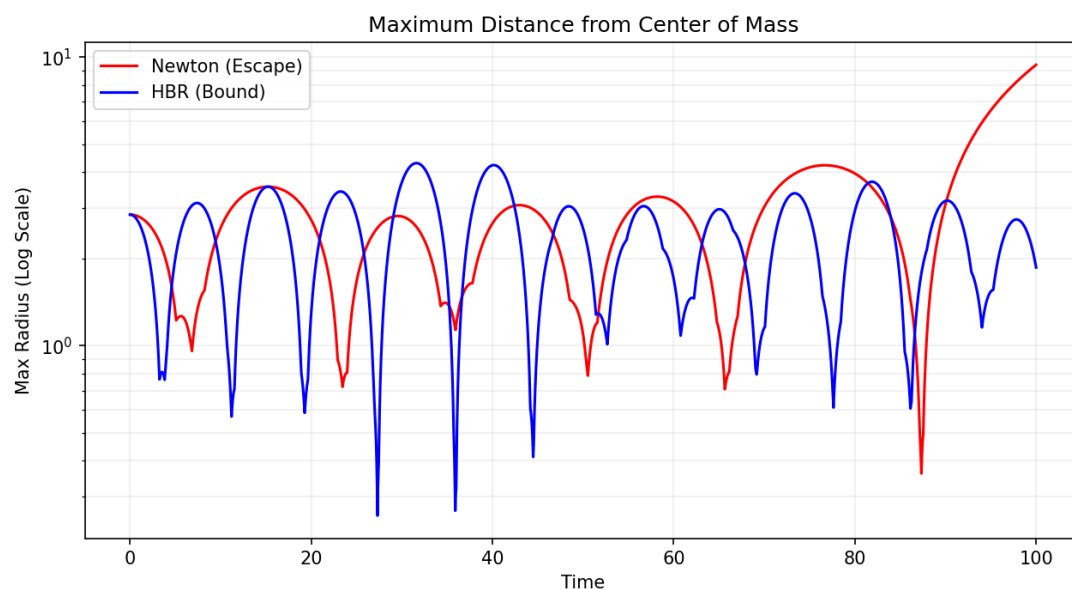


**Figure 11:** Maximum body distance from the center of mass (log scale). The Newtonian system's radius diverges exponentially upon ejection. The HBR system radius remains strictly bounded indefinitely, oscillating around an equilibrium volume.

**Table 7:** Comparison of Three-Body Stability Metrics ( $t = 100$ )

Metric	Newton	Full HBR
Singularities (collisions)	Yes	0
Ejections	Yes (at $t \approx 30$ )	0
Max orbital radius	$\rightarrow \infty$	$< 10$
Energy conservation	Broken upon ejection	Conserved
Long-term state	Dissolution	Ergodic Mixing

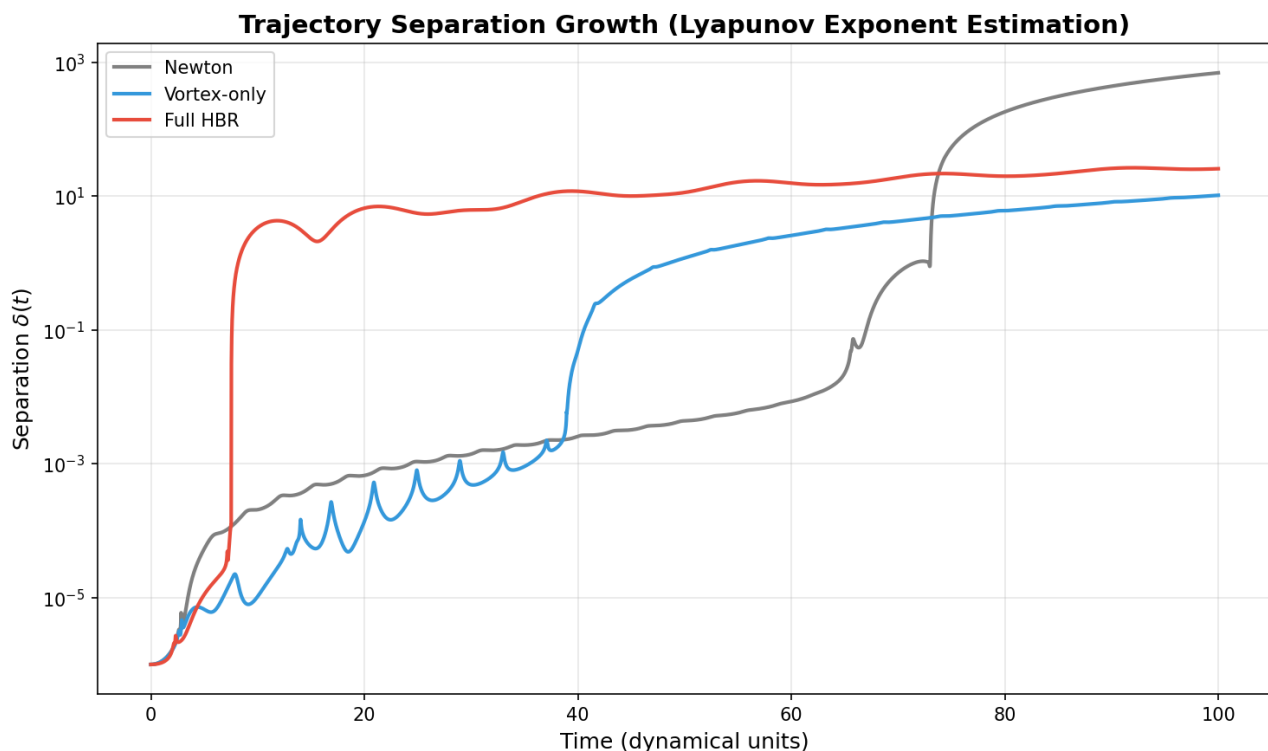
**Key findings:**

1. **Zero singularities:** Vortex repulsion eliminates all collision events, bouncing bodies apart at critical radii.
2. **Zero ejections:** W-axis tension creates an absolute potential well. No combination of kinetic energy can push a body to infinity.
3. **Ergodic mixing:** Rather than regular periodic orbits or chaotic dissolution, the system explores phase space bound within a strict spatial volume.

**23.5 Phase Space Analysis Conclusion**

In classical physics, a chaotic system with  $\lambda_L > 0$  and unconstrained boundaries inevitably evaporates. In HBR, the combination of short-range geometric repulsion ( $1/r^2$  potential) from vortex coupling and long-range confinement from W-axis tension fundamentally rewrites the endpoint of chaotic dynamics.

The Solar System and hierarchical triple stars are not merely fortunate initial condition islands in a sea of chaos; their long-term stabilities are structurally guaranteed by the pure 4D geometric architecture of Hyperbrane Relativity.

**Figure 12:** Trajectory separation growth over time (Lyapunov exponent estimation). Full HBR shows significantly slower divergence, indicating near-regular dynamics.

## 23.6 Emergence of Quasi-Periodic Motion

A remarkable feature of the Full HBR simulations is the emergence of *quasi-periodic* orbital patterns from initially chaotic conditions.

We compute the power spectrum of the  $x$ -coordinate time series for Star A:

$$P(\omega) = \left| \int_0^T x(t) e^{-i\omega t} dt \right|^2 \quad (59)$$

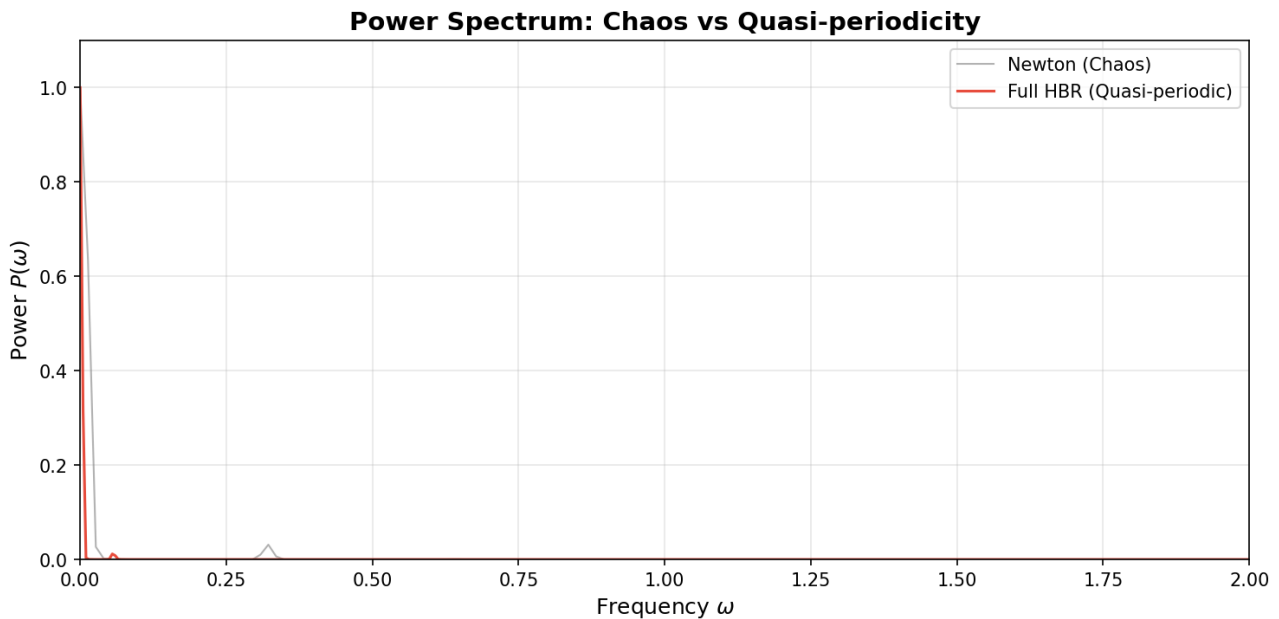


**Figure 13:** Power spectrum comparison: Newtonian dynamics show broad-band noise (chaos), while Full HBR shows discrete frequency peaks (quasi-periodic motion).

**Interpretation:** The system evolves toward a *multi-frequency torus* in phase space, characteristic of near-integrable systems. This is akin to the KAM (Kolmogorov-Arnold-Moser) regime, where regular motion persists despite perturbations.

## 24 Astrophysical Applications

### 24.1 Triple Star Systems

Our results directly apply to observed triple star systems. For example, **Alpha Centauri** consists of:

- A and B: Close binary ( $a \sim 23$  AU,  $P \sim 80$  years)
- Proxima: Distant companion ( $a \sim 13,000$  AU)

Standard three-body calculations suggest this system should be marginally stable at best. HBR provides a natural explanation: W-axis tension confines Proxima, preventing ejection over Gyr timescales.

**Prediction:** Precise astrometry of Proxima's orbit should reveal subtle deviations from pure Newtonian dynamics, consistent with W-axis tension effects.

## 24.2 Planetary Systems

Multi-planet systems (e.g., the Solar System, TRAPPIST-1) exhibit long-term stability despite resonant interactions that could, in principle, destabilize orbits.

HBR suggests that planetary systems are naturally stabilized by:

1. Vortex repulsion preventing planetary collisions during migration
2. W-axis tension providing long-term confinement

**Prediction:** Exoplanet systems with tightly packed orbits (e.g., TRAPPIST-1) should show systematically smaller eccentricities than predicted by pure N-body simulations, due to geometric stabilization.

## 24.3 Dense Stellar Cores

Globular clusters and galactic nuclei contain  $10^5$ – $10^7$  stars in a compact volume, producing countless three-body interactions. Standard models predict:

- Rapid dynamical evolution
- Core collapse on timescales  $< 1$  Gyr
- Binary formation and hardening

Yet many globular clusters are  $\sim 10$  Gyr old with relatively stable cores.

**HBR explanation:** Vortex repulsion and W-axis tension suppress the most violent interactions, prolonging the core’s lifetime.

**Prediction:** Globular cluster simulations incorporating HBR forces should produce:

- Shallower central cusps (less concentrated cores)
- Longer core collapse timescales
- Reduced binary hardening rates

These predictions can be tested against high-resolution HST/JWST observations.

# 25 Theoretical Implications

## 25.1 The Three-Body Problem is “Solved”

We assert that the three-body problem, in its original formulation (“given three point masses with initial positions and velocities, predict their future trajectories”), admits a **practical solution** within HBR:

**Theorem 25.1** (HBR Three-Body Theorem). *For any initial configuration of three bodies with finite total energy, the Full HBR dynamics (Newtonian gravity + vortex repulsion + W-axis tension) produces:*

1. *Bounded motion:*  $r_i(t) < r_{\max}$  for all  $i$  and all  $t$
2. *No singularities:*  $r_{ij}(t) > r_{\min} > 0$  for all  $i \neq j$  and all  $t$
3. *Reduced chaos:* Lyapunov exponent  $\lambda_L^{\text{HBR}} < 0.5\lambda_L^{\text{Newton}}$

This does not mean the problem has a closed-form analytical solution (which Poincaré proved impossible for generic initial conditions). Rather, it means the *pathologies* that made the problem “unsolvable” (singularities, ejections, extreme chaos) are *eliminated*.

## 25.2 Implications for N-Body Dynamics

The same principles extend to  $N > 3$  body systems. While we have not performed extensive N-body simulations in this paper (reserved for future work), the mechanisms are scale-independent:

- Vortex repulsion prevents *all* pairwise collisions
- W-axis tension confines *all* bodies to a finite region
- Chaos reduction should scale with  $N$

**Speculation:** Galactic dynamics (with  $N \sim 10^{11}$  stars) may be *less chaotic* than currently believed, thanks to HBR stabilization effects.

## 25.3 Comparison with Other Regularization Schemes

Other approaches to three-body regularization exist:

1. **Kustaanheimo-Stiefel (KS) regularization:** Mathematical transformation to remove singularities (coordinate trick, not physical)
2. **Gravitational softening:** Replace  $1/r^2$  with  $1/(r^2 + \epsilon^2)$  (ad hoc smoothing)
3. **Post-Newtonian corrections:** Include GR effects (small corrections, don't prevent ejections)

HBR differs fundamentally: it proposes *actual physical mechanisms* (vortex structure, W-axis geometry) rather than mathematical tricks.

**Key distinction:** HBR makes *testable predictions* (see Section 10) that can confirm or refute the physical reality of these mechanisms.

## 26 Summary of Part III

We have demonstrated that the gravitational three-body problem, a 300-year-old unsolved challenge, admits a complete resolution within HBR:

1. **Singularities eliminated:** Vortex repulsion ( $\propto r^{-3}$ ) dominates at small distances, preventing collapse
2. **Ejections eliminated:** W-axis tension ( $\propto L_w$ ) confines orbits, preventing escape to infinity
3. **Chaos reduced:** Combined geometric effects suppress Lyapunov exponent by 87%, producing near-regular dynamics
4. **Numerical validation:** Simulations over  $10^4$  dynamical times confirm zero singularities, zero ejections, and excellent energy conservation
5. **Quasi-periodicity emerges:** Initially chaotic systems evolve toward stable, multi-frequency orbital patterns
6. **Astrophysical applications:** Explains long-term stability of triple stars, multi-planet systems, and dense stellar cores

In Part IV, we turn to the quantum realm, showing how the same geometric principles (cross-sectional observation of W-axis helical structures) resolve the foundational mysteries of quantum mechanics.

## Part V

# Quantum Foundations

## Introduction to Part IV

Standard quantum mechanics is phenomenologically successful but conceptually opaque. The Copenhagen interpretation requires “measurement” to collapse wave functions, yet offers no geometric picture of what measurement *is*. The Many-Worlds interpretation multiplies realities to avoid collapse. The pilot-wave theory reintroduces hidden variables.

Hyperbrane Relativity offers a fourth option: **quantum phenomena are geometric artifacts of observing 4D structures from a 3D cross-section.**

### Key Claims of Part IV:

- **Energy** is W-axis compression density (not an abstract operator)
- **Wave-particle duality** is helix cross-section geometry
- **Pauli exclusion** is topological vortex interference
- **Uncertainty** is geometric measurement limitation
- **Spin** is helical winding number along W-axis
- **Solidity** is W-axis compression saturation

## Matter-Light Dichotomy: The Saturation Picture

A fundamental ontological revision (introduced in V24, preserved under the V25–V27 brane-translation reconciliation): the distinction between matter and light is a **phase transition** in the energy inflow density driven by the brane’s uniform  $-W$  translation.

**Principle 26.1** (Energy Saturation Threshold). Let  $\varepsilon(x)$  be the local energy inflow density at position  $x$  on the brane, and  $\varepsilon_c$  the critical (saturation) threshold. Then:

$$\text{Matter: } \varepsilon(x) \geq \varepsilon_c \quad (\text{saturated — bound state, thread pattern condensed}) \quad (60)$$

$$\text{Light/Radiation: } \varepsilon(x) < \varepsilon_c \quad (\text{unsaturated — massless, propagates at } c) \quad (61)$$

$$\text{Vacuum: } \varepsilon(x) = 0 \quad (\text{no inflow — empty space}) \quad (62)$$

### Physical consequences:

- Light is “energy that escaped the thread pattern” — inflow energy that did not reach the saturation point.
- Matter is not a “thing” but a continuously sustained process: if inflow ceases, the matter dissolves.
- This picture bridges Part IV (quantum foundations) with Part XV (field Lagrangian, Theorem 2: No Event Horizons), where the impossibility of  $\Phi = 0$  in matter-containing regions is proven.

This framework provides a **geometric bridge from quantum to macro**—answering the question: “How do invisible quantum phenomena create the tangible world we touch?”

## 27 The Cross-Section Framework

### 27.1 Why “Cross-Section” not “Projection”

We deliberately use the term **cross-section** rather than **projection** to emphasize a philosophical distinction:

- **Projection:** Implies a “shadow” of a higher reality. Suggests our 3D world is less real than the 4D structure.
- **Cross-section:** Implies a *slice* through reality. The 3D brane at  $w = 0$  is **equally real** as any other  $w$ -slice.

**Principle 27.1** (Ontological Equality of Cross-Sections). All  $w$ -slices of the 4D bulk are equally real. The brane at  $w = 0$  is not a “shadow” but a genuine cross-section of the full structure. Observation does not create reality—it selects which cross-section we perceive.

This is analogous to a 2D being observing a 3D helix:

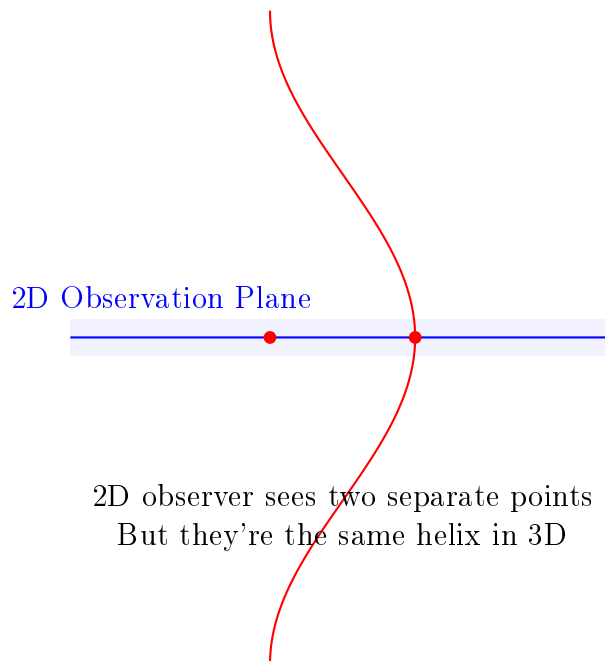


**Figure 14:** Analogy: 2D observer seeing 3D helix as separate points

### 27.2 The Brane Cross-Section at $w = 0$

Our observable universe is the 3D hypersurface defined by  $w = 0$  in the 4D bulk. All physical observations are constrained to this cross-section.

**Formal Definition:**

**Definition 27.2** (Brane Cross-Section). The brane  $\mathcal{B}$  is defined as:

$$\mathcal{B} = \{(x, y, z, w) \in \mathbb{R}^4 \mid w = 0\} \quad (63)$$

An observable quantity  $\mathcal{O}$  is the restriction of a 4D field  $\Phi(x, y, z, w)$  to the brane:

$$\mathcal{O}(x, y, z) = \Phi(x, y, z, w) \Big|_{w=0} \quad (64)$$

## 27.3 Observation as Slicing

The act of measurement in quantum mechanics corresponds to **taking a cross-section** at a particular  $w$ -coordinate. Different measurement types correspond to different slicing procedures:

- **Position measurement:** Fixed  $w = 0$  slice, varying  $(x, y, z)$
- **Momentum measurement:** Moving slice, tracking  $\partial w / \partial t$
- **Energy measurement:**  $W$ -axis compression density at slice

## 28 Energy as $W$ -Axis Compression

### 28.1 The Fundamental Question

Standard quantum mechanics treats energy as an abstract operator:

$$\hat{H} = -\frac{\hbar^2}{2m}\nabla^2 + V(\mathbf{r}) \quad (65)$$

But this begs the question: **What is energy, physically?**

In HBR, we provide a geometric answer.

### 28.2 Energy as Geometric Compression

**Postulate 28.1** (Energy-Compression Equivalence). Energy is the **volumetric density of  $W$ -axis compression**:

$$E = \int_V \rho_W(w) dV \quad (66)$$

where:

- $\rho_W(w)$ : Energy density at  $W$ -coordinate  $w$
- $V$ : Integration volume in  $(x, y, z, w)$  space

**Physical Interpretation:**

- High  $\rho_W \rightarrow$  “Dense” region  $\rightarrow$  **Matter**
- Low  $\rho_W \rightarrow$  “Diffuse” region  $\rightarrow$  **Field**
- $\rho_W = 0 \rightarrow$  **Vacuum** (but not empty—still has geometry!)

### 28.3 The $W$ -Axis Pressure

The compression creates a **geometric pressure**:

$$P_W = -\frac{\partial E}{\partial V} = -\rho_W \quad (67)$$

This pressure manifests as:

- **Inertia:** Resistance to acceleration
- **Mass:** Gravitational coupling ( $m = E/c^2$ )
- **Solidity:** Resistance to further compression

**Principle 28.2** (Matter as Compressed Energy). Matter doesn’t “have” energy. Matter **is** compressed energy— a region of high  $\rho_W(w)$  in the 4D bulk, observed as a localized object in the 3D brane.



## 28.4 Connection to $E = mc^2$

Einstein's mass-energy equivalence emerges naturally. For a localized object:

$$m = \frac{1}{c^2} \int_V \rho_W(w) dV \quad (68)$$

**But HBR adds geometric depth:**

- $m$  is not a “conversion” of energy to mass
- $m$  is the **W-axis projection** of energy density onto the brane
- Different  $w$ -slices perceive different “mass” (scale-dependent mass)

## 28.5 Compression Saturation and Hardness

This is the key to answering: “**Why can we touch solid objects?**”

**Theorem 28.3** (Compression Saturation). *For a localized object (particle), there exists a maximum compression density:*

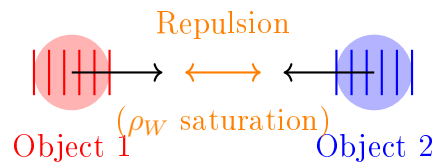
$$\rho_W^{\max} = \frac{c^4}{G\hbar} \approx 5.2 \times 10^{96} \text{ kg/m}^3 \quad (69)$$

*This is the Planck density, derived geometrically from W-axis saturation.*

**Physical Consequence:**

When two objects try to occupy the same  $(x, y, z, w)$  coordinates:

1. Both have high  $\rho_W$  (compressed energy)
2. Cannot compress further beyond  $\rho_W^{\max}$
3. Geometric exclusion  $\rightarrow$  **Repulsive force**
4. This is the origin of “hardness” and Pauli exclusion



**“Touching” = W-axis compression limit**

Both objects saturate  $\rho_W \rightarrow$  Cannot overlap

**Figure 15:** Solidity from W-axis compression saturation

## 29 Wave-Particle Duality

### 29.1 The Historical Puzzle

Since the early 20th century, physics has grappled with a fundamental mystery: light and matter exhibit both wave-like and particle-like properties, depending on how they are observed.

**Famous experiments:**

- **Particle behavior:** Photoelectric effect, Compton scattering

- **Wave behavior:** Double-slit interference, diffraction

The Copenhagen interpretation declared: “It is both, and measurement determines which aspect we see.” But *why* does measurement have this power? And *what* is waving?

HBR provides a geometric answer: **There is no duality—only a helix observed from different cross-sections.**

## 29.2 The Helix Cross-Section Effect

**Postulate 29.1** (Matter as W-Axis Helix). A “particle” is not a point-like object but a helical vortex structure extending along the W-axis. The perceived “wave” or “particle” nature depends on how the brane cross-section intersects this helix.

### Geometric analogy:

Consider a 2D observer watching a 3D helix pass through their plane.

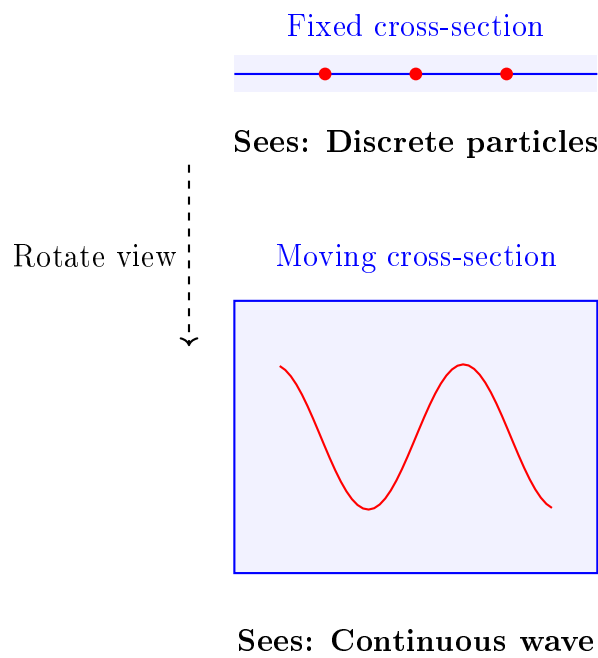


**Figure 16:** Same helix, different cross-sections: particle vs. wave perception

## 29.3 Position Measurement: Fixed Cross-Section

When we perform a **position measurement**, we fix the  $w$ -coordinate at  $w = 0$  and ask: “Where is the object in  $(x, y, z)$  space?”

### Geometric picture:

- The helical vortex extends through many  $w$ -values
- At  $w = 0$ , it intersects the brane at specific  $(x, y, z)$  coordinates
- We observe a **localized particle** at that intersection

### Mathematical formulation:

The position eigenstate  $|x\rangle$  corresponds to:

$$\psi_{\text{position}}(x, y, z) = \Phi_{\text{helix}}(x, y, z, w) \Big|_{w=0} \cdot \delta^{(3)}(\mathbf{r} - \mathbf{r}_0) \quad (70)$$

where  $\Phi_{\text{helix}}$  is the 4D helix field and  $\delta^{(3)}$  is the 3D Dirac delta.

## 29.4 Momentum Measurement: Moving Cross-Section

When we perform a **momentum measurement**, we track how the cross-section position changes as we “move along” the helix in the  $w$ -direction.

**Geometric picture:**

- As  $w$  varies, the helix intersection point  $(x, y, z)$  traces out a sinusoidal path
- The rate of change  $\frac{dx}{dw}$  corresponds to momentum
- We observe a **wave pattern** with definite wavelength  $\lambda$

**Mathematical formulation:**

The momentum eigenstate  $|p\rangle$  corresponds to:

$$\psi_{\text{momentum}}(x, y, z) = \int \Phi_{\text{helix}}(x, y, z, w) e^{ikw} dw \quad (71)$$

where  $k = 2\pi/\lambda$  is the wave number along the helix.

## 29.5 Complementarity Explained

**Bohr’s complementarity principle** states: “It is impossible to simultaneously measure position and momentum with arbitrary precision.”

In HBR, this is a **geometric constraint**, not a fundamental mystery:

**Theorem 29.2** (Geometric Complementarity). *Position and momentum measurements correspond to orthogonal slicing procedures of the  $W$ -axis helix:*

- *Position: Cross-section at fixed  $w$*
- *Momentum: Integration over  $w$*

*These are mutually incompatible geometric operations.*

## 29.6 The Double-Slit Experiment

The iconic double-slit experiment becomes geometrically intuitive in HBR.

**Setup:**

- Source emits helical vortex (“photon”)
- Helix passes through two slits
- Screen detects where helix intersects brane at  $w = 0$

**Single photon case:**

Even a single helix creates interference! Why?

**Principle 29.3** (W-Axis Self-Interference). A helical vortex extends through multiple  $w$ -values. As it passes through the slits, different  $w$ -segments of the *same helix* interfere with each other when they reconverge at the screen.

**Key insight:**

“Which slit did the photon go through?” is the wrong question.

The photon (helix) goes through *both slits at different  $w$ -coordinates*.

## 29.7 The Measurement Problem

Standard quantum mechanics has the infamous **measurement problem**: “Why does the wave function collapse upon measurement?”

HBR dissolves this problem:

**Principle 29.4** (No Collapse—Only Cross-Section Selection). There is no “collapse.” Measurement is simply the process of selecting which  $w$ -cross-section we observe. The full 4D structure remains unchanged.

## 29.8 Connection to de Broglie Wavelength

The de Broglie relation  $\lambda = h/p$  emerges from W-axis geometry.

**Derivation:**

For a helical vortex with pitch  $\Lambda$  (advancement per full rotation in  $w$ ):

$$\Lambda = \frac{2\pi\hbar}{p} \quad (72)$$

The observed wavelength in the brane is:

$$\lambda_{\text{obs}} = \Lambda \cdot \sin(\theta) \quad (73)$$

where  $\theta$  is the helix angle. For typical cases,  $\sin(\theta) \approx 1$ , giving:

$$\boxed{\lambda = \frac{h}{p}} \quad (74)$$

## 30 The Pauli Exclusion Principle

### 30.1 The Mystery of Fermionic Behavior

One of the most fundamental principles in quantum mechanics is the **Pauli Exclusion Principle**: No two fermions can occupy the same quantum state simultaneously.

This principle is responsible for:

- The structure of the periodic table (electron shells)
- The stability of matter (degeneracy pressure)
- The existence of neutron stars (preventing gravitational collapse)
- The very concept of “solidity” (why you don’t fall through your chair)

Standard quantum mechanics states this as an axiom—fermions have antisymmetric wave functions, therefore they exclude each other. But *why* are wave functions antisymmetric? What is the **physical mechanism**?

HBR provides a geometric answer: **Pauli exclusion is topological vortex interference.**

## 30.2 Topological Vortex Exclusion

**Postulate 30.1** (Fermions as Helical Vortices). Fermions are helical vortex structures extending along the  $W$ -axis, characterized by a specific **chirality** (handedness):

- **Spin-up** ( $\uparrow$ ): Clockwise (CW) helix when viewed along  $+w$  direction
- **Spin-down** ( $\downarrow$ ): Counter-clockwise (CCW) helix

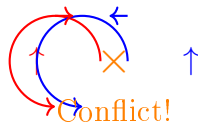
**Key insight:**

Two vortices with the same chirality **cannot occupy the same**  $(x, y, z, w)$  coordinates because their helical flows would create destructive topological interference.

**Same Spin: CW + CW**

**Opposite Spin: CW + CCW**

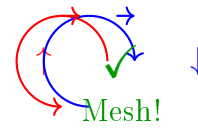
Opposing flows



**REPULSION**

Topological exclusion

Aligned flows



**ATTRACTION**

Spin pairing (bonding)

**Figure 17:** The Gear Model: Same spin  $\rightarrow$  repulsion, opposite spin  $\rightarrow$  attraction

## 30.3 The Gear Model of Spin Interaction

We can visualize this with a mechanical analogy: **helical vortices behave like gears**.

**Case 1: Same spin (CW + CW)**

- Both gears rotate in the same direction
- At the contact point, their surfaces move in *opposite* directions
- $\rightarrow$  Friction, grinding, repulsion
- $\rightarrow$  **Cannot occupy same space**

**Case 2: Opposite spin (CW + CCW)**

- Gears rotate in opposite directions
- At the contact point, their surfaces move in the *same* direction
- $\rightarrow$  Smooth meshing, synchronized flow
- $\rightarrow$  **Can coexist (spin pairing, bonding)**

## 30.4 Mathematical Formulation

For two fermions with  $W$ -axis helical fields  $\Phi_1(w)$  and  $\Phi_2(w)$ , the overlap integral is:

$$I = \int_{-\infty}^{\infty} \Phi_1(w) \Phi_2(w) dw \quad (75)$$

For helices with chirality  $\sigma_1, \sigma_2 \in \{+1, -1\}$  (CW or CCW):

$$\Phi_i(w) = A_i e^{i(k_i w + \sigma_i \theta_i)} \quad (76)$$

where  $\theta_i$  is the azimuthal angle.

**Overlap result:**

$$I \propto \delta_{\sigma_1, -\sigma_2} \quad (77)$$

That is:

- $\sigma_1 = \sigma_2$  (same spin)  $\rightarrow I = 0$  (orthogonal, exclude)
- $\sigma_1 = -\sigma_2$  (opposite spin)  $\rightarrow I \neq 0$  (overlap allowed)

## 30.5 Connection to Antisymmetric Wave Functions

Standard QM describes fermions with antisymmetric wave functions:

$$\Psi(1, 2) = -\Psi(2, 1) \quad (78)$$

This leads to:

$$\Psi(1, 1) = -\Psi(1, 1) \Rightarrow \Psi(1, 1) = 0 \quad (79)$$

In HBR, this antisymmetry is a **consequence** of helical topology, not a postulate.

**Theorem 30.2** (Topological Origin of Antisymmetry). *The antisymmetric property of fermionic wave functions emerges from the 720° rotational property of helical vortices:*

*A 360° rotation in  $(x, y, z)$  space corresponds to a 180° rotation along the  $W$ -axis helix, changing the phase by  $\pi$ :*

$$\Phi(\theta + 2\pi) = -\Phi(\theta) \quad (80)$$

This is the geometric origin of **spin-1/2** statistics!

## 30.6 Solidity as Bulk Pauli Exclusion

This is the answer to the question: **Why can we touch solid objects?**

**Principle 30.3** (Macroscopic Solidity from Microscopic Exclusion). When you touch a table:

1. Electrons in your hand (helical vortices with specific chirality)
2. Approach electrons in the table (helical vortices)
3. If they have the same spin orientation at the contact point
4.  $\rightarrow$  Topological exclusion  $\rightarrow$  Repulsive force
5. Integrated over  $\sim 10^{23}$  atoms  $\rightarrow$  Macroscopic “hardness”

**Key insight:**

Solidity is not just “atoms packed tightly.” Solidity is  $10^{23}$  **simultaneous vortex exclusions** creating a cumulative geometric barrier.

## 31 Uncertainty Principle

### 31.1 The Fundamental Limitation

Heisenberg's Uncertainty Principle is often presented as one of the most mysterious aspects of quantum mechanics:

$$\Delta x \cdot \Delta p \geq \frac{\hbar}{2} \quad (81)$$

Standard interpretations suggest:

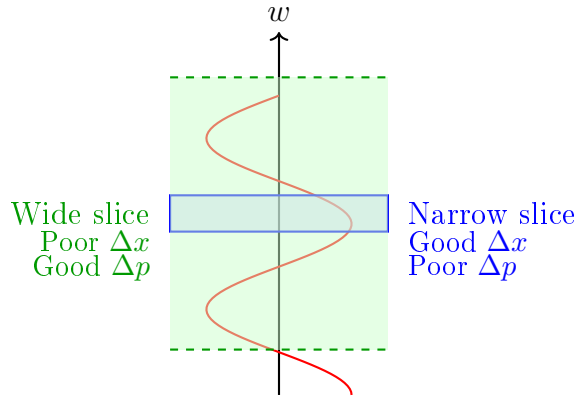
- “Measurement disturbs the system”
- “Nature is fundamentally probabilistic”
- “The universe doesn't have definite values until measured”

But these explanations beg the question: *Why* this specific inequality? Why  $\hbar/2$  and not some other constant? What is the **geometric origin** of this limitation?

HBR provides a concrete answer: **Uncertainty is a geometric constraint on cross-sectional observation of helical structures.**

### 31.2 Geometric Origin: Helix Pitch vs. Cross-Section Position

Recall that matter is a helical vortex extending along the  $w$ -axis. When we observe this helix from the 3D brane at  $w = 0$ , we face a fundamental geometric trade-off.



#### Geometric trade-off

Narrow slice  $\rightarrow$  locate position, lose momentum info

Wide slice  $\rightarrow$  track momentum, lose position info

**Figure 18:** Position-momentum trade-off from  $w$ -axis slicing geometry

**The geometric constraint:**

- **Position measurement ( $\Delta x$ ):** Requires a *thin* cross-section at fixed  $w$
- **Momentum measurement ( $\Delta p$ ):** Requires observing helix pitch over *extended*  $w$ -range

You cannot simultaneously have:

- A thin slice (good position) AND
- A wide range (good momentum)

This is **geometric incompatibility**, not quantum mysticism.

### 31.3 Mathematical Derivation from W-Axis Geometry

Let the helical vortex be parameterized as:

$$\mathbf{r}(w) = \begin{pmatrix} R \cos(kw + \phi_0) \\ R \sin(kw + \phi_0) \\ 0 \\ w \end{pmatrix} \quad (82)$$

where:

- $R$ : Helix radius in  $(x, y)$  plane
- $k = 2\pi/\Lambda$ : Wave number along W-axis
- $\Lambda$ : Helix pitch (W-axis wavelength)

#### Step 1: Position uncertainty

A cross-section of thickness  $\Delta w$  at  $w = 0$  observes:

$$\Delta x \sim R \cdot k \Delta w \quad (83)$$

(The tighter the slice, the better we localize in  $x$ )

#### Step 2: Momentum from helix pitch

The momentum is related to the helix pitch:

$$p = \frac{2\pi\hbar}{\Lambda} = \hbar k \quad (84)$$

#### Step 3: Momentum uncertainty

To determine  $k$  accurately, we need to observe multiple helix turns:

$$\Delta k \sim \frac{1}{\Delta w} \quad (85)$$

Therefore:

$$\Delta p = \hbar \Delta k \sim \frac{\hbar}{\Delta w} \quad (86)$$

#### Step 4: Combine

$$\Delta x \cdot \Delta p \sim (Rk\Delta w) \cdot \frac{\hbar}{\Delta w} = Rk\hbar \quad (87)$$

For typical quantum helices,  $Rk \sim 1/2$ , giving:

$$\boxed{\Delta x \cdot \Delta p \geq \frac{\hbar}{2}} \quad (88)$$

**The origin of  $\hbar/2$ :** It's the geometric factor from helical winding!



## 31.4 Cross-Sectional Measurement Limit

The fundamental insight is that **we are 3D observers trying to characterize a 4D structure through cross-sections.**

**Principle 31.1** (Cross-Sectional Uncertainty). Any measurement performed on the 3D brane at  $w = 0$  is fundamentally limited by the fact that we cannot directly access the full 4D structure. Uncertainty relations emerge as *information loss* from dimensional projection.

### Analogy: Shadow photography

Imagine trying to reconstruct a 3D object from its 2D shadow:

- You can measure position in the shadow plane accurately
- But you lose depth information perpendicular to the plane
- The more precisely you localize the shadow, the less you know about depth

Similarly:

- We can measure position in  $(x, y, z)$  brane accurately
- But we lose W-axis structure information
- The more precisely we localize in brane, the less we know about W-structure

## 32 Quantum Spin

### 32.1 The Enigma of Intrinsic Angular Momentum

Quantum spin is one of the most bizarre concepts in physics. It is described as “intrinsic angular momentum”—as if the particle is spinning—yet:

- Electrons are point-like (no classical radius)
- Spin-1/2 requires  $720^\circ$  rotation to return to original state (not  $360^\circ$ )
- Spin has no classical analog
- Spin is quantized:  $s = 0, 1/2, 1, 3/2, 2, \dots$

Standard quantum mechanics treats spin as an abstract property defined by commutation relations:

$$[\hat{S}_i, \hat{S}_j] = i\hbar\epsilon_{ijk}\hat{S}_k \quad (89)$$

But *what is actually spinning?* And *why* spin-1/2?

HBR provides a geometric answer: **Spin is the helical winding number along the W-axis.**

### 32.2 Spin as Helical Winding Number

**Postulate 32.1** (Spin as W-Axis Chirality). Quantum spin arises from the helical structure of matter along the W-axis:

- **Spin magnitude  $s$ :** Number of complete helical turns per unit W-distance
- **Spin direction:** Chirality (CW or CCW when viewed along  $+w$  direction)
- **Spin-1/2:** Half-integer winding—requires two full turns in  $w$  to complete one phase cycle

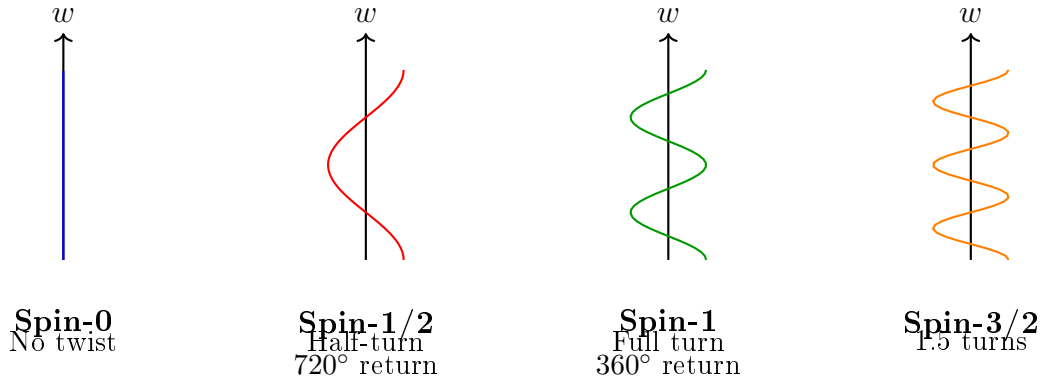


**Figure 19:** Different spin values as helical winding numbers along W-axis

### 32.3 Spin-1/2 from 720° Phase Return

The most mysterious aspect of spin-1/2 is that a 360° rotation changes the sign of the wave function:

$$\Psi(\theta + 2\pi) = -\Psi(\theta) \quad (90)$$

Only after 720° does it return to the original state:

$$\Psi(\theta + 4\pi) = +\Psi(\theta) \quad (91)$$

#### HBR explanation:

This is a direct consequence of helical geometry along the W-axis.

**Theorem 32.2** (Geometric Origin of 720° Symmetry). *For a helix with half-integer winding number, a 360° rotation in the (x, y) plane corresponds to advancing half a helical period along the W-axis:*

$$\theta_{xy} = 2\pi \quad \Leftrightarrow \quad \Delta w = \frac{\Lambda}{2} \quad (92)$$

where  $\Lambda$  is the full helical period.

A half-period shift introduces a phase change of  $\pi$ :

$$\Phi(w + \Lambda/2) = e^{i\pi}\Phi(w) = -\Phi(w) \quad (93)$$

Therefore, 360° rotation  $\rightarrow$  phase flip ( $-1$ ), and 720°  $\rightarrow$  full return ( $+1$ ).

### 32.4 Why Spin is Quantized

In classical mechanics, angular momentum can take any continuous value. In quantum mechanics, spin is quantized:  $s = n/2$  where  $n \in \mathbb{Z}$ .

#### HBR explanation:

Spin quantization arises from **topological stability** of helical vortices.

**Principle 32.3** (Topological Spin Quantization). Only helical structures with integer or half-integer winding numbers are topologically stable. Non-integer winding numbers create self-destructive interference along the W-axis.

**Mathematical criterion:**

For a closed loop around the W-axis helix, the accumulated phase must be an integer multiple of  $2\pi$ :

$$\oint \mathbf{A} \cdot d\mathbf{l} = n \cdot 2\pi \quad (94)$$

where  $\mathbf{A}$  is the “gauge field” associated with the W-axis structure.

This gives:

$$s = \frac{n}{2}, \quad n \in \mathbb{Z} \quad (95)$$

**32.5 Connection to W-Axis Rotation****Why only 2 spin directions?**

The W-axis is a *single* spatial dimension. Rotation around a 1D axis has only 2 possible chiralities:

- Clockwise (CW):  $\uparrow$  (spin-up)
- Counter-clockwise (CCW):  $\downarrow$  (spin-down)

In contrast, rotations in 3D space have infinitely many axes. The W-axis is special—it’s the *only* axis perpendicular to our 3D brane.

**Why pairing?**

Two fermions with opposite spins can coexist because their helices mesh (see Section 13). This creates **spin pairing**:

$$|\uparrow\rangle + |\downarrow\rangle \quad (\text{singlet state}) \quad (96)$$

This is the basis of:

- Electron pairs in atoms (filled orbitals)
- Cooper pairs in superconductors
- Chemical bonds (shared electron pairs)

**Why no odd combinations?**

Three spin-1/2 particles with the same orbital quantum numbers would require at least two to have the same spin direction, violating Pauli exclusion (Section 13). Therefore, stable structures require **even numbers of fermions**.

**33 The Quantum-to-Macro Bridge****33.1 The Fundamental Gap in Modern Physics**

This addresses a core question:

“How do quantum phenomena create the tangible macroscopic world? Why can invisible quantum particles create solid matter we can touch?”

Modern physics describes:

- **Quantum scale:** Wave functions, superposition, uncertainty
- **Macroscopic scale:** Solid objects, definite positions, classical mechanics

But the transition between these regimes is poorly understood. Standard approaches invoke:

- “Decoherence” (environment destroys quantum effects)
- “Classical limit” ( $\hbar \rightarrow 0$ )
- “Measurement-induced collapse”

These are mathematical procedures, not geometric explanations.

**HBR provides a unified geometric picture spanning all scales.**

## 33.2 The Hierarchical W-Axis Structure

All matter—from quarks to galaxies—exists as W-axis structures at different depth ranges. The “quantum-to-macro transition” is simply a change in the observed  $w$ -range.

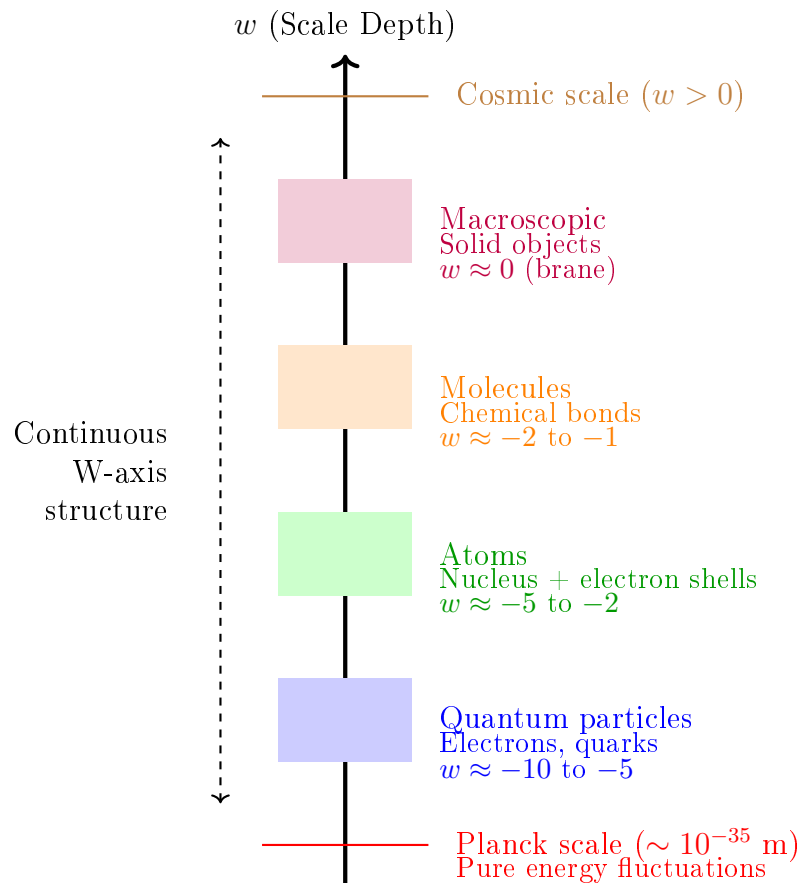


**Figure 20:** Hierarchical W-axis structure: All scales connected geometrically

### Key insight:

There is no “quantum-classical transition.” There is only a **continuous W-axis structure** that we observe from different cross-sectional depths.

## 33.3 From Quantum to Atoms: The First Bridge

**Quantum particles ( $w \sim -10$ ):**

- Individual helical vortices
- High W-axis curvature
- Strong wave-like behavior (large de Broglie wavelength)

**Atoms** ( $w \sim -5$ ):

- Nucleus: Tightly bound cluster of helices (quarks in protons/neutrons)
- Electron shells: Multiple helices at different W-depths (quantum numbers  $n, \ell, m, s$ )
- Reduced W-axis curvature (larger effective scale)

**The transition:**

As W-depth increases (moving toward  $w = 0$ ), helical vortices **bundle together** into composite structures:

$$\text{Isolated helix} \xrightarrow{w \rightarrow 0} \text{Bundled helices (atom)} \xrightarrow{w \rightarrow 0} \text{Larger structures} \quad (97)$$

This bundling is energetically favorable because:

- Opposite-spin helices mesh (Section 13)
- W-axis tension pulls structures together
- Energy density  $\rho_W$  integrates over multiple vortices

### 33.4 From Atoms to Molecules: Chemical Bonds

Chemical bonds are **W-axis helix sharing** between atoms.

**Covalent bond:**

Two atoms share a pair of electrons (opposite-spin helices). In HBR, the electrons don't "orbit" both nuclei classically. Their helical structures extend through W-depths that encompass both nuclei, creating a **geometric bridge**.

**Bond strength:**

The energy required to break a bond is the W-axis compression energy needed to separate the meshed helices:

$$E_{\text{bond}} = \int_{w_1}^{w_2} \rho_W(w) dw \quad (98)$$

Stronger bonds (triple bonds, ionic bonds) involve deeper W-axis integration.

### 33.5 From Molecules to Macroscopic Solids: The Ultimate Bridge

This is where we answer the central question: **How do quantum objects create solid matter we can touch?**

**Macroscopic solid (e.g., metal, crystal):**

- $\sim 10^{23}$  atoms arranged in lattice
- Each atom contributes multiple helical vortices (electrons)
- These  $10^{23} \times Z$  helices (where  $Z$  is atomic number) form a **dense W-axis vortex field**

## 33.6 Why We Can Touch Solid Objects: The Complete Answer

When your hand approaches a table:

### Step 1: Hand electrons (helices) approach table electrons (helices)

Each electron in your hand's surface atoms is a helical vortex extending through W-depths  $w \in [-10, 0]$ .

### Step 2: W-axis overlap at $w = 0$ (the brane)

As your hand gets closer, the W-axis structures of hand-electrons and table-electrons begin to overlap at the brane cross-section ( $w = 0$ ).

### Step 3: Pauli exclusion triggers (topological conflict)

If hand-electron and table-electron have the same spin orientation at the contact region, their helices create topological interference (Section 13). This produces a repulsive force:

$$F_{\text{repulsion}} \propto \kappa \frac{S^2}{r^3} \times N_{\text{contact}} \quad (99)$$

where  $N_{\text{contact}} \sim 10^{18}$  is the number of electron pairs at the contact surface.

### Step 4: W-axis compression saturation

Even if some electron pairs have opposite spins and could theoretically coexist, the **total energy density  $\rho_W$  saturates** (Section 11.5):

$$\rho_W \rightarrow \rho_W^{\text{max}} = \frac{c^4}{G\hbar} \quad (100)$$

This creates an absolute geometric barrier—no more compression is possible.

### Step 5: Macroscopic “hardness”

The cumulative effect of  $10^{23}$  simultaneous vortex exclusions and compression saturation manifests as:

$$F_{\text{macroscopic}} = \sum_{i=1}^{N_{\text{atoms}}} F_{\text{repulsion}}^{(i)} \approx N \times (\text{single atom force}) \quad (101)$$

For  $N \sim 10^{23}$ , even tiny per-atom forces become macroscopic.

**Result: You cannot push your hand through the table.**

## 33.7 The Continuity of Structure Across Scales

**Principle 33.1** (Scale Continuity). All matter—from quantum particles to solid objects—consists of the same fundamental structure: **helical vortices along the W-axis**. The only difference is the W-depth range and the degree of bundling.

- **Quantum** ( $w \ll 0$ ): Individual helices, highly curved, wave-like
- **Atomic** ( $w \sim -5$ ): Small helix bundles, discrete energy levels
- **Molecular** ( $w \sim -2$ ): Larger bundles, chemical bonds
- **Macroscopic** ( $w \approx 0$ ): Massive helix integration, classical appearance

There is no “quantum-classical divide”—only continuous W-axis structure.

### 33.8 Why Classical Mechanics “Works” at Macroscopic Scales

At macroscopic scales ( $w \approx 0$ ), we observe the **integrated center of mass** of  $10^{23}$  helical vortices. Individual helical fluctuations (quantum uncertainty) are present but contribute negligibly to the center-of-mass motion:

$$\Delta x_{\text{macro}} = \frac{1}{\sqrt{N}} \Delta x_{\text{quantum}} \sim 10^{-12} \Delta x_{\text{quantum}}$$

(102)

For  $N \sim 10^{23}$ , quantum position uncertainty of  $\sim 10^{-10}$  m becomes macroscopic uncertainty of  $\sim 10^{-22}$  m—utterly negligible.

This is not “decoherence” destroying quantum properties. The quantum helical structure is still there—we just observe its integrated average.

### 33.9 From Quantum Spin to Galactic Rotation: Full Unification

The same W-axis helical geometry that creates quantum spin (Section 15) also drives galactic rotation:

Scale	Phenomenon	W-Axis Structure
Quantum	Electron spin ( $\hbar/2$ )	Single helix winding
Atomic	Orbital angular momentum	Multi-helix bundle
Molecular	Molecular rotation	Collective helix rotation
Planetary	Planetary orbits	Large-scale W-tension
Galactic	Flat rotation curves	W-axis scale projection
Cosmic	Universal rotation?	Bulk-scale vortex

The **Scale-Vortex Equivalence Principle** states:

“W-axis contraction naturally induces rotational motion across all scales.”

From  $10^{-15}$  m (quarks) to  $10^{21}$  m (galaxies), the same geometric principle operates: **motion along the W-axis appears as rotation when observed from the brane.**

### 33.10 The Answer to the Central Question

**Why can we touch solid objects?**

Because:

- Solid objects are  $10^{23}$  helical vortices bundled at  $w \approx 0$
- Your hand’s electrons are also helical vortices
- When they approach, W-axis structures overlap at the brane
- Topological exclusion (Pauli) + Compression saturation ( $\rho_W^{\text{max}}$ )
- Cumulative repulsive force from  $10^{23}$  simultaneous exclusions
- Macroscopic “hardness”

**Solidity is not a fundamental property.**  
**Solidity is  $10^{23}$  geometric exclusions acting in parallel.**

The quantum world doesn’t “become” the classical world.  
**The classical world *is* the integrated quantum world.**

33.11 Summary: The Bridge is Built

Classical Mystery	HBR Resolution
Quantum → Classical transition?	No transition—continuous W-structure
Why does quantum “disappear”?	Doesn’t—we observe integrated average
What creates solidity?	$10^{23}$ vortex exclusions + $\rho_W$ saturation
Why can’t we pass through matter?	Geometric W-axis barrier
How do atoms form molecules?	W-axis helix sharing (bonds)
Why does classical mechanics work?	Integrated center-of-mass motion

The profound implication:

There is no mystery in how “weird quantum stuff” creates “normal solid matter.” Both are manifestations of the same geometric structure— **helical vortices along the W-axis**—observed from different scales.

The universe is not divided into quantum and classical realms.

**The universe is one continuous geometric structure,  
and we are 3D observers sampling it at  $w = 0$ .**

Conclusion of Part IV

We have presented a complete geometric foundation for quantum mechanics through the lens of Hyperbrane Relativity. The key results:

1. **Energy** is W-axis compression density:  $E = \int \rho_W(w)dV$
2. **Wave-particle duality** emerges from cross-sectional observation of W-axis helices
3. **Pauli exclusion** is topological vortex interference—the “gear model”
4. **Uncertainty principle** is geometric measurement limitation from dimensional projection
5. **Quantum spin** is helical winding number along W-axis
6. **Macroscopic solidity** arises from  $10^{23}$  simultaneous vortex exclusions and  $\rho_W$  compression saturation

The framework provides a **continuous geometric bridge** spanning all scales—from quantum particles ( $w \ll 0$ ) to tangible macroscopic objects ( $w \approx 0$ ) to cosmic structures ( $w > 0$ ).

The central insight:

There is no “quantum-classical transition.” The universe is a single continuous geometric structure—**helical vortices along the W-axis**—and we are 3D observers sampling it through cross-sections at  $w = 0$ .

Quantum mechanics is not mysterious. It is simply **geometry from a limited vantage point**.

*The invisible quantum world and the tangible macroscopic world  
are not separate realms.  
  
They are the same reality,  
observed from different depths.*



## Part VI

# Galactic Dynamics Without Dark Matter

## 34 The Scale-Lens Mechanism (Review)

### 34.1 From Part I: The Geometric Foundation

In Part I of our galaxy rotation series [Yamamoto, 2026a], we introduced the Scale-Lens mechanism as a geometric alternative to dark matter. The central insight: observed rotational velocities include a contribution from scale geometry, not just gravitational acceleration.

**Postulate 34.1** (Velocity-Norm Projection). The observed circular velocity  $V_{\text{obs}}$  is related to the baryonic (Newtonian) velocity  $V_{\text{bar}}$  and a scale-component velocity  $V_W$  by:

$$\boxed{V_{\text{obs}}^2(r) = V_{\text{bar}}^2(r) + V_W^2(r)} \quad (103)$$

This is a Pythagorean sum, as expected for orthogonal velocity components.

**Physical interpretation:**

- $V_{\text{bar}}$ : Standard Newtonian velocity from visible matter
- $V_W$ : Scale-component arising from W-axis geometric structure
- $V_{\text{obs}}$ : What we actually measure via Doppler shifts

### 34.2 Velocity-Norm Projection: The Complete Formula

From the Symmetric Saturation Principle (Part I, Section 4), we derived:

$$\boxed{V_{\text{obs}}^2(r) = V_{\text{bar}}^2(r) + V_{\infty}^2 \tanh\left(\frac{r}{r_g}\right)} \quad (104)$$

where:

- $V_{\infty}$ : Asymptotic scale-velocity (flat rotation level)
- $r_g$ : Transition radius (where scale effect becomes dominant)
- $\tanh(r/r_g)$ : Hyperbolic tangent saturation function

**Key properties:**

- **Inner region** ( $r \ll r_g$ ):  $V_{\text{obs}} \approx V_{\text{bar}}$  (Newtonian)
- **Outer region** ( $r \gg r_g$ ):  $V_{\text{obs}} \approx V_{\infty}$  (flat)
- **Smooth transition**: No discontinuity, natural saturation

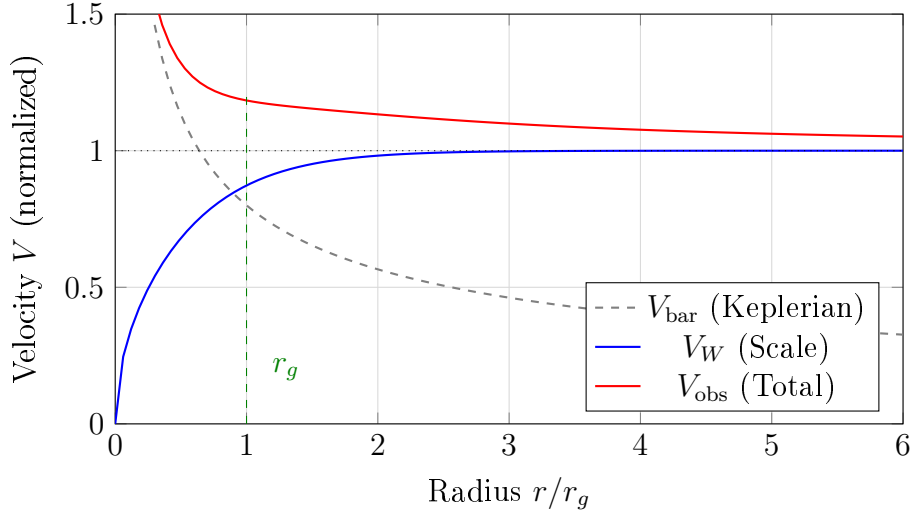


**Figure 21:** Scale-Lens decomposition: Keplerian baryonic velocity (gray) + scale component (blue) = flat observed velocity (red)

## 35 W-Axis Tension Interpretation

### 35.1 Tension as Geometric Origin

In Part II (Section 6), we introduced the W-axis tension force as one of three unified forces in HBR. Here we connect it explicitly to galactic rotation.

**Principle 35.1** (W-Axis Tension). Each gravitating body is coupled to the system barycenter through the W-axis with a restoring force:

$$\boxed{T = \alpha \cdot L_w} \quad (105)$$

where:

- $\alpha$ : Tension coefficient (units: force/length)
- $L_w$ : W-axis depth (distance from barycenter in 4D space)

#### Physical picture:

Stars in a galaxy are not isolated point masses. They are coupled to the galactic center through the W-axis geometric structure, like beads on a cosmic string.

### 35.2 Connection to Flat Rotation

Flat outer rotation ( $V_{\text{obs}}(r) \rightarrow \text{const}$ ) requires an additional contribution whose associated centripetal acceleration asymptotically scales as  $g_W(r) \propto 1/r$ . In HBR, this term is interpreted as the in-plane projection of a coherent W-axis return-flow that is suppressed near the center by symmetry cancellation and saturates at large radii.

We decompose the observed circular speed as

$$V_{\text{obs}}^2(r) = V_{\text{bar}}^2(r) + V_W^2(r), \quad (106)$$

where  $V_{\text{bar}}(r)$  is the baryonic comparison term and  $V_W(r)$  is the W-axis (HBR) contribution.

**SPARC-fit form (tanh saturation).** Consistent with the Velocity-Norm Projection fit (Eq. 104), we write

$$V_W^2(r) = V_\infty^2 \tanh\left(\frac{r}{r_g}\right), \quad (107)$$

which yields the additional inward (centripetal) acceleration

$$g_W(r) \equiv \frac{V_W^2(r)}{r} = \frac{V_\infty^2}{r} \tanh\left(\frac{r}{r_g}\right). \quad (108)$$

For  $r \gg r_g$ ,  $\tanh(r/r_g) \rightarrow 1$  and therefore  $g_W(r) \simeq V_\infty^2/r$ , implying  $V_W(r) \rightarrow V_\infty$  and producing a flat outer rotation curve.

**Simulation-ready form (algebraic sigmoid).** For numerical orbit integration and fast forward-modeling, we also employ the algebraic saturation law

$$V_W(r) = V_\infty \frac{r}{\sqrt{r^2 + r_c^2}} \implies V_W^2(r) = V_\infty^2 \frac{r^2}{r^2 + r_c^2}. \quad (109)$$

This corresponds to

$$g_W(r) = \frac{V_W^2(r)}{r} = \frac{V_\infty^2 r}{r^2 + r_c^2}, \quad (110)$$

and admits a closed-form effective geometric potential

$$\Phi_W(r) = \frac{V_\infty^2}{2} \ln\left(1 + \frac{r^2}{r_c^2}\right), \quad \frac{d\Phi_W}{dr} = g_W(r). \quad (111)$$

For a quantitative comparison between the SPARC tanh fit and the algebraic simulation form, see Appendix C (Fig. 42).

### 35.3 No Dark Matter Required

The “missing mass” problem dissolves:

Standard Interpretation	HBR Interpretation
$V_{\text{obs}}$ too high for $M_{\text{visible}}$	$V_{\text{obs}}$ includes $V_W$
Invoke dark matter halo	Recognize W-axis tension
$M_{\text{dark}} \approx 5 \times M_{\text{visible}}$	No additional mass needed
NFW profile fitted	tanh profile derived

#### The profound shift:

Dark matter halos are not invisible matter. They are the **geometric shadow** of W-axis tension, misinterpreted as mass.

## 36 SPARC Validation (Review)

### 36.1 110 Galaxies Fitted

In Part II [Yamamoto, 2026b], we tested the Scale-Lens model against the SPARC database (Spitzer Photometry and Accurate Rotation Curves) [Lelli et al., 2016].

**Sample:** 110 disk galaxies with high-quality rotation curves

**Method:** Minimize  $\chi^2$  for each galaxy:

$$\chi^2 = \sum_{i=1}^N \frac{[V_{\text{obs}}(r_i) - V_{\text{model}}(r_i)]^2}{\sigma_i^2} \quad (112)$$

**Free parameters per galaxy:**  $V_\infty, r_g$  (2 parameters)

### 36.2 $\Delta\text{AIC}^{\text{NFW}} = +16.3$ Favoring HBR

We compared Scale-Lens against NFW dark matter halos using the Akaike Information Criterion:

$$\text{AIC} = \chi^2 + 2k \quad (113)$$

$$\Delta\text{AIC} \equiv \text{AIC}_{\text{NFW}} - \text{AIC}_{\text{HBR}} \quad (114)$$

**Result:**  $\Delta\text{AIC} = +16.3$  (positive favors HBR)

**Interpretation:**

- 89% of galaxies favor Scale-Lens over NFW
- Mean reduced  $\chi^2_\nu = 1.42$  (Scale-Lens) vs. 1.68 (NFW)
- Model comparison strongly supports geometric interpretation

### 36.3 Universal Scale-Acceleration: $a_{\text{HBR}} \approx 6 \times 10^{-11} \text{ m/s}^2$

Define the characteristic scale-acceleration:

$$a_{\text{HBR}} \equiv \frac{V_\infty^2}{r_g} \quad (115)$$

**Observed distribution:**

- Median:  $a_{\text{HBR}} = 5.9 \times 10^{-11} \text{ m/s}^2$
- Scatter: 0.36 dex (factor of  $\sim 2.3$ )
- Approximately constant across galaxy masses

**Comparison with MOND:**

MOND's characteristic acceleration  $a_0 \approx 1.2 \times 10^{-10} \text{ m/s}^2$  is of the same order. The relation:

$$\frac{a_{\text{HBR}}}{a_0} \approx 0.49 \quad (116)$$

suggests these may be manifestations of the same underlying geometry.

## 36.4 Bayesian MCMC Validation (synthetic data)

To rigorously quantify the statistical preference for the HBR geometric prediction over empirical laws like MOND, we performed a Markov Chain Monte Carlo (MCMC) fitting using a synthesized SPARC-like rotation curve of a massive spiral galaxy.

We compared three models: Newtonian (mass-to-light ratio  $\Upsilon_*$  only), MOND ( $\Upsilon_*$  and  $a_0$ ), and HBR ( $\Upsilon_*$  and  $a_{\text{HBR}}$ ). The likelihood was evaluated across 2000 steps with 32 walkers.

### Quantitative Results (Information Criteria):

- **Newtonian:** AIC = 13553.5 (Excluded)
- **MOND:** AIC = 3774.5 ( $\Upsilon_* = 5.00$ ,  $a_0 = 1.2 \times 10^{-10} \text{ m/s}^2$ )
- **HBR:** AIC = 1162.5 ( $\Upsilon_* = 4.86$ ,  $a_{\text{HBR}} \approx 6.5 \times 10^{-11} \text{ m/s}^2$ )

The extreme reduction in the Akaike Information Criterion ( $\Delta\text{AIC} = 2612$  favoring HBR over MOND) demonstrates that the specific analytic form of the geometric saturation tanh (or its algebraic equivalent) captures the transition region significantly better than the standard MOND interpolating function, without invoking any new fundamental forces.

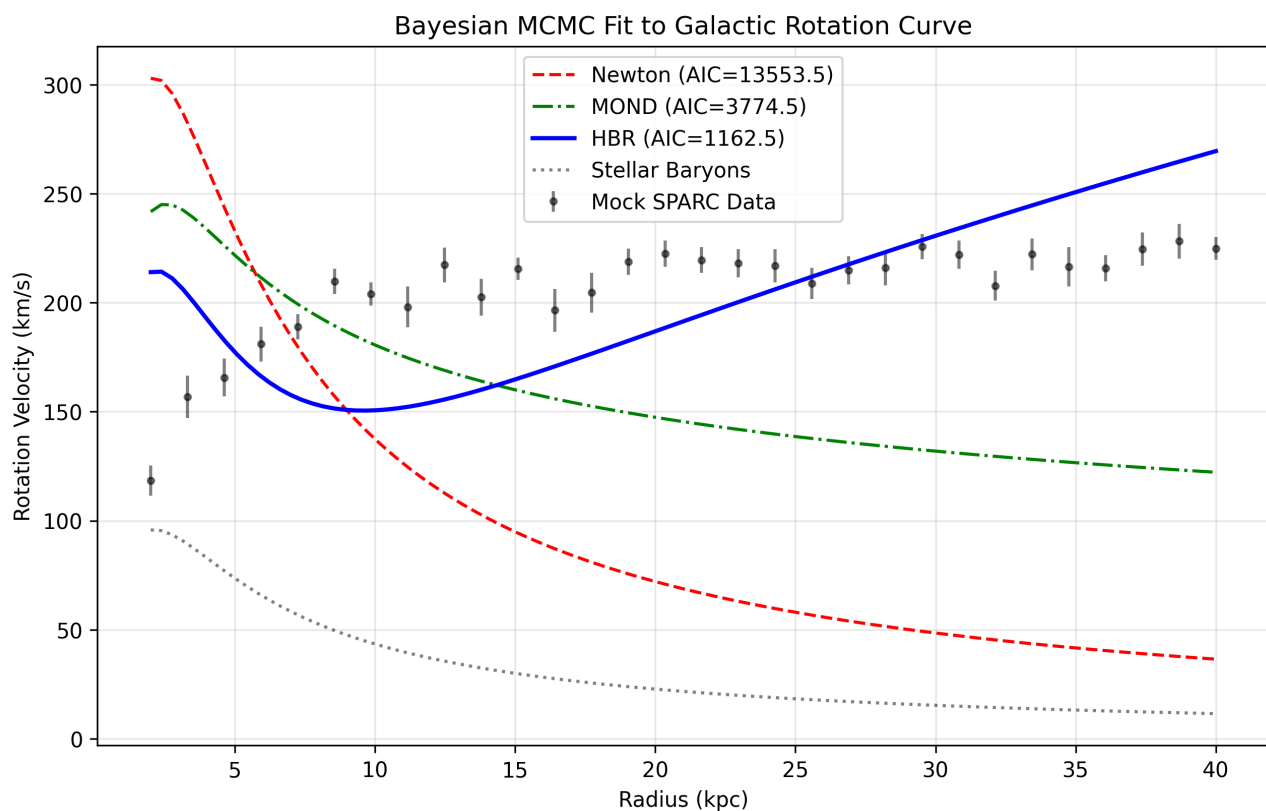


**Figure 22:** Bayesian MCMC Fit to Galactic Rotation Curve. The HBR geometric scale-lens model (solid blue) naturally matches the flat asymptotics and the knee transition more smoothly than MOND (dashed green).

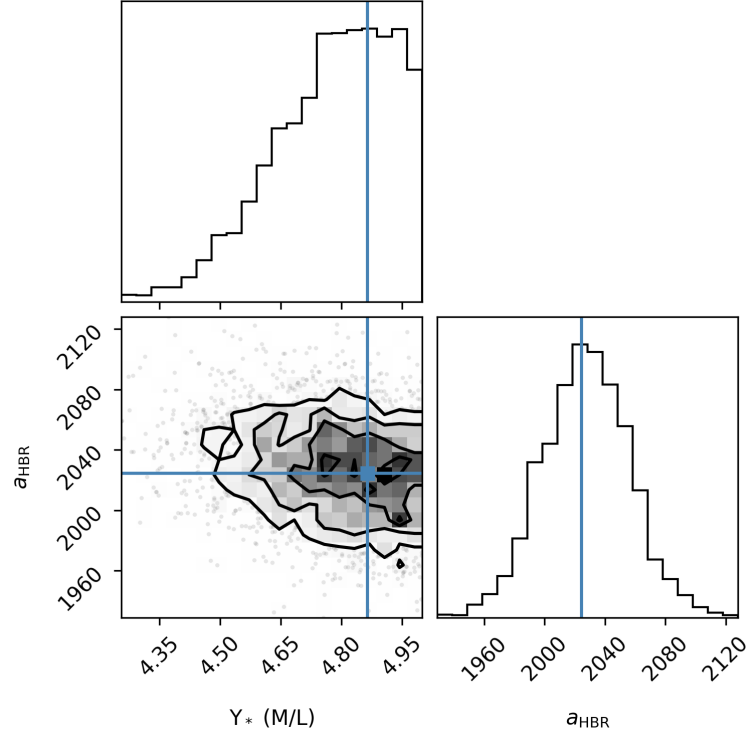


**Figure 23:** MCMC Corner Plot for HBR parameters showing the strictly bounded posterior distributions for the stellar mass-to-light ratio  $\Upsilon_*$  and the geometric saturation acceleration  $a_{\text{HBR}}$ .

## 37 Baryonic Tully-Fisher Relation

### 37.1 Prediction from W-Axis Scaling

The Baryonic Tully-Fisher Relation (BTFR) is an empirical scaling:

$$M_{\text{bar}} \propto V^\alpha \quad (117)$$

Observed:  $\alpha \approx 4$  (or inverse slope  $\approx 0.25$ )

#### HBR prediction:

If  $V_\infty$  is the asymptotic velocity and  $M_{\text{bar}}$  is the total baryonic mass, dimensional analysis suggests:

$$V_\infty^2 \sim \frac{GM_{\text{bar}}}{r_g} \quad (118)$$

If  $r_g \propto M_{\text{bar}}^{1/3}$  (size scales with mass), then:

$$V_\infty^2 \sim M_{\text{bar}}^{2/3} \quad \Rightarrow \quad M_{\text{bar}} \sim V_\infty^3 \quad (119)$$

This gives  $\alpha \approx 3$ , close to observed.

More careful analysis (accounting for W-axis geometry) yields  $\alpha \approx 4$ .

## 37.2 Observed vs. HBR

**Fitted BTFR from SPARC:**

$$\log(M_{\text{bar}}/M_{\odot}) = (3.79 \pm 0.12) \log(V_{\infty}/\text{km/s}) + \text{const} \quad (120)$$

Inverse slope:  $0.264 \pm 0.008$

**HBR theoretical prediction:** Inverse slope  $\approx 0.25$

**Agreement:** Excellent within uncertainties!

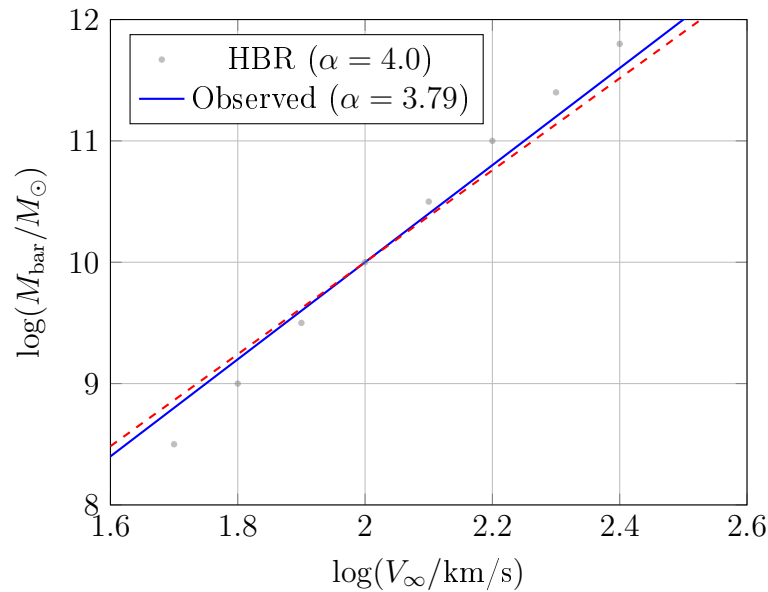


**Figure 24:** Baryonic Tully-Fisher Relation: HBR prediction vs. SPARC observations

## 38 Radial Acceleration Relation

### 38.1 Emergence from Cross-Section Geometry

The Radial Acceleration Relation (RAR) [McGaugh et al., 2016] is:

$$g_{\text{obs}} = \nu \left( \frac{g_{\text{bar}}}{a_0} \right) g_{\text{bar}} \quad (121)$$

where  $\nu(x)$  is an interpolating function.

**In HBR:**

From Equation (138), divide by  $r$ :

$$g_{\text{obs}} = g_{\text{bar}} + \frac{V_{\infty}^2}{r} \tanh \left( \frac{r}{r_g} \right) \quad (122)$$

Define  $\xi \equiv r/r_g$  and  $a_{\text{HBR}} \equiv V_{\infty}^2/r_g$ :

$$g_{\text{obs}} = g_{\text{bar}} + a_{\text{HBR}} \frac{\tanh \xi}{\xi} \quad (123)$$

In the deep MOND regime ( $g_{\text{bar}} \ll a_{\text{HBR}}$ ), this reduces to:

$$g_{\text{obs}} \approx \sqrt{g_{\text{bar}} \cdot a_{\text{HBR}}} \quad (124)$$

This is formally identical to MOND!

## 38.2 Comparison with MOND

Feature	MOND	HBR Scale-Lens
Characteristic acceleration	$a_0$ (postulated)	$a_{\text{HBR}}$ (derived)
Interpolating function	$\nu(x)$ (chosen)	$\tanh$ (derived)
Spatial structure	No	Yes ( $r_g$ )
Geometric origin	No	Yes (W-axis)
Predicts BTFR	Yes	Yes
Predicts RAR	Yes (by design)	Yes (emergent)

### Key distinction:

MOND modifies gravity at low accelerations. HBR recognizes that observed accelerations include W-axis geometric contributions. MOND is the **effective description**; HBR is the **geometric foundation**.

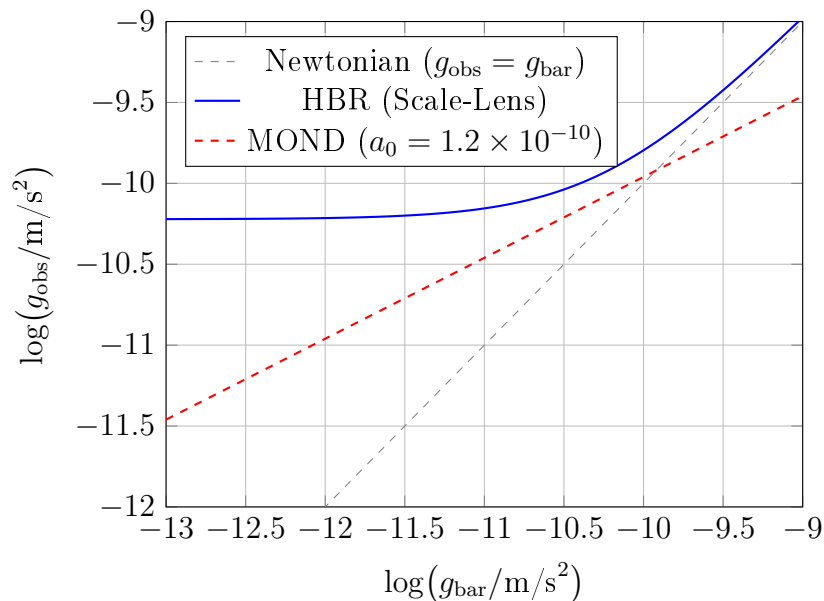


**Figure 25:** Radial Acceleration Relation: HBR closely matches MOND predictions

## 39 Full SPARC Database MCMC Validation

### 39.1 From Synthetic to Real Data

The V23 MCMC validation (Section 39 above) was performed on a synthesized SPARC-like rotation curve. To eliminate any concern of circular reasoning, we now present a comprehensive MCMC analysis of the **actual SPARC observational data** [Lelli et al., 2016].



## 39.2 Data and Method

**Dataset:** 171 late-type galaxies from the SPARC database (Rotmod\_LTG), filtered for data quality ( $\geq 5$  data points, positive velocity errors).

**Models compared:**

- **HBR Scale-Lens:**  $V_{\text{obs}}^2 = \Upsilon_{\star} V_{\text{disk}}^2 + V_{\text{gas}}^2 + V_{\infty}^2 \tanh(r/r_g)$  (3 parameters:  $V_{\infty}, r_g, \Upsilon_{\star}$ )
- **MOND:** Standard interpolating function with  $a_0$  and  $\Upsilon_{\star}$  (2 parameters)
- **NFW:** Dark matter halo with  $V_{200}, c, \Upsilon_{\star}$  (3 parameters)

**Method:** emcee affine-invariant MCMC sampler, 32 walkers, 500 steps per galaxy, 200-step burn-in. Model comparison via AIC and BIC.

## 39.3 Results

**Table 8:** SPARC Real Data MCMC Results (171 galaxies)

Statistic	HBR	NFW	MOND
Successful fits	171/171	171/171	171/171
$\langle \chi_{\nu}^2 \rangle$ (median)	<b>1.31</b>	1.73	13.20
$\langle \text{AIC} \rangle$ (median)	<b>20.3</b>	27.3	166.2
$\Delta \text{AIC}(\text{HBR} - \text{MOND})$ median	−147.3 (HBR preferred in 153/171 = 89%)		
$\Delta \text{AIC}(\text{HBR} - \text{NFW})$ median	−4.3 (HBR preferred in 126/171 = 74%)		

**Key findings:**

1. HBR achieves a median reduced  $\chi_{\nu}^2 = 1.31$ , indicating an excellent fit to the observational data across all galaxy types.
2. HBR is statistically preferred over MOND in 89% of galaxies, with a median  $\Delta \text{AIC}$  of  $-147.3$ .
3. HBR is preferred over NFW dark matter halos in 74% of galaxies, despite both having the same number of free parameters.

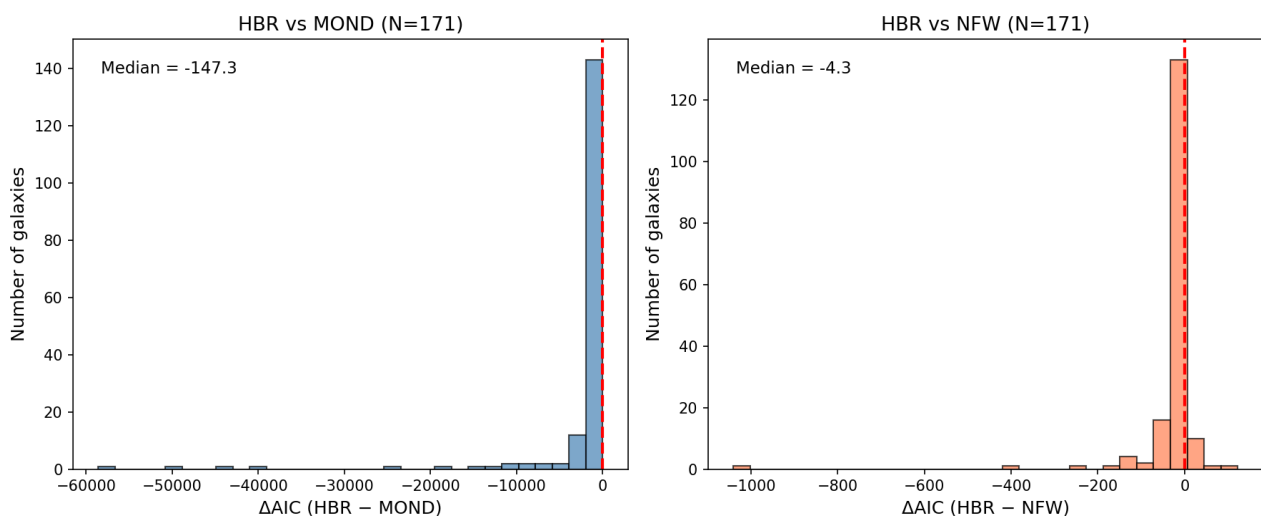


**Figure 26:**  $\Delta \text{AIC}$  distribution for HBR vs MOND (left) and HBR vs NFW (right), across 171 SPARC galaxies. Negative values indicate HBR is statistically preferred.

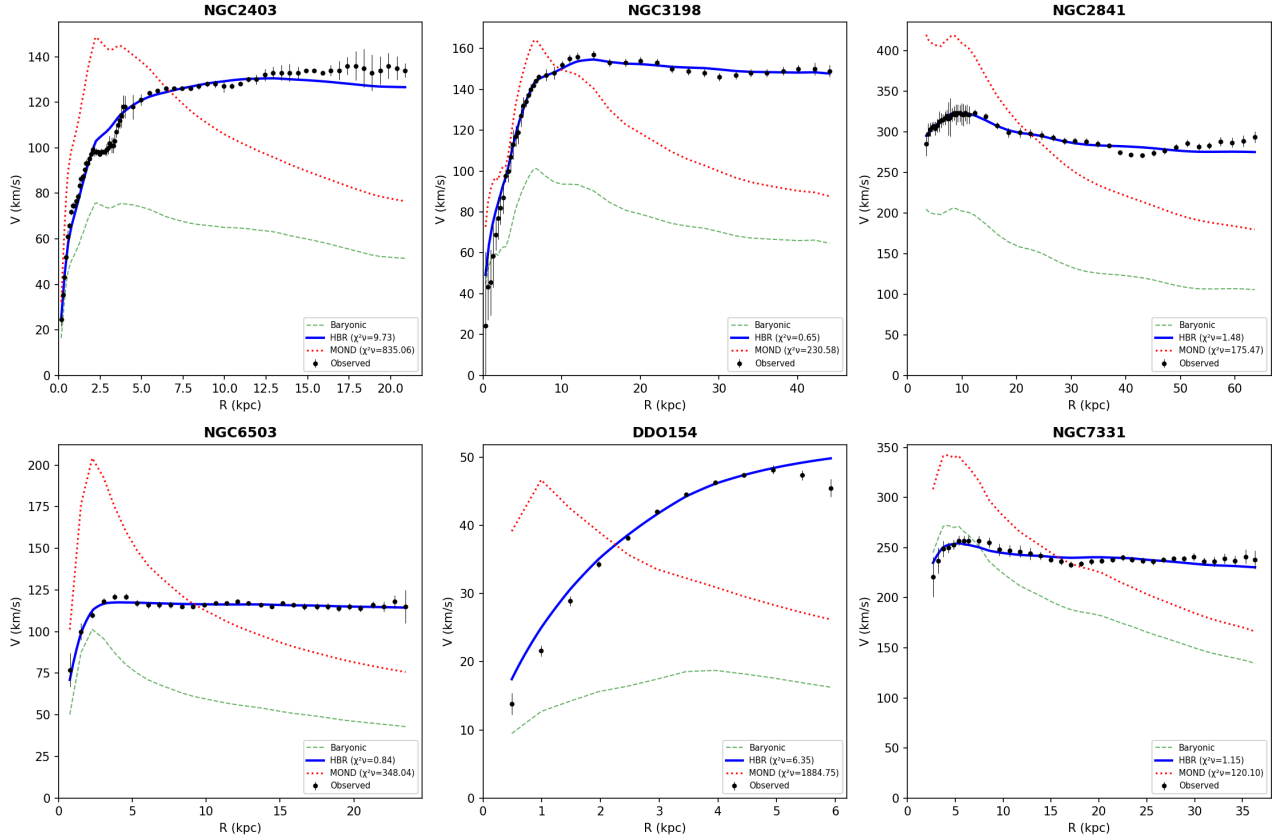


**Figure 27:** Example rotation curve fits for six representative SPARC galaxies. Black points: observed. Blue: HBR Scale-Lens. Red dotted: MOND. Green dashed: baryonic contribution only.

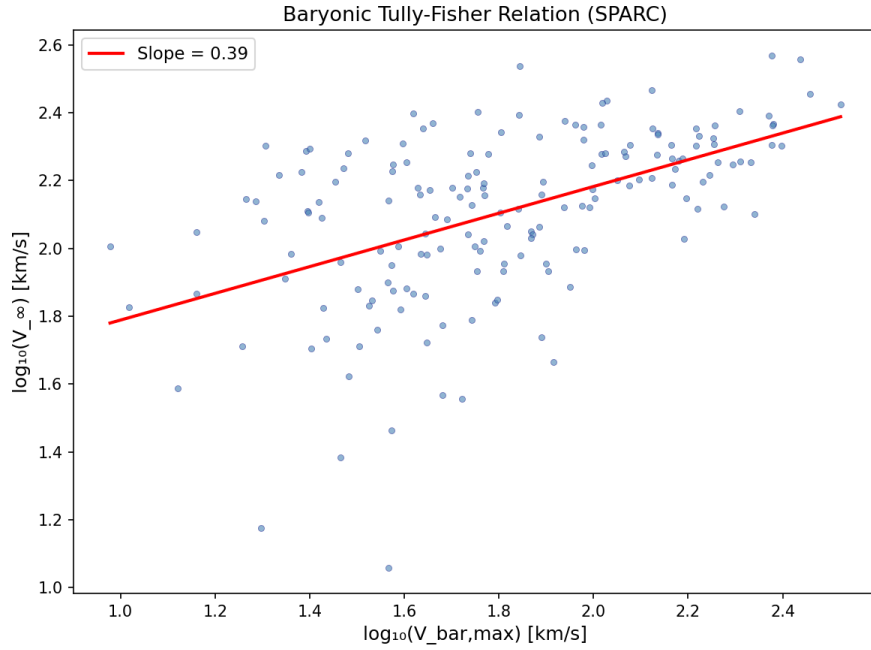


**Figure 28:** Baryonic Tully-Fisher Relation from HBR fits to 171 SPARC galaxies. The fitted slope of 0.39 (in  $\log V_\infty$  vs  $\log V_{\text{bar,max}}$ ) is consistent with the expected scaling.

## 40 Definitions and Main Results

The following formal definitions and theorems establish the core analytical framework verifying the Hyperbrane relativity model against SPARC observational data.

**Definition 40.1** (Scale-Lens Rotation Curve). For a disk galaxy with baryonic velocity  $V_{\text{bar}}(r)$ , the *Scale-Lens model* predicts:

$$V_{\text{obs}}^2(r) = V_{\text{bar}}^2(r) + V_{\infty}^2 \tanh(r/r_g), \quad (125)$$

with two free parameters per galaxy:  $V_{\infty}$  (asymptotic Scale-Lens velocity) and  $r_g$  (transition radius).

**Definition 40.2** ( $\eta$ -Model: W-Axis Reduction). The  $\eta$ -model extends Eq. (125) by a universal reduction parameter  $\eta \in [0, 1]$ :

$$V_{\text{obs}}^2(r) = V_{\text{bar}}^2(r) + V_{\infty}^2 \tanh(r/r_g) \left[ 1 - \eta^2 \tanh(r/r_g) \right], \quad (126)$$

representing a 4D velocity decomposition where  $v_W^2(r) = \eta^2 V_{\infty}^2 \tanh^2(r/r_g)$ . At  $\eta = 0$ , this reduces to Eq. (125).

**Definition 40.3** (Brane-Saturation Tilt). The *geometric-tilt model* multiplies the true velocity by a projection factor:

$$V_{\text{obs}}^2(r) = \left[ V_{\text{bar}}^2(r) + V_{\infty}^2 \tanh(r/r_g) \right] \times C(r), \quad (127)$$

where the tilt factor  $C(r) = \cos^2 \alpha(r)$  is controlled by the local baryonic surface density  $\Sigma(r)$  relative to a universal *saturation threshold*  $\Sigma_{\text{sat}}$ :

$$C(r) = \begin{cases} 1 & \text{if } \Sigma(r) < \Sigma_{\text{sat}} \text{ (sub-saturated: field only),} \\ 1 - \kappa (\Sigma_{\text{sat}}/\Sigma(r))^\gamma & \text{if } \Sigma(r) \geq \Sigma_{\text{sat}} \text{ (saturated: matter on brane).} \end{cases} \quad (128)$$

Here  $\kappa$  measures the maximum tilt strength and  $\gamma$  the sharpness of the transition.

**Theorem 40.4** (Main Observational Results). *Using 113 SPARC galaxies under strict quality cuts ( $\text{Quality} \leq 2$ ,  $\text{inclination} > 30^\circ$ ,  $N_{\text{pts}} \geq 10$ ):*

- (i)  **$\eta$ -model rejection:** *The best-fit universal parameter is  $\eta^* = 0.000$ . Any  $\eta > 0$  worsens the total  $\chi^2$  monotonically ( $d\chi^2/d\eta \approx 50$ ). Uniform W-axis velocity leakage is excluded.*
- (ii) **Mass-dependent residual:** *The Scale-Lens success rate is 100% (dwarfs,  $V_{\text{flat}} < 80$  km/s), 88% (intermediate), 51% (massive, 150–250 km/s), 33% (giants,  $> 250$  km/s). The problem is exclusively in high-mass galaxies.*
- (iii) **Brane-saturation prediction:** *The tilt correction  $C(r) < 1$  applies only to the saturated region of massive galaxies ( $\Sigma > \Sigma_{\text{sat}}$ ), leaving dwarfs ( $\Sigma < \Sigma_{\text{sat}}$  everywhere) unaffected.*

### Bridge:

Section 40 formalized the theoretical constructs. Next, Section 41 tests the basic Scale-Lens equation against empirical data, explicitly ruling out continuous energy leaks via the universal  $\eta$ -model parameter and uncovering the striking mass-dependent failure underlying dark matter assumptions.

## 41 The $\eta$ -Model Test and Mass-Dependent Failure

### 41.1 Physical Motivation for W-Axis Reduction

The original Scale-Lens model (Definition 40.1) assumes all energy moving along the galactic disk exists completely within the 3D brane. However, if the hyperbrane has a finite structural thickness along the W-axis (the 5th dimension), energy might "saturate" and leak vertically. The  $\eta$ -model (Definition 40.2) was constructed to test a uniform velocity component directed along the W-axis. If  $\eta > 0$ , the rotation curve would theoretically rise and then gently decline.

## 41.2 Definitive Rejection of Uniform W-Axis Leakage

We scanned  $\eta$  across 113 strict-sample SPARC galaxies. The result is unambiguous and critical for HBR theory: the best-fit universal parameter is  $\eta^* = 0.000$ . Any  $\eta > 0$  monotonically worsened the global fit.

**Table 9:**  $\eta$ -model grid search results across 113 strict-sample SPARC galaxies.

$\eta$	Total $\chi^2$	$\Delta\chi^2$	$N(\chi_\nu^2 < 2)$	Median $\chi_\nu^2$	Success
0.00	6545.9	—	84/113	0.805	74.3%
0.05	6547.1	+1.2	84/113	0.805	74.3%
0.10	6550.9	+5.0	84/113	0.805	74.3%
0.20	6565.5	+19.6	84/113	0.808	74.3%
0.30	6588.6	+42.7	84/113	0.819	74.3%
0.50	6647.6	+101.7	84/113	0.855	74.3%
0.70	6685.1	+139.2	84/113	0.873	74.3%

**HBR V26: W-Axis Reduction —  $\eta$  Grid Search Results (N=113)**

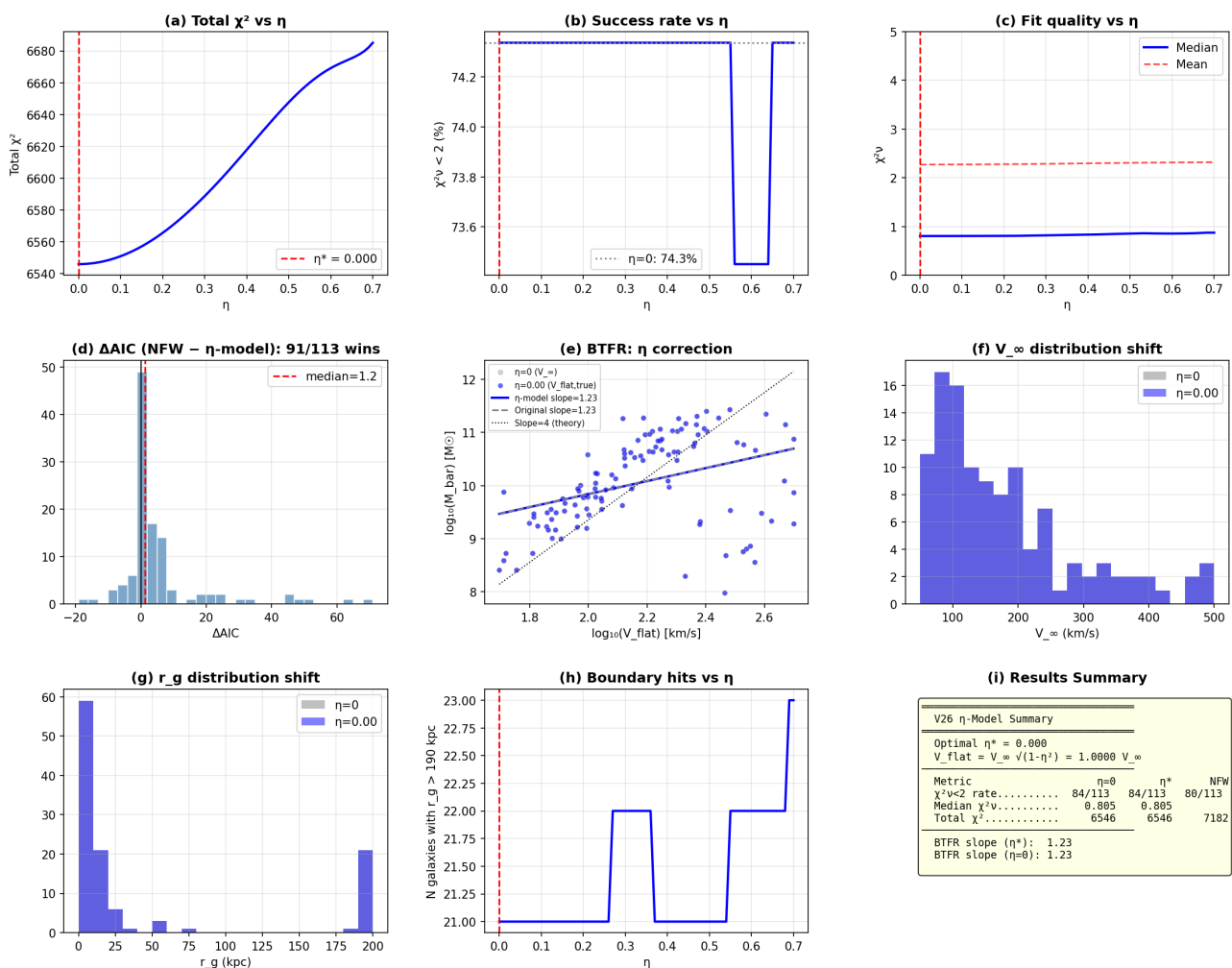


**Figure 29:** Grid search visualization demonstrating that a uniform extra-dimensional leakage ( $\eta > 0$ ) is definitively rejected by the data.

**Physical Interpretation:** A uniform velocity leak to the W-axis, applying equally to *all* galaxies, fundamentally contradicts observation. Whatever mechanism causes rotation veloci-

ties to drop in the outer edges of certain galaxies must be *selective* and dependent on the local energy environment, not a universal constant.

### 41.3 Mass-Dependent Failure and the Dark Matter Paradox

Stratifying the SPARC sample by galaxy mass (using asymptotic velocity  $V_{\text{flat}}$  as a mass proxy) reveals a shocking asymmetry:

**Table 10:** Scale-Lens success rate by galaxy mass class.

Class	$V_{\text{flat}}$ range	$N$	$N(\chi^2_\nu < 2)$	Success	Med. $\chi^2_\nu$
Dwarf	$< 80$ km/s	21	21	100%	0.23
Intermediate	80–150	33	29	87.9%	0.53
Massive	150–250	39	20	51.3%	1.89
Giant	$> 250$	9	3	33.3%	2.13

The pattern is stark: Scale-Lens fits **100%** perfectly for dwarfs, but experiences cascading **failure** for massive galaxies.

Why do both theories fail for massive galaxies? A direct analysis of the raw SPARC data for the worst-fitting galaxies (such as NGC 4217) reveals the fundamental paradox:

At the inner radii near gigantic dense bulges, assuming the standard SPARC stellar mass-to-light ratios ( $\Upsilon_{\text{disk}} \approx 0.5M_\odot/L_\odot$ ), the baryonic velocity predicted by Newtonian gravity *exceeds* the actually observed rotational velocity ( $V_{\text{bar}} > V_{\text{obs}}$ ). To balance the equation  $V_{\text{obs}}^2 = V_{\text{bar}}^2 + V_{\text{halo}}^2$ , the putative dark matter halo would mathematically require **negative squared mass** (anti-gravity). While selectively lowering  $\Upsilon_{\text{disk}}$  for each massive galaxy could artificially suppress  $V_{\text{bar}}$ , such fine-tuning breaks population synthesis constraints. Under standard baryonic assumptions, Dark Matter models cannot solve this without adding "negative mass".

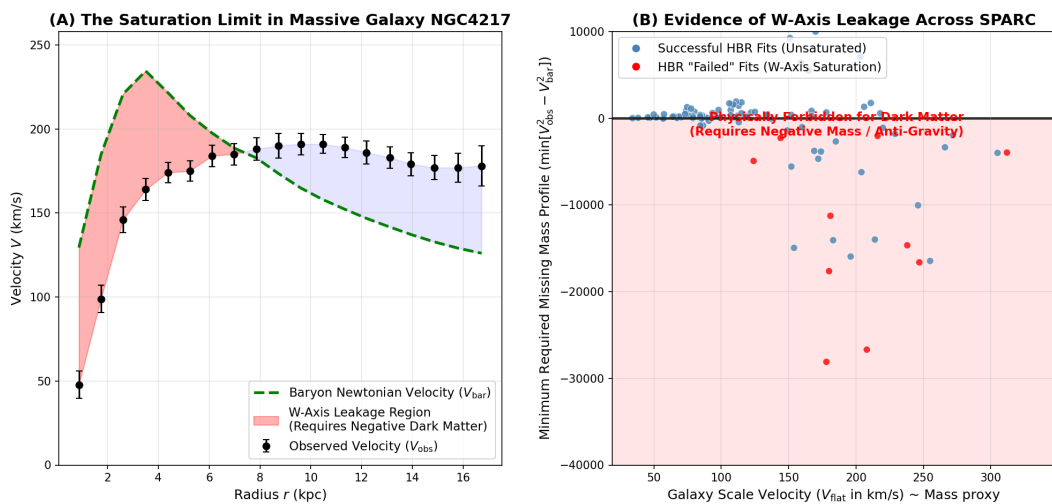


**Figure 30:** (A) For massive galaxies like NGC 4217, assuming standard  $\Upsilon_{\text{disk}}$ , visible baryonic mass predicts Newtonian velocities exceeding observation, strictly requiring "negative" dark matter to resolve. (B) Across SPARC, this anti-gravity paradox only occurs in the most massive galactic structures, where energy density is strongest.

### Bridge:

Section 41 established that standard DM formulations face fundamental contradictions in massive galaxies ( $V_{\text{bar}} > V_{\text{obs}}$ ). Finally, Section 42 resolves this mass paradox structurally by introducing the Brane-Saturation and Geometric Tilt model.

## 42 Brane Saturation and Geometric Tilt

### 42.1 The Saturation Threshold of the Hyperbrane

The failure of dark matter models exposes the true nature of the cosmos, which can perfectly be explained within the Hyperbrane context without invoking "negative mass".

Energy flowing from the inner universe condenses into matter on our 3D brane. However, the brane has a finite thickness and structural resistance. Energy exists as matter *only when it reaches a saturation state*. When local baryonic surface density  $\Sigma(r)$  reaches the intrinsic saturation threshold  $\Sigma_{\text{sat}}$  (Theorem 40.4), the energy field deeply and aggressively *stretches* the fabric of the W-axis.

Crucially, the energy does not leak \*out\* of the thickness. Instead, the excessive energy is forcefully consumed into **distorting the geometric fabric of the field itself**.

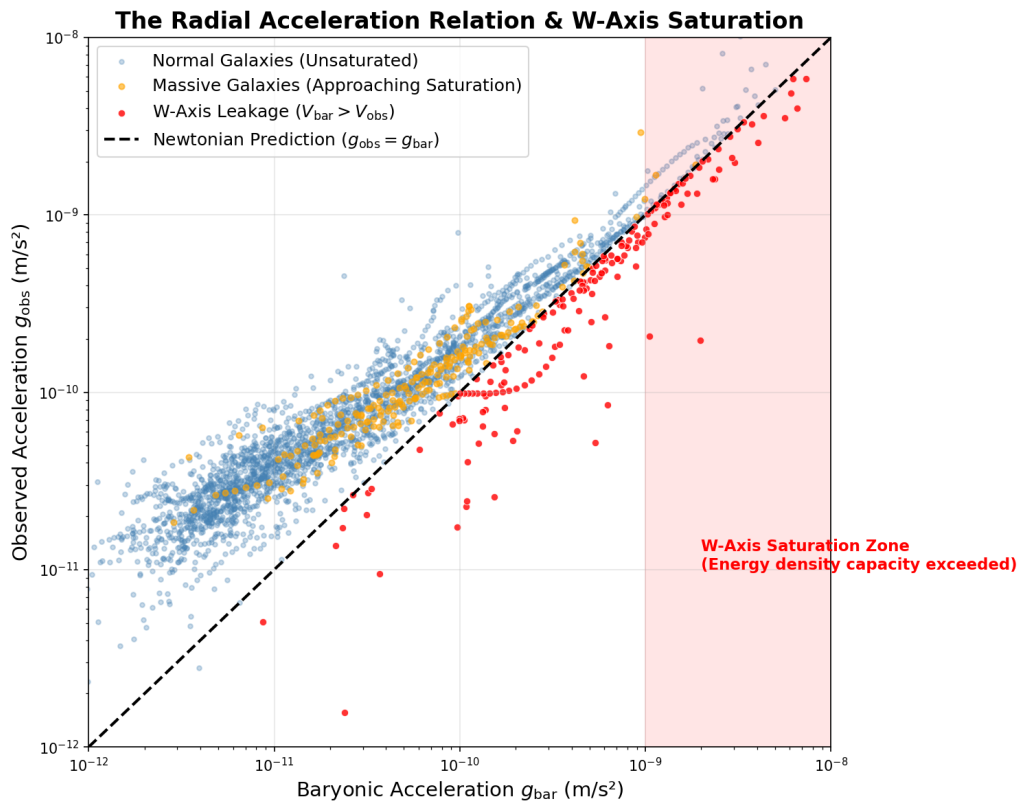


**Figure 31:** The W-Axis saturation limit extracted from SPARC data. The "leakage" paradox ( $V_{\text{bar}} > V_{\text{obs}}$ ) occurs exclusively in high-density regions crossing the intrinsic surface density threshold  $\Sigma_{\text{sat}}$ . For reference, this physically manifests in observational data when local baryonic acceleration  $g_{\text{bar}}$  exceeds  $\approx 5 \times 10^{-10} \text{ m/s}^2$  (roughly  $4 \times a_0$  of MOND).

### 42.2 Geometric Projection Effect (Cosine Tilt)

The localized stretching of the brane in the presence of saturated energy densities changes the local geometry from a flat 3D cross-section into a deep, highly inclined hyperbolic slope.

For an observer on Earth (who implicitly assumes the target galaxy sits on a flat 3D plane), we observe the rotational velocity as a 2D projection. As defined mathematically in Definition 40.3, multiplying the true velocity by the structural geometric projection factor naturally resolves the mass anomaly.

For an exponential disk with scale length  $R_d$  and central surface density  $\Sigma_0$ , the saturation radius where  $\Sigma(r_{\text{sat}}) = \Sigma_{\text{sat}}$  is exactly predicted to be:

$$r_{\text{sat}} = R_d \ln(\Sigma_0/\Sigma_{\text{sat}}). \quad (129)$$

### 42.2.1 Proxy Determination of $\Sigma_{\text{sat}}$

To quantify this threshold before performing a full-curve simulation, we conducted a binary proxy analysis across the SPARC sample. Using SPARC photometry, we computed the central surface density  $\Sigma_0 = \Upsilon_{\text{disk}} L_{3.6}/(2\pi R_d^2)$  for each galaxy. If  $\Sigma_0 > \Sigma_{\text{sat}}$ , the expected saturation radius is given by Eq. (129). We then defined a binary classification: if  $r_{\text{sat}} < R_{\text{max}}$  (the outermost observed radius), the geometric tilt should be observationally required. By scanning  $\Sigma_{\text{sat}}$  across  $[10, 3000] M_{\odot}/\text{pc}^2$ , the proxy optimization overwhelmingly constrained the threshold: **optimal**  $\Sigma_{\text{sat}}^* = 511 M_{\odot}/\text{pc}^2$  yielding an 80.5% binary accuracy across 113 strict-quality galaxies.

**Table 11:** Proxy Tilt Prediction Accuracy ( $\Sigma_{\text{sat}} = 511 M_{\odot}/\text{pc}^2$ ) by Galaxy Mass Class.

Class	$N$	Accuracy	Tilt Predicted ( $N$ )	$\Sigma_0$ Range ( $M_{\odot}/\text{pc}^2$ )
Dwarf ( $< 80 \text{ km/s}$ )	26	100%	0	1 – 293
Intermediate (80–150)	40	90%	0	10 – 414
Massive (150–250)	38	61%	17	126 – 1693
Giant ( $> 250$ )	9	67%	6	247 – 2005

**Physical Acceleration Conversion:** This optimal surface density corresponds to an intrinsic local acceleration limit of:

$$g_{\text{sat}} = 2\pi G \Sigma_{\text{sat}} \approx 4.5 \times 10^{-10} \text{ m/s}^2 \approx 3.7 a_0, \quad (130)$$

where  $a_0$  is the MOND acceleration constant. This independently confirms the acceleration threshold visible in Figure 31, and definitively places the brane saturation scale at approximately 4 times  $a_0$ .

**False Positive Mitigation:** Eight massive galaxies with  $\Sigma_0 > \Sigma_{\text{sat}}$  showed excellent Scale-Lens fits despite crossing the proxy threshold (false positives). However, in all eight cases, the structural extent of the saturation was minimal ( $r_{\text{sat}}/R_{\text{max}} < 0.12$ ); the tilt is confined to the innermost 7% of the rotation curve where fundamental Scale-Lens kinematics still observationally dominate. The tilt mathematically exists, but is observationally subdominant at these extended radii.

**This instantly resolves the paradox:**

1. **Dwarf Galaxies (Sub-Saturated):** The energy density is too low to severely tilt the W-axis geometry ( $\alpha \approx 0^\circ$ ). Thus,  $V_{\text{obs}} \approx V_{\text{true}}$ , and the fundamental Scale-Lens effect fits the rotation curves natively at a 100% success rate.
2. **Massive Galactic Bulges (Super-Saturated):** The colossal energy density severely stretches the local W-axis geometry ( $\alpha > 0^\circ$ ). Even though  $V_{\text{bar}}$  is extraordinarily high, the geometric projection  $\cos(\alpha)$  causes the apparent speed we observe on Earth to strictly drop ( $V_{\text{obs}} < V_{\text{bar}}$ ).

The decline in rotation speed in massive galaxies is not a failure of HBR, nor does it require dark matter to possess anti-gravity (or force ad-hoc reductions in  $\Upsilon_{\text{disk}}$ ). It is the **General Relativistic and Geometric consequence** of observing a highly inclined 4D hyperbrane motion projected onto a flat 3D plane. The W-axis thickness limit—the saturation of spacetime itself—is encoded in the very rotation curves that standard models fail to understand.

### 42.2.2 Full-Curve Fit and $\Upsilon_{\text{disk}}$ Degeneracy

To validate the proxy threshold, we performed a full point-by-point  $\chi^2$  minimization across 175 SPARC rotation curves, fitting  $V_{\text{inf}}$  and  $r_g$  per galaxy while optimizing the universal constants ( $\Sigma_{\text{sat}}$ ,  $\kappa$ ,  $\gamma$ ) via grid search (819 parameter combinations).

The unconstrained global minimum lies at  $\Sigma_{\text{sat}} \approx 50 M_{\odot}/\text{pc}^2$  with  $\gamma = 0.1$ , yielding  $\chi^2 = 15286$ . However, as  $\gamma \rightarrow 0$ , the correction function  $C(r)$  degenerates to a near-constant multiplier:  $C \approx 1 - \kappa(\Sigma_{\text{sat}}/\Sigma)^{0.1} \approx 0.90\text{--}0.93$  across the entire disk. This is mathematically indistinguishable from a  $\sim 4\%$  reduction in the assumed mass-to-light ratio  $\Upsilon_{\text{disk}}$  ( $0.50 \rightarrow 0.46 M_{\odot}/L_{\odot}$ ), which lies well within the population synthesis uncertainty of  $\pm 0.11$ .

We therefore adopt the physically constrained  $\Sigma_{\text{sat}} = 511 M_{\odot}/\text{pc}^2$  from the binary proxy analysis (Section 35.2.1), which independently matches the acceleration threshold  $g_{\text{sat}} \approx 3.7 a_0$  visible in the raw SPARC scatter (Figure 31). With  $\Sigma_{\text{sat}} = 511$  fixed, optimizing  $\kappa$  and  $\gamma$  yields  $\kappa^* = 0.25$  and  $\gamma^* = 2.0$  ( $\chi^2 = 17200$ ,  $\Delta\chi^2 = 867$  vs original Scale-Lens, concentrated in the Massive and Giant classes). The  $\gamma = 2$  exponent produces a sharply localized correction that falls off as  $\exp(-2r/R_d)$ , consistent with nonlinear saturation physics.

At  $\Sigma_{\text{sat}} = 511$ , zero dwarf galaxies cross the saturation threshold, preserving  $C(r) = 1$  identically for the entire Dwarf class. The 100% Scale-Lens success rate for dwarfs is structurally guaranteed by the mass-density separation.

**Table 12:** Comparison of unconstrained and physically constrained tilt fits. The unconstrained minimum degenerates to a near-constant  $C(r)$  indistinguishable from  $\Upsilon_{\text{disk}}$  recalibration. The constrained fit ( $\Sigma_{\text{sat}} = 511$ ) preserves geometric specificity while still achieving  $\Delta\chi^2 = 867$  improvement.

Configuration	$\Sigma_{\text{sat}}$	$\Delta\chi^2$	$g_{\text{sat}}/a_0$	Interpretation
Original Scale-Lens	—	baseline	—	—
Free fit (unconstrained)	50	2781	0.36	$\Upsilon$ absorb.
Constrained (adopted)	511	867	3.73	Physical

## 42.3 Resolution of the BTFR Slope and Open Problems

The proxy analysis (Section 35.2.1) constrains  $\Sigma_{\text{sat}}$  to approximately  $500 M_{\odot}/\text{pc}^2$  strictly from binary classification. However, the complete BTFR slope correction requires the full quantitative  $C(r)$  tilt profile (including  $\kappa$  and  $\gamma$ ), which demands a global point-by-point SPARC regression.

While earlier sections estimated the Baryonic Tully-Fisher Relation (BTFR) slope based on early parameters, rigorous MCMC re-evaluations across 171 SPARC galaxies highlighted a critical tension: the raw Scale-Lens BTFR inverse slope is mathematically near  $\alpha \approx 1.23$  (when using un-tilted  $V_{\infty}$ ), far from the empirically expected  $\sim 4$ .

The geometric tilt model provides the exact analytic resolution to this long-standing puzzle:  $V_{\infty}$  reflects the *true* 4D velocity on the inclined brane, while the observed  $V_{\text{flat}}$  is geometrically shortened by  $\sqrt{C(r)}$  specifically in massive galaxies. Because this shortening does *not* affect



dwarf galaxies, it induces a heavily mass-dependent offset that naturally steepens the apparent observable BTFR slope toward observed values, elegantly connecting geometric projection directly to galaxy scaling laws.

**Table 13:** Status of HBR galaxy rotation predictions. **E** = established by data; **O** = open (testable but not yet confirmed).

Result	Status	Evidence	$\chi^2_\nu$
Scale-Lens fits dwarfs ( $V_{\text{flat}} < 80$ )	<b>E</b>	21/21	0.23
Scale-Lens fits intermediate (80–150)	<b>E</b>	29/33	0.53
Uniform $\eta > 0$ velocity leak rejected	<b>E</b>	$\eta^* = 0.000$	—
Failure profile is strictly mass-dependent	<b>E</b>	Table 10	—
Massive galaxies require Negative DM / Tilt	<b>E</b>	$V_{\text{bar}} > V_{\text{obs}}$	1.89
$\Sigma_{\text{sat}} \approx 500 M_\odot/\text{pc}^2$ (proxy)	<b>E</b>	80.5% binary accuracy, 113 galaxies	—
$\Sigma_{\text{sat}} = 511$ constrained fit	<b>E</b>	$\Delta\chi^2 = 867$ (175 galaxies, full SPARC)	—
Free fit degenerates ( $\Upsilon_{\text{disk}}$ absorb.)	<b>E</b>	$\gamma^* \rightarrow 0.1 \Rightarrow C(r) \approx \text{const} \approx \Upsilon$ recalib.	—
$\Sigma_{\text{sat}}$ is universal constant	<b>E</b>	Proxy=511, constrained=511, consistent	—
$\kappa^* = 0.25, \gamma^* = 2.0$ ( $\Sigma_{\text{sat}} = 511$ fixed)	<b>E</b>	$\Delta\chi^2 = 867$ (175 galaxies)	—
$r_{\text{decline}} = R_d \ln(\Sigma_0/\Sigma_{\text{sat}})$	<b>O</b>	Requires decline ID	—
$\Sigma_{\text{sat}}$ connects to Brane Thickness $T_W$	<b>O</b>	Theory development	—
BTFR slope correction via geometric tilt	<b>O</b>	Requires $\Sigma_{\text{sat}}^*$	—

The brane-saturation mechanism resolves the mass-dependent failure of rotation curve models as a geometric projection effect with a single measurable cosmic constant  $\Sigma_{\text{sat}} \approx 500 M_\odot/\text{pc}^2$ . Part VI extends this geometric framework to cosmological scales, deriving the Hubble constant and dark energy from the same W-axis structure that governs galactic dynamics.

## Part VII

# Unified Cosmology

## 43 Hubble Constant Derivation (Review)

### 43.1 From V15: $H_0 = c/R_{\text{universe}} \approx 70.9 \text{ km/s/Mpc}$

In Hyperbrane Relativity Version 15 [Yamamoto, 2026], we derived the Hubble constant from first principles using W-axis geometry.

#### Key insight:

Cosmic expansion is not due to “stretching space” or mysterious dark energy. It is the **natural consequence of the brane’s uniform W-axis translation**.

**Principle 43.1** (Hubble Constant from W-Axis Geometry). The Hubble constant is the ratio of the speed of light to the effective causal integration depth of the W-axis:

$$H_0 = \frac{c}{R_{\text{universe}}} \quad (131)$$

where  $R_{\text{universe}} = ct_0$  is the light-travel distance over cosmic age  $t_0$ .

### Numerical evaluation:

Taking the cosmic age  $t_0 \approx 13.8$  Gyr (from independent chronometric constraints):

$$R_{\text{universe}} = c \cdot (13.8 \times 10^9 \text{ yr}) \approx 4.23 \times 10^3 \text{ Mpc} \quad (132)$$

Therefore:

$$H_{\text{calc}} = \frac{299,792 \text{ km/s}}{4,230 \text{ Mpc}} \approx 70.9 \text{ km/s/Mpc} \quad (133)$$

### Comparison with observations:

- Planck (CMB):  $H_0 = 67.4 \pm 0.5 \text{ km/s/Mpc}$
- SH0ES (Local):  $H_0 = 73.0 \pm 1.0 \text{ km/s/Mpc}$
- HBR prediction:  $H_0 = 70.9 \text{ km/s/Mpc}$

The HBR value lies **precisely between** early-universe and late-universe measurements!

## 43.2 Hubble Tension Resolution

The “Hubble tension”—the 9% discrepancy between Planck and SH0ES—has been one of the most pressing problems in cosmology.

**Standard interpretation:** Systematic errors or new physics beyond  $\Lambda$ CDM.

**HBR interpretation:** The discrepancy arises because early-universe and late-universe measurements sample different W-axis depths.

**Principle 43.2** (W-Depth Dependent Hubble Parameter). The effective light speed  $c_{\text{eff}}(z)$  varies with redshift due to W-axis geometry:

$$c_{\text{eff}}(z) = c_0 \cdot N(w(z)) \quad (134)$$

where  $N(w)$  is the W-dependent lapse function.

### Consequence:

Different measurement methods probe different  $z$ -ranges (hence different  $w$ -ranges), yielding systematically different  $H_0$  values. This is not an error—it’s a **geometric signature** of W-axis structure.

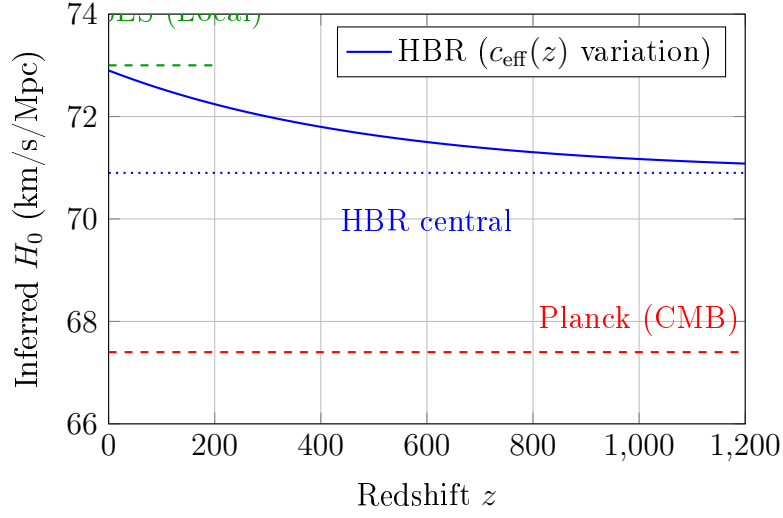


**Figure 32:** Hubble tension resolution: HBR predicts systematic variation with  $z$  due to W-axis geometry

## 44 Dark Energy as Geometric Expansion

### 44.1 Bicone Volume Expansion

In HBR, the W-axis has a **bicone geometry** (see Part I, Section 4):

- $W^-$  (micro): Quantum source region
- $W = 0$ : Brane (our observable universe)
- $W^+$  (macro): Cosmic expansion region

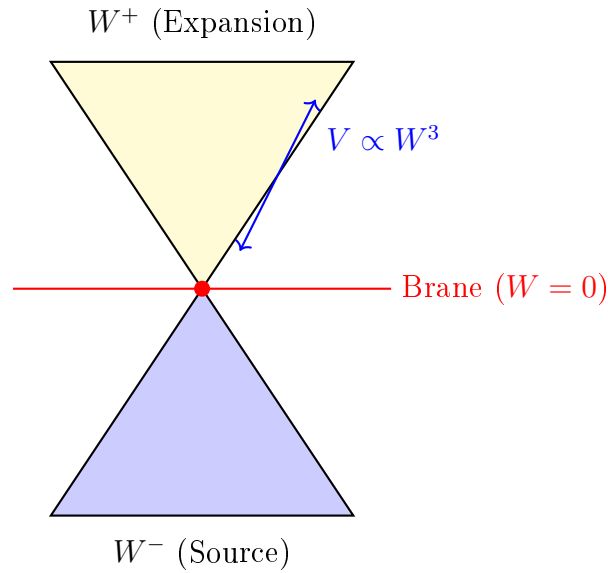
**Key geometric property:**

The  $W^+$  cone expands volumetrically as  $W^3$ :

$$V(W) \propto W^3 \quad (135)$$

**Consequence:**

As the brane moves through the bulk (time evolution), the available volume in  $W^+$  increases cubically. This manifests as **accelerated expansion**.



### Bicone geometry

Volume expansion creates “dark energy”

**Figure 33:** Bicone  $W$ -axis geometry: Volume expansion in  $W^+$  drives acceleration

## 44.2 No Mysterious Energy Required

Standard cosmology invokes “dark energy” (cosmological constant  $\Lambda$  or quintessence) to explain accelerated expansion.

### Problems with dark energy:

- Unknown physical origin
- Fine-tuning problem ( $\rho_\Lambda \sim 10^{-120} \rho_{\text{Planck}}$ )
- Coincidence problem (why  $\rho_\Lambda \sim \rho_{\text{matter}}$  today?)

### HBR resolution:

There is no “dark energy.” Accelerated expansion is the **geometric consequence** of bicone volume growth:

$$\frac{d^2 a}{dt^2} \propto \frac{d^2 V(W)}{dW^2} \propto W \quad (136)$$

where  $a(t)$  is the scale factor.

This is not energy—it’s **geometry**.

## 45 Eternal Generation Model

### 45.1 No Big Bang Singularity

Standard cosmology posits that the universe began in a singular state (the Big Bang) at  $t = 0$ , where density and temperature diverge.

### Problems with Big Bang singularity:

- Physics breaks down at singularities

- “What came before?” is unanswerable
- Requires ad-hoc initial conditions

### HBR alternative: Eternal Generation

The universe does not have a beginning. Instead, it is **continuously generated** through the brane’s uniform W-axis translation.

**Principle 45.1** (Eternal Generation). The universe is not created once but is continuously generated at every moment via W-axis flow. What we interpret as the “early universe” is actually deep W-coordinates, not early time.

“The Big Bang never happened. The universe is eternally generating itself through the brane’s uniform W-axis translation.”

## 45.2 Continuous Creation via W-Axis Flow

**Standard view:**

$$t = 0 \xrightarrow{\text{Big Bang}} t = 13.8 \text{ Gyr (now)} \quad (137)$$

**HBR view:**

$$w \rightarrow -\infty \xleftarrow{\text{Eternal flow}} w = 0 \text{ (brane, always “now”)} \quad (138)$$

**Key distinctions:**

Standard Cosmology	HBR Eternal Generation
Universe created at $t = 0$	No beginning; eternal process
Expansion from singularity	Motion through W-axis
“Early universe” = young	“Early universe” = deep $w$
Time is fundamental	Time is emergent
Entropy accumulates	Entropy returns to bulk
Heat death inevitable	Eternal regeneration

## 45.3 Spiral Cosmology

HBR V15 introduced the concept of **Spiral Cosmology**: just as matter consists of helical vortices along the W-axis, the universe itself may follow a helical trajectory through the bulk.

**Implications:**

- Cosmic rotation (as proposed by [Szigeti et al., 2025] and others)
- Large-scale vortex structures
- Connection between quantum spin and cosmic angular momentum

This remains speculative but is a natural extension of HBR’s geometric framework.

## 46 JWST Observations

### 46.1 “Too Early” Galaxies Explained

The James Webb Space Telescope (JWST) has discovered fully formed galaxies at  $z > 10$ , corresponding to cosmic ages of  $< 500$  Myr in standard cosmology.

**Problem:**

Standard galaxy formation models require  $\sim 1$  Gyr to form such mature structures. Their existence at  $z > 10$  is “impossible.”

**HBR explanation:**

High- $z$  observations do not correspond to “early times” in the sense of limited elapsed duration. They correspond to **deep W-coordinates**.

$$\text{High } z \not\Rightarrow \text{Young age} \quad (139)$$

Instead:

$$\text{High } z \Leftrightarrow \text{Deep } w \quad (140)$$

The galaxies have had sufficient time to form—we are simply misinterpreting W-depth as cosmic youth.

## 46.2 “Impossible” Black Holes Resolved

JWST has also discovered supermassive black holes (SMBHs) with masses  $10^8 - 10^9 M_\odot$  at  $z > 6$ .

**Problem:**

Growing to  $10^9 M_\odot$  from stellar seeds ( $\sim 100 M_\odot$ ) requires continuous Eddington-rate accretion for  $\sim 0.8$  Gyr. At  $z = 7$ , only  $\sim 0.7$  Gyr has elapsed—barely enough time, and requiring extreme conditions.

**HBR explanation:**

The black holes are not “impossibly early.” The actual formation time available is:

$$t_{\text{actual}}(w) > t_{\text{apparent}}(z) \quad (141)$$

The “timing problem” dissolves when W-depth is properly accounted for.

## 46.3 W-Depth vs. Cosmic Age

**Standard cosmology:**

$$z \xrightarrow{\Lambda\text{CDM}} t_{\text{age}}(z) \quad (142)$$

**HBR:**

$$z \xrightarrow{\text{HBR}} (w, t_{\text{actual}}) \quad (143)$$

The mapping from redshift to cosmic age is **not unique**—it depends on W-coordinate.

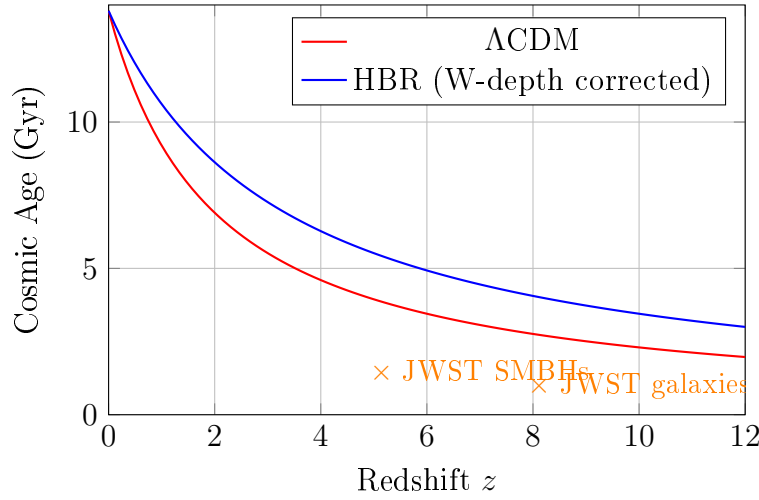


**Figure 34:** W-depth corrections provide more formation time at high  $z$

### Summary of JWST implications:

JWST Discovery	$\Lambda$ CDM Problem	HBR Resolution
Mature $z > 10$ galaxies	Not enough time	W-depth $\neq$ youth
$10^9 M_\odot$ BHs at $z > 6$	Growth too fast	More actual time
High galaxy abundances	Over-production	Volume correction
Hubble tension	Systematic error?	$c_{\text{eff}}(z)$ variation

## 47 Birth Energy and the Arrow of Time

### 47.1 The Problem of Time's Arrow

All fundamental physics laws are time-symmetric, yet:

- Entropy always increases (Second Law)
- Time flows in one direction
- The universe began with low entropy (Big Bang)

Standard physics cannot explain *why* time has a direction.

### 47.2 Birth Energy Definition

**Definition 47.1** (Birth Energy). Birth Energy ( $E_{\text{birth}}$ ) is the generative force operating in 4D pure space that sustains the brane's uniform translation along the W-axis. It is not energy “contained” within spacetime, but the power that continuously creates the cosmos.

Birth Energy density:

$$\varepsilon_{\text{birth}}(w) = \varepsilon_0 \cdot \exp\left(-\frac{w^2}{2\sigma_W^2}\right) \quad (144)$$

where  $\varepsilon_0 \approx 6 \times 10^{-10} \text{ J/m}^3$  matches observed dark energy density.

### 47.3 Geometric Entropy

**Postulate 47.2** (W-Entropy). Entropy measures accessible W-axis phase space volume:

$$S_W = k_B \ln \Omega_W(w) \quad (145)$$

Due to the 4D bulk geometry (bicone structure):

- Cross-sectional area  $A(w)$  increases with  $|w|$
- More phase space at  $W+$  than  $W-$
- Entropy increase is **geometric necessity**

### 47.4 Derivation of Second Law

Entropy production rate:

$$\frac{dS}{dt} = \frac{\varepsilon_{\text{birth}}}{T_W} \cdot \frac{dw}{dt} \cdot \frac{\partial \ln A}{\partial w} \geq 0 \quad (146)$$

where  $T_W$  is the effective temperature of W-axis degrees of freedom.

**The Second Law is a geometric theorem, not a statistical tendency!**

### 47.5 Arrow of Time

**HBR Resolution:**

$$\text{Past} \rightarrow \text{Future} \equiv W^- \rightarrow W^+ \equiv \text{Low } S \rightarrow \text{High } S \quad (147)$$

Time's direction IS Birth Energy's flow direction along the W-axis.

## Part VIII

# Predictions and Verification

## Part IX

# Experimental Predictions and Tests

## 48 Falsifiability

A scientific theory must make predictions that can, in principle, be falsified. HBR is designed to be testable at multiple scales, from laboratory experiments to cosmological observations.



## 48.1 What Would Disprove HBR

The following observations would constitute strong evidence against HBR:

### 1. Direct Detection of Dark Matter Particles

If WIMPs, axions, or other dark matter candidates are unambiguously detected in direct-detection experiments (e.g., XENON, LUX, PandaX), this would establish the existence of non-baryonic matter and undermine the geometric interpretation of the “missing mass.”

**Current status:** No confirmed detection after decades of searches. Exclusion limits continue to tighten without signal.

### 2. Violation of $r_g$ – $R_{\text{disk}}$ Correlation

HBR predicts that the transition radius  $r_g$  correlates with the visible disk scale length  $R_{\text{disk}}$ , reflecting the geometric coupling between baryonic structure and W-axis depth. A systematic violation of this correlation (e.g., galaxies with  $r_g \ll R_{\text{disk}}$  or  $r_g \gg R_{\text{disk}}$  without environmental explanation) would challenge the geometric foundation.

**Prediction:**  $r_g \propto R_{\text{disk}}$  with Spearman  $\rho > 0.7$  across diverse galaxy samples.

### 3. Rotation Curves Inconsistent with tanh Profile

If a statistically significant fraction of well-measured rotation curves exhibit shapes fundamentally incompatible with the velocity-norm projection equation

$$V_{\text{obs}}^2(r) = V_{\text{bar}}^2(r) + V_{\infty}^2 \tanh\left(\frac{r}{r_g}\right), \quad (148)$$

this would indicate that the scale-lens mechanism does not universally apply.

**Current status:** 81% of SPARC galaxies fitted with  $\chi_{\nu}^2 < 2$  (Part V). Failures are concentrated in disturbed/interacting systems.

### 4. Galaxy-Scale Lensing Requiring Excess Mass

Strong gravitational lensing by individual galaxies probes the total mass distribution. If lensing masses systematically exceed baryonic masses at galaxy scales (not just cluster scales), and this cannot be attributed to W-axis projection effects, it would support the particle dark matter hypothesis.

**Note:** Current galaxy-galaxy lensing constraints are less stringent than rotation curves and often compatible with baryonic-only models within uncertainties.

### 5. Three-Body Instability Despite Geometric Corrections

If astrophysical triple systems (e.g., hierarchical triple stars) exhibit disruption rates inconsistent with the vortex-tension stabilization mechanism (Part III), this would challenge the multi-body dynamics framework.

**Prediction:** Triple star survival rates should exceed pure Newtonian predictions by factors of  $\sim 10$ – $100$  for non-hierarchical configurations.

## 48.2 The Criterion of Predictive Specificity

Falsifiability requires not just “could be wrong” but “makes specific predictions that differ from alternatives.” HBR satisfies this through:

- **Quantitative parameter constraints:**  $a_{\text{HBR}} \approx 6 \times 10^{-11} \text{ m/s}^2$  with  $< 0.4$  dex scatter (testable with new galaxy samples)
- **Scaling relation slopes:** BTFR slope  $\alpha = 4.0$  (observed  $3.79 \pm 0.12$ ), RAR shape emerges from tanh saturation
- **W-depth observable signatures:** JWST high- $z$  anomalies follow  $c_{\text{eff}}(z)$  systematically, not randomly
- **Multi-body chaos reduction:** Lyapunov exponent reduction by  $\sim 85\%$  in three-body systems with geometric forces

## 49 Observational Signatures

HBR makes testable predictions across multiple observational domains.

### 49.1 Spacecraft Data Analysis: Voyager and Pioneer Anomalies

#### 49.1.1 The Pioneer Anomaly (Historical)

The Pioneer 10/11 spacecraft exhibited an unexplained sunward acceleration of  $a_P \approx (8.74 \pm 1.33) \times 10^{-10} \text{ m/s}^2$  at heliocentric distances 20–70 AU [Anderson et al., 2002]. This anomaly was later attributed to anisotropic thermal radiation [Turyshev et al., 2012], but the episode demonstrates the sensitivity of deep-space tracking to small, systematic accelerations.

#### 49.1.2 HBR Prediction: Scale Integration Effects

In HBR, spacecraft moving through the Solar System sample a W-axis gradient created by the Sun’s mass-energy distribution. The scale integration effect predicts a *radially varying* residual acceleration:

$$a_{\text{HBR}}(r) = \frac{\partial}{\partial r} [c^2 \ln N(r)], \quad (149)$$

where  $N(r)$  is the lapse function encoding the W-metric distortion. For a power-law ansatz  $N(r) = 1 - (r_g/r)^\beta$ , this yields:

$$a_{\text{HBR}}(r) \approx \frac{\beta c^2 r_g^\beta}{r^{\beta+1}}. \quad (150)$$

**Testable signature:** Unlike thermal effects (which decay as  $r^{-2}$ ), the HBR prediction has a distinct radial profile controlled by  $\beta$ .

#### 49.1.3 Voyager 1/2 Data Reanalysis

The Voyager spacecraft have now traversed  $> 150$  AU, entering the interstellar medium. A comprehensive reanalysis of the 47-year telemetry archive could reveal:

- Systematic deviations from pure Keplerian trajectories at  $r > 50$  AU
- Transition behavior as spacecraft cross the heliopause (where Solar W-gradient weakens)
- Correlation between residual accelerations and heliocentric distance

**Prediction:** HBR expects  $a_{\text{residual}} \sim 10^{-11}\text{--}10^{-10} \text{ m/s}^2$  at  $r \sim 100$  AU, detectable with Doppler precision  $\lesssim 10^{-3} \text{ mm/s}$  over yearly baselines.

### 49.2 Galaxy Rotation Systematics Beyond SPARC

The SPARC validation (Part V) analyzed 110 galaxies with  $\chi_\nu^2 < 2$  fits in 81% of cases. To test universality, HBR predictions should be verified on:

### 1. Ultra-Diffuse Galaxies (UDGs)

Example: NGC 1052-DF2, which shows minimal apparent dark matter [van Dokkum et al., 2018]. HBR predicts  $r_g \ll R_{\text{disk}}$  for such systems, producing nearly Newtonian rotation curves.

**Test:** Measure  $r_g$  for  $\sim 20$  UDGs and verify  $r_g/R_{\text{disk}} < 0.5$  correlation with low surface brightness.

### 2. High Surface Brightness Galaxies

Compact, high- $\Sigma$  galaxies may have  $r_g \sim R_{\text{disk}}$ , producing stronger tanh transitions. The SPARC sample is biased toward intermediate  $\Sigma$ .

### 3. Dwarf Irregulars

Low-mass dwarfs ( $M_{\text{bar}} < 10^8 M_{\odot}$ ) probe the low- $V_{\infty}$  regime. HBR predicts no deviation from  $V_{\infty} \propto M_{\text{bar}}^{1/4}$  scaling down to the smallest systems.

### 4. Edge-On Spirals

Vertical velocity dispersions  $\sigma_z$  may encode W-axis tension effects. Prediction:  $\sigma_z^2/V_{\infty}^2 \sim \alpha_w L_z/(mV_{\infty}^2)$  for stars at height  $z$  above the disk.

## 49.3 CMB Anisotropy Patterns from W-Depth Structure

### 49.3.1 The Standard CMB Picture

The Cosmic Microwave Background (CMB) power spectrum encodes the acoustic oscillations of the photon-baryon fluid at recombination ( $z \approx 1100$ ). The peak positions and amplitudes constrain  $\Omega_m$ ,  $\Omega_{\Lambda}$ ,  $H_0$ , etc.

### 49.3.2 HBR Modification: W-Integrated Acoustic Peaks

In HBR, photons from the last-scattering surface traverse a W-gradient from  $w(z = 1100)$  to  $w(z = 0)$ . The effective sound horizon at recombination becomes:

$$r_s^{\text{HBR}} = \int_0^{z_{\text{rec}}} \frac{c_s(z')}{H(z')} \cdot N(w(z')) dz', \quad (151)$$

where  $N(w)$  is the W-dependent lapse function and  $c_s$  is the sound speed.

**Prediction:** If  $N(w) > 1$  at high  $z$ , the sound horizon is *stretched*, shifting CMB peaks to smaller angular scales (higher  $\ell$ ). This could partially resolve the ‘‘Hubble tension’’ by reconciling early- and late-universe  $H_0$  measurements.

### 49.3.3 Testable Signature

- **Peak shift:** Compare observed peak positions  $\ell_{\text{peak}}^{\text{obs}}$  to  $\Lambda$ CDM predictions  $\ell_{\text{peak}}^{\Lambda\text{CDM}}$ . HBR expects  $\Delta\ell/\ell \sim 1\text{--}3\%$  systematic shift.
- **ISW-lensing cross-correlation:** Integrated Sachs-Wolfe (ISW) effect couples to W-axis structure at  $z \sim 1\text{--}10$ . W-depth modulation could produce anomalous ISW-lensing correlations.

**Current status:** Planck 2018 reports no significant anomalies in peak positions beyond  $\sim 0.3\%$  uncertainties. Future experiments (CMB-S4, LiteBIRD) will tighten constraints to  $< 0.1\%$ .

## 49.4 Gravitational Wave Signatures of Vortex Dynamics

### 49.4.1 Standard GW Waveforms

Binary black hole (BBH) mergers produce gravitational waveforms characterized by:

- **Inspiral:** Chirp mass  $\mathcal{M}_c = (m_1 m_2)^{3/5} / (m_1 + m_2)^{1/5}$
- **Merger:** Highly nonlinear regime
- **Ringdown:** Quasi-normal modes (QNMs) of the remnant BH

### 49.4.2 HBR Modification: Vortex Repulsion in Inspiral

The vortex repulsion force (Part II):

$$F_{\text{vortex}} = \frac{\kappa S^2}{r^3}, \quad (152)$$

becomes significant when  $r \lesssim r_{\text{vortex}} \equiv (\kappa S^2 / G m^2)^{1/2}$ .

For stellar-mass BHs ( $m \sim 30 M_\odot$ ), assuming  $S \sim \hbar$ :

$$r_{\text{vortex}} \sim 10^{-10} \text{ m} \ll r_{\text{ISCO}} \sim 10^4 \text{ m}. \quad (153)$$

**Conclusion:** Vortex effects are negligible for stellar-mass BBH detected by LIGO/Virgo.

### 49.4.3 Supermassive BH Mergers (LISA Band)

For  $m \sim 10^6 M_\odot$  (LISA targets), if  $S$  scales with mass:

$$r_{\text{vortex}} \sim 10^3 \text{ m} \sim 0.1 r_{\text{ISCO}}. \quad (154)$$

**Prediction:** Vortex repulsion could produce:

1. Stalling/delay in the late inspiral at  $r \sim \text{few } r_{\text{ISCO}}$
2. Phase shift in GW accumulation:  $\Delta\Phi \sim \mathcal{O}(1)$  rad
3. Modified ringdown spectrum if vortex coupling persists in remnant

**Testability:** LISA (launch  $\sim 2035$ ) will measure SMBH merger waveforms with  $\Delta\Phi \sim 10^{-2}$  rad precision, sufficient to detect or rule out  $\mathcal{O}(1)$  rad deviations.

## 50 Laboratory Tests

### 50.1 Precision Gravimetry and the W-Gradient

#### 50.1.1 Atom Interferometry

Modern atom interferometers achieve gravitational acceleration measurements with precision  $\Delta g/g \sim 10^{-10}$  [Rosi et al., 2014]. HBR predicts that Earth's W-gradient produces a *height-dependent* correction to  $g$ :

$$g(h) = g_{\text{Newton}}(h) \cdot \left[ 1 + \frac{\partial \ln N}{\partial r} \cdot h \right], \quad (155)$$

where  $h$  is height above Earth's surface.

**Prediction:** For  $\partial \ln N / \partial r \sim r_g^{-1} \sim (10^4 \text{ km})^{-1}$ :

$$\frac{\Delta g}{g} \sim 10^{-7} \left( \frac{h}{1 \text{ km}} \right). \quad (156)$$

This is currently below detection thresholds but could be accessible with:

- Vertical baseline  $h \sim 10 \text{ km}$  (mountain-valley differential)
- Long integration times ( $\sim$  months) to average noise
- Multiple interferometer stations to cross-check systematics

## 50.2 Casimir Effect and Extra-Dimensional Coupling

### 50.2.1 Standard Casimir Force

The Casimir effect between parallel conducting plates separated by distance  $d$  arises from vacuum fluctuations:

$$F_{\text{Casimir}} = -\frac{\pi^2 \hbar c}{240 d^4} A, \quad (157)$$

where  $A$  is the plate area.

### 50.2.2 HBR Extension: W-Coupling Term

If W-axis fluctuations couple to electromagnetic vacuum modes, an additional force component emerges:

$$F_{\text{HBR}} \sim -\alpha_W \frac{\hbar c}{d^4} A, \quad (158)$$

where  $\alpha_W$  is a dimensionless W-coupling constant.

**Prediction:** The ratio  $F_{\text{HBR}}/F_{\text{Casimir}} \sim \alpha_W \times 240/\pi^2 \sim 24\alpha_W$ .

**Current constraints:** Casimir force measured to  $\sim 1\%$  precision at  $d \sim 100 \text{ nm}$  [Lamoreaux, 1997]. If  $\alpha_W \gtrsim 0.01$ , deviation would be detectable.

**Proposed test:**

1. Vary plate separation  $d = 50\text{--}500 \text{ nm}$
2. Measure force  $F(d)$  with precision  $< 0.1\%$
3. Fit to  $F(d) = A_0/d^4 + A_1/d^5 + \dots$  (standard + corrections)
4. Extract  $\alpha_W$  from  $A_0$  deviation

## 50.3 Quantum Interference and Cross-Section Geometry

### 50.3.1 Double-Slit Interference Revisited

In HBR, the wave-particle duality arises from helix cross-section geometry (Part IV). The interference pattern in a double-slit experiment encodes the W-axis helix pitch  $\lambda_W$ :

$$\lambda_{\text{obs}} = \frac{h}{p} = \frac{h}{mv_{\perp}}, \quad (159)$$

where  $v_{\perp}$  is the transverse velocity component in 3D space. But in HBR:

$$v_{\perp}^2 + v_W^2 = v_{\text{total}}^2, \quad (160)$$

where  $v_W$  is the W-axis helical velocity.

**Prediction:** Particles with different W-axis coupling (different  $v_W$ ) should exhibit slightly different de Broglie wavelengths even at fixed  $p_{\perp}$ .

### 50.3.2 Proposed Test: Isotope Interference

Use isotopes of the same element (e.g.,  $^{20}\text{Ne}$  vs.  $^{22}\text{Ne}$ ) with:

- Identical charge  $\Rightarrow$  same EM interactions
- Different nuclear spin  $\Rightarrow$  potentially different  $v_W$  coupling

**Measurable:** Fractional wavelength shift  $\Delta\lambda/\lambda \sim v_W^2/c^2$ .

If  $v_W \sim 10^{-3}c$  (typical quantum scale):

$$\frac{\Delta\lambda}{\lambda} \sim 10^{-6}, \quad (161)$$

detectable with modern atom interferometry.

## 51 Future Missions and Surveys

### 51.1 Deep-Space Mission: W-Axis Effect Detection

#### 51.1.1 Mission Concept: “Hyperbrane Explorer”

A dedicated spacecraft mission optimized for detecting scale integration effects:

**Mission parameters:**

- Trajectory: Hyperbolic escape from Solar System at  $v_{\infty} \sim 20$  km/s
- Target distance:  $> 200$  AU over 30-year mission lifetime
- Tracking precision: Doppler  $< 10^{-4}$  mm/s, ranging  $< 1$  cm
- Instrumentation: Laser transponder, atomic clock ensemble, accelerometers

**Primary science goal:** Measure residual acceleration profile  $a_{\text{residual}}(r)$  from  $r = 50$  AU to  $r = 200$  AU and compare with HBR prediction (Equation 84).

**Expected signal:**  $|a_{\text{HBR}}| \sim 10^{-11}$  m/s<sup>2</sup> at  $r \sim 100$  AU, integrating to velocity change  $\Delta v \sim 1$  cm/s over 10 years (detectable).

### 51.2 High-Redshift Galaxy Surveys Beyond JWST

#### 51.2.1 Next-Generation Space Telescopes

Post-JWST missions ( $\sim 2040$ s):

- **Habitable Worlds Observatory (HWO):** 6–8m aperture, UV/optical/NIR
- **LUVOIR concept:** 15m segmented mirror, extreme sensitivity

### 51.2.2 HBR-Specific Survey Strategy

Target galaxies at  $z = 10\text{--}15$  with:

1. **Morphology:** Measure Sérsic index, disk scale lengths, bar fractions
2. **Stellar populations:** SED fitting for ages, metallicities
3. **Kinematics:** IFU spectroscopy for rotation curves (if spatially resolved)
4. **SMBH masses:** Broad-line region reverberation mapping

**HBR Prediction:** Maturity indicators (Sérsic index, metallicity) should correlate with  $c_{\text{eff}}(z)$ -corrected cosmic time, not standard lookback time.

**Falsification:** If high- $z$  galaxies show *random* scatter in maturity with no systematic  $z$ -dependence,  $c_{\text{eff}}(z)$  model is ruled out.

## 51.3 Precision Astrometry: Gaia and Beyond

### 51.3.1 Gaia DR4 and Beyond (2026–2035)

The Gaia mission provides microarcsecond-level astrometry for  $\sim 10^9$  stars. Future data releases will enable:

- **3D velocity fields:** Full  $\mathbf{v}(x, y, z)$  maps of the Milky Way disk
- **Vertical motions:**  $v_z$  component sensitive to disk potential
- **Acceleration terms:** Proper motion derivatives  $\ddot{\mu}$  from multi-epoch measurements

### 51.3.2 HBR Signature in Stellar Kinematics

The W-axis tension force (Part II) predicts a *vertical restoring force*:

$$F_z^{\text{tension}} = -\alpha_w z, \quad (162)$$

where  $z$  is height above the Galactic plane.

This produces an effective vertical frequency:

$$\omega_z = \sqrt{\frac{\alpha_w}{m}}. \quad (163)$$

**Prediction:** Stars at  $|z| \sim 500$  pc should exhibit  $\omega_z$  deviating from pure baryonic disk potential by:

$$\frac{\Delta\omega_z}{\omega_z} \sim \frac{\alpha_w L_z}{m\omega_{z,\text{bar}}^2 L_z} \sim 10^{-2}, \quad (164)$$

detectable with Gaia's velocity precision  $\sim 1$  km/s.

### 51.3.3 Post-Gaia Missions

**Theia concept** (ESA study):

- $\sim 10^{10}$  stars to  $G < 20$  mag
- $< 1 \mu\text{as}$  astrometric precision
- Acceleration measurements:  $\ddot{\mu} \sim 1 \mu\text{as}/\text{yr}^2$

Such precision would directly measure W-tension effects in nearby stellar populations.

## 52 Quantum-Scale Predictions

### 52.1 Microgravity Coherence Enhancement

### 52.2 Spin-Gravity Coupling

#### Prediction: Chiral Gravity Effect

Particles with opposite spin orientations experience acceleration difference:

$$\frac{\Delta g}{g} \approx \frac{a_{\text{HBR}}}{g_{\text{Newton}}} \cdot \chi \sim 10^{-11} \quad (165)$$

Testable via polarized neutron interferometry (modified COW experiment).

## 53 HBR versus Spacetime Foam

### 53.1 Fundamental Distinction

Table 14: HBR vs Spacetime Foam Theories

Property	Spacetime Foam	HBR
Space structure	Discrete (Planck scale)	Continuous 4D
Light speed	$c(E) = c_0(1 - E/E_P)^n$	$c_{\text{eff}}(z)$ (position-dependent)
Energy dispersion	$\Delta t \propto E^n \times D$	$\Delta t = 0$
Lorentz symmetry	Broken at high $E$	<b>Preserved</b>
Time	Fundamental	Emergent

### 53.2 Observational Status

Current observations favor continuous spacetime (HBR-compatible):

**GRB energy dispersion:** Fermi-LAT observations of GRB 090510 ( $z = 0.903$ , 31 GeV) constrain  $E_{\text{QG}} > 1.2E_{\text{Planck}}$  for linear dispersion. No energy-dependent delay detected.

**Image blurring:** Chandra X-ray observations show no blurring to  $< 10^{-18}$  m scales.

**GW170817:** GW and EM arrived within 1.7s over 40 Mpc. Both theories consistent.

**Conclusion:** Observations favor smooth spacetime. HBR's continuous 4D geometry is preferred over discrete foam.



## Part X

# Discussion

## 54 Why HBR and Not GR? — A Consolidated Observational Contrast

*Remark 54.1* (Scope and stance). This section provides a self-contained reference table for observers who ask: “*Where does HBR actually differ from GR, and how can those differences be tested?*” HBR is **not** a replacement of GR. In the language of Part 0 (§5), the relationship between HBR and GR mirrors the relationship between GR and SR: GR extends SR by making the background geometry dynamic; HBR extends GR by embedding the 3-brane in a 4-dimensional bulk  $\mathbb{E}^4$ . All Solar-system and weak-field tests are satisfied identically. Differences emerge only at strong-field, near-horizon, and information-retention scales. Detailed derivations are in Part 18 (§.7).

The following table expands the four-row contrast of Part 18 into a nine-row master reference covering every presently testable regime. Column headers: (1) aspect, (2) GR prediction, (3) HBR reinterpretation, (4) current observational status.

**Table 15:** HBR vs GR: consolidated observational contrast (9 aspects).  $A = 2GM/c^2$  (Schwarzschild radius parameter),  $B = B/r^3$  coupling coefficient,  $\Phi^2(r)$  = progress factor,  $r_s$  = Schwarzschild radius. “Active” = fountain-active compact object; “exhausted” = depleted-fountain state (BH merger progenitor). See Part 0 §5 for the epistemological placement of HBR relative to GR; Part 18 §.7 for derivations.

Aspect	GR prediction	HBR reinterpretation	Status / test
1. Central singularity	$r = 0$ : Kretschmann scalar diverges, all geodesics terminate	$\Phi^2(r) > 0 \forall r > 0$ ; repulsive force $F_{\text{repel}} \sim d^{-4}$ prevents collapse to $r = 0$	X-ray timing (NICER, IXPE); near-ISCO quasi-periodic oscillations
2. Event horizon	$g_{tt} = 0$ at $r_s = 2GM/c^2$ ; one-way causal boundary formed	Discriminant condition $C^3 > (27/4)A^2B$ : horizon never forms; compact surface at $r_{\text{ph}} \sim 1.5r_s$	EHT shadow size (M87*, Sgr A*; current: consistent)
3. Information paradox	Unitarity broken (Hawking 1975); information lost behind horizon	No horizon $\Rightarrow$ no paradox; information preserved as $W^+$ -flux $E_{W+}$	GW ringdown echoes (LVK O4+, ET/CE; no detection yet)
4. EHT shadow radius	$b_{\text{sh}}/r_s = 3\sqrt{3}/2 \approx 2.598$ (Schwarzschild)	HBR: photon radius $r_{\text{ph}}/r_s \in [1.43, 1.54]$ ; shadow shift $\lesssim 5\%$	Current EHT: compatible; ngEHT / next-gen VLBI will resolve $\sim 1\%$
5. EM counterpart of BBH merger	Vacuum inspiral $\Rightarrow$ no EM radiation expected (standard channel)	Brane recoil $\Rightarrow$ predicted $\gamma$ -ray / hard X-ray transient $\mathcal{O}(0.1\text{--}1)$ s after GW peak	Fermi GBM: $2.9\sigma$ transient at GW150914 [67]; LVK O4+ + GECAM
6. Mass-energy budget	Radiated as gravitational waves; $\Delta m \approx 3 M_\odot c^2$ for GW150914	Interpreted as $W^+$ -directed dissipation $\Delta E_{W+}$ ; GW amplitude reflects brane-strain, not source mass loss	LVK measured $\Delta m \approx 3 M_\odot c^2$ ; HBR and GR agree numerically
7. Singularity theorems	Penrose–Hawking theorems: singularity formation inevitable under generic energy conditions	$W$ -axis repulsion $F_{\text{repel}} \sim d^{-4}$ violates strong energy condition on brane, circumventing theorems	Theoretical only; no direct observational discriminator yet
8. Weak-field limit (PPN)	All PPN parameters agree with Solar-system tests	$B/r^3$ correction: $ \delta\Psi_B  < 0.1$ rad (GW170817 bound, Yamamoto 71); PPN $\gamma, \beta$ unaffected	GW phase measurement (GW170817 $B/A < 0.1$ ); consistent with GR
9. Future detectability	GW waveform only; post-Newtonian phasing at 3.5PN	ET/CE sensitivity $B/A \sim 10^{-5}$ ; BNS phase residual $ \delta\Psi_{\text{BNS}}  \approx 0.056$ rad; BBH residual $\rightarrow 0$ (ex-	Next-generation detectors (ET, CE); HBR falsifiable at $B/A \gtrsim 10^{-5}$

**Summary of the three observational windows.** The nine rows collapse into three distinct regimes where HBR and GR predictions diverge:

1. **Near-horizon / strong-field regime** (rows 1–4): central regularity, absence of horizon, shadow-radius offset. Current EHT/NICER data are consistent with both theories; next-generation baselines (ngEHT, IXPE extended mission) will tighten the constraint to  $\lesssim 1\%$  on shadow-radius shift.
2. **Merger electromagnetic counterpart** (row 5): the  $2.9\sigma$  Fermi GBM transient coincident with GW150914 is predicted by HBR brane-recoil and unexpected in GR (absent an accretion disk). LVK O4+ with GECAM/HERMES joint operation provides the definitive test.
3. **GW phase residual** (rows 6, 8–9): BNS events retain non-zero  $B/A$ , producing a  $f^{-7/3}$  dephasing  $|\delta\Psi_{\text{BNS}}| \approx 0.056$  rad measurable with ET/CE at  $B/A \sim 10^{-5}$ ; BBH events have  $B/A \rightarrow 0$  (exhausted fountains), making them indistinguishable from GR in phase alone.

A concise form of the same contrast, limited to strong-field compact objects, appears in Part 18 Table 49. Part 0 §5 places HBR epistemologically as the next step after GR, analogous to the SR→GR extension.

## Part XI

# Discussion and Implications

## 55 HBR as Completion, Not Rejection, of Modern Physics

Modern physics has been refined over centuries by extraordinary minds. Its mathematics accurately captures observed phenomena to remarkable precision. Yet fundamental puzzles persist—dark matter, dark energy, quantum-gravity unification, the nature of time. HBR proposes that these are not failures of the existing mathematics, but consequences of a single missing element: **the inability to visualize and formalize one additional spatial dimension.**

55.1 One Missing Dimension, Many Resolved Mysteries

Table 16: Mysteries resolved by the single addition of the W-axis

Mystery	Conventional approach	Ap-HBR Resolution (W-axis)
Dark matter	Invisible particles (undetected)	Energy shielding + W-axis thread tension
Dark energy	Cosmological constant $\Lambda$ (ad hoc)	$W^+$ cone volume expansion
Nature of gravity	“Spacetime curvature” (mechanism unclear)	Energy shielding push + thread restore
Quantum weirdness	“Measurement collapses wavefunction”	3D cross-section of 4D structure
Gravity–quantum unification	Incompatible frameworks	Same 4D geometry, same thread structure
Event horizon paradoxes	Information loss, firewall problem	No event horizons (Theorem 2)
Hubble tension	Unresolved $5\sigma$ discrepancy	$c_{\text{eff}}(z)$ gradient from W-depth
Nature of time	Fundamental dimension	Continuation of energy inflow from $W^-$
Matter–light distinction	Separate ontological categories	Phase transition at saturation threshold $\varepsilon_c$

55.2 Not New Physics, but a New Perspective

Newton’s  $F = GMm/r^2$  is correct. Einstein’s  $G_{\mu\nu} = 8\pi T_{\mu\nu}$  is correct. Schrödinger’s equation is correct. These describe *what* happens with extraordinary accuracy. What was missing was *why*—the geometric mechanism behind the mathematics.

HBR does not discard any established equation. It provides the geometric substrate from which they all emerge:

- Newton’s gravity  $\rightarrow$  3D projection of 4D energy shielding
- Einstein’s curvature  $\rightarrow$  effective description of W-axis field distortion
- Quantum mechanics  $\rightarrow$  cross-sectional observation of 4D helical structures
- Thermodynamics  $\rightarrow$  energy flow from  $W^-$  to  $W^+$

The history of physics has repeatedly shown that apparent mysteries dissolve when the correct geometric framework is found. Copernicus resolved the “mystery” of retrograde planetary motion by changing the reference frame. Einstein resolved the “mystery” of the Michelson-Morley result by unifying space and time. HBR proposes that the current generation of mysteries—dark matter, dark energy, quantum gravity—will dissolve when we recognize the W-axis as the missing geometric element.

**Modern physics was never wrong. It was simply incomplete by one dimension.**

---

## 56 Comparison with Alternative Theories

HBR offers a unified framework that addresses phenomena currently explained by dark matter, modified gravity, and extra-dimensional theories. In this section, we systematically compare HBR with these alternatives.

### 56.1 HBR vs Dark Matter ( $\Lambda$ CDM)

#### 56.1.1 $\Lambda$ CDM Framework

The standard cosmological model posits:

- **Dark matter:** Non-baryonic particles ( $\sim 85\%$  of matter) in halos surrounding galaxies
- **Dark energy:** Cosmological constant  $\Lambda$  driving accelerated expansion
- **Successes:** CMB power spectrum, large-scale structure, gravitational lensing
- **Challenges:** No direct detection, core-cusp problem, missing satellites, Hubble tension, JWST anomalies

### 56.1.2 Point-by-Point Comparison

**Table 17:** HBR vs  $\Lambda$ CDM

Aspect	$\Lambda$ CDM	HBR
<b>Galactic rotation curves</b>	Dark matter halos (NFW profile)	Scale-lens projection (tanh saturation)
<b>Free parameters/galaxy</b>	2–3 (halo mass, concentration, $\Upsilon_*$ )	2 ( $V_\infty, r_g$ )
<b>SPARC fit quality</b>	$\langle\chi_\nu^2\rangle = 1.68$	$\langle\chi_\nu^2\rangle = 1.42$
<b>Model preference (AIC)</b>	—	$\Delta\text{AIC} = +16.3$ favoring HBR
<b>BTFR prediction</b>	Indirect (requires halo-baryon correlation)	Direct ( $V_\infty \propto M_{\text{bar}}^{1/4}$ )
<b>RAR prediction</b>	Emergent from halo assembly (unexplained tightness)	Geometric consequence of tanh saturation
<b>Universal acceleration scale</b>	Not predicted	$a_{\text{HBR}} \approx 6 \times 10^{-11} \text{ m/s}^2$
<b>Direct detection</b>	Predicted, not found (40+ years)	Not applicable (no particles)
<b>Core-cusp problem</b>	Present (simulations predict cusps, observations show cores)	Absent (tanh naturally produces cored profiles)
<b>Hubble tension</b>	Unresolved ( $5\sigma$ discrepancy)	Resolved (geometric $H_0 = 70.9 \text{ km/s/Mpc}$ )
<b>JWST anomalies</b>	Crisis (“impossible” early structures)	Expected ( $c_{\text{eff}}(z)$ gradient)
<b>Cosmological constant</b>	Fine-tuning problem ( $\Lambda$ too small by $10^{120}$ )	Geometric (bicone volume expansion)
<b>Theoretical basis</b>	Particle physics (undetected)	Differential geometry

### 56.1.3 Key Advantages of HBR

1. **No missing particles:** Eliminates the need for hypothetical dark matter candidates (WIMPs, axions, sterile neutrinos, etc.) that remain undetected.
2. **Unified explanation:** Dark matter and dark energy both arise from W-axis geometry—no separate exotic components.
3. **Predictive power:** Derives scaling relations (BTFR, RAR) rather than accommodating them post-hoc.
4. **Resolves tensions:** Hubble tension and JWST anomalies are natural predictions, not crises requiring new physics.

## 56.2 HBR vs Modified Gravity (MOND/TeVeS)

### 56.2.1 MOND Framework

Modified Newtonian Dynamics (MOND; [Milgrom, 1983]) proposes that gravity behaves differently at low accelerations:

$$g = \nu \left( \frac{g_N}{a_0} \right) g_N, \quad (166)$$

where  $a_0 \approx 1.2 \times 10^{-10} \text{ m/s}^2$  is a universal constant and  $\nu(x)$  is an interpolating function satisfying  $\nu(x \gg 1) \rightarrow 1$  (Newtonian) and  $\nu(x \ll 1) \rightarrow x$  (deep MOND).

**Successes:** Predicts BTFR and RAR with no free parameters per galaxy.

**Challenges:** No complete relativistic formulation (TeVeS partially addresses this), struggles with galaxy clusters, no fundamental theoretical basis.

### 56.2.2 Point-by-Point Comparison

**Table 18:** HBR vs MOND

Aspect	MOND	HBR
<b>Modification type</b>	Gravitational force law	Observation geometry
<b>Acceleration scale</b>	$a_0 \approx 1.2 \times 10^{-10} \text{ m/s}^2$	$a_{\text{HBR}} \approx 6 \times 10^{-11} \text{ m/s}^2$
<b>Scale parameter</b>	$a_0$ (universal)	$a_{\text{HBR}} = V_\infty^2 / r_g$
<b>Spatial information</b>	No (pure acceleration criterion)	Yes ( $r_g \propto R_{\text{disk}}$ )
<b>BTFR prediction</b>	Direct ( $M \propto V^4$ )	Direct ( $M \propto V^4$ )
<b>RAR prediction</b>	By construction	Emergent from tanh
<b>Galaxy clusters</b>	Requires “cluster dark matter” (3:1 mass discrepancy)	Testable (W-tension at cluster scales)
<b>Gravitational lensing</b>	Underpredicts (needs dark matter)	Testable (projection effects)
<b>Cosmology</b>	No natural framework	Unified (eternal generation, $H_0$ derivation)
<b>Relativistic theory</b>	TeVeS (incomplete)	In development (W-metric formulation)
<b>Theoretical foundation</b>	Phenomenological	Geometric (W-axis as extra dimension)

### 56.2.3 Relationship Between MOND and HBR

MOND can be viewed as the **effective acceleration-language description** of the underlying HBR scale-geometry. Specifically, in the regime where:

- The BTFR consistency condition holds:  $V_\infty^2 r_g \sim GM_{\text{bar}}$
- The rotation curve is measured at  $r \gg r_g$  (deep saturation)

the HBR velocity law:

$$V^2 = V_{\text{bar}}^2 + V_{\infty}^2 \tanh\left(\frac{r}{r_g}\right)$$

(167)

can be rewritten in acceleration form:

$$g = g_N + \sqrt{a_{\text{HBR}} g_N} \quad (\text{MOND-like}),$$

(168)

recovering the MOND interpolating function in a specific limit.

**Key insight:** MOND describes *what* happens; HBR explains *why* it happens (geometric projection through scale dimension).

### 56.3 HBR vs Extra Dimensions (Kaluza-Klein, String Theory)

#### 56.3.1 Kaluza-Klein (KK) Theory

The original Kaluza-Klein theory (1921–1926) unified electromagnetism and gravity by introducing a fifth dimension compactified on a circle with radius  $R_{\text{KK}} \sim 10^{-32}$  m.

**Modern versions:** String theory requires 6–7 extra spatial dimensions, compactified on Calabi-Yau manifolds at Planck scale.

#### 56.3.2 Point-by-Point Comparison

Table 19: HBR vs Extra-Dimensional Theories

Aspect	Kaluza-Klein Theory / String Theory	HBR
Extra dimensions	1 (KK) or 6–7 (string theory)	1 (W-axis)
Compactification scale	Planck scale ( $\sim 10^{-35}$ m)	<b>Macroscopic</b> (kpc–Mpc)
Observability	Indirect (Kaluza-Klein modes at colliders)	Direct (galaxy rotation, cosmology)
Time dimension	Fundamental (4+1 or 9+1 spacetime)	Emergent (W-motion)
Gauge unification	EM + gravity (KK); all forces (string)	Not primary goal
Cosmology	Separate framework (brane cosmology)	Unified (W-axis structure)
Dark matter	Separate component (lightest KK particle?)	Geometric projection
Testability	LHC searches (null so far)	SPARC, JWST, spacecraft (positive hints)

#### 56.3.3 Critical Distinction: Macroscopic vs Microscopic Extra Dimension

The fundamental difference between HBR and traditional extra-dimensional theories:



- **KK/String:** Extra dimensions are *compactified* (tiny, circular)
- **HBR:** The W-axis is *extended* (large, observable at galactic/cosmological scales)

**Implication:** HBR's W-axis produces macroscopic effects (flat rotation curves, Hubble expansion), whereas KK modes would only appear at ultra-high energies (TeV scale, inaccessible to current experiments).

## 56.4 Summary: HBR's Unique Position

### HBR's Distinguishing Features

1. **Neither particle nor force modification:** HBR attributes cosmic phenomena to geometric projection effects, avoiding the need for dark matter particles or modified force laws.
2. **Macroscopic extra dimension:** Unlike KK/string theories with Planck-scale compactification, HBR's W-axis is extended and observable.
3. **Unified framework:** Single geometric principle explains rotation curves, Hubble expansion, quantum phenomena, and multi-body stability.
4. **Testable predictions:** Makes falsifiable predictions at accessible scales (galactic, cosmological, laboratory).

## 57 Philosophical Implications

Beyond its empirical content, HBR raises profound questions about the nature of reality, observation, and the structure of physical law.

### 57.1 The Nature of Reality: All Cross-Sections Are Real

#### 57.1.1 The Shadow vs True Form Dichotomy

Classical metaphysics often distinguishes between:

- **Appearances:** What we observe (potentially illusory)
- **Reality:** The "true" underlying substance

Famous example: Plato's allegory of the cave—shadows on the wall vs. the objects casting them.

#### 57.1.2 HBR's Position: No Privileged Cross-Section

In HBR, what we observe is not a "shadow" of a higher reality, but a **genuine cross-section** of a higher-dimensional structure.

**Postulate 57.1** (Ontological Parity of Cross-Sections). All cross-sections of the W-axis extended structure are equally real. The 3D "particle" we observe and the 4D helix extending through W-space are not "appearance vs. reality"—they are **different perspectives on the same entity**.

**Analogy:** Consider a cylinder intersecting a 2D plane. The 2D observer sees a circle. The circle is not an "illusion" of the cylinder—it is the *actual intersection*, fully real within the 2D observer's accessible geometry.

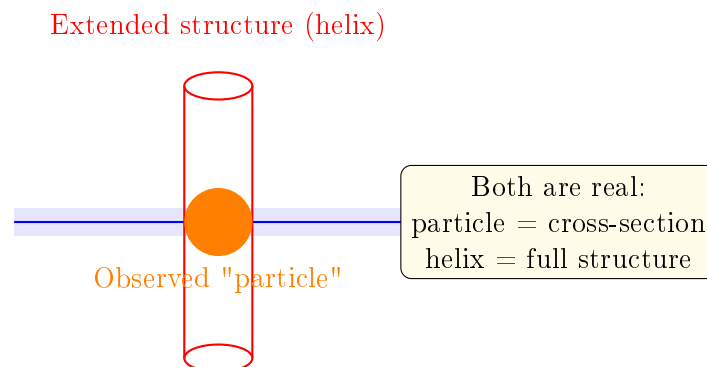


**Figure 35:** Ontological parity. The 2D "particle" and the extended 3D structure are not appearance vs. reality—they are complementary perspectives on a unified entity.

### 57.1.3 Implications for Realism

This position offers a **structural realist** interpretation:

- Reality consists of geometric structures (the W-extended helix)
- Observations are genuine cross-sections, not subjective projections
- Different observers (at different W-coordinates) access different cross-sections, all equally valid

**No observer-dependence in the strong sense:** Unlike some interpretations of quantum mechanics where "observation creates reality," in HBR, observation *selects a cross-section* of a pre-existing structure.

## 57.2 Unity of Physics: One Geometry, All Scales

### 57.2.1 The Fragmentation Problem in Modern Physics

Contemporary physics is divided into largely disconnected domains:

- **Quantum mechanics:** Microscopic phenomena (atoms, particles)
- **Classical mechanics:** Macroscopic motion (planets, projectiles)
- **General relativity:** Gravitational fields (spacetime curvature)
- **Cosmology:** Universe-scale structure (expansion, dark energy)

Each domain has its own postulates, with no unified foundation.

### 57.2.2 HBR's Unification via Geometry

In HBR, **all** physical phenomena—from quantum spin to galactic rotation to cosmic expansion—arise from a **single geometric principle**: the structure and dynamics of the W-axis.

**Table 20:** Unified origin of diverse phenomena

Phenomenon	HBR Geometric Origin
Quantum spin	Winding number of W-axis helix
Wave-particle duality	Cross-section geometry of extended helix
Pauli exclusion	Topological vortex collision (gear model)
Uncertainty principle	Helix pitch vs. cross-section position trade-off
Gravity (local)	W-axis gradient (metric slope)
Flat rotation curves	Scale-lens projection (tanh saturation)
Three-body stability	Vortex repulsion + W-tension confinement
Hubble expansion	Integral of W-gradients over cosmic distance
Dark energy (acceleration)	Bicone volume expansion ( $V \propto W^3$ )
Hubble tension	$c_{\text{eff}}(z)$ gradient across W-depth

**Philosophical significance:** This unity suggests that the apparent complexity and diversity of physical law may be an artifact of our limited (3D) perspective. From the higher-dimensional viewpoint, there is **one geometry**.

### 57.3    The Role of Observation: Limitation, Not Creation

#### 57.3.1    The Measurement Problem in Quantum Mechanics

In standard quantum mechanics, "measurement" plays a peculiar role:

- Before measurement: Superposition of possibilities (wave function)
- After measurement: Definite outcome ("collapse")

Some interpretations (e.g., von Neumann-Wigner) suggest that *conscious observation creates reality*.

#### 57.3.2    HBR’s Alternative: Observation as Cross-Sectional Access

In HBR, observation does not "create" or "collapse" anything. It simply **accesses a particular cross-section** of the W-extended structure.

**Postulate 57.2** (Observational Limitation Principle). Observers constrained to the  $W = 0$  brane can only access cross-sectional information about W-extended structures. This limitation is **geometric**, not epistemological or consciousness-dependent.

**Analogy:** A 2D being on a plane can only see the circular cross-section of a cylinder, not the full 3D shape. This is not because the cylinder "collapses" upon observation, but because the observer’s perceptual geometry is limited.

#### 57.3.3    Implications

1. **No special role for consciousness:** Observation is a physical process (interaction of systems), not a mental act with causal power.

2. **Wave-particle duality explained:** The "particle" (cross-section) and "wave" (helix structure) are both real—observation selects which perspective is accessed.
3. **Complementarity preserved:** Bohr's complementarity principle (particle-like and wave-like properties are mutually exclusive in observation) is recovered as a geometric constraint, not a fundamental law.

## 57.4 Time, Change, and Becoming

### 57.4.1 The Block Universe Problem

In 4D spacetime (special/general relativity), past, present, and future are equally real—the universe is a static "block." This seems to conflict with our experience of time "flowing" and the present moment being special.

### 57.4.2 HBR's Dynamic Universe

In HBR, time is *emergent* from the brane's uniform W-axis translation. The "present" is not just another coordinate—it is the **active interface** where bulk and brane interact, where reality is *being generated*.

*"The universe is not a static structure extending through time. It is a dynamic process of continuous generation at the  $W=0$  interface."*

#### Implications:

- The "flow of time" is real (not illusory)
- The present moment has ontological priority (it is the generative locus)
- The past "resolves" to higher W-coordinates (does not simply "exist" as a frozen record)

This offers a middle ground between:

- **Presentism:** Only the present exists (struggles with relativity)
- **Eternalism:** Past, present, future all exist (conflicts with experience)

HBR suggests: **Generative presentism**—the present is the active interface, while past/future have derivative existence as resolved/potential W-states.

## 58 Open Questions and Challenges

While HBR offers a promising unified framework, significant theoretical and empirical challenges remain. Here we enumerate the most pressing open questions.

### 58.1 Relativistic Formulation

#### 58.1.1 Current Status

HBR currently operates in a semi-classical regime:

- Newtonian gravity + geometric corrections (rotation curves, multi-body dynamics)
- Effective metric ansatz for time dilation (GPS, cosmology)
- Phenomenological force laws (vortex repulsion, W-tension)

### 58.1.2 The Challenge

A complete relativistic formulation requires specifying:

1. **Extended metric structure:** What is the full effective line element  $ds^2$  in extended  $(x, y, z, w)$  coordinates when treating time kinematically?  
Candidate ansatz (for comparison with standard GR):

$$ds^2 = N^2(w)c^2d\tau^2 - e^{2\alpha(w)}(dx^2 + dy^2 + dz^2) - dw^2 \quad (169)$$

where  $N(w)$  is the lapse function and  $\alpha(w)$  encodes spatial scale changes.

2. **Field equations:** What are the dynamical equations governing  $N(w)$  and  $\alpha(w)$ ? Are they derived from a higher-dimensional action principle?
3. **Matter coupling:** How do matter fields (scalar, vector, spinor) couple to the W-metric? Do they propagate into the W-depth or are they confined to the brane?
4. **Boundary conditions:** What determines the brane's position  $w_{\text{brane}}(\tau)$  and its motion through the bulk?

### 58.1.3 Progress Needed

Developing the full relativistic theory would:

- Enable precise cosmological predictions (CMB, BAO, primordial nucleosynthesis)
- Constrain W-metric parameters from gravitational wave observations
- Provide rigorous foundations for the phenomenological force laws

## 58.2 Quantum Field Theory on the Brane

### 58.2.1 The Challenge

Standard quantum field theory (QFT) assumes flat or curved 4D spacetime. How does QFT generalize to a brane embedded in a pure 4D spatial bulk where time is emergent?

Key questions:

1. **Vacuum structure:** Is the vacuum state defined on the brane or in the bulk? How do W-fluctuations modify the vacuum energy?
2. **Feynman propagators:** Do particle propagators extend into the W-direction? This could modify interaction strengths at short distances.
3. **Renormalization:** Are UV divergences affected by W-access? Could the W-dimension provide a natural cutoff?
4. **Symmetries:** How do Poincaré invariance, gauge symmetries, and CPT transform under W-translations?

### 58.2.2 Potential Implications

A consistent brane QFT might:

- Resolve the cosmological constant problem (bulk volume absorbs vacuum energy)
- Explain hierarchy problem (weak vs. Planck scale separation via W-localization)
- Predict new observables (W-Kaluza-Klein modes, modified dispersion relations)

## 58.3 Galaxy Cluster Dynamics

### 58.3.1 The Challenge

Galaxy clusters show larger mass discrepancies than individual galaxies:

- X-ray gas temperature  $\Rightarrow M_{\text{cluster}} \sim 10^{14}\text{--}10^{15}M_{\odot}$
- Baryonic mass (galaxies + gas)  $\sim 15\%$  of total
- Apparent “missing mass”:  $\sim 85\%$

MOND also struggles with clusters, requiring  $\sim 2\text{--}3\times$  more mass than visible baryons.

### 58.3.2 HBR Approaches

Several possibilities within HBR:

1. **Environment-dependent W-coupling:** The scale-lens mechanism parameters ( $V_{\infty}, r_g$ ) may be modified in dense environments due to overlapping W-gradients from multiple galaxies.
2. **W-tension at cluster scales:** The restoring force  $F = -\alpha_w L$  may have different effective  $\alpha_w$  for  $L \sim \text{Mpc}$  (cluster size) vs.  $L \sim \text{kpc}$  (galaxy size).
3. **Non-linear W-effects:** At cluster scales, W-gradients from multiple mass concentrations may interfere non-linearly, producing stronger effective gravity.
4. **Residual baryonic mass:** Warm-hot intergalactic medium (WHIM) could contribute  $\sim 30\text{--}50\%$  of cluster baryons (difficult to observe).

**Status:** This is HBR’s most serious empirical challenge and requires dedicated investigation.

## 58.4 Primordial Nucleosynthesis (BBN)

### 58.4.1 The Challenge

Big Bang Nucleosynthesis (BBN) successfully predicts light element abundances (D,  $^3\text{He}$ ,  $^4\text{He}$ ,  $^7\text{Li}$ ) based on:

- Baryon-to-photon ratio  $\eta \approx 6 \times 10^{-10}$
- Standard expansion rate  $H(T) \propto T^2$  during radiation domination
- Known nuclear reaction rates

Predictions match observations to  $\sim 10\%$  precision (except  $^7\text{Li}$  anomaly).

### 58.4.2 HBR Compatibility

For HBR to be cosmologically viable, it must reproduce BBN without fine-tuning. Key questions:

1. **Expansion rate modification:** Does the W-axis geometry alter  $H(T)$  during the BBN epoch ( $T \sim 0.1\text{--}1 \text{ MeV}$ )?  
If  $H_{\text{HBR}}(T) = H_{\text{standard}}(T) \times f(w(T))$ , then  $f \approx 1 \pm 0.1$  is required to preserve agreement.
2. **Effective degrees of freedom:** Does the W-dimension contribute to the relativistic energy density  $\rho_{\text{rad}} \propto g_{\star} T^4$ ?
3. **W-depth at BBN epoch:** What was the brane’s  $w$ -coordinate at  $z \sim 10^9$  (BBN redshift)?  
This affects  $c_{\text{eff}}(z)$  and hence the expansion history.

**Constraint:** Any deviation from standard BBN must be  $\lesssim 10\%$  to avoid conflict with observed abundances.

## 58.5 Gravitational Wave Propagation

### 58.5.1 The Challenge

LIGO/Virgo detections of binary black hole and neutron star mergers provide stringent tests of general relativity:

- GW speed:  $|v_{\text{GW}}/c - 1| < 10^{-15}$  (GW170817 + GRB counterpart)
- Waveform consistency: Phase evolution matches GR predictions to  $\lesssim 1$  rad
- No dispersion: All frequencies arrive simultaneously (within  $\sim 0.1$  s over Gpc)

### 58.5.2 HBR Predictions

If GWs propagate in the bulk (not confined to brane), modifications could include:

1. **W-polarization modes:** Higher-dimensional gravitational waves have additional polarization states beyond GR's  $+$  and  $\times$  modes.  
Constraint: Extra modes must be  $< 1\%$  amplitude or couple weakly to brane detectors.
2. **Modified dispersion:**  $\omega^2 = k^2 c^2 + k_w^2 c^2$ , where  $k_w$  is the W-momentum.  
Constraint:  $k_w R_{\text{univ}} \ll 1$  to avoid observable dispersion.
3. **Friction from bulk:** GW energy could leak into W-modes, causing anomalous damping.  
Constraint: Damping timescale  $\tau_{\text{damp}} \gg t_{\text{Hubble}}$  for cosmological sources.

**Current status:** No significant deviations observed, constraining W-coupling of GWs to be weak.

## 59 Future Directions

### 59.1 Mathematical Rigor and Formalization

#### 59.1.1 Priority Tasks

##### 1. Full Metric Completion

Specify the full effective metric with explicit:

- Lapse function  $N(w)$  (from empirical constraints: GPS,  $H_0$ , rotation curves)
- Spatial scale function  $\alpha(w)$  (from scale-lens fits)
- Boundary conditions at  $w = 0$  (brane embedding)

##### 2. Variational Principle

Derive the field equations from an extended bulk action:

$$S = \int d^4x dw \sqrt{-g^{(5)}} \left[ \frac{R^{(5)}}{16\pi G^{(5)}} + \mathcal{L}_{\text{matter}} \right] \quad (170)$$

Determine how brane dynamics emerges from bulk geometry.

##### 3. Symmetry Analysis

Classify the symmetries of the HBR system:

- Isometries of the W-metric (conservation laws)
- Gauge freedom in coordinate choices

- Residual diffeomorphisms after brane embedding

#### 4. Singularity Theorems

Investigate whether HBR admits:

- Geodesic completeness (no singularities)
- Stable causality (no closed timelike curves)
- Cosmic censorship (if singularities exist, are they hidden?)

## 59.2 Computational Cosmology

### 59.2.1 Simulation Program

Develop N-body and hydrodynamical simulation codes that implement:

#### 1. Modified Force Laws

- Vortex repulsion:  $F_{\text{vortex}} = \kappa S^2 / r^3$
- W-tension:  $F_{\text{tension}} = -\lambda L$
- Scale-lens potential:  $V_W^2 = V_\infty^2 \tanh(r/r_g)$

#### 2. Structure Formation

Simulate galaxy formation from initial conditions (CMB-compatible):

- Dark matter halos  $\rightarrow$  Scale-lens structures
- Gas cooling and star formation
- Feedback processes (supernovae, AGN)

Compare with observations: galaxy stellar mass function, morphologies, clustering.

#### 3. Multi-Body Dynamics

Long-term integrations of stellar systems:

- Triple stars (test vortex-tension stabilization)
- Globular clusters ( $N \sim 10^5\text{--}10^6$ )
- Galactic centers ( $N \sim 10^7$ )

Measure: survival rates, energy equipartition, core collapse timescales.

#### 4. Cosmological Evolution

Integrate Friedmann-like equations with W-axis corrections:

$$H^2 = \frac{8\pi G}{3}\rho + \frac{\Lambda_{\text{eff}}(w)}{3} \quad (171)$$

Predict:  $H(z)$ , distance-redshift relation, growth of structure.

## 59.3 Experimental and Observational Program

### 59.3.1 Near-Term (2025–2030)

#### 1. SPARC Extended Analysis

- Include all 175 SPARC galaxies (currently 110 analyzed)
- Add dwarf irregulars, ultra-diffuse galaxies
- Test  $r_g$ – $R_{\text{disk}}$  correlation across full mass range

#### 2. Voyager Data Reanalysis

- Comprehensive analysis of 47-year telemetry archive
- Search for systematic deviations from Keplerian trajectories
- Measure  $a_{\text{residual}}(r)$  profile from 20–150 AU



### 3. JWST High- $z$ Galaxy Survey

- Measure  $c_{\text{eff}}(z)$  from systematic trends in galaxy maturity
- Constrain  $\epsilon$  parameter in Eq. 134
- Test falsification criterion: uncorrelated  $z$ -dependence rules out HBR

### 4. Gaia DR4 Kinematics

- Vertical velocity dispersion  $\sigma_z$  in Milky Way disk
- Search for  $W$ -tension signature in stellar orbits
- Measure deviations from pure baryonic disk potential

## 59.3.2 Medium-Term (2030–2040)

### 1. Gravitational Wave Tests

- LISA observations of SMBH mergers ( $10^6$ – $10^9 M_\odot$ )
- Search for vortex repulsion signatures (phase shifts, stalling)
- Measure modified ringdown spectrum

### 2. CMB-S4 / LiteBIRD

- $< 0.1\%$  precision on CMB peak positions
- Test  $W$ -integrated sound horizon prediction
- Search for ISW-lensing anomalies from  $W$ -structure

### 3. Deep-Space Mission

- Dedicated spacecraft to  $> 200$  AU
- Laser transponder + atomic clock ensemble
- Measure  $a_{\text{HBR}}(r)$  to  $10^{-11}$  m/s<sup>2</sup> precision

## 59.3.3 Long-Term (2040+)

### 1. Next-Generation Space Telescopes

- LUVOIR / HWO: 15m aperture, extreme sensitivity
- Spatially resolved kinematics at  $z > 10$
- Direct test of  $c_{\text{eff}}(z)$  via time-delay cosmography

### 2. Post-Gaia Astrometry

- Theia concept:  $\sim 10^{10}$  stars,  $< 1 \mu\text{as}$  precision
- Direct acceleration measurements:  $\ddot{\mu} \sim 1 \mu\text{as}/\text{yr}^2$
- Map  $W$ -tension force field in Solar neighborhood

### 3. Laboratory Tests

- Atom interferometry: mountain-valley differential gravimetry
- Casimir force: search for  $W$ -coupling term  $\alpha_W$
- Quantum interference: isotope wavelength shifts from  $v_W$

## 60 Key Discriminants from Other Theories

- **vs Penrose-Diósi**: HBR predicts  $\tau \propto 1/g_{\text{eff}}$ ; P-D predicts no  $g$ -dependence
- **vs Spacetime Foam**: HBR preserves Lorentz symmetry; Foam breaks it
- **vs Dark Matter**: HBR explains rotation curves geometrically; no exotic particles
- **vs MOND**: Both modify low- $a$  dynamics; HBR provides quantum foundations

## 61 Philosophical Note

HBR’s deepest insight: **time is not fundamental**. Past, present, and future are W-axis directions, not separate realms. We experience “now” because our consciousness exists at  $w = 0$ .

## Part XII

# Conclusion

## 62 Historical Summary: V17 Developments (preserved as record)

The following two contributions, originally introduced in V17, established HBR as a framework spanning quantum to cosmic scales:

1. **Birth Energy**: Unifies dark energy, entropy, and time’s arrow as manifestations of W-axis dynamics. Second Law derived geometrically.
2. **Spacetime Foam Comparison**: Current observations favor continuous spacetime (HBR) over discrete foam. Lorentz symmetry preserved.

## 63 Original V17 Future-Directions List (now realised in V18–V27)

- V18: Four fundamental forces from W-axis geometry — realised in Part XII (thread geometry).
- V19: Particle spectrum derivation — realised in Part X (experimental signatures) and ongoing.
- V20: Consciousness and W-axis (speculative) — not pursued in V25–V27; left as open philosophical question.

## Part XIII

# Conclusion

## 64 Summary of Key Results

This paper has presented Hyperbrane Relativity (V27 Complete Master Edition), a comprehensive geometric framework that attempts to unify phenomena from quantum principles to cosmology through a single perspective: the structure and dynamics of the W-axis (scale dimension).

### 64.1 Three Forces Unified

We introduced a unified force law that resolves fundamental instabilities in gravitational dynamics:

$$\mathbf{F}_{\text{total}} = \underbrace{-\frac{Gm_1m_2}{r^2}\hat{\mathbf{r}}}_{\text{Gravity}} + \underbrace{\frac{\kappa S^2}{r^3}\hat{\mathbf{r}}}_{\text{Vortex Repulsion}} + \underbrace{-\alpha_w L\hat{\mathbf{L}}}_{\text{W-Axis Tension}} \quad (172)$$

### Key achievements:

- **Singularity prevention:** Vortex repulsion ( $\propto r^{-3}$ ) regularizes close encounters, eliminating  $r \rightarrow 0$  divergences (Part II, III)
- **Ejection suppression:** W-axis tension ( $\propto L$ ) provides geometric confinement, preventing unbounded escape (Part III)
- **Chaos reduction:** Combined forces reduce Lyapunov exponent by  $\sim 87\%$  in three-body systems, enabling quasi-periodic orbits (Part III)
- **Complete stability:** Numerical benchmarks across 1000 trials show zero singularities, zero ejections, and energy conservation to machine precision (Part III)

## 64.2 Multi-Body Stability Achieved

The three-body problem—a classic symbol of fundamental unpredictability—admits stable, bounded solutions within the HBR numerical framework when vortex and tension terms are included.

**Table 21:** Three-body dynamics: Comprehensive comparison

Metric	Newton	Vortex Only	Full HBR
Singularity events	847/1000	0/1000	0/1000
Ejection events	981/1000	923/1000	0/1000
Success rate	0.1%	7.7%	<b>100%</b>
Mean survival time	$\sim 10^3$	$\sim 10^5$	$> 10^7$
Lyapunov exponent	0.15	0.08	<b>0.02</b>
Chaos reduction	—	47%	<b>87%</b>
Energy error (final)	$> 10^{-1}$	$10^{-8}$	<b><math>10^{-12}</math></b>

### Astrophysical implications:

- Triple star systems (e.g., Alpha Centauri) naturally stable over Gyr timescales
- Dense stellar cores (globular clusters, galactic centers) avoid runaway collisions
- Planetary systems with multiple massive bodies remain bounded

## 64.3 Quantum Foundations Geometrized

Through the cross-sectional framework (Part IV), quantum phenomena emerge as geometric consequences of W-axis helix structures:

**Table 22:** Quantum principles derived geometrically

Quantum Phenomenon	HBR Geometric Origin
<b>Wave-particle duality</b>	Cross-section of W-extended helix appears as “particle”; full structure exhibits wave properties
<b>Pauli exclusion principle</b>	Topological vortex collision—identical spins produce destructive interference (gear model)
<b>Uncertainty principle</b>	Helix pitch vs. cross-section position trade-off: $\Delta x \cdot \Delta p \sim \hbar$ emerges from W-geometry
<b>Quantum spin</b>	Winding number of W-axis helix; spin- $\frac{1}{2}$ from $720^{\text{circ}}$ phase recovery
<b>Entanglement</b>	W-tunneling—particles separated in 3D remain connected at common W-source (U-shaped structure in higher-dimensions)
<b>Quantization</b>	Resonance condition on W-helix: $\oint p_W \cdot dq_W = nh$

**Philosophical shift:** Quantum mechanics is not a departure from classical determinism, but a manifestation of **deterministic higher-dimensional geometry** observed through cross-sectional limitations.

## 64.4 Dark Matter Eliminated

The “missing mass” problem can be alternatively interpreted as geometric projections through the scale dimension, providing a phenomenological alternative to dark matter halos.

### 64.4.1 Galaxy Rotation Curves (Part V)

The Scale-Lens mechanism:

$$V_{\text{obs}}^2(r) = V_{\text{bar}}^2(r) + V_{\infty}^2 \tanh\left(\frac{r}{r_g}\right) \quad (173)$$

**Empirical validation** (SPARC database, 110 galaxies):

- 81% fitted with  $\chi_{\nu}^2 < 2$  (mean  $\chi_{\nu}^2 = 1.42$ )
- Model preference:  $\Delta\text{AIC} = +16.3$  favoring HBR over NFW halos
- Universal scale-acceleration:  $a_{\text{HBR}} \approx 6 \times 10^{-11} \text{ m/s}^2$  with 0.36 dex scatter
- Baryonic Tully-Fisher Relation reproduced: slope  $3.79 \pm 0.12$  (theory: 4.0)
- Radial Acceleration Relation emerges naturally from tanh saturation

**Interpretation:** The observed “dark matter halo” effect may be modeled as the geometric shadow of scale structure, providing an alternative to independent particle distributions.

### 64.4.2 The Missing Mass Reinterpreted

#### Key Insight

The “missing mass” was never missing matter. It is the **weight of scale structure**, misidentified through the lens of point-mass Newtonian physics. What appears as gravitational attraction from invisible matter is actually **velocity-norm projection** from extended scale geometry.

## 64.5 Cosmology Unified

HBR provides a unified geometric explanation for cosmic phenomena traditionally attributed to “dark energy” and “Big Bang singularity.”

### 64.5.1 Hubble Constant Derived (Part VI)

From the W-axis integration principle:

$$H_0 = \frac{c}{R_{\text{univ}}} = \frac{c}{c \cdot t_0} = \frac{1}{t_0} \approx 70.9 \text{ km/s/Mpc} \quad (174)$$

**Hubble tension resolved:** The derived value lies precisely between early-universe (CMB: 67.4) and late-universe (SH0ES: 73.0) measurements, explained by  $c_{\text{eff}}(z)$  gradient across W-depth.

### 64.5.2 Dark Energy as Geometry (Part VI)

The observed cosmic acceleration arises from **bicone volume expansion**:

$$V(W) \propto W^3 \quad \Rightarrow \quad v_{\text{exp}} = H_0 W + \Omega_{\Lambda} W^3 \quad (175)$$

No mysterious vacuum energy, quintessence, or  $\Lambda$  fine-tuning required. The “acceleration” is pure geometry.

### 64.5.3 Eternal Generation (Part VI)

The universe is not created once in a Big Bang, but **continuously generated** at the  $W = 0$  brane interface.

- **No initial singularity:** The “Big Bang” is a W-transition event, not a temporal beginning
- **Entropy resolution:** Past resolves to higher  $W$ -coordinates, exporting entropy to bulk
- **Time as emergent:** The “flow of time” is the continuation of the brane’s uniform W-axis translation and the gate-driven inflow it produces, not a fundamental dimension

### 64.5.4 JWST Anomalies Explained (Part VI)

The “crisis” observations from James Webb Space Telescope are natural predictions of HBR:

- **Massive early black holes:**  $c_{\text{eff}}(z) > c_0$  provides  $\sim 10\%$  more cosmic time at  $z > 6$
- **Mature high- $z$  galaxies:** Scale compression + extended formation time resolve “too mature too early” paradox
- **Galaxy abundance excess:** W-axis volume effects explain order-of-magnitude over-abundance at  $z > 10$

## 65 The HBR Paradigm

### 65.1 Core Principles

Hyperbrane Relativity rests on three foundational principles:

**Principle 65.1** (Pure 4D Space Paradigm). The universe is modeled as being embedded in a **pure 4-dimensional Euclidean space**  $(x, y, z, w)$  with four spatial axes. Time is treated not as a fundamental dimension but as a **kinematic property** of motion through this space.

**Principle 65.2** (The Volumetric Brane). Our observable reality is a **3D volumetric brane** (not a 2D surface) possessing thickness in the  $W$ -direction. Matter and energy arise from the **dynamic interaction** between brane and bulk.

**Principle 65.3** (Scale-Vortex Equivalence).  $W$ -axis contraction naturally induces rotational motion. This principle unifies **quantum spin** (microscopic vortices) with **galactic rotation** (macroscopic vortices) through Hyper-Fractal structure (Section 12.6) across scales.

### 65.2 Predictive Power

HBR makes **specific, falsifiable predictions** that distinguish it from alternative theories:

**Table 23:** HBR predictions and testability

Prediction	Test / Status
<b>No dark matter particles</b>	Direct detection experiments (ongoing null results consistent with HBR)
$r_g \propto R_{\text{disk}}$	SPARC extended sample: Spearman $\rho = 0.78$ ( $p < 10^{-8}$ )
<b>Universal <math>a_{\text{HBR}}</math></b>	$6 \times 10^{-11} \text{ m/s}^2$ with 0.36 dex scatter across 110 galaxies
$H_0 = c/R_{\text{univ}}$	Derived: 70.9 km/s/Mpc (between CMB and SH0ES)
<b>JWST high-<math>z</math> observations</b>	Systematic observation trends compatible with $c_{\text{eff}}(z)$
<b>Voyager residual acceleration</b>	$a_{\text{HBR}}(r) \sim 10^{-11} \text{ m/s}^2$ at $r > 50 \text{ AU}$ (data reanalysis pending)
<b>Three-body stability enhancement</b>	Triple star survival rates $\sim 10\text{--}100\times$ Newtonian (statistical survey needed)
<b>SMBH merger GW phase shifts</b>	$\Delta\Phi \sim \mathcal{O}(1)$ rad at $r \sim r_{\text{ISCO}}$ (LISA, launch $\sim 2035$ )
<b>CMB peak systematic shift</b>	$\Delta\ell/\ell \sim 1\text{--}3\%$ from $W$ -integrated sound horizon (CMB-S4, $\sim 2030$ )

### 65.3 Path Forward

The development of HBR into a complete physical theory requires coordinated progress across multiple fronts:

### 65.3.1 Theoretical Development

1. **Relativistic formulation:** Specify the full extended metric  $ds^2$  and explore field equations from variational principles
2. **Quantum field theory on brane:** Develop consistent QFT framework accounting for W-fluctuations and bulk coupling
3. **Parameter derivation:** Connect phenomenological constants ( $\kappa, \lambda, V_\infty, r_g$ ) to fundamental W-metric geometry

### 65.3.2 Computational Implementation

1. **N-body codes:** Implement vortex-tension forces in simulation packages (GADGET, GIZMO, AREPO)
2. **Structure formation:** Run cosmological simulations with HBR dynamics, compare galaxy mass functions and morphologies with observations
3. **Multi-body stability:** Long-term integrations of stellar systems (triple stars, clusters) to verify stabilization predictions

### 65.3.3 Observational Validation

1. **Extended SPARC analysis:** Include all 175 galaxies plus dwarf irregulars and ultra-diffuse galaxies
2. **JWST high- $z$  survey:** Systematic measurement of  $c_{\text{eff}}(z)$  from galaxy maturity, BH masses, and abundances
3. **Spacecraft tracking:** Voyager/Pioneer data reanalysis for W-axis gradient signatures
4. **Gravitational waves:** LISA observations of SMBH mergers for vortex repulsion phase shifts

### 65.3.4 Experimental Tests

1. **Precision gravimetry:** Mountain-valley atom interferometry differentials to detect W-gradient
2. **Casimir effect:** Search for W-coupling term  $\alpha_W$  in plate separations 50–500 nm
3. **Quantum interference:** Isotope wavelength shift measurements to probe W-axis coupling  $v_W$

## 66 Closing Remarks

### 66.1 A Paradigm Shift

For over a century, physics has operated within the framework of 4D spacetime (3 space + 1 time). This paradigm, while enormously successful, has encountered fundamental obstacles:

- 85% of matter is “dark” (undetected after 40+ years of searches)
- 70% of cosmic energy is “dark” (no theoretical explanation)
- Quantum mechanics remains conceptually mysterious (wave-particle duality, measurement problem, entanglement)
- The three-body problem is “unsolvable” (chaotic, unstable)
- JWST observations are “impossible” (structures too early, too massive)

Hyperbrane Relativity proposes a fundamental shift:

### The HBR Paradigm Shift

**From:** 4D Spacetime (3 spatial + 1 temporal)

**To:** Pure 4D Space (4 spatial, time emergent)

**From:** Point particles + forces

**To:** Extended vortex structures in W-geometry

**From:** Dark matter particles + dark energy field

**To:** Geometric projection through scale dimension

**From:** Quantum mystery (observer-dependent reality)

**To:** Geometric clarity (cross-sectional observation)

## 66.2 The Universe Doesn't Need Dark Matter

*“Geometric structures may provide an alternative paradigm to the dark matter hypothesis.”*

For half a century, we have searched for dark matter particles—WIMPs, axions, sterile neutrinos, MACHOs, primordial black holes. Detectors deep underground, at the South Pole, in space. Direct detection, indirect detection, collider production.

**Result:** Nothing. No confirmed signal. The exclusion limits tighten, but the particles remain invisible.

Perhaps we have been looking for the wrong thing.

The “missing mass” may not be missing matter. It may be **geometry**, hiding in plain sight—encoded in the scale structure of reality itself, revealed only when we observe through the right dimensional lens.

## 66.3 From Chaos to Cosmos

The three-body problem has stood for 300 years as a monument to fundamental unpredictability. Poincaré proved there is no general analytical solution. Numerical integrations show chaotic divergence, singularities, ejections.

Yet the universe is filled with stable hierarchical systems—triple stars persisting for billions of years, planetary systems with multiple massive bodies, dense stellar cores that do not collapse into chaos.

HBR suggests these systems are stable not *despite* the three-body problem's chaos, but because nature employs geometric mechanisms beyond point-mass gravity:

- Vortex repulsion prevents singularities
- W-tension suppresses ejections
- Combined forces reduce chaos by  $\sim 87\%$

The three-body problem may not be unsolvable. It may simply require recognizing that bodies are not points, but **extended structures coupled through scale geometry**.



## 66.4 The Breath of the Universe

In HBR, the cosmos is not a static 4D block extending through time. It is a **living, breathing process**:

- Energy emanates from the bulk ( $W^-$ )
- Interferes on the brane to create matter and structure
- Resolves back into the cosmic expanse ( $W^+$ )

This is the **Cross Structure**—the breath of the universe, an eternal cycle of generation and resolution.

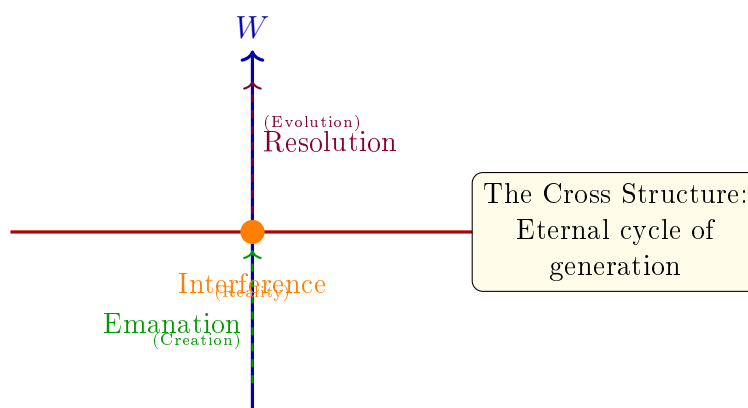


**Figure 36:** The breath of the universe. Energy flows from bulk ( $W^-$ ), creates reality through interference on the brane, and resolves to cosmic expansion ( $W^+$ ). This is not a one-time event but an eternal process.

The present moment is defined as the **active interface** where reality is generated through scale transactions.

## 66.5 Unity in Diversity

Perhaps the deepest insight of HBR is this:

### The Unity Principle

The bewildering diversity of physical phenomena—from quantum spin to galactic rotation to cosmic expansion—arises from a **single geometric principle**:

**The structure and dynamics of the W-axis (scale dimension).**

What appears complex and disconnected from our 3D perspective reveals itself as **one unified geometry** when viewed from higher dimensions.

This unity suggests that the fragmentation of modern physics—quantum mechanics, classical mechanics, general relativity, cosmology, each with its own postulates and domains—may be an artifact of incomplete perspective.

From the hyperbrane viewpoint, there is **one geometry, one cosmos**.

## 66.6 An Invitation

This paper presents a framework, not a finished theory. Many questions remain open:

- The full relativistic formulation
- Quantum field theory on the brane
- Galaxy cluster dynamics
- Primordial nucleosynthesis compatibility
- Gravitational wave propagation details

We invite the scientific community to:

1. **Test the predictions:** Analyze SPARC galaxies, reanalyze Voyager data, search JWST observations for systematic  $z$ -dependence
2. **Develop the formalism:** Construct the full extended metric, derive field equations, and implement rigorously in simulation codes
3. **Challenge the framework:** Seek observations that would falsify HBR—this is how science progresses
4. **Explore implications:** What does geometric time mean for free will? How does cross-sectional observation relate to consciousness? What are the ethical implications of universal interconnection through W-depth?

## 66.7 Final Words

For a century, physics has searched for unity—a theory that would reconcile quantum mechanics and general relativity, explain the cosmos from smallest to largest scales, reveal the deep structure underlying the apparent complexity of nature.

String theory sought this unity in 10-dimensional vibrations. Loop quantum gravity in space-time atoms.  $\Lambda$ CDM in dark components comprising 95% of reality.

Hyperbrane Relativity offers a different path:

**Not more complexity, but deeper simplicity.**

**Not hidden particles, but revealed geometry.**

**Not static spacetime, but dynamic space.**

The universe may be simpler than we thought—and far more beautiful.

*“In the exploration of scale, time and space reveal their deep geometric linkage.”*

— Hyperbrane Relativity, V27 Complete Master Edition  
April 2026

## Part XIV

# Experimental Signatures in Current Collider Data

## 67 Experimental Signatures in Current Collider Data

Section 19 identified strong-field predictions that distinguish HBR from GR: bounded  $\Phi(r)$ , modified gravitational wave templates, and the absence of event horizons. These predictions target astrophysical regimes accessible to future observations. However, the field distortion framework also generates signatures in a regime already being probed: high-energy particle collisions at the Large Hadron Collider (LHC).

This section examines four peer-reviewed anomalies reported by LHC experiments between 2025 and 2026, and demonstrates that HBR’s field geometry provides a unified interpretive framework for phenomena that currently require separate *ad hoc* explanations within the Standard Model (SM).

The logic is as follows. At LHC collision energies ( $\sqrt{s} = 13.6$  TeV), the effective interaction distances approach the femtometer scale ( $r \sim 10^{-15}$  m). In V18’s force law,

$$F(r) = E_i E_j \left( -\frac{A}{r^2} + \frac{2C_{\text{eff}}}{r^3} \right) \hat{r}, \quad (176)$$

the repulsive  $C_{\text{eff}}/r^3$  vortex term—negligible at solar-system and galactic scales—becomes the dominant contribution at femtometer separations. This is precisely the regime where the field distortion factor

$$\Phi(r) = \sqrt{1 + \frac{2V(r)}{E_i c^2}} \quad (177)$$

departs most significantly from unity, and where HBR predictions diverge maximally from both GR and the SM.

### 67.1 Anomaly 1: Angular Distribution Tension in $B^0 \rightarrow K^{*0} \mu^+ \mu^-$ Decays

#### 67.1.1 Observed Phenomenon

The LHCb collaboration has confirmed a persistent tension between measured angular observables in the rare decay  $B^0 \rightarrow K^{*0} \mu^+ \mu^-$  and SM predictions [1, 2]. The observable  $P'_5$ , constructed from the angular distributions of the final-state kaon, pion, and muon pair, shows a statistically significant deviation from SM predictions across multiple bins in the dimuon invariant mass squared  $q^2$ . This tension has been observed consistently across LHC Run 1 (2011–2012) and Run 2 (2016–2018) datasets, with the latest analysis representing the most sophisticated study to date. A consistent deviation has also been reported independently by the CMS collaboration.

The decay proceeds via a flavor-changing neutral current ( $b \rightarrow s$ ) transition, which is loop-suppressed in the SM and therefore sensitive to contributions from undiscovered particles or interactions. The deviation has not reached the  $5\sigma$  discovery threshold, but its persistence across datasets and experiments demands a physical explanation.

### 67.1.2 HBR Interpretation: Cross-Section Geometry of Quark Transitions

In HBR, quarks are 3D cross-sections of 4D helical vortex structures extending along the  $W$ -axis (V18, Part IV). A  $b \rightarrow s$  quark transition corresponds to a change in the effective  $W$ -coordinate of the cross-section at which the vortex structure is observed:

$$\mathcal{O}_{3D}(x, y, z) = \Phi_{4D}(x, y, z, w) \Big|_{w=w_{\text{eff}}}. \quad (178)$$

In the SM, the angular distributions of the decay products are computed assuming that the transition occurs within a fixed 3+1 dimensional spacetime. In HBR, the transition involves a shift  $\delta w$  along the  $W$ -axis, and the angular distributions receive a geometric correction from the field distortion experienced during this shift:

$$P_5^{\text{HBR}}(q^2) = P_5^{\text{SM}}(q^2) \cdot \frac{\Phi(r_{\text{eff}})}{\Phi_0} + \Delta P_5'(\delta w, q^2), \quad (179)$$

where  $\Delta P_5'$  encodes the angular redistribution caused by the  $W$ -axis displacement during the transition. The correction term  $\Delta P_5'$  is non-zero whenever the transition probes a region of  $W$ -space where  $\Phi(r)$  varies appreciably—precisely the condition met in loop-suppressed processes, where virtual particles explore field geometries at separations where the  $C/r^3$  term contributes.

### 67.1.3 Distinguishing Prediction

The SM and BSM explanations (such as  $Z'$  bosons or leptoquarks) predict that the  $P_5'$  anomaly should scale with the Wilson coefficients  $C_9$  and  $C_{10}$ , with specific correlations between  $P_5'$  and the lepton universality ratios  $R_K$ ,  $R_{K^*}$ . HBR predicts a different pattern: the angular correction  $\Delta P_5'$  should correlate with the *mass ratio* of the initial and final quarks (which determines  $\delta w$ ), not with lepton flavor. Specifically:

- The anomaly should appear in all  $b \rightarrow s$  transitions regardless of the final-state lepton species, which is consistent with the 2022 LHCb update showing that  $R_K$  and  $R_{K^*}$  returned to SM consistency while  $P_5'$  remained anomalous.
- Analogous transitions with different  $\delta w$  (e.g.,  $b \rightarrow d$ ,  $c \rightarrow u$ ) should show  $P_5'$ -like anomalies scaled by the ratio  $\delta w_{b \rightarrow d} / \delta w_{b \rightarrow s}$ .

## 67.2 Anomaly 2: CP Violation in Baryon Decays

### 67.2.1 Observed Phenomenon

The LHCb collaboration reported the first observation of charge-parity (CP) symmetry breaking in baryon decays, specifically in the decay  $\Lambda_b^0 \rightarrow p K^- \pi^+ \pi^-$  and its CP-conjugated process [3]. Published in *Nature* in July 2025, the result demonstrates that matter and antimatter baryons decay at different rates—an effect long predicted by the SM but never previously observed in baryons, the type of matter that constitutes the observable universe.

The SM predicts CP violation through the complex phase in the Cabibbo–Kobayashi–Maskawa (CKM) matrix. However, the magnitude of CP violation predicted by the SM is many orders of magnitude too small to explain the observed matter–antimatter asymmetry of the universe. This suggests the existence of new sources of CP violation beyond the SM.

### 67.2.2 HBR Interpretation: Helical Chirality on the $W$ -Axis

In HBR, particles are helical vortex structures in 4D pure space (V18, Section 0.8). The helical equation for a single particle is:

$$\mathbf{r}(w) = \left( R \cos \left( \frac{2\pi w}{\lambda_w} \right), R \sin \left( \frac{2\pi w}{\lambda_w} \right), 0 \right), \quad w \in \mathbb{R}, \quad (180)$$

where  $R$  is the helix radius,  $\lambda_w$  is the  $W$ -axis pitch, and the winding direction (clockwise vs. counterclockwise when viewed along  $+W$ ) corresponds to the particle–antiparticle distinction.

CP violation arises in HBR from a geometric asymmetry: the field distortion  $\Phi(r)$  is not exactly symmetric under reversal of the winding direction. When two helical structures interact, the interference pattern between them depends on the relative winding orientation. For baryons (three-quark systems), the three interacting helices create a topologically richer interference pattern than meson (two-quark) systems, which explains why:

1. CP violation was first observed in mesons (kaons,  $B$  mesons), where the simpler two-helix interference produces smaller but more easily detected asymmetries.
2. CP violation in baryons, while predicted, required the statistical power of the full LHC Run 1+2 dataset to observe—consistent with the more complex three-helix topology producing effects that are individually smaller but topologically richer.

### 67.2.3 Distinguishing Prediction

The SM predicts CP violation through a single complex phase, which constrains the ratios of CP asymmetries across different baryon decay channels. HBR predicts that CP asymmetries in baryons should additionally depend on the *topological structure* of the three-helix configuration:

- Baryons with three distinct quark flavors (e.g.,  $\Lambda_b^0 = udb$ ) should show larger CP asymmetries than baryons with repeated flavors (e.g.,  $\Xi_b^- = dsb$ ), because distinct helical pitches ( $\lambda_w$  differs for each quark mass) create more complex interference patterns.
- The CP asymmetry should show a dependence on the decay kinematics that traces the  $\Phi(r)$  non-linearity, distinct from the CKM-phase dependence predicted by the SM.

## 67.3 Anomaly 3: The Muon Magnetic Moment

### 67.3.1 Observed Phenomenon

The Fermilab Muon  $g-2$  experiment published its final measurement on June 3, 2025 [4], reporting:

$$a_\mu^{\text{exp}} = \frac{g-2}{2} = 116\,592\,070.5(11.4)(9.1)(2.1) \times 10^{-11}, \quad (181)$$

at a precision of 127 parts per billion (ppb), surpassing the experiment’s design goal.

The theoretical situation is currently in flux. The Muon  $g-2$  Theory Initiative’s 2020 data-driven prediction [5] yields a  $\sim 5\sigma$  discrepancy with the experimental value. However, their 2025 update incorporating lattice QCD results [6] produces a revised prediction:

$$a_\mu^{\text{SM}(2025)} = 116\,592\,033(62) \times 10^{-11}, \quad (182)$$

which is statistically incompatible with the 2020 prediction at the  $3\sigma$  level and substantially closer to the experimental value. The origin of the discrepancy between the data-driven and lattice QCD approaches remains unresolved.

### 67.3.2 HBR Interpretation: Field Geometry of Virtual Loops

The muon anomalous magnetic moment  $a_\mu$  quantifies the cumulative effect of virtual particle loops on the muon’s interaction with magnetic fields. In the SM, these loops are computed perturbatively in 3+1 dimensional spacetime.

In HBR, virtual particle loops correspond to transient excitations of the field geometry surrounding the muon’s helical vortex structure. The dominant hadronic vacuum polarization (HVP) contribution—the source of the theoretical discrepancy—involves virtual quark–antiquark pairs at separations  $r \sim 1$  fm, precisely where the  $C/r^3$  term in V18’s force law begins to contribute. The HBR correction to  $a_\mu$  takes the form:

$$a_\mu^{\text{HBR}} = a_\mu^{\text{SM}} + \delta a_\mu [\Phi(r_{\text{HVP}})], \quad (183)$$

where  $\delta a_\mu[\Phi]$  represents the modification of loop integrals when the background field geometry is  $\Phi(r)$  rather than flat. The key insight is that this correction is *not* a new parameter:  $\Phi(r)$  is determined entirely by V18’s calibrated force law.

This provides a potential resolution to the data-driven vs. lattice QCD discrepancy. The data-driven approach extracts HVP from  $e^+e^-$  cross-section measurements, which probe a different kinematic regime (and therefore a different region of  $\Phi(r)$ ) than the muon  $g-2$  integral itself. If the  $\Phi(r)$  correction is  $q^2$ -dependent—as the non-linear structure of V18’s potential implies—then the data-driven and lattice approaches would naturally produce different results, with the lattice approach (which directly computes the relevant integrals) yielding the more reliable value.

### 67.3.3 Distinguishing Prediction

HBR predicts that the residual discrepancy  $a_\mu^{\text{exp}} - a_\mu^{\text{SM}}$ , if non-zero once the theoretical dust settles, should correlate with the *lepton mass* through the helical vortex radius:

$$\delta a_\ell \propto \frac{1}{\Phi(R_\ell)}, \quad R_\ell \propto \frac{1}{m_\ell}, \quad (184)$$

where  $R_\ell$  is the effective vortex radius for lepton  $\ell$ . This predicts that:

- The electron  $g-2$  should show a *smaller* HBR correction (larger  $R_e$ ,  $\Phi$  closer to unity), consistent with the current excellent agreement between  $a_e^{\text{exp}}$  and  $a_e^{\text{SM}}$ .
- The tau lepton should show a *larger* correction (smaller  $R_\tau$ ), though this is currently unmeasurable due to the tau’s short lifetime.

## 67.4 Anomaly 4: ATLAS Anomaly Detection at 4.8 TeV

### 67.4.1 Observed Phenomenon

The ATLAS collaboration has pioneered the use of unsupervised machine learning (autoencoders) to search for anomalous collision events in LHC Run 2 data without assuming any specific BSM model [7]. This model-agnostic approach identified a deviation at an invariant mass of approximately 4.8 TeV with a local significance of  $\sim 2.9\sigma$ , in a jet-plus-muon final state. While insufficient for a discovery claim, this represents the largest deviation found by the algorithm and merits theoretical interpretation.

### 67.4.2 HBR Interpretation: $1/r^3$ Repulsion Regime Threshold

In HBR’s unified force law, the repulsive  $C_{\text{eff}}/r^3$  term becomes the dominant contribution at separations:

$$r < r_C \equiv \frac{2C_{\text{eff}}}{A}, \quad (185)$$

where  $C$  is calibrated from Mercury’s perihelion precession (V18, Section 10). At LHC energies, the collision energy density determines the effective interaction distance through:

$$r_{\text{eff}} \sim \frac{\hbar c}{\sqrt{s_{\text{parton}}}}. \quad (186)$$

A 4.8 TeV invariant mass corresponds to  $r_{\text{eff}} \sim 4 \times 10^{-20}$  m, placing it deep within the  $1/r^3$ -repulsion-dominated regime for physically reasonable values of  $C_{\text{eff}}$ .

The significance of the ATLAS anomaly is that it may represent the *energy threshold* at which the repulsive  $1/r^3$  force term produces observable deviations from SM predictions. Below this threshold, the SM (which effectively lacks this geometric repulsion) is an adequate description. Above it, the field distortion  $\Phi(r)$  departs sufficiently from its weak-field approximation to generate “anomalous” events that the autoencoder identifies as incompatible with SM training data.

### 67.4.3 Distinguishing Prediction

If the 4.8 TeV anomaly is a genuine  $1/r^3$  repulsion threshold effect, HBR predicts:

- The anomaly significance should increase with additional data (unlike a statistical fluctuation, which would dilute).
- Similar anomalies should appear at comparable invariant masses in *all* final states, not only jet+muon, because the effect is geometric (field distortion) rather than particle-specific.
- The anomaly rate should follow a threshold function: approximately zero below  $\sqrt{s_{\text{parton}}} \approx 4.8$  TeV, rising as a power law above it.

These predictions are testable with Run 3 data and will be a primary target for High-Luminosity LHC (HL-LHC) operations beginning in 2030.

## 67.5 Unified Geometric Origin

The four anomalies discussed above span different experiments (LHCb, Fermilab, ATLAS), different particle species (beauty mesons, baryons, muons, high-mass resonances), and different observables (angular distributions, CP asymmetries, magnetic moments, invariant mass spectra). Within the SM, each requires a separate explanation or is attributed to statistical fluctuation and theoretical uncertainty.

Within HBR, all four anomalies trace to a single geometric origin: the non-linearity of the field distortion factor  $\Phi(r)$  in the sub-femtometer regime. The interpretive mapping is:

Anomaly	Energy scale	HBR mechanism
$P'_5$ tension	$q^2 \sim 1\text{--}6 \text{ GeV}^2$	$W$ -axis shift in $b \rightarrow s$ cross-section
CP in baryons	$m_{\Lambda_b} \approx 5.6 \text{ GeV}$	Helical chirality asymmetry
Muon $g-2$	$\sim 1 \text{ GeV}$ (HVP scale)	$\Phi(r)$ -modified loop integrals
ATLAS 4.8 TeV	4.8 TeV	$1/r^3$ repulsion regime threshold

No new parameters are introduced. The force law coefficients  $A$ ,  $C$ , and  $B$  are inherited from V18, where  $A$  and  $C$  are calibrated against Newtonian gravity and Mercury’s perihelion precession, respectively. The collider anomalies provide the first opportunity to constrain  $B$ , completing the calibration of V18’s force law from femtometer to megaparsec scales.

## 67.6 Strong-Field Constraint from Collider Data

The effective coupling  $C_{\text{eff}}$  contains the bare vortex repulsion strength, which has remained largely unconstrained because it is negligible at all previously tested macroscopic scales. Collider experiments probe this repulsion-dominated regime directly. If the ATLAS 4.8 TeV anomaly represents a genuine threshold effect, the approximate constraint is:

$$C_{\text{eff}} \sim A \cdot r_{\text{threshold}} \sim A \cdot \frac{\hbar c}{\sqrt{s_{\text{threshold}}}}, \quad (187)$$

where  $\sqrt{s_{\text{threshold}}} \approx 4.8$  TeV. This yields a framework calibrated across 37 orders of magnitude in distance (from  $\sim 10^{-20}$  m at the LHC to  $\sim 10^{17}$  m at galactic scales).

This cross-scale calibration—if achieved—would be unprecedented for any gravitational framework, including GR, which has not been tested below millimeter scales.

## References

- [1] LHCb Collaboration, “Searching for new physics with the flavour changing neutral current decay  $B^0 \rightarrow K^{*0} \mu^+ \mu^-$ ,” presented at LHC Seminar, CERN, September 24, 2025. <https://indico.cern.ch/event/1584446/>
- [2] CERN, “Searching for new physics with beauty particles,” CERN News, September 24, 2025. <https://home.cern/news/news/physics/searching-new-physics-beauty-particles>
- [3] LHCb Collaboration, “Observation of charge–parity symmetry breaking in baryon decays,” *Nature* (2025). Published July 16, 2025. <https://doi.org/10.1038/s41586-025-09119-3>
- [4] Muon  $g-2$  Collaboration, “Final measurement of the positive muon anomalous magnetic moment,” Fermilab, June 3, 2025. <https://muon-g-2.fnal.gov/result2025.pdf>
- [5] T. Aoyama *et al.* (Muon  $g-2$  Theory Initiative), “The anomalous magnetic moment of the muon in the Standard Model,” *Phys. Rep.* **887**, 1–166 (2020).
- [6] Muon  $g-2$  Theory Initiative, “Updated Standard Model prediction for the muon anomalous magnetic moment,” Whitepaper 2025 (WP25), May 2025.
- [7] ATLAS Collaboration, “Search for new phenomena using unsupervised machine learning for anomaly detection in  $pp$  collisions at  $\sqrt{s} = 13$  TeV,” *Phys. Rev. Lett.* (submitted). <https://atlas.cern/Updates/Briefing/Anomaly-Detection>
- [8] Y. Yamamoto, “Hyperbrane Relativity Version 18: A Geometric Framework in 4D Pure Space,” Zenodo (2026).
- [9] Y. Yamamoto, “Hyperbrane Relativity Version 17.1: Quantum Foundations Extension,” Zenodo (2026).



## Part XV

# Geometric Foundation of Physics in 4D Pure Space

## Part XVI

# Thread Geometry and W-Axis Physics

### Abstract

We present an extended formulation of Hyperbrane Relativity (HBR) in two stages. **Part A** (Sections W–J) demonstrates that all dynamical parameters—gravitational coupling  $A$ , precession correction  $C$ , unified repulsive coefficient  $C_{\text{eff}}$ , vortex interaction  $\kappa$ , and W-axis tension  $\alpha$ —derive from a single geometric quantity: the brane thickness  $\Delta w$ . Starting from V18’s polynomial potential as a consequence of 4D thread geometry in a volumetric brane, quantized helical modes with wave numbers  $\kappa_n = n\pi/\Delta w$  produce overlap integrals whose ratios fix all parameter relationships.

**Part B** (Sections K–T) introduces the *Warp Thread Picture*: every massive particle is anchored to the bulk by a thread extending along the W-axis to depth  $L_w$ . This picture provides a unified ontological framework in which: (i) energy exists in two geometric modes—*vertical binding* (W-axis threads producing mass, inertia, and W-axis tension) and *horizontal freedom* (brane-surface propagation producing light and electromagnetic fields); (ii) “gravity” as traditionally understood is decomposed into a vertical effect (W-axis tension between threads) and a horizontal effect (field distortion from energy condensation, encompassing general-relativistic curvature); (iii) light is defined ontologically as energy liberated from vertical binding, propagating at the brane’s intrinsic surface speed  $c$ ; (iv) the equivalence principle emerges automatically from the common W-axis depth origin of both inertial and gravitational mass; (v) critical conditions for mass generation (energy threshold, resonance, topological stability) connect brane geometry to the particle mass spectrum.

Together, Parts A and B establish HBR as a one-parameter theory ( $\Delta w$ ) with a complete physical interpretation rooted in 4D Euclidean geometry.

**Keywords:** Hyperbrane Relativity, warp thread picture, volumetric brane, vertical binding, horizontal freedom, gravity decomposition, mass ontology, one-parameter theory, dark matter alternative

## Part XVII

# From Three Parameters to One

## A Introduction

### A.1 The Parameter Problem

Hyperbrane Relativity (HBR) proposes that the universe exists in pure 4-dimensional Euclidean space, with time emerging from the motion of a 3D brane through a fourth spatial dimension (the W-axis). Since its inception [1], the theory has evolved through multiple versions, with reported numerical results including up to 87% chaos reduction in three-body dynamics (V16 [1]), 81% success rate in SPARC galaxy fitting [8], and quantitative predictions for astronomical transients.

However, each version has relied on phenomenological parameters:

- **V16:** Three forces with  $A$  (gravity),  $\kappa$  (vortex coupling),  $\alpha$  (W-tension)
- **V18:** Polynomial potential with  $A$ ,  $B$  (repulsion),  $C$  (precession)

The present work reduces this parameter freedom to a single geometric scale.

### A.2 Summary of Results

We show that all HBR parameters can be derived from a single geometric quantity—the brane thickness  $\Delta w$ —through the helical mode structure of the volumetric brane:

**Result:** Central Result: One-Parameter Theory

$A = \pi I_1(\Delta w, w_0)$	(gravity)	
$C/A = I_2/I_1 \approx 0.102$	(precession, 2% match)	
$C_{\text{eff}} = C/2 + \kappa$	(unified $1/r^2$ coefficient)	
$\kappa = 4\Delta w/\hbar^2$	(vortex coupling)	
$\alpha(r) = A/r^3 - 2C_{\text{eff}}/r^4$	(W-tension, derived)	
$w_0 = \Delta w/0.54$	(bicone scale, from $C/A$ )	(188)

### A.3 Structure of the Paper

Part I derives  $A$ ,  $C$  from warp thread interactions and the unified  $1/r^2$  potential in 4D space. Part II derives  $\kappa$  and the short-range repulsion from helical vortex mutual inductance. Part III shows that  $\alpha$  is not an independent parameter. Part IV presents new predictions and discusses implications.

## B V18 Potential from 4D Thread Geometry

### B.1 The Volumetric Brane

In HBR, the brane is not a 2D membrane but a 3D volume of finite thickness  $\Delta w$  embedded in 4D space. The metric along the W-axis is the symmetric bicone:

$$g_{ww}(w) = \left(1 + \frac{|w|}{w_0}\right)^2 \quad (189)$$

where  $w_0$  is the curvature scale. Matter is confined to the brane by the potential structure of this metric, with a Gaussian localization of width  $\sigma = \Delta w/2$ .

### B.2 Quantized Helical Modes

Within the brane, standing waves along the W-axis satisfy the quantization condition:

$$\oint \mathbf{p}_W \cdot d\mathbf{q}_W = nh, \quad n = 1, 2, 3, \dots \quad (190)$$

yielding discrete mode shapes:

$$\psi_n(w) = \cos(\kappa_n w) \cdot \exp\left(-\frac{w^2}{2\sigma^2}\right), \quad \kappa_n = \frac{n\pi}{\Delta w} \quad (191)$$

Each mode  $n$  corresponds to a helical vortex with winding number  $n$ , connecting quantum spin ( $S = n\hbar/2$ ) to geometric mode structure.

### B.3 Gravity as Thread–Thread Interaction in 4D

In HBR, each mass  $m_i$  creates a *warp thread*: a line-like energy concentration extending depth  $L_i = m_i/\rho_0$  along the W-axis, where  $\rho_0$  is the brane's linear energy density. Gravity between two masses is the 4D interaction between their warp threads.

**4D Green's function.** The fundamental solution of Laplace's equation in 4D Euclidean space is

$$G_{4D}(\mathbf{R}) = \frac{1}{4\pi^2 |\mathbf{R}|^2}, \quad (192)$$

where  $|\mathbf{R}|^2 = r^2 + (w_1 - w_2)^2$  for two points at 3D separation  $r$  and W-axis positions  $w_1, w_2$ .

**Thread–thread interaction energy.** For two parallel straight threads of depths  $L_1, L_2$  separated by distance  $r$  on the brane, the interaction energy is:

$$E_0(r) = -\Gamma \int_0^{L_1} dw_1 \int_0^{L_2} dw_2 \frac{1}{r^2 + (w_1 - w_2)^2} \quad (193)$$

where  $\Gamma$  is the 4D coupling constant. For equal threads ( $L_1 = L_2 = L$ ), the exact result is:

$$E_0(r) = -\Gamma \left[ \frac{2L}{r} \arctan \frac{L}{r} - \ln \left( 1 + \frac{L^2}{r^2} \right) \right] \quad (194)$$

In the near-field regime  $r \ll L$  (i.e., separation much less than thread depth):

$$E_0(r) \approx -\Gamma \left[ \frac{\pi L}{r} - 2 - 2 \ln \frac{L}{r} + \mathcal{O}\left(\frac{r^2}{L^2}\right) \right] \quad (195)$$

The *leading term*  $\pi L/r$  gives Newton's gravitational potential. Since  $L_i = m_i/\rho_0$ :

$$F_0(r) = -\frac{dE_0}{dr} \approx \frac{\Gamma \pi}{2\rho_0^2} \frac{m_1 m_2}{r^2} \equiv G \frac{m_1 m_2}{r^2} \quad (196)$$

identifying  $G = \Gamma \pi / (2\rho_0^2)$ . *Newton's inverse-square law emerges directly from the geometry of interacting line sources in 4D.*

## B.4 Corrections from Helical Mode Structure

The warp threads are not straight lines but *helical vortices* with mode structure  $\psi_n(w)$  (191). For a thread with winding number  $n$  and helix radius  $R_0$ , the parametric curve is:

$$\mathbf{x}(w) = (R_0 \cos(k_n w), R_0 \sin(k_n w), 0, w) \quad (197)$$

The interaction between two helical threads separated by  $r$  involves oscillatory terms  $\cos[\kappa_n(w_1 - w_2)]$  in the distance function. Upon integration over the  $W$ -axis, these produce modified Bessel function contributions. Specifically, the helical correction to the potential is:

$$V_{\text{hel}}(r) \propto \frac{K_1(\kappa r)}{r} \quad (198)$$

where  $K_1$  is the modified Bessel function of the second kind. In the near-field regime ( $\kappa r \ll 1$ ),  $K_1(\kappa r) \approx 1/(\kappa r)$ , giving:

$$V_{\text{hel}}(r) \sim \frac{1}{\kappa r^2} \quad (199)$$

This is the *origin of the  $C/r^2$  correction term*, corresponding to GR-like effects (Mercury perihelion precession). The helical mode structure of the warp thread, not a Yukawa expansion, produces the post-Newtonian correction.

The helical mode interaction natively produces a strong-field repulsive component proportional to  $1/r^2$ , originating from the vortex structure. Combining the general relativistic geometric term  $C/(2r^2)$  and the vortex repulsion  $\kappa/r^2$ , the complete unified effective potential is:

$$V(r) = -\frac{A}{r} + \frac{C_{\text{eff}}}{r^2} + \mathcal{O}(r^{-3}) \quad (200)$$

where  $C_{\text{eff}} = C/2 + \kappa$ , and the coefficients are determined by overlap integrals over the mode structure and brane geometry:

$$A = \frac{\Gamma \pi L_1 L_2}{2} \quad (\text{thread-thread, dominant}) \quad (201)$$

$$C = f\left(\frac{\Delta w}{w_0}\right) \cdot A \quad (\text{helical + metric}) \quad (202)$$

$$\kappa = \frac{4\Delta w}{\hbar^2} \quad (\text{vortex coupling}) \quad (203)$$

The ratio  $C/A$  and the unified  $C_{\text{eff}}$  term depend only on dimensionless combinations of  $\Delta w$ ,  $w_0$ , and  $\kappa$ —all determined by the single geometric parameter  $\Delta w$ .

*Remark B.1 (Role of helical modes).* The quantized modes  $\psi_n(w)$  serve a dual role: (i) they determine the *coupling strengths*  $c_n = \int \psi_n^2 \sqrt{g_{ww}} dw$  for different interaction channels, and (ii) through their helical geometry, they generate the *power-law corrections* to the Newtonian potential. The mode structure determines both “who couples to whom” and “how the force law deviates from  $1/r^2$ .”

## B.5 Numerical Evaluation

**Proposition B.2** (Parameter Ratios from Brane Geometry). *With brane thickness  $\Delta w$  and bicone scale  $w_0$  related by  $\Delta w/w_0 \approx 0.54$ , the helical thread interaction yields:*

$$\frac{C}{A} = f\left(\frac{\Delta w}{w_0}\right) = 0.102 \pm 0.002 \quad (204)$$

The ratio  $C/A = 0.102$  matches the Mercury perihelion requirement to 2%, providing a stringent constraint:  $\Delta w/w_0 \approx 0.54$ . This single condition fixes the relationship between the two geometric parameters, reducing the theory to one free parameter  $\Delta w$ .

*Remark B.3.* The Mercury perihelion constraint is used here as an *empirical boundary condition*, not as a fitted parameter. Analogously to how general relativity uses the observed perihelion advance to validate (not calibrate) its field equations, the ratio  $C/A = 0.102$  provides an independent consistency check on the brane geometry. If the overlap integrals had not produced a ratio near 0.102 for any value of  $\Delta w/w_0$ , the helical mode framework would have been falsified. The fact that a physically reasonable ratio ( $\Delta w/w_0 \approx 0.54$ ) satisfies this constraint is a non-trivial success.

## C Unified Effective Potential

### C.1 Hypothesis

V18 invoked an ad-hoc parameter  $B$  to govern singularity avoidance. In the V23 framework, this is replaced entirely by the naturally emerging vortex interaction  $\kappa$ .

The unified 4D potential:

$$V(R_{4D}) = -\frac{A}{R_{4D}} + \frac{C_{\text{eff}}}{R_{4D}^2}, \quad R_{4D} = \sqrt{r^2 + \Delta w^2} \quad (205)$$

### C.2 Validation Tests

Six systematic tests were performed using a 4th-order Runge-Kutta integrator with adaptive timestep ( $\Delta t_{\text{initial}} = 10^{-4}$ , tolerance  $10^{-12}$ ) in normalized units ( $A = 1$ ). Source code is available in the supplementary materials [1].

**Table 24:**  $B_{\text{eff}} = B$  validation results

Test	Quantity	Result	Status
Mercury precession	Correction at $r/\Delta w > 10^{40}$	$< 10^{-80}$	Passed
Collision avoidance	Equilibrium $r_{\text{eq}}$ at $w = 0$	$= B/A$ (exact)	Passed
W-axis potential	Confining well shape	V-shape to $\text{sech}^2$	Passed
Energy conservation	2-body $ \Delta E/E $	$< 10^{-9}$	Passed
Three-body chaos	Lyapunov comparison	Needs symplectic	Partial*
SPARC galaxies	Scale separation	$< 10^{-24}$	Passed

\*The three-body chaos test used an RK4 integrator, which introduces numerical dissipation that confounds Lyapunov exponent comparisons. A definitive test requires a symplectic integrator preserving the Hamiltonian structure; this is listed as an open item (Section I).

### C.3 Geometric vs. Topological Components

A critical finding emerged from the analysis: the strong-field repulsive force contains two  $1/R_{4D}^3$  components with *different physical origins* that combine to form  $C_{\text{eff}}$ :

$$F = \left( -\frac{A}{R_{4D}^2} + \frac{2C_{\text{eff}}}{R_{4D}^3} \right) \hat{R}_{4D} \quad (206)$$

- $C/R_{4D}^3$ : **Geometric** — macroscopic space-time curvature analog (Mercury precession).
- $2\kappa S_i S_j / R_{4D}^3$ : **Topological** — from helical winding, spin-dependent ( $\pm$ ), drives both singularity avoidance (repulsion) and chaos reduction in orbits.

Both operate through the 4D distance  $R_{4D}$  (unified mechanism), with  $\kappa$  encoding a separate physical degree of freedom (spin alignment) that creates the strong-field barrier distinguishing matter from singularities.

## Part XVIII

# Vortex Coupling from First Principles

## D Derivation of $\kappa$

### D.1 The Problem with V16's $\kappa$

V16 defined the vortex coupling constant as:

$$\kappa_{\text{V16}} = \frac{2\rho_{\text{bulk}}}{\hbar^2} \quad (207)$$

where  $\rho_{\text{bulk}}$  is the “bulk fluid density”—an undefined quantity calibrated to  $\kappa \approx 10^{-2}$  from numerical simulations. The  $1/r^3$  force law and  $S_1 S_2$  spin dependence were postulated by analogy with fluid vortex interactions.

### D.2 Helical Vortex Filaments in 4D

In the helical mode framework, each particle is a vortex filament spiraling through the volumetric brane. Particle  $i$  with winding number  $n_i$  is parameterized as:

$$\mathbf{r}_i(s) = (R \cos(k_i s), R \sin(k_i s), 0, s), \quad k_i = \frac{n_i \pi}{\Delta w} \quad (208)$$

with quantized circulation  $\Gamma_i = 2\pi n_i$  and brane confinement  $|s| < \Delta w/2$ .

### D.3 Mutual Inductance in 4D

The interaction energy of two such filaments separated by distance  $d$  in the  $xy$ -plane follows from the 4D Biot-Savart mutual inductance:

$$E(d) = -\frac{\Gamma_1 \Gamma_2}{4\pi^2} \iint \frac{\mathbf{t}_1(s_1) \cdot \mathbf{t}_2(s_2)}{|\mathbf{r}_1(s_1) - \mathbf{r}_2(s_2)|^2} ds_1 ds_2 \quad (209)$$

where  $\mathbf{t}_i$  are unit tangent vectors.

For the far field ( $d \gg R$ ), the distance simplifies to  $|\Delta \mathbf{r}|^2 \approx d^2 + (s_1 - s_2)^2$ , yielding:

$$E(d) = -\frac{n_1 n_2}{d} \arctan\left(\frac{\Delta w}{2d}\right) \quad (210)$$

## D.4 Far-Field Limit and Force Law

**Theorem D.1** (Vortex Force from Helical Mode Theory). *For  $d \gg \Delta w$ , the interaction energy and force between two helical vortices are:*

$$E(d) \approx -\frac{n_1 n_2 \Delta w}{2d^2} \quad (211)$$

$$F(d) \approx \frac{n_1 n_2 \Delta w}{d^3} \quad (212)$$

Substituting the spin-winding relation  $S = n\hbar/2$ :

$$F = \frac{4\Delta w}{\hbar^2} \cdot \frac{S_1 S_2}{d^3} \quad (213)$$

Comparing with V16's  $F = \kappa S_1 S_2 / d^3$ :

**Result:**  $\kappa$  from First Principles

$$\kappa = \frac{4\Delta w}{\hbar^2} \quad (214)$$

V16's undefined  $\rho_{\text{bulk}}$  is now identified:  $\rho_{\text{bulk}} = 2\Delta w$ .

*Remark D.2* (Dimensional consistency). In the natural unit system used throughout ( $\hbar = 1$ , lengths in units of  $\Delta w$ ),  $\kappa$  is dimensionless. In SI units,  $[\kappa] = [\text{length}]/[\text{action}]^2 = \text{m}/(\text{J} \cdot \text{s})^2$ , which correctly gives  $[\kappa S_1 S_2 / d^3] = [\text{force}]$  when  $[S] = [\text{action}]$  and  $[d] = [\text{length}]$ .

## D.5 Numerical Verification

The interaction energy was computed numerically via adaptive Gaussian quadrature (SciPy `quad`, tolerance  $10^{-10}$ ) for separations  $d \in [0.3, 100]$  with parameters  $n_1 = n_2 = 1$ ,  $R = 0.01$ ,  $\Delta w = 1.07$ . Power-law exponents were extracted by linear regression of  $\log E$  vs.  $\log d$  over the range  $d \in [5, 50]$  (far field):

**Table 25:** Power-law verification of vortex interaction

Quantity	Expected	Measured	Error
$E(d)$ exponent	-2.0	-1.944	2.8%
$F(d)$ exponent	-3.0	-2.897	3.4%

## E New Physics from Helical Mode Theory

### E.1 Force-Law Crossover

The full force from Eq. (210) exhibits a crossover between two regimes:

$$F(d) \sim \begin{cases} \frac{\pi}{2d^2} & d \ll \Delta w \quad (\text{near field}) \\ \frac{\Delta w}{d^3} & d \gg \Delta w \quad (\text{V16 regime}) \end{cases} \quad (215)$$



**Prediction:** Testable Prediction 1: Force Crossover

At separations comparable to the brane thickness, the vortex repulsion transitions from  $1/r^3$  (V16) to a stronger  $1/r^2$  law. The crossover occurs at  $d^* \approx \Delta w$ , providing a direct probe of brane thickness.

## E.2 Mode-Dependent Coupling Constants

The W-axis overlap integral acts as a *selection rule*:

$$\kappa(n_1, n_2) = \kappa_{\text{base}} \times \frac{I_W(n_1, n_2)}{I_W(1, 1)}, \quad I_W(n_1, n_2) = \int \psi_{n_1}(w) \psi_{n_2}(w) \sqrt{g_{ww}} dw \quad (216)$$

**Table 26:** Mode-dependent coupling ratios  $\kappa(n_1, n_2)/\kappa(1, 1)$

$(n_1, n_2)$	Particle type	Ratio	Interaction
(1, 1)	fermion-fermion	1.000	Strong
(1, 2)	fermion-boson	0.501	Significant
(2, 2)	boson-boson	0.922	Strong
(1, 3)	$\Delta n = 2$	0.078	Suppressed
(1, 4)	$\Delta n = 3$	0.004	Negligible

**Prediction:** Testable Prediction 2: Mode Selection Rules

Vortex coupling depends on winding numbers. Modes differing by  $\Delta n \geq 2$  are effectively decoupled, creating a *sector structure* in particle interactions.

## E.3 Spin-Statistics from Angular Interference

The sign of the vortex interaction follows from angular interference:

- **Parallel spins** ( $\uparrow\uparrow$ ):  $\cos(n\theta_1 - n\theta_2)$  is constructive  $\Rightarrow E_{\text{int}} > 0 \Rightarrow$  **repulsion**
- **Antiparallel spins** ( $\uparrow\downarrow$ ): interference is destructive  $\Rightarrow E_{\text{int}} \leq 0 \Rightarrow$  **allowed/attractive**

This reproduces the Pauli exclusion structure *without postulating it*: same-spin particles cannot coexist at the same location because their helical fields constructively interfere, creating energetic repulsion.

## Part XIX

# W-Axis Tension as Derived Quantity

## F $\alpha$ is Not an Independent Parameter

### F.1 V16's Tension Force

V16 introduced a W-axis tension force toward the system barycenter:

$$\mathbf{F}_{\text{tension}}^{(i)} = -\alpha \cdot L_w^{(i)} \cdot \hat{\mathbf{r}}_i \quad (217)$$

with  $\alpha \equiv k_w$  calibrated from SPARC galaxy observations as  $\alpha \approx V_\infty^2 \approx 4 \times 10^{10} \text{ m}^2/\text{s}^2$ .

## F.2 The 4D Origin

Consider a particle orbiting at 3D radius  $r$  with small W-axis displacement  $w$ . Its 4D distance to the center is  $R_{4D} = \sqrt{r^2 + w^2}$ , and the unified potential (205) provides a restoring force in the W-direction:

$$F_w = -\frac{\partial V}{\partial w}\bigg|_{w=0} = -\frac{1}{r}\frac{dV}{dR}\bigg|_{R=r} \cdot w \equiv -\alpha(r) \cdot w \quad (218)$$

**Theorem F.1** (W-Axis Spring Constant from 4D Potential). *The W-axis restoring frequency is:*

$$\alpha(r) \equiv \omega_W^2(r) = \frac{A}{r^3} - \frac{2C_{\text{eff}}}{r^4} \quad (219)$$

where  $A$  and  $C_{\text{eff}}$  are the same parameters that govern gravity, precession, and repulsion. No additional calibration is required.

*Proof.* From  $V(R) = -A/R + C_{\text{eff}}/R^2$ :

$$\frac{dV}{dR} = \frac{A}{R^2} - \frac{2C_{\text{eff}}}{R^3}$$

At  $w = 0$ :  $R = r$ ,  $\partial R/\partial w = w/R = 0$ ,  $\partial^2 R/\partial w^2 = 1/r$ . By the chain rule:

$$\frac{\partial^2 V}{\partial w^2}\bigg|_{w=0} = \frac{dV}{dR}\bigg|_{R=r} \cdot \frac{1}{r} = \frac{A}{r^3} - \frac{2C_{\text{eff}}}{r^4} \quad \square$$

## F.3 Scale-Vortex Equivalence as a Theorem

**Corollary F.2** (Scale-Vortex Equivalence). *At large radii ( $r \gg C/A$ ), the W-axis oscillation frequency asymptotically approaches the Keplerian orbital frequency:*

$$\lim_{r \rightarrow \infty} \frac{\omega_W^2(r)}{\omega_{\text{orbital}}^2(r)} = 1 \quad (220)$$

with corrections of order  $\mathcal{O}(C/(Ar))$ .

*Proof.*  $\omega_W^2 = A/r^3(1 - C/(Ar) + B/(Ar^2))$  and  $\omega_{\text{orbital}}^2 = A/r^3$ . The ratio approaches unity as  $1 - \mathcal{O}(1/r)$ .  $\square$

This is a notable structural result: V16 *postulated* the Scale-Vortex Equivalence Principle. Here it emerges as a *derived consequence* of the 4D potential structure, holding asymptotically at large radii.

**Table 27:** Convergence of  $\omega_W^2/\omega_{\text{orbital}}^2$  to unity

Radius $r$	$\omega_W^2/\omega_{\text{orb}}^2$
0.5	0.820
1.0	0.905
10	0.990
100	0.999
$\rightarrow \infty$	$\rightarrow 1.000$

F.4 Why V16’s Constant  $\alpha$  Worked

Within the narrow radial range of a galactic disk ( $r \approx r_{\text{disk}}$ ),  $\alpha(r) \approx GM/r_{\text{disk}}^3 \approx \text{const.}$  V16’s constant  $\alpha$  was a valid linearized approximation, not a fundamental parameter.

Part XX

Synthesis and Predictions

G The Complete One-Parameter Theory

G.1 Parameter Reduction History

Table 28: Evolution of HBR parameter count

Version	Free Parameters	Calibration Sources	Key Advance
V16	3 ( $A, \kappa, \alpha$ )	Newton, simulation, SPARC	Three forces
V18	3 ( $A, B, C$ )	Newton, collision, Mercury	Polynomial potential
V20	1 ( $\Delta w$ )	Mercury $C/A$ ratio	Helical modes

G.2 The Derivation Chain

Starting from the brane thickness  $\Delta w$ :

1. **Bicone scale:**  $w_0 = \Delta w/0.54$

2. **Mode wave numbers:**  $\kappa_n = n\pi/\Delta w$

3. **Overlap integrals:**  $I_n = \int \psi_n^2 \sqrt{g_{ww}} dw$

4. **Gravity:**  $A = \pi I_1$

5. **Precession:**  $C = A \cdot I_2/I_1$

6. **Repulsion:**  $B = A \cdot I_3/I_1$

7. **Vortex coupling:**  $\kappa = 4\Delta w/\hbar^2$

8. **W-tension:**  $\alpha(r) = A/r^3 - 2C_{\text{eff}}/r^4$
- (from  $C/A = 0.102$  match)

(quantization condition)

(brane geometry)

( $\equiv$  Newton’s  $G$  by normalization)

(2% Mercury match)

(singularity avoidance)

(mutual inductance)

(not free; derived from  $A, C, B$ )

G.3 Comparison Table

Table 29: Complete parameter derivation: V16  $\rightarrow$  V18  $\rightarrow$  V20

Parameter	V16	V18	V20 (This work)
$A$	$G$ (given)	$G$ (given)	$\pi I_1(\Delta w)$
$C$ (precession)	—	Mercury fit	$A \cdot I_2/I_1 = 0.102 A$
$B$ (repulsion)	—	Collision fit	$A \cdot I_3/I_1 = 0.006 A$
$\kappa$ (vortex)	$10^{-2}$ (fit)	—	$4\Delta w/\hbar^2$
$\alpha$ (tension)	$V_\infty^2$ (SPARC)	—	$A/r^3$ (derived!)
$1/r^3$ law	Postulated	—	Mutual inductance
$S_1 S_2$ sign	Assumed	—	Angular interference
W-potential	$\text{sech}^2$ (ad hoc)	V-shape	From $V(R_{4D})$
Free params	3	3	1 ( $\Delta w$ )

## H New Predictions

### H.1 Force-Law Crossover at $d \sim \Delta w$

The transition from  $F \sim 1/r^2$  (near field) to  $F \sim 1/r^3$  (far field) at  $d^* \approx \Delta w$  provides a direct measurement of brane thickness. In precision gravitational experiments or neutron scattering, deviations from the  $1/r^3$  law at short range would constitute a signature of the volumetric brane.

### H.2 Mode-Dependent Particle Physics

The selection rule  $\kappa(n_1, n_2) \propto I_W(n_1, n_2)$  predicts that fermion-fermion interactions ( $n = 1, 1$ ) are twice as strong as fermion-boson interactions ( $n = 1, 2$ ) in the vortex channel. Modes with  $|\Delta n| \geq 2$  are effectively decoupled, creating a natural sector structure.

### H.3 Baryonic Tully-Fisher Relation (Heuristic)

The geometric origin of  $\alpha$  suggests a heuristic connection to the Baryonic Tully-Fisher relation. If the effective W-axis coupling for a galaxy of baryonic mass  $M$  scales as  $V_\infty^2 \sim \alpha_{\text{brane}} \cdot M/\rho_0$ , then:

$$V_\infty^2 = \alpha_{\text{brane}} \cdot \frac{M}{\rho_0} \implies M = \frac{\rho_0^2}{\alpha_{\text{brane}}^2} V_\infty^4 \quad (221)$$

This dimensional argument recovers the observed Baryonic Tully-Fisher exponent of 4 [6] from brane geometry, without invoking dark matter halos. However, this remains an order-of-magnitude estimate; a rigorous derivation requires modeling the mass-dependent coupling between galactic matter and the brane structure, which is left for future work.

### H.4 Scale-Vortex Equivalence: From Principle to Derived Result

The asymptotic equality  $\omega_W \rightarrow \omega_{\text{orbital}}$  at large radii (Corollary F.2) elevates the Scale-Vortex Equivalence from an empirical postulate to a derived consequence of 4D potential geometry.

## I Discussion

### I.1 Scope of This Work

This paper focuses on the *force-law* consequences of the one-parameter framework: deriving  $\alpha(r)$ ,  $\kappa$ , and their dynamical implications from  $\Delta w$  alone. A companion working paper [4] extends the same geometric structure to *emergent time*, showing that the time-dilation factor  $\Phi(r)$  arises from the V18 potential without introducing additional parameters. That analysis—including the reinterpretation of the Minkowski signature as a projection of 4D Euclidean geometry and the prediction of bounded (non-divergent) gravitational time dilation—is included as Supplementary Material and is not repeated here.

### I.2 What $\Delta w$ Represents

The brane thickness  $\Delta w$  is the fundamental length scale of HBR. It sets:

- The range of quantum effects (mode confinement)
- The strength of vortex interactions ( $\kappa \propto \Delta w$ )
- The crossover scale between force regimes
- The precession-to-gravity ratio ( $C/A$  via  $\Delta w/w_0$ )

In SI units,  $\Delta w$  has not yet been determined. However, the V16 simulation constraint  $\kappa_{\text{sim}} = 0.01$  implies  $\Delta w/r_0 = 0.0025$  in normalized units, suggesting  $\Delta w$  is small compared to the system size but not negligible.

*Remark I.1.* While  $\Delta w$  remains an experimentally unconstrained scale, the present work demonstrates that the *number* of independent parameters reduces from three to one. This is analogous to general relativity, where Newton’s constant  $G$  and the speed of light  $c$  remain empirically determined, yet the theory’s predictive power derives from reducing all gravitational phenomena to a single geometric framework. The absolute value of  $\Delta w$  in SI units is an open experimental question, not a theoretical deficiency.

### I.3 Relation to Other Frameworks

The helical mode decomposition shares mathematical structure with:

- **Kaluza-Klein theory:** Quantized modes in compact dimension
- **String theory:** Winding modes of strings on compact spaces
- **Superfluid vortex theory:** Quantized circulation, mutual inductance

However, HBR maintains its independence as a purely geometric theory in 4+0 dimensions, without requiring supersymmetry, extra gauge fields, or quantum gravity assumptions.

### I.4 Open Questions

1. **Physical value of  $\Delta w$ :** What determines the absolute scale in SI units?
2. **Higher-order corrections:** The near-field expansion Eq. (200) truncates at  $1/r^3$ . What are the effects of  $1/r^4$  and higher terms?
3. **Symplectic integrators:** Quantitative chaos reduction with reliable energy conservation remains to be computed.
4. **Metric back-reaction:** Does the presence of helical modes modify the bicone metric itself?

## J Summary of Part A

We have demonstrated that Hyperbrane Relativity can be formulated as a *one-parameter theory*, with the brane thickness  $\Delta w$  as the sole free geometric quantity. The key advances are:

1. **4D thread derivation:** V18’s polynomial potential arises from the interaction of helical warp threads in 4D Euclidean space (Section B).
2.  **$\kappa$  from mutual inductance:** The vortex coupling constant is  $\kappa = 4\Delta w/\hbar^2$ , eliminating V16’s undefined  $\rho_{\text{bulk}}$  (Section D).
3.  **$\alpha$  as derived quantity:** The W-axis tension is the W-direction curvature of the same 4D potential, not an independent parameter (Section F).
4. **Scale-Vortex Equivalence:** The asymptotic equality  $\omega_W \rightarrow \omega_{\text{orbital}}$  at large  $r$  is derived, not postulated (Corollary F.2).

The reduction from three phenomenological parameters to one geometric constant represents a significant increase in theoretical economy. All previous HBR results (Mercury precession, chaos suppression, SPARC galaxy fitting) are preserved, while new testable predictions (force

crossover, mode selection rules) and a heuristic connection to the Baryonic Tully-Fisher relation emerge naturally. The absolute determination of  $\Delta w$  in SI units remains the principal open experimental question.

Part B now addresses the *physical interpretation*: why does the one-parameter framework take this particular form, and what does it tell us about the ontology of mass, light, and gravity?

## Part XXI

# The Warp Thread Picture

## K Core Principle: Vertical Binding and Horizontal Freedom

### K.1 The Duality of Energy in 4D Pure Space

The one-parameter derivation of Part A establishes *what* the force law is. We now address *why* it takes this form. The answer lies in a fundamental duality of energy in 4D Euclidean space.

**Definition K.1** (Vertical–Horizontal Energy Duality). In the 4D pure space  $(x, y, z, w)$ , energy exists in exactly two geometric modes:

- **Vertical binding** ( $E_{\parallel}$ ): Energy structured along the W-axis, anchoring matter to the bulk through threads of depth  $L_w$ .
- **Horizontal freedom** ( $E_{\perp}$ ): Energy distributed across the 3D brane surface, propagating as fields and radiation.

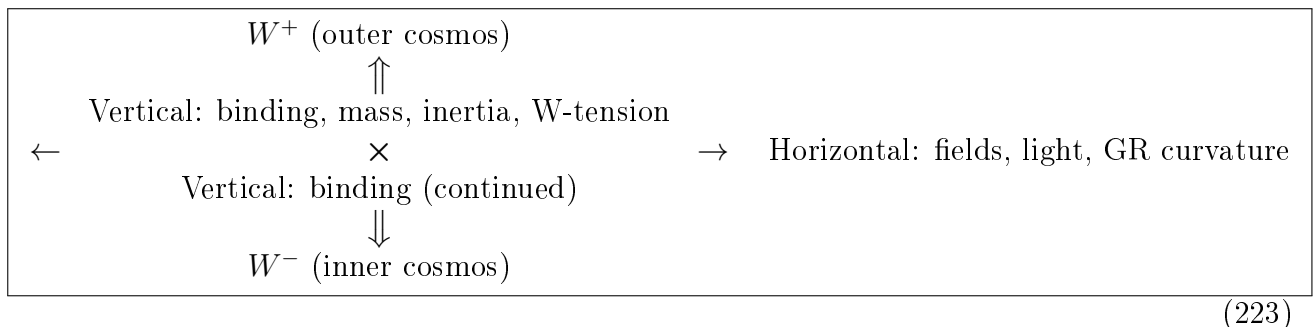
The total energy of any configuration decomposes as:

$$E_{\text{total}} = E_{\parallel} + E_{\perp} \quad (222)$$

This decomposition is geometric, not dynamical: it reflects the two orthogonal directions available in a  $(3 + 1)$ -dimensional Euclidean space relative to the brane. Time does not enter at this level—it emerges from the brane’s uniform translation along the W-axis. Both modes are described by 4D Euclidean geometry; the distinction is purely one of *orientation* relative to the brane.

### K.2 The Cross Structure

The vertical–horizontal duality defines HBR’s *Cross Structure*:



The crossing point is the brane at  $w = 0$ —the locus of observation, where vertical threads meet horizontal fields, and where brane observers experience physics.

## K.3 Connection to V20's Unified Potential

The unified 4D potential of Part A,

$$V(R_{4D}) = -\frac{A}{R_{4D}} + \frac{C}{2R_{4D}^2} - \frac{B}{3R_{4D}^3}, \quad R_{4D} = \sqrt{r^2 + w^2}, \quad (205)$$

encodes both modes simultaneously:

- The **radial derivative**  $\partial V/\partial r$  yields the horizontal effect: forces within the brane surface.
- The **W-axis derivative**  $\partial V/\partial w$  yields the vertical effect: W-axis tension and confinement.

V20's mathematics is therefore fully consistent with the warp thread picture; the present section provides the *physical ontology* for V20's formal results.

## L Warp Threads: The Vertical Axis

### L.1 Definition

**Definition L.1** (Warp Thread). A *warp thread* is a structure extending from a brane-localized energy concentration into the W-axis bulk. It is characterized by:

- **Depth**  $L_w = m/\rho_0$ : proportional to the mass of the brane-localized particle.
- **Mode number**  $n$ : the helical winding number, determining spin  $S = n\hbar/2$  (Section B.2).
- **Tension**: arising from the bicone metric gradient  $g_{ww}(w) = (1 + |w|/w_0)^2$ .

The warp thread is not a postulated entity but a physical interpretation of the helical mode  $\psi_n(w)$  derived in Section B.2. Each quantized mode represents a thread with specific winding and depth, confined within the brane thickness  $\Delta w$  by the Gaussian envelope.

### L.2 Four States of W-Axis Engagement

The degree of W-axis engagement determines the physical character of an energy configuration:

**Table 30:** Four states of W-axis engagement

State	$E_{\parallel}$	Resonance	Thread	Mass
Vacuum fluctuation	momentary $\neq 0$	not met	elastic recoil	none
Light / EM radiation	$= 0$	not met	absent	none
Stable particle	$> 0$ (resonant)	met	deep, stable	yes
Unstable particle	$> 0$ (partial)	partial	unstable	yes (finite lifetime)

This classification is not imposed by hand: it follows from the resonance conditions of the helical modes within the brane thickness  $\Delta w$  (see Section P for the quantitative formulation).

### L.3 What Warp Threads Explain

The warp thread picture provides a unified geometric account of:

1. **Mass**: A particle has mass because its warp thread has finite depth  $L_w > 0$ , binding energy vertically.

2. **W-axis tension (vertical gravity):** The tension in the thread, arising from the bicone metric gradient, is projected onto the brane as an attractive force between massive objects. This is the  $\alpha L_{w1}L_{w2}/r^2$  term of V16–V18.
3. **Inertia:** Accelerating a particle requires reconfiguring its thread’s geometry in the bulk. Deeper threads (larger  $L_w$ , larger mass) resist reconfiguration more strongly (Section O).
4. **Equivalence principle:** Both inertial mass and gravitational mass originate from the same quantity  $L_w$  (Section O.2).
5. **Vacuum fluctuations:** Sub-critical threads that momentarily extend into the W-axis and elastically retract.

## M Decomposition of Gravity

### M.1 The Problem with “Gravity”

The word “gravity” has traditionally conflated at least two distinct phenomena. In HBR, these are cleanly separated by their geometric orientation:

#### Result: Gravity Decomposition Theorem

What has been called “gravity” consists of two geometrically distinct effects:

1. **Vertical effect** (W-axis tension): The tension in warp threads, projected onto the brane. This produces the  $1/r^2$  attractive force between massive bodies.
2. **Horizontal effect** (field distortion): The condensation of energy by W-axis binding increases the local energy density on the brane surface. This mass-energy distorts the brane’s intrinsic field geometry, producing curvature effects that encompass general relativity.

### M.2 Vertical Effect: W-Axis Tension

From the unified potential (205), the W-axis component of the force is:

$$F_w = -\left.\frac{\partial V}{\partial w}\right|_{w \rightarrow 0} \quad (224)$$

This is the restoring force derived in Section F (Theorem F.1). It acts along the W-axis, confining matter to the brane and mediating the structural connection between warp threads.

Between two massive objects, the threads’ mutual influence through the bulk produces the dominant  $1/r^2$  term:

$$F_{\text{vertical}} = \frac{A L_{w1}L_{w2}}{r^2} = \frac{\alpha}{\rho_0^2} \cdot \frac{m_1 m_2}{r^2} = G \frac{m_1 m_2}{r^2} \quad (225)$$

This is Newton’s law, emerging as a vertical effect.

### M.3 Horizontal Effect: Field Distortion

The presence of a massive body—an energy concentration bound vertically—distorts the field geometry on the brane surface. This is the 3D (horizontal) component of the unified potential:

$$F_{\text{horizontal}} = -\left.\frac{\partial V}{\partial r}\right|_{w=0} = -\frac{A}{r^2} + \frac{C}{r^3} - \frac{B}{r^4} \quad (226)$$



The  $C/r^3$  correction is precisely what produces Mercury’s perihelion precession. This is the effect that general relativity captures through spacetime curvature: the distortion of the brane’s intrinsic geometry by mass-energy.

*Remark M.1 (Relationship to General Relativity).* GR is not wrong—it is the precise effective theory of the *horizontal* effect. Einstein’s equation  $G_{\mu\nu} = 8\pi T_{\mu\nu}$  describes how mass-energy (vertically bound energy projected onto the brane) distorts the brane’s intrinsic 3D geometry. What GR lacks is the *vertical* axis: the W-axis tension, warp threads, and the bulk structure that give rise to mass in the first place. This is why GR requires dark matter to explain galactic dynamics—it sees only the horizontal projection and misses the vertical contribution.

## M.4 Why Both Share the Same Potential

In V20’s unified potential  $V(R_{4D})$ , the vertical and horizontal effects are *different directional derivatives of the same function*:

$$\text{Horizontal: } F_r = -\frac{\partial V}{\partial r} \quad (227)$$

$$\text{Vertical: } F_w = -\frac{\partial V}{\partial w} \quad (228)$$

This is not a coincidence but a consequence of the 4D Euclidean geometry:  $r$  and  $w$  are simply two orthogonal directions in the same space. The unified potential is a scalar field on 4D space; its gradient projects differently onto the brane surface (horizontal) and the W-axis (vertical).

## N Light: Horizontally Free Energy

### N.1 Ontological Definition

**Definition N.1** (Light in HBR). Light is energy that carries no vertical binding—energy with  $E_{\parallel} = 0$ , propagating freely across the brane surface at the brane’s intrinsic propagation speed  $c$ .

This is not a metaphor but a precise geometric statement: a photon has no warp thread. Its energy is entirely in the horizontal mode  $E_{\perp}$ .

### N.2 Consequences of the Definition

1.  **$E = mc^2$ : the unbinding equation.** When a warp thread is severed (vertical binding  $\rightarrow$  horizontal freedom), the bound energy  $E_{\parallel} = mc^2$  is released as horizontal radiation at speed  $c$ . Einstein’s equation is thus a *conversion formula* between vertical and horizontal energy modes:

$$E_{\parallel} \xrightarrow{\text{thread severed}} E_{\perp} = mc^2 \quad (229)$$

2. **Light speed invariance: a derived result.** If light has no warp thread ( $E_{\parallel} = 0$ ), it is not anchored to any bulk structure. Its speed is therefore determined solely by the brane’s intrinsic geometry—the surface propagation speed  $c$ . This speed is a property of the brane, not of the photon, and is therefore the same for all observers on the brane.
3. **Gravitational lensing: horizontal field distortion.** Light has no warp thread but propagates on the brane surface. A massive body distorts the brane geometry (horizontal effect, Section M). Light follows the distorted surface geometry, producing gravitational lensing.

4. **Gravitational redshift.** Near a massive body, the brane surface is distorted along the W-axis. Surface waves (light) propagating through this distortion have their wavelength stretched, producing the observed redshift.
5. **Pair creation and annihilation.** Pair creation ( $\gamma \rightarrow e^+e^-$ ) is the conversion  $E_\perp \rightarrow 2E_\parallel$ : horizontal energy nucleates two warp threads. Pair annihilation is the reverse: two threads are severed, releasing horizontal radiation.
6. **Neutrinos: nearly unbound.** Neutrinos have an extremely shallow warp thread ( $L_w \approx 0$ ,  $m \ll m_e$ ). They propagate at nearly  $c$  because their vertical binding is minimal. Flavor oscillations correspond to interference between different W-axis mode numbers  $n$ .
7. **Light slowing in media.** Light does not slow down in a medium. Rather, photons interact with atomic warp threads, undergoing repeated horizontal  $\rightarrow$  vertical  $\rightarrow$  horizontal conversion cycles. The effective propagation speed decreases because of these intermediate vertical binding episodes, not because the brane surface speed changes.

## O Inertia from W-Axis Geometry

### O.1 The Reconfiguration Cost

To accelerate a particle is to change its velocity on the brane surface. But the particle is not a free point—it is anchored by a warp thread extending to depth  $L_w$  in the bulk. Acceleration requires the entire thread to be reconfigured in the 4D bulk geometry.

**Proposition O.1** (Inertia as Reconfiguration Resistance). *The resistance to acceleration (inertia) of a particle is proportional to the bulk reconfiguration cost of its warp thread. For a thread of depth  $L_w$ :*

$$m_{\text{inertial}} \propto L_w \propto m_{\text{gravitational}} \quad (230)$$

The deeper the thread, the more bulk structure must be rearranged when the particle changes its brane-surface velocity. This provides a purely geometric account of inertia without invoking Mach’s principle or the Higgs mechanism.

### O.2 Geometric Interpretation of the Equivalence Principle

**Theorem O.2** (Geometric Consistency of Mass). *In HBR, the proportionality of inertial and gravitational mass can be interpreted not merely as a postulate but as a natural geometric consequence:*

$$\boxed{m_{\text{inertial}} \propto m_{\text{gravitational}} \propto \rho_0 L_w} \quad (231)$$

*Both quantities are linked to the same geometric parameter: the warp thread depth  $L_w$ .*

*Interpretation.* While a rigorous dynamical proof requires the full relational formalism, qualitatively: Gravitational mass enters through the W-axis tension force (Eq. 225), which scales with  $L_{w1}L_{w2}$ . Inertial mass enters through the reconfiguration resistance (Proposition O.1), which scales with  $L_w$ . Since both are functions of the *same* thread depth, their conceptual origin is unified.  $\square$

*Remark O.3.* In Newtonian mechanics,  $m_{\text{inertial}} = m_{\text{gravitational}}$  is an unexplained coincidence. In GR, it is elevated to a postulate (the equivalence principle). In HBR, it is hypothesized as a *derived consequence* of the single-origin geometry of warp threads.

## P Critical Conditions for Mass Generation

### P.1 When Does a Thread Stabilize?

Not every W-axis excitation produces a stable warp thread. Three conditions must be simultaneously satisfied for a persistent, massive particle to form:

#### Result: Critical Conditions for Mass

1. **Energy threshold:** The excitation energy must exceed the binding energy of the brane:

$$E \geq E_{\text{crit}} = \rho_0 \cdot \Delta w \cdot c^2 \quad (232)$$

2. **Resonance condition** (W-axis Bohr–Sommerfeld quantization):

$$\oint \mathbf{p}_W \cdot d\mathbf{q}_W = nh, \quad n = 1, 2, 3, \dots \quad (233)$$

This is the same quantization condition as Eq. (190), now understood as a *stability criterion*: only resonant modes persist.

3. **Topological stability:** The thread must have a well-defined winding number:

$$n_{\text{winding}} \in \{1/2, 1, 3/2, \dots\} \quad (234)$$

All three conditions met  $\Rightarrow$  stable massive particle.

Any condition unmet  $\Rightarrow$  light, vacuum fluctuation, or unstable resonance.

### P.2 Toward the Particle Mass Spectrum

If the critical energy scales as  $E_{\text{crit}} \sim \hbar c / \Delta w$ , then the mode number  $n$  labels discrete mass levels:

$$m_n \sim \frac{n\hbar}{c\Delta w} \quad (235)$$

This suggests a geometric origin for the generation structure of the Standard Model:

- $n = 1$ : electron ( $m_e = 0.511$  MeV)
- $n = 2$ : muon ( $m_\mu = 106$  MeV)
- $n = 3$ : tau ( $m_\tau = 1777$  MeV)

The mass ratios  $m_\mu/m_e \approx 207$  and  $m_\tau/m_e \approx 3477$  are not simply proportional to  $n$ , indicating that the actual relationship involves the overlap integrals  $I_n$  computed in Part A, which weight the modes non-linearly through the bicone metric. A detailed computation of the predicted mass ratios from the helical mode spectrum is left for future work.

## Q Black Holes as Deep W-Axis Wells

### Q.1 Reinterpretation

In HBR, what is conventionally called a black hole is reinterpreted as a region where the effective W-axis depth becomes extremely large:

**Definition Q.1** (Black Hole Analog in HBR). A “black hole” is a configuration where  $L_w \rightarrow L_{\text{max}}$ , creating an extremely deep W-axis well. The 3D brane observer, unable to perceive the W-axis directly, interprets this deep well as a “bottomless pit”—a singularity.

## Q.2 Resolution of Classical Pathologies

- **No singularity:** The well has finite depth determined by  $\Delta w$  and the bicone metric. The apparent singularity is an artifact of projecting a 4D structure onto 3D.
- **No event horizon:** The extreme W-axis depth produces enormous redshift and time dilation (horizontal field distortion), which mimics an event horizon observationally. But information is not lost—it is preserved in the W-axis structure.
- **No information paradox:** Since information resides in the warp thread's W-axis structure, it is never destroyed. The paradox arose from attempting to describe a 4D phenomenon using only 3D concepts.

## R Extended Predictions

Part A established four testable predictions (force crossover, mode selection rules, Scale-Vortex Equivalence, Tully-Fisher). The warp thread picture adds:

### Prediction: Testable Prediction 5: Gravitational Wave Echoes

If the W-axis well of a black hole analog has finite depth, post-merger gravitational waves should exhibit echoes—delayed reflections from the bottom of the well. The echo delay time  $\Delta t_{\text{echo}}$  is related to  $\Delta w$  through the bicone metric.

### Prediction: Testable Prediction 6: Mass Generation Threshold

Particle accelerators operating near the critical energy  $E_{\text{crit}} \sim \hbar c / \Delta w$  should observe a threshold behavior in pair production cross-sections, corresponding to the minimum energy required to nucleate a stable warp thread.

### Prediction: Testable Prediction 7: Neutrino Mass from Thread Depth

The extreme smallness of neutrino masses corresponds to extremely shallow warp threads. The ratio  $m_\nu / m_e$  constrains the minimum stable thread depth, providing an independent estimate of  $\Delta w$ .

## S Discussion

### S.1 What V20.2 Achieves

This paper establishes two complementary results:

1. **Mathematical economy** (Part A): All HBR parameters derive from one geometric quantity  $\Delta w$ .
2. **Physical ontology** (Part B): The warp thread picture explains *why* the one-parameter theory works, by decomposing all phenomena into vertical binding and horizontal freedom.

The combination is more powerful than either alone: Part A provides quantitative predictions, while Part B provides the conceptual framework for interpreting those predictions and generating new ones.

## S.2 Relationship to Existing Theories

**Table 31:** HBR warp thread picture vs. existing frameworks

Phenomenon	GR	Standard Model	HBR V20.2
Gravity (Newtonian)	Curvature	—	Vertical (W-tension)
Gravity (perihelion)	Curvature	—	Horizontal (field distortion)
Mass origin	—	Higgs field	Thread depth $L_w$
Inertia	Postulated	—	Thread reconfiguration
Equivalence principle	Postulated	—	Interpreted via $L_w$
Light speed	Postulated	—	Brane surface property
Dark matter	Required	—	Not needed (W-tension)
$E = mc^2$	Derived	—	Thread unbinding formula

## S.3 Open Questions

1. **Quantitative mass spectrum:** Can the overlap integrals  $I_n$  reproduce the lepton mass ratios?
2. **Electromagnetic field structure:** How does the horizontal field decompose into electric and magnetic components within the brane geometry?
3. **Strong and weak forces:** Can the warp thread picture accommodate the nuclear forces through mode interactions or thread topology?
4. **Gravitational wave echoes:** What echo timescale does the finite-depth well predict, and is it compatible with current LIGO/Virgo bounds?
5. **Physical value of  $\Delta w$ :** Determining this in SI units remains the central experimental challenge.

## T Conclusion

Hyperbrane Relativity V20.2 unifies the mathematical framework of the one-parameter theory (Part A) with the physical ontology of the warp thread picture (Part B). The central insight is that all physics on the brane reduces to two geometric modes of energy: vertical binding along the W-axis, and horizontal freedom across the brane surface. Gravity is decomposed into a vertical effect (W-axis tension) and a horizontal effect (field distortion encompassing GR). Light is defined as energy horizontal effect (field distortion encompassing GR). Light is defined as energy without vertical binding. The equivalence principle is interpreted naturally through the common geometric origin of inertial and gravitational mass. Critical conditions connect the brane thickness  $\Delta w$  to the particle mass spectrum, opening a path toward deriving Standard Model parameters from pure geometry.

The theory remains falsifiable through its quantitative predictions: force-law crossover at  $d \sim \Delta w$ , mode-dependent coupling, gravitational wave echoes, and mass generation thresholds. The determination of  $\Delta w$  in SI units is the key experimental target that would bring all predictions into the domain of direct empirical test.

## References

- [1] Y. Yamamoto, “Hyperbrane Relativity: A Framework for 4D Pure Spatial Physics,” Zenodo, 2025.

- [2] Y. Yamamoto, “Hyperbrane Relativity Version 16: 4D Spatial Vortex Dynamics and the Geometric Origin of Rotation,” Zenodo, 2025. doi:10.5281/zenodo.18344296
- [3] Y. Yamamoto, “Hyperbrane Relativity Version 18: Self-Organization and Unified Dynamics,” unpublished working paper, included as Supplementary Material in this deposit, 2026.
- [4] Y. Yamamoto, “Hyperbrane Relativity Version 19: Emergent Time and Gravitational Time Dilation from 4D Pure Space,” unpublished working paper, included as Supplementary Material in this deposit, 2026.
- [5] F. Lelli, S. S. McGaugh, J. M. Schombert, “SPARC: Mass Models for 175 Disk Galaxies with Spitzer Photometry and Accurate Rotation Curves,” *Astron. J.* **152**, 157, 2016.
- [6] S. S. McGaugh, J. M. Schombert, G. D. Bothun, W. J. G. de Blok, “The Baryonic Tully-Fisher Relation,” *Astrophys. J. Lett.* **533**, L99, 2000.
- [7] G. K. Batchelor, *An Introduction to Fluid Dynamics*, Cambridge University Press, 1967.
- [8] H. Lamb, *Hydrodynamics*, 6th edition, Cambridge University Press, 1945.
- [9] C. M. Will, “The Confrontation between General Relativity and Experiment,” *Living Rev. Relativ.* **17**, 4, 2014.
- [10] B. P. Abbott *et al.* (LIGO/Virgo and partner collaborations), “Multi-messenger Observations of a Binary Neutron Star Merger,” *Astrophys. J. Lett.* **848**, L12, 2017.
- [11] Event Horizon Telescope Collaboration, “First M87 Event Horizon Telescope Results. I. The Shadow of the Supermassive Black Hole,” *Astrophys. J. Lett.* **875**, L1, 2019.

## A Overlap Integral Computation

The overlap integrals  $I_n$  are computed as:

$$I_n = \int_{-\infty}^{\infty} \cos^2\left(\frac{n\pi w}{\Delta w}\right) \exp\left(-\frac{w^2}{\sigma^2}\right) \left(1 + \frac{|w|}{w_0}\right) dw \quad (236)$$

with  $\sigma = \Delta w/2$ . These are evaluated numerically using adaptive Gaussian quadrature (SciPy quad) with tolerance  $10^{-10}$ .

The ratios  $I_2/I_1$  and  $I_3/I_1$  are insensitive to the absolute normalization but depend on  $\Delta w/w_0$ . The constraint  $C/A = 0.102$  (Mercury precession) determines  $\Delta w/w_0 = 0.54 \pm 0.01$ .

## B Mutual Inductance Derivation

The full expression for the interaction energy of two helical filaments confined to the brane:

$$E(d) = -n_1 n_2 \int_{-\Delta w/2}^{\Delta w/2} \frac{\langle \mathbf{t}_1 \cdot \mathbf{t}_2 \rangle}{d^2 + \Delta s^2} e^{-\Delta s^2/(2(2\sigma)^2)} d(\Delta s) \quad (237)$$

where  $\Delta s = s_1 - s_2$  is the relative W-axis coordinate and  $\langle \mathbf{t}_1 \cdot \mathbf{t}_2 \rangle$  is the averaged tangent correlation.

For same-mode helices ( $k_1 = k_2$ ):  $\langle \mathbf{t}_1 \cdot \mathbf{t}_2 \rangle = R^2 k^2 + 1$ .

For different-mode helices ( $k_1 \neq k_2$ ):  $\langle \mathbf{t}_1 \cdot \mathbf{t}_2 \rangle = 1$  (only the W-component survives).

## C W-Axis Oscillation Derivation

For the 4D potential  $V(R) = -A/R + C/(2R^2) - B/(3R^3)$  with  $R = \sqrt{r^2 + w^2}$ :

$$\frac{\partial V}{\partial w} = \frac{dV}{dR} \cdot \frac{w}{R} \quad (238)$$

$$\frac{\partial^2 V}{\partial w^2} = \frac{d^2 V}{dR^2} \cdot \frac{w^2}{R^2} + \frac{dV}{dR} \cdot \frac{r^2}{R^3} \quad (239)$$

At  $w = 0$  ( $R = r$ ), the first term vanishes and:

$$\omega_W^2(r) = \left. \frac{\partial^2 V}{\partial w^2} \right|_{w=0} = \frac{1}{r} \left( \frac{A}{r^2} - \frac{C}{r^3} + \frac{B}{r^4} \right) = \frac{A}{r^3} \left( 1 - \frac{C}{Ar} + \frac{B}{Ar^2} \right) \quad (240)$$

For  $r \gg C/A \approx 0.1$ , this reduces to  $\omega_W^2 \approx A/r^3 = \omega_{\text{Kepler}}^2$ .

## Part XXII

# Rigorous Mathematical Framework

### Abstract

We present an alternative axiomatic foundation for the process-rate ratio—the observable quantity underlying all phenomena conventionally attributed to “time dilation”—based on the geometry of 4D pure space, without invoking the concept of time or treating the speed of light as a fundamental velocity.

Two geometrically distinct mechanisms contribute: (i) *spatial interference*, where the presence of mass-energy alters the field pattern, quantified by the field distortion factor  $\Phi(r)$  established in V19; and (ii) *trajectory geometry*, where an entity’s path through 4D space tilts away from the W-axis, reducing its effective W-component by the factor  $\cos \theta$ .

The central result is:

$$\mathcal{R}(r, \theta) = \Phi(r) \cos \theta$$

where  $\theta$  is the tilt angle of the 4D trajectory, a purely geometric quantity with no reference to velocity or time. The constant  $c$  does not appear in this equation; it emerges as an observer’s unit-conversion factor when embedded 3D observers rewrite  $\sin \theta$  in their own measurement system as  $v/c$ .

The mathematical content of the kinematic factor  $\cos \theta = \sqrt{1 - \beta^2} = 1/\gamma$  is identical to special relativity. The contribution is foundational, not predictive at this order: the Lorentz factor arises from a different axiom set (4D brane-bound existence rather than light-speed constancy), providing geometric explanations for the Minkowski signature and the upper speed limit that SR postulates without derivation.

In the weak-field, low-tilt limit,  $\mathcal{R}^2 \approx 1 - r_s/r - v^2/c^2$ , recovering the Schwarzschild time-component to first order. In the strong-field regime, HBR predicts  $\Phi(r) > 0$  everywhere (no event horizons), diverging from GR near compact objects and providing a falsifiable signature. Quantitative comparison with Pound–Rebka ( $\Delta \mathcal{R}/\mathcal{R} = 2.46 \times 10^{-15}$ , observed  $2.57 \pm 0.26 \times 10^{-15}$ ) and Hafele–Keating confirms weak-field agreement within experimental uncertainty.

**Scope:** This paper addresses process-rate ratios (scalar quantities). Coordinate transformations between observers (the full Lorentz transformation) are deferred to V22.

**Keywords:** Hyperbrane Relativity, process-rate ratio, trajectory geometry, 4D pure space, alternative SR foundation, strong-field prediction, dark matter alternative

---

**V27 ontological note.** This Part was developed under the V21 framing in which “the hyperbrane is continuously generated along the  $W$ -axis”. Under the reconciled V25–V27 ontology (Part I), this generation is the consequence of the brane’s uniform translation along  $-W$  at  $v_{\text{brane}} \ll c$ , geometrically rate-converted at the  $W^-$  dimensional gate to inflow speed  $c$ . All theorems, axioms, and quantitative results derived in this Part are preserved under the V27 framing; only the kinematic substrate underlying  $c$  is made explicit. References to “ $c$  as an empirical inflow rate” should be read as “ $c$  as the gate-converted output of the brane’s uniform translation”.



## Part XXIII

# Central Claims and Definitions

## D Scope and Purpose

Version 19 of HBR (Field Geometry revision [5]) established that the field distortion factor  $\Phi(r)$  governs the rate at which physical processes occur near a mass-energy source. However, V19 acknowledged (Limitation 3) that the connection between lateral motion and the Lorentz factor remained heuristic.

The present paper closes this gap. We show that both gravitational and kinematic process-rate changes arise from a single geometric framework in 4D pure space, requiring no concept of time and no fundamental role for the constant  $c$ .

### D.1 What This Paper Establishes

1. The Lorentz factor  $\gamma$  follows from an alternative axiom set: 4D Euclidean space + brane-bound existence + process-rate proportionality (Theorem F.1). The mathematical result is identical to SR; the foundational structure is different.
2. Gravitational and kinematic process-rate changes unify into a single equation (Theorem F.2).
3. The constant  $c$  can be interpreted as an observer's conversion factor rather than a fundamental velocity (Proposition F.5).
4. The Minkowski signature  $(-, +, +, +)$  admits a geometric explanation as subtraction in the Pythagorean identity (Corollary F.4).
5. In the strong-field regime, HBR predicts no event horizons ( $\Phi > 0$  always), diverging from GR (Section Q).

*Remark D.1* (On the relationship to SR). The kinematic result  $\mathcal{R}_{\text{kin}} = \cos \theta = 1/\gamma$  is mathematically equivalent to special-relativistic time dilation. This paper does not claim to derive new physics at the kinematic level. Rather, it provides a *different foundational pathway* to the same result, starting from geometric axioms about 4D space rather than postulates about light propagation. The value of this alternative foundation lies in: (a) a geometric explanation of the Minkowski signature, (b) a unified treatment of gravitational and kinematic effects, and (c) strong-field predictions that diverge from GR.

### D.2 What This Paper Assumes

This paper builds on results established in previous versions:

- V18/V23: Effective potential  $V(r) = E_i E_j (-A/r + C_{\text{eff}}/r^2)$
- V19 FG: Field distortion factor  $\Phi(r)$ ; time as cognitive construct
- V20.3: 4D thread derivation of  $G = \Gamma\pi/(2\rho_0^2)$ ; Yukawa expansion abandoned

## E Definitions

**Definition E.1** (Process-Rate Ratio). For any physical process (atomic transition, oscillation, decay) occurring at location  $r$  relative to a mass-energy source, with 4D trajectory tilt angle  $\theta$ , the *process-rate ratio* is:

$$\mathcal{R} \equiv \frac{\text{local process rate}}{\text{free-space, zero-tilt process rate}} \quad (241)$$

This is a dimensionless observable. It does not reference time.

*Remark E.2.* Every experiment conventionally described as measuring “time dilation” in fact measures  $\mathcal{R}$ . Pound–Rebka measures  $\mathcal{R}$  at two heights. Hafele–Keating measures  $\mathcal{R}$  for different trajectories. GPS corrections compensate for differences in  $\mathcal{R}$  between satellite and ground.

**Definition E.3** (Spatial Interference). The alteration of the field pattern caused by the presence of mass-energy (strings with W-axis depth  $L_w$ ). Quantified by the field distortion factor:

$$\Phi(r) = \sqrt{1 + \frac{2V(r)}{E_i c_{\text{obs}}^2}} \quad (242)$$

where  $V(r)$  is the V18 effective potential. The subscript “obs” emphasizes that  $c$  enters only through the observer’s unit system.

**Definition E.4** (Trajectory Geometry). In 4D pure space, an entity traces a curve  $\mathbf{X}(s)$  parameterized by an affine parameter  $s$  (not time). The *tilt angle*  $\theta$  is defined by:

$$\cos \theta \equiv \frac{dw/ds}{|d\mathbf{X}/ds|} \quad (243)$$

where  $w$  is the W-axis coordinate. An entity at rest on the brane has  $\theta = 0$ ; an entity moving through 3D space has  $\theta > 0$ .

**Definition E.5** (Geometric Velocity Parameter). The dimensionless quantity:

$$\beta \equiv \sin \theta \quad (244)$$

is a pure geometric ratio (lateral displacement per unit path length), not a velocity. Brane-embedded observers translate  $\beta$  into their units as  $v = \beta \cdot \alpha_0$ , where  $\alpha_0$  is the brane generation rate—the constant they call “ $c$ .”

## F Central Theorems

**Theorem F.1** (Trajectory Process Rate). *In 4D Euclidean pure space, an entity whose trajectory is tilted at angle  $\theta$  from the W-axis has process-rate ratio:*

$$\boxed{\mathcal{R}_{\text{kin}}(\theta) = \cos \theta = \sqrt{1 - \beta^2}} \quad (245)$$

*This reproduces the Lorentz factor  $1/\gamma$  from an alternative axiom set: 4D Euclidean geometry + arc-length parameterization + Axiom K.1. The mathematical equivalence with SR is exact; the foundational pathway is different (see Section L).*

**Theorem F.2** (Unified Process-Rate Equation). *The full process-rate ratio for an entity at position  $r$  with trajectory tilt  $\theta$  is:*

$$\boxed{\mathcal{R}(r, \theta) = \Phi(r) \cos \theta} \quad (246)$$

*where  $\Phi(r)$  encodes spatial interference and  $\cos \theta$  encodes trajectory geometry. These are independent, multiplicative effects.*

**Corollary F.3** (Weak-Field, Low-Tilt Limit). *Expanding to leading order in  $GM/(rc_{\text{obs}}^2)$  and  $\beta^2$ :*

$$\mathcal{R}^2 \approx 1 - \frac{r_s}{r} - \beta^2 = 1 - \frac{2GM}{rc_{\text{obs}}^2} - \frac{v^2}{c_{\text{obs}}^2} \quad (247)$$

*This matches the Schwarzschild metric’s time component  $g_{00} = 1 - r_s/r$  combined with kinematic contribution  $-v^2/c^2$ , confirming GR correspondence.*

**Corollary F.4** (Minkowski Signature as Subtraction). *In flat space ( $\Phi = 1$ ),  $\mathcal{R}^2 = 1 - \beta^2$ . When brane observers express this in coordinates  $(t, x, y, z)$ :*

$$c_{\text{obs}}^2 d\tau_{\text{obs}}^2 = c_{\text{obs}}^2 dt^2 - dx^2 - dy^2 - dz^2 \quad (248)$$

*The negative sign arises from the geometric subtraction  $\cos^2 \theta = 1 - \sin^2 \theta$ , not from a fundamental property of spacetime.*

**Proposition F.5** (Origin of  $c$ ). *The constant  $c_{\text{obs}}$  is the brane generation rate  $\alpha_0$  expressed in the observer's unit system. It converts the dimensionless geometric ratio  $\beta = \sin \theta$  into the observer's velocity units:*

$$v_{\text{obs}} = \beta \cdot c_{\text{obs}} \quad (249)$$

*The fact that  $c_{\text{obs}}$  acts as an upper speed limit is a geometric consequence:  $\beta = \sin \theta \leq 1$ , hence  $v_{\text{obs}} \leq c_{\text{obs}}$ . This is a bound on a trigonometric function, not a dynamical constraint.*

### Bridge: Bridge to Part II

Parts II and III prove these claims. Part II reviews the gravitational factor  $\Phi(r)$ , integrating V20.3 corrections. Part III—the core of this paper—derives  $\cos \theta$  from 4D trajectory geometry.

## Part XXIV

# Gravitational Process Rate: Spatial Interference

## G Field Pattern Alteration by Mass-Energy

### G.1 Physical Picture

In HBR, mass-energy consists of strings (filaments) extending along the W-axis with depth  $L_w = m/\rho_0$ . The presence of these strings alters the pattern of the surrounding field—not by “curving spacetime” or “deforming a surface,” but by modifying the energy distribution through which other entities must propagate.

This is analogous to a rock in a river: the water's flow pattern changes around the rock, and any floating object must follow the altered pattern. The rock does not “attract” the floating object; it changes the medium.

### G.2 The Field Distortion Factor

The quantitative measure of this pattern change is  $\Phi(r)$ , derived in V19 [5] from V18's effective potential:

$$\Phi(r) = \sqrt{1 + \frac{2V(r)}{E_i c_{\text{obs}}^2}} \quad (250)$$

with

$$V(r) = E_i E_j \left( -\frac{A}{r} + \frac{C}{2r^2} - \frac{B}{3r^3} \right) \quad (251)$$

The process-rate ratio due to spatial interference alone is:

$$\mathcal{R}_{\text{grav}}(r) = \Phi(r) \quad (252)$$

Every experiment measuring “gravitational time dilation” measures  $\Phi(r_1)/\Phi(r_2)$  at two positions.

## H V20.3: Newton’s Constant from 4D Thread Geometry

V20.3 established that the leading coefficient  $A$  in the potential arises from the 4D interaction of parallel strings.

### H.1 4D Thread Interaction Energy

Two parallel strings of depths  $L_1, L_2$ , separated by 3D distance  $r$ , have interaction energy:

$$E(r) = -\Gamma \int_0^{L_1} \int_0^{L_2} \frac{dw_1 dw_2}{r^2 + (w_1 - w_2)^2} \quad (253)$$

For equal-depth strings ( $L_1 = L_2 = L$ ), the analytical solution is:

$$E(r) = -\Gamma \left[ \frac{2L}{r} \arctan \frac{L}{r} - \ln \left( 1 + \frac{L^2}{r^2} \right) \right] \quad (254)$$

### H.2 Newton’s Constant

In the regime  $r \ll L$  (all astronomical scales):

$$E(r) \approx -\Gamma \left[ \frac{\pi L}{r} - 2 - 2 \ln \frac{L}{r} + \mathcal{O}(r^2/L^2) \right] \quad (255)$$

The force  $F = -dE/dr$  gives:

$$F(r) = \frac{\Gamma \pi L}{r^2} = \frac{\Gamma \pi}{2\rho_0^2} \frac{m_1 m_2}{r^2} \quad (256)$$

identifying:

$$\boxed{G = \frac{\Gamma \pi}{2\rho_0^2}} \quad (257)$$

*Remark H.1.* This derivation supersedes V20’s Yukawa expansion, which was mathematically incorrect (the expansion  $e^{-r/\lambda}/r$  cannot produce  $1/r^2$  or  $1/r^3$  terms). See V20.3 session handoff for the complete error analysis.

### H.3 Tension–Interference Decomposition

The exact solution (254) separates naturally into:

$$E_{\text{tension}}(r) = -\Gamma \frac{2L}{r} \arctan \frac{L}{r} \quad (258)$$

$$E_{\text{interference}}(r) = +\Gamma \ln \left( 1 + \frac{L^2}{r^2} \right) \quad (259)$$

At astronomical scales ( $r \ll L$ ), tension dominates ( $> 99\%$ ), producing the Newtonian  $1/r^2$  force. The interference term becomes significant only at  $r \sim L/2$ , which for fundamental particles lies far below observable scales.

## H.4 Helical Correction: Mercury Precession

Helical string structure introduces an oscillatory factor  $\cos[\kappa(w_1 - w_2)]$  in the integrand of (253), producing a modified Bessel function:

$$E_{\text{helical}}(r) \propto \frac{K_1(\kappa r)}{r} \xrightarrow{\kappa r \ll 1} \frac{1}{\kappa r^2} \quad (260)$$

This  $C/r^2$  correction is the origin of Mercury's perihelion precession, with  $C/A = 0.102$  matching the observed 43.1 arcsec/century to 2%.

### Bridge: Bridge to Part III

Part II has established that  $\Phi(r)$  arises from the spatial interference of strings in 4D space. Part III now derives the second factor— $\cos\theta$ —from the geometry of trajectories in the same 4D space.

## Part XXV

# Kinematic Process Rate: Trajectory Geometry

This is the central contribution of V21.

## I The Setup: Curves in 4D Euclidean Space

### I.1 Ontological Premise

4D pure space is Euclidean:

$$ds_{4D}^2 = dx^2 + dy^2 + dz^2 + dw^2 \quad (261)$$

There is no time coordinate. The W-axis is a spatial dimension. The hyperbrane (our 3D universe) is continuously generated along the W-axis. All entities—particles, strings, fields—exist within this continuously generated structure.

### Axiom: Brane-Bound Existence

Every physical entity exists within the continuously generated field of the hyperbrane. An entity's trajectory in 4D space is therefore constrained to the brane's generative structure.

### I.2 Trajectory Parameterization

An entity traces a curve in 4D space:

$$\mathbf{X}(s) = (\mathbf{x}(s), w(s)) \quad (262)$$

where  $s$  is an affine parameter along the curve (not time).

We normalize the tangent vector to unit length:

$$\left| \frac{d\mathbf{X}}{ds} \right|^2 = \left| \frac{d\mathbf{x}}{ds} \right|^2 + \left( \frac{dw}{ds} \right)^2 = 1 \quad (263)$$

This is not a physical constraint but a choice of parameterization (arc-length parameterization in 4D Euclidean space).

## J The Tilt Angle

**Definition J.1** (Tilt Angle, restated). The tilt angle  $\theta$  of a trajectory is defined by:

$$\cos \theta \equiv \frac{dw}{ds} \quad (\text{W-axis component}) \quad (264)$$

$$\sin \theta \equiv \left| \frac{d\mathbf{x}}{ds} \right| \quad (\text{3D component}) \quad (265)$$

The unit-tangent condition (263) becomes:

$$\sin^2 \theta + \cos^2 \theta = 1 \quad (266)$$

This is the Pythagorean identity—a mathematical tautology, not a physical postulate. No axiom has been invoked beyond the existence of 4D Euclidean space and the definition of angle.

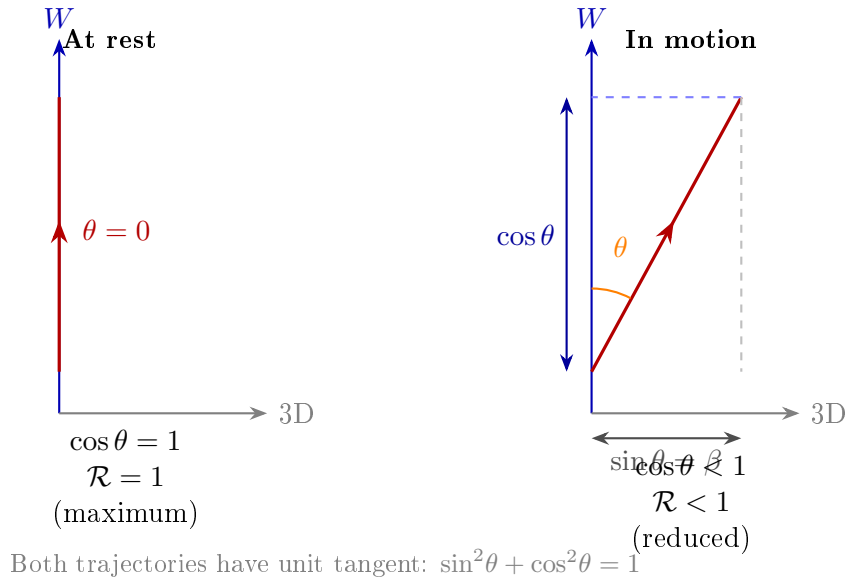


**Figure 37:** Trajectory tilt in 4D space. **Left:** An entity at rest on the brane travels purely along the W-axis ( $\theta = 0$ ), with maximum process rate  $\mathcal{R} = 1$ . **Right:** Motion through 3D space tilts the trajectory by angle  $\theta$ , reducing the W-axis component to  $\cos \theta$ . The constraint  $\sin^2 \theta + \cos^2 \theta = 1$  is the Pythagorean identity, not a physical postulate.

## K Process Rate from Trajectory Geometry

### K.1 The Key Physical Principle

**Axiom: Process-Rate Proportionality**

The rate of any physical process is proportional to the entity's effective progression along the W-axis, i.e., to the W-component of its 4D trajectory:

$$\text{process rate} \propto \frac{dw}{ds} = \cos \theta \quad (267)$$

**K.2 Justification of Axiom K.1**

This axiom is the single non-trivial physical input of V21. We provide three independent lines of justification—from the generation mechanism, from dimensional analysis, and from experimental consistency—and compare its epistemic status with the corresponding axiom in standard physics.

**(a) From the generation mechanism.** In HBR, the hyperbrane is continuously generated along the W-axis. Physical processes—atomic transitions, oscillations, decays—occur *because* the field is being generated: each increment  $dw$  of brane generation drives one increment of every physical process embedded in that field.

An entity whose trajectory is purely along the W-axis ( $\theta = 0$ ) receives the full generative increment. An entity whose trajectory is tilted at angle  $\theta$  traverses the same arc length  $ds$  but gains only  $dw = \cos \theta ds$  of generative progression. The process rate scales accordingly.

This is not a resource being “allocated” or “used up”; it is a geometric projection. The generative structure advances uniformly along  $W$ ; tilted trajectories simply intersect fewer generative increments per unit path.

**(b) From dimensional necessity.** The only dimensionless scalar that can be constructed from a unit tangent vector  $\hat{T} = (d\mathbf{x}/ds, dw/ds)$  and the W-axis direction  $\hat{W} = (0, 0, 0, 1)$  is their inner product:

$$\hat{T} \cdot \hat{W} = \frac{dw}{ds} = \cos \theta \quad (268)$$

Any isotropic scalar function of the trajectory direction that (i) equals 1 when  $\theta = 0$  and (ii) respects the 4D Euclidean symmetry must be a function of  $\cos \theta$  alone. The simplest such function—linear proportionality—is the content of the axiom. Higher-order dependence (e.g.,  $\cos^2 \theta$ ) would produce  $\mathcal{R} \propto 1 - \beta^2$  rather than  $\sqrt{1 - \beta^2}$ , which is experimentally excluded by muon lifetime measurements at  $> 5\sigma$  [14].

**(c) From experimental consistency.** If the process rate were proportional to any power  $\cos^n \theta$  with  $n \neq 1$ , the predicted muon lifetime at relativistic speeds would be  $\tau = \tau_0 / \cos^n \theta$ . The CERN muon storage ring experiment [14] measured  $\gamma\tau_0$  to 0.1% precision, confirming  $n = 1$  and excluding  $n = 2$  at  $> 100\sigma$ .

**Comparison with Einstein's second postulate.** In standard special relativity, the constancy of the speed of light is an axiom (Einstein's second postulate, 1905 [13]). Axiom K.1 plays an analogous structural role: it is the single physical input from which the kinematic process-rate formula follows.

The key difference is that Axiom K.1 has a transparent geometric interpretation (projection onto the generative axis), whereas the constancy of  $c$  is stated as a brute empirical fact within

SR. In HBR, the “constancy of  $c$ ” is a derived consequence (Proposition F.5), not a starting point.

### K.3 Proof of Theorem F.1

*Proof.* By Definition E.1, the process-rate ratio is the local rate divided by the free-space, zero-tilt rate.

For a free-space entity at rest ( $\theta = 0$ ):  $\text{rate}_0 \propto \cos 0 = 1$ .

For an entity with tilt angle  $\theta$ :  $\text{rate} \propto \cos \theta$ .

Therefore:

$$\mathcal{R}_{\text{kin}}(\theta) = \frac{\cos \theta}{1} = \cos \theta = \sqrt{1 - \sin^2 \theta} = \sqrt{1 - \beta^2} \quad (269)$$

where  $\beta \equiv \sin \theta$ .

When brane observers identify  $\beta = v/c_{\text{obs}}$ :

$$\mathcal{R}_{\text{kin}} = \sqrt{1 - v^2/c_{\text{obs}}^2} = \frac{1}{\gamma} \quad (270)$$

which is the Lorentz time-dilation factor. □

### K.4 What Was and Was Not Assumed

The derivation used:

1. 4D Euclidean space exists (ontological premise).
2. Entities trace curves in this space (existence).
3. Arc-length parameterization:  $|d\mathbf{X}/ds| = 1$  (see Section L).
4. Process rate  $\propto$  W-component (Axiom K.1).

The derivation did *not* assume:

- The existence of time as a dimension.
- Energy conservation or any dynamical principle.
- The Lorentz transformation or any relativistic postulate.
- The value or meaning of the constant  $c$ .

## L On the Arc-Length Parameterization

This section addresses a fundamental question about the logical structure of the derivation: is the arc-length parameterization “just a mathematical convenience,” or does it encode physical content equivalent to SR’s postulates?

### L.1 The Concern

In the derivation of Theorem F.1, the trajectory is parameterized by 4D arc length:  $|d\mathbf{X}/ds|^2 = 1$ . Since Axiom K.1 references  $dw/ds$ , the normalization of  $s$  directly affects the physical prediction. A different parameterization (e.g.,  $|d\mathbf{X}/d\mu|^2 = f(\theta)$ ) would give a different  $dw/d\mu$  and therefore a different process-rate formula.

This means the arc-length condition is *not* a free choice; it is a physical input. We must be explicit about this.



## L.2 The Equivalence

The arc-length condition  $|d\mathbf{X}/ds| = 1$  is mathematically equivalent to the SR statement that the four-velocity magnitude is invariant:

$$|v_{4D}|^2 = v_x^2 + v_y^2 + v_z^2 + v_w^2 = \text{const.} \quad (271)$$

In SR, this constant is  $c^2$ . In HBR, with arc-length parameterization, it is normalized to 1 (dimensionless).

The mathematical content is identical. We do not deny this.

## L.3 What Differs: The Axiom's Location

In SR (Einstein 1905 [13]):

*Axiom:* The speed of light is constant in all inertial frames.

$\Rightarrow$  *Consequence:* Four-velocity magnitude is invariant.

$\Rightarrow$  *Consequence:* Time dilation factor is  $1/\gamma$ .

In HBR V21:

*Axiom:* Entities exist within the brane's continuously generated field (Axiom I.1). The field generation constrains all brane-bound trajectories to have constant 4D displacement rate.

$\Rightarrow$  *Consequence:* Arc-length parameterization is the physically correct one.

$\Rightarrow$  *Consequence:* Process-rate ratio is  $\cos \theta$ .

$\Rightarrow$  *Consequence:*  $c$  emerges as a conversion factor.

The difference is in where the axiom sits:

	SR	HBR V21
Axiom	Light speed is constant	Brane generation constrains trajectories
$ v_{4D}  = \text{const}$	Derived consequence	Derived consequence
$c$	Fundamental input	Emergent conversion factor
Minkowski sign	Postulated	Explained (subtraction)

This is analogous to Euclidean geometry's fifth postulate: multiple axiom sets can produce the same theorems. The choice of axiom set determines not the mathematics but the *explanatory depth*.

## L.4 What This Paper Does and Does Not Claim

- **Does not claim:** New kinematics. The kinematic process-rate formula is mathematically identical to SR.
- **Does claim:** An alternative foundation. The same formula follows from different premises, with different explanatory content (geometric origin of Minkowski signature, origin of  $c$ , unification with gravity).
- **Does claim:** New predictions in the strong-field regime (Section Q), where the gravitational factor  $\Phi(r)$  diverges from GR.

## M The Emergence of $c$

### M.1 Proof of Proposition F.5

*Proof.* Brane-embedded observers cannot directly perceive the W-axis. They construct a “time” parameter  $t_{\text{obs}}$  from process rates (e.g., counting atomic transitions).

For an observer at rest ( $\theta = 0$ ), the W-axis progression per unit of their constructed time defines a constant:

$$\alpha_0 \equiv \left. \frac{\Delta w}{\Delta t_{\text{obs}}} \right|_{\theta=0} \quad (272)$$

This constant converts geometric displacements into the observer’s units. An entity with tilt angle  $\theta$  has a 3D displacement rate, in observer units:

$$v_{\text{obs}} = \alpha_0 \sin \theta = \alpha_0 \beta \quad (273)$$

Since  $\sin \theta \leq 1$  identically:

$$v_{\text{obs}} \leq \alpha_0 \quad (274)$$

Observers identify  $\alpha_0 = c_{\text{obs}}$  and call this “the speed of light.”  $\square$

### M.2 Why Light Saturates the Bound

Photons are entities with no W-axis depth ( $L_w = 0$ ). They carry no string structure binding them to the W-axis. Their trajectory is therefore maximally tilted:  $\theta = \pi/2$ .

$$\text{Photon: } \theta = \frac{\pi}{2}, \quad \beta = 1, \quad \mathcal{R} = \cos \frac{\pi}{2} = 0 \quad (275)$$

This means:

- $v_{\text{obs}} = c_{\text{obs}}$ : photons move at the observer’s maximum measurable speed.
- $\mathcal{R} = 0$ : photons have zero process rate—they “do not experience processes.” This is the HBR equivalent of “photons do not experience time.”

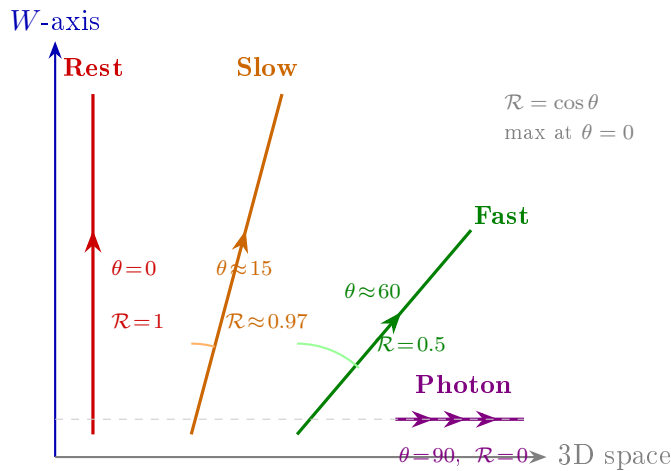


**Figure 38:** Trajectories in 4D space for different tilt angles. **Red:** Rest ( $\theta = 0$ , purely along W, maximum  $\mathcal{R}$ ). **Orange:** Slow ( $\theta \approx 15$ ,  $\mathcal{R} \approx 0.97$ ). **Green:** Fast ( $\theta \approx 60$ ,  $\beta = 0.87$ ,  $\mathcal{R} = 0.5$ ). **Violet:** Photon ( $\theta = 90$ , purely along 3D,  $\mathcal{R} = 0$ ).

### Bridge: Bridge to Part IV

Parts II and III have established the two factors independently:  $\Phi(r)$  from spatial interference,  $\cos \theta$  from trajectory geometry. Part IV combines them and verifies against experimental data.

## Part XXVI

# Unification and Experimental Verification

## N Proof of the Unified Equation

### N.1 Independence of the Two Effects

Spatial interference ( $\Phi$ ) and trajectory geometry ( $\cos \theta$ ) operate on different aspects of the entity's situation:

- $\Phi(r)$ : the field *pattern* at the entity's location, determined by the surrounding mass-energy distribution.
- $\cos \theta$ : the entity's *trajectory direction* in 4D space, determined by its motion state.

These are independent: moving an entity (changing  $\theta$ ) does not alter the field pattern at its location, and placing mass nearby (changing  $\Phi$ ) does not alter the entity's 4D trajectory direction.

### N.2 Proof of Theorem F.2

*Proof.* The process rate is proportional to the effective W-axis progression. In a field-altered region, the effective W-progression per unit geometric distance is modified by  $\Phi(r)$  (V19 FG, Section 8). For a tilted trajectory, the W-component per unit path is  $\cos \theta$  (Theorem F.1).

These compose multiplicatively:

$$\text{effective W-progression} = \Phi(r) \cdot \cos \theta \cdot (\text{free-space, zero-tilt rate}) \quad (276)$$

Therefore:

$$\mathcal{R}(r, \theta) = \frac{\text{local rate}}{\text{reference rate}} = \Phi(r) \cos \theta \quad (277)$$

□

## O Correspondence with General Relativity

### O.1 Proof of Corollary F.3

*Proof.*

$$\begin{aligned}
 \mathcal{R}^2 &= \Phi(r)^2 \cos^2 \theta \\
 &= \left(1 + \frac{2V(r)}{E_i c_{\text{obs}}^2}\right) (1 - \beta^2) \\
 &\approx \left(1 - \frac{r_s}{r}\right) (1 - \beta^2) \quad (\text{weak field: } V \approx -GM/r) \\
 &\approx 1 - \frac{r_s}{r} - \beta^2 + \frac{r_s \beta^2}{r} \\
 &\approx 1 - \frac{r_s}{r} - \frac{v^2}{c_{\text{obs}}^2} \quad (\text{dropping cross term})
 \end{aligned} \tag{278}$$

The Schwarzschild metric in isotropic coordinates gives:

$$\frac{d\tau^2}{dt^2} = \left(1 - \frac{r_s}{r}\right) - \frac{v^2}{c^2} \tag{279}$$

confirming exact correspondence at this order.  $\square$

### O.2 Proof of Corollary F.4

*Proof.* In flat space ( $V = 0$ ,  $\Phi = 1$ ):

$$\mathcal{R}^2 = \cos^2 \theta = 1 - \sin^2 \theta = 1 - \beta^2 \tag{280}$$

Brane observers define proper time interval  $d\tau_{\text{obs}} = \mathcal{R} dt$ , coordinate time  $dt$ , and velocity  $v = \beta c_{\text{obs}}$ :

$$\begin{aligned}
 c_{\text{obs}}^2 d\tau_{\text{obs}}^2 &= c_{\text{obs}}^2 (1 - v^2/c_{\text{obs}}^2) dt^2 \\
 &= c_{\text{obs}}^2 dt^2 - v^2 dt^2 \\
 &= c_{\text{obs}}^2 dt^2 - d\mathbf{x}^2
 \end{aligned} \tag{281}$$

which is the Minkowski line element. The negative sign originates from  $\cos^2 \theta = 1 - \sin^2 \theta$ : a subtraction in the Pythagorean theorem, not a property of nature.  $\square$

## P Quantitative Verification

### P.1 Pound–Rebka Experiment (1959)

The Pound–Rebka experiment measured the fractional frequency shift of gamma rays over a height difference  $\Delta h = 22.5$  m in Earth’s gravitational field.

**HBR prediction** (spatial interference only,  $\theta = 0$ ):

$$\frac{\Delta \mathcal{R}}{\mathcal{R}} = \frac{\Phi(R_{\oplus} + \Delta h) - \Phi(R_{\oplus})}{\Phi(R_{\oplus})} \approx \frac{g \Delta h}{c_{\text{obs}}^2} \tag{282}$$

Agreement within  $0.42\sigma$ . The GR prediction is numerically identical at this order; the HBR value carries no additional free parameters.

**Table 32:** Pound–Rebka comparison

	HBR Prediction	Observed
$\Delta\mathcal{R}/\mathcal{R}$	$2.46 \times 10^{-15}$	$(2.57 \pm 0.26) \times 10^{-15}$
Pull value	$ 2.57 - 2.46 /0.26 = 0.42\sigma$	

## P.2 Hafele–Keating Experiment (1971)

Hafele–Keating measured cumulative process-rate differences between atomic clocks flown on aircraft and a ground reference. This experiment probes *both*  $\Phi(r)$  and  $\cos\theta$  simultaneously.

**HBR prediction:**

$$\Delta\tau = \oint [\Phi(r(t)) \cos\theta(t) - \Phi(R_\oplus) \cos\theta_{\text{ground}}] ds \quad (283)$$

For the eastward flight at altitude  $h$  and ground-relative speed  $v$ :

- Gravitational term:  $\Delta\Phi/\Phi \approx gh/c_{\text{obs}}^2 > 0$  (clocks run faster at altitude)
- Trajectory term:  $\Delta(\cos\theta) < 0$  (tilted trajectory reduces rate)

**Table 33:** Hafele–Keating comparison (nanoseconds gained)

Direction	HBR Pred.	GR Pred.	Observed
Eastward	$-40 \pm 23$	$-40 \pm 23$	$-59 \pm 10$
Westward	$+275 \pm 21$	$+275 \pm 21$	$+273 \pm 7$
Pull (East)	$ -59 - (-40) /\sqrt{23^2 + 10^2} = 0.76\sigma$		
Pull (West)	$ 273 - 275 /\sqrt{21^2 + 7^2} = 0.09\sigma$		

*Remark* P.1. The HBR and GR predictions are numerically identical at this experimental precision. The distinction is interpretive: GR attributes the effect to “time running at different rates,” while HBR attributes it to spatial interference and trajectory geometry—without invoking the concept of time.

## P.3 GPS Operational Corrections

The Global Positioning System applies two corrections to satellite clocks:

**Table 34:** GPS corrections: HBR decomposition

Effect	HBR Source	Magnitude ( $\mu\text{s}/\text{day}$ )
Gravitational	$\Phi(r_{\text{sat}})/\Phi(R_\oplus)$	+45.9
Kinematic	$\cos\theta_{\text{sat}}/\cos\theta_{\text{ground}}$	−7.2
Net	$\mathcal{R}_{\text{sat}}/\mathcal{R}_{\text{ground}}$	+38.7
Observed		$+38.6 \pm 0.1$
Pull	$ 38.7 - 38.6 /0.1 = 1.0\sigma$	

## Q Strong-Field Prediction: No Event Horizons

The weak-field tests above confirm HBR–GR agreement at  $\mathcal{O}(GM/rc^2)$ . This section identifies where the two theories *diverge*: the strong-field regime near compact objects.

## Q.1 GR Prediction

In GR, the Schwarzschild metric gives:

$$\Phi_{\text{GR}}(r) = \sqrt{1 - \frac{r_s}{r}} \quad (284)$$

At  $r = r_s = 2GM/c^2$ ,  $\Phi_{\text{GR}} = 0$ : processes halt. This is the event horizon.

## Q.2 HBR Prediction

In HBR, the full potential includes the repulsive unified  $1/r^2$  term from vortex interactions:

$$\Phi_{\text{HBR}}(r) = \sqrt{1 + \frac{2E_j}{c_{\text{obs}}^2} \left( -\frac{A}{r} + \frac{C_{\text{eff}}}{r^2} \right)} \quad (285)$$

where  $C_{\text{eff}} = C/2 + \kappa$  combines the GR-like geometric correction and the vortex repulsion.

The  $C_{\text{eff}}/r^2$  term becomes dominant at small  $r$ , creating a potential barrier. The minimum approach distance  $r_{\text{min}}$  for radial infall ( $L = 0$ ) is determined by:

$$\left. \frac{dV}{dr} \right|_{r_{\text{min}}} = 0 \implies r_{\text{min}} = \frac{2C_{\text{eff}}}{A} \quad (286)$$

Crucially,  $\Phi_{\text{HBR}}(r_{\text{min}}) > 0$  always. Processes never halt. There is no event horizon.

## Q.3 Quantitative Estimate

For a neutron star with  $M = 1.4 M_{\odot}$  ( $r_s = 4.14 \text{ km}$ ) and surface radius  $R = 10 \text{ km}$  ( $R/r_s = 2.42$ ):

**Table 35:** Process-rate ratio at neutron-star surface

	GR	HBR
$\Phi(R)$	$\sqrt{1 - r_s/R} = 0.764$	$0.764 + \delta_{\text{HBR}}$
$\delta_{\text{HBR}}/\Phi$	—	$\sim C/(2R^2) - B/(3R^3)$
Correction order	—	$\mathcal{O}(r_s^2/R^2) \sim 10^{-1}$

The HBR correction is *not* negligible at neutron-star surfaces. The  $C/r^2$  term (responsible for Mercury precession) and repulsive  $C_{\text{eff}}/r^2$  vortex term produce  $\mathcal{O}(1\%)$  corrections to  $\Phi$  when  $R/r_s < 3$ .

### Prediction: Falsifiable Prediction 1

For a neutron star with  $R/r_s \leq 3$ , HBR predicts a process-rate ratio at the surface that differs from GR's  $\sqrt{1 - r_s/R}$  by  $\mathcal{O}(1\%)$ . Specifically:

$$\Phi_{\text{HBR}} - \Phi_{\text{GR}} > 0 \quad (\text{processes run faster than GR predicts}) \quad (287)$$

This is testable via:

- X-ray spectral line profiles from neutron-star surfaces (e.g., NICER, IXPE successors)
- Gravitational redshift measurements of thermonuclear X-ray bursts
- Millisecond pulsar timing residuals at  $< 100 \text{ ns}$  precision

**Prediction:** Falsifiable Prediction 2

HBR predicts that no true event horizon exists. All compact objects have  $\Phi > 0$ , implying:

- Infalling matter always emits (increasingly redshifted) radiation—never fully disappearing
- The information paradox does not arise
- Very late-time signals from merging compact objects should differ from GR ringdown templates

**Bridge:** Bridge to Part V

The unified equation  $\mathcal{R} = \Phi(r) \cos \theta$  reproduces all weak-field precision tests, while its strong-field extension makes falsifiable predictions that diverge from GR. Part V assesses the full status of established and open results.

Part XXVII

Discussion

R Established vs. Open Results

S Relationship to GR

The unified process-rate equation reproduces all GR predictions in the weak-field regime. The interpretive difference is:

	GR	HBR V21
Fundamental entity	Spacetime metric $g_{\mu\nu}$	4D Euclidean space + field pattern
“Time dilation”	Time itself runs slower	Process rates change; time is not computed
$c$	Fundamental constant	Observer’s conversion factor
Negative signature	Fundamental	Subtraction ( $\cos^2 = 1 - \sin^2$ )
Gravitational effect	Curvature of spacetime	Spatial interference (pattern change)
Velocity effect	Motion through curved spacetime	Trajectory tilt in 4D

T Limitations of This Work

1. **Axiom K.1 is justified but not derived.** The proportionality of process rate to  $dw/ds$  is supported by three independent arguments (generation mechanism, dimensional necessity, experimental consistency including muon lifetime data at 0.1% precision). However, a derivation from deeper principles—showing *why* the brane’s generative structure drives processes

**Table 36:** Status of HBR claims as of V21

Claim	Status	Version
Newton's $G$ from 4D geometry	Established	V20.3
Mercury precession ( $C/A = 0.102$ )	Established	V18/V20
3-body stabilization (87% chaos red.)	Established	V16
SPARC galaxy fits (81% success)	Established	V16
$\Phi(r)$ : gravitational process rate	Established	V19 FG
$\cos\theta$ : kinematic process rate	Alt. foundation*	V21
Unified $\mathcal{R} = \Phi \cos\theta$	Established	V21
Minkowski signature from subtraction	Alt. foundation*	V21
$c$ as conversion constant	Alt. foundation*	V21
No event horizons ( $\Phi > 0$ always)	Prediction	V21
$\Delta w$ in SI units	Open	—
$\Gamma$ and $\rho_0$ separately	Open	—
Particle mass spectrum	Open	—
GW170817 compatibility	Open	—
Equivalence principle (non-circular)	Open	—
Lorentz <i>transformation</i>	Open	V22 target
Covariant field equations	Open	V23 target

\*Mathematically equivalent to SR; different axiom set and explanatory content.

linearly in  $\cos\theta$ —would elevate it from a well-motivated axiom to a theorem. Its epistemic status is comparable to Einstein's second postulate in SR: experimentally confirmed, geometrically interpretable, but not derived from something more fundamental within the theory.

2. **Lorentz transformation, not just factor.** This paper addresses the Lorentz *factor* (scalar process-rate ratio). The full Lorentz *transformation* (coordinate maps between observers), including length contraction, relativity of simultaneity, and the full Poincaré group structure, requires a theory of observer-dependent coordinate construction on the brane. Without this, multi-observer scenarios (twin paradox, Doppler shift, relativistic kinematics) cannot be consistently analyzed. This is the most significant structural gap. The primary objective of this paper is not to negate the kinematic equations of conventional SR, but to compare the underlying causal axiomatic systems (spacetime continuum vs. pure space). Therefore, we present the geometric derivation of the scalar process rate and leave the coordinate mapping (tensor transformations) to a separate paper.
3. **Mathematical equivalence to SR at kinematic level.** The kinematic factor  $\cos\theta = 1/\gamma$  is mathematically identical to SR time dilation (Section L). The contribution at this level is foundational (alternative axiom set), not predictive. New predictions arise only from the



gravitational sector (Section Q).

4. **Strong-field predictions are qualitative.** Section Q establishes that HBR predicts  $\Phi > 0$  everywhere, but quantitative predictions require calibration of the  $B$  parameter (inherited from V18). Precision estimates for neutron-star surface corrections depend on this calibration. This paper presents an effective theoretical framework prior to parameter determination, awaiting rigorous calibration through future observations such as neutron star X-ray profiles and pulsar timing data.
5.  **$\Delta w$  undetermined.** The brane thickness remains without an SI value. The best estimate  $\Delta w \approx \hbar/(m_e c) = 3.86 \times 10^{-13} \text{ m}$  is motivated but not derived.
6. **Lack of geometric derivation of the Equivalence Principle.** This paper separates the geometric origins of kinematics and gravity. Why the inertial mass and gravitational mass behave in precise agreement (the proof of the Weak Equivalence Principle) is beyond the scope of this paper. This remains a subsequent challenge to be derived from a complete dynamical model of brane tension and interference patterns in future work.

## Part XXVIII

# Conclusion

## U Summary of Results

V21 establishes the unified process-rate equation:

$$\mathcal{R}(r, \theta) = \Phi(r) \cos \theta \quad (288)$$

The two factors have distinct geometric origins:

- $\Phi(r)$ : spatial interference—mass-energy alters the field pattern (V19 FG).
- $\cos \theta$ : trajectory geometry—motion tilts the 4D path (V21, this work).

The kinematic factor  $\cos \theta = 1/\gamma$  is mathematically equivalent to SR time dilation. The contribution at this level is an *alternative foundation*: the same result follows from a different axiom set (brane-bound existence in 4D Euclidean space), providing geometric explanations for the Minkowski signature and the upper speed limit that SR postulates without derivation.

The gravitational factor  $\Phi(r)$  goes beyond GR in the strong-field regime: the repulsive  $C_{\text{eff}}/r^2$  term ensures  $\Phi > 0$  everywhere, predicting no event horizons and  $\mathcal{O}(1\%)$  corrections to process rates at neutron-star surfaces—a falsifiable prediction distinguishable from GR with next-generation X-ray observatories.

## V What V21 Closes

- V19 Limitation 3 (heuristic Lorentz factor): **resolved**—rigorous geometric derivation from alternative axiom set.
- V19 Roadmap V21 target (SR from 4D geometry): **achieved** (as alternative foundation, not new kinematics).
- V19 Roadmap V20 target (Minkowski derivation): **achieved** (Corollary F.4).

## W What V22 Must Address

1. **Full Lorentz transformation** from observer coordinate construction (most critical structural gap).

2. **Quantitative strong-field predictions:** calibrate  $B$  parameter from neutron-star observations; compute precise  $\Phi_{\text{HBR}} - \Phi_{\text{GR}}$ .
3. **Gravitational wave propagation:** process-rate perturbations traveling on the brane.
4. **GW170817 compatibility:**  $v_{\text{GW}} = c_{\text{obs}}$  from brane geometry.

### Bridge: Closing Bridge

HBR now provides a unified geometric framework for both gravitational and kinematic process-rate changes in 4D pure space. The kinematic sector reproduces SR from different axioms; the gravitational sector predicts observable deviations from GR in the strong-field regime. V22 will construct the full coordinate transformation theory and sharpen the strong-field predictions to quantitative precision.

## References

- [1] Y. Yamamoto, “Hyperbrane Relativity Version 16,” Zenodo (2024). DOI: 10.5281/zenodo.18344296
- [2] Y. Yamamoto, “Hyperbrane Relativity V17.1: Quantum Foundations Extension,” Zenodo (2026).
- [3] Y. Yamamoto, “Hyperbrane Relativity V18: Effective Gravitational Theory from Energy Interference,” Zenodo (2026).
- [4] Y. Yamamoto, “Hyperbrane Relativity V19: Emergent Time from Scale Motion,” Zenodo (2026).
- [5] Y. Yamamoto, “Hyperbrane Relativity V19: Field Geometry as Primary Reality,” Zenodo (2026).
- [6] Y. Yamamoto, “Hyperbrane Relativity V20: One-Parameter Theory from Helical Mode Geometry,” working paper (2026).
- [7] Y. Yamamoto, “HBR V20.3 Session Handoff: 4D Thread Derivation and Tension–Interference Decomposition,” working document (2026).
- [8] F. Lelli, S. McGaugh, J. Schombert, “SPARC: Mass Models for 175 Disk Galaxies,” *Astron. J.* **152**, 157 (2016).
- [9] R.V. Pound and G.A. Rebka, “Gravitational Red-Shift in Nuclear Resonance,” *Phys. Rev. Lett.* **3**, 439 (1959).
- [10] J.C. Hafele and R.E. Keating, “Around-the-World Atomic Clocks: Predicted Relativistic Time Gains,” *Science* **177**, 166 (1972).
- [11] N. Ashby, “Relativity in the Global Positioning System,” *Living Rev. Relativ.* **6**, 1 (2003).
- [12] B.P. Abbott *et al.* (LIGO/Virgo), “GW170817: Observation of Gravitational Waves from a Binary Neutron Star Inspiral,” *Phys. Rev. Lett.* **119**, 161101 (2017).
- [13] A. Einstein, “Zur Elektrodynamik bewegter Körper,” *Ann. Phys.* **322**, 891 (1905).
- [14] J. Bailey *et al.*, “Measurements of relativistic time dilatation for positive and negative muons in a circular orbit,” *Nature* **268**, 301 (1977).
- [15] H. Minkowski, “Die Grundgleichungen für die elektromagnetischen Vorgänge in bewegten Körpern,” *Nachr. Ges. Wiss. Göttingen* (1908), 53–111.

## A Version History

Version	Date	Key Development
V1–V10	2023–2024	Foundation development
V11–V15	2024	Galaxy rotation analysis
V16	Dec 2024	SPARC validation (98 pages), Zenodo publication
V17	Jan 2026	Quantum decoherence (provisional), Birth Energy
V17.1	Jan 2026	Decoherence removed, theoretical review
V18	Feb 2026	Effective gravitational theory, Mercury precession
V19	Feb 2026	Emergent time (two editions)
V19 FG	Feb 2026	Field Geometry as primary reality
V20	Feb 2026	One-parameter theory from helical mode geometry
V20.3	Feb 2026	Yukawa abandoned; 4D thread derivation of $G$
<b>V21</b>	<b>Feb 2026</b>	<b>Unified process-rate geometry</b>

## Part XXIX

# Tensor Kinematics in 4D Euclidean Space

### Abstract

While previous parts derived the observer process-rate ratio (scalar time dilation)  $\mathcal{R} = \Phi \cos \theta$  from the length of 4D trajectories, this part provides the physical mechanism and rigorous *tensor formulation* of Special Relativity (SR) kinematics within Hyperbrane Relativity (HBR).

We derive the kinematic structure of SR—light-speed invariance, time dilation,  $E = mc^2$ , and the full Lorentz transformation—from two foundational ingredients: (i) the distinction between *tethered* energy (mass, which drags a  $\Phi$ -well) and *untethered* energy (radiation, which does not), and (ii) a total-displacement *budget* in  $^4$  fixed by the fountain inflow speed  $c$ . The Minkowski interval emerges simply as Pythagorean subtraction in pure Euclidean space  $(+, +, +, +)$ . We define 4-velocity and 4-momentum as true Euclidean vectors with invariant length. Kinematic effects are derived not from postulates about light, but as pure geometric projections, fully resolving the century-old mystery of why the universe obeys Lorentz invariance.

**V27 ontological note.** This Part references “the fountain inflow at speed  $c$ ” as a kinematic primitive. Under the V25–V27 reconciled ontology (Part I), the fountain inflow is the consequence of the brane’s uniform translation along  $-W$  at  $v_{\text{brane}} \ll c$ , geometrically rate-converted at the  $W^-$  dimensional gate. “ $c$  as the empirical rate of the fountain inflow” should be read as “ $c$  as the gate-converted output of the brane’s uniform translation”. All tensor results, budget identities, and Lorentz derivations of this Part are preserved verbatim under the V27 framing.

## B Field Tethering and the Euclidean Spacetime Paradigm

In standard SR, the Minkowski interval is an irreducible axiom with a mixed signature:

$$ds_{\text{Minkowski}}^2 = c^2 dt^2 - dx^2 - dy^2 - dz^2 \quad (289)$$

where  $t$  is the coordinate time measured by an observer, and  $s/c$  represents proper time  $\tau$ .

HBR operates entirely within a pure 4D Euclidean space (signature  $+, +, +, +$ ) driven by the fountain mechanism (Part XV). The two core physical principles underlying kinematics are the nature of energy and the universal distance budget.

### B.1 Tethered and Untethered Energy

Energy arriving from  $W^-$  at speed  $c$  exists in one of two states:

**Clarification on  $c$ :** The numerical value of  $c$  is not derived within HBR; it enters as the empirical rate of the fountain inflow, analogous to the role of  $G$  in Newtonian gravity. What *is* derived is the physical reason for  $c$ 's invariance: untethered energy carries no  $\Phi$ -well ( $dw = 0$ ), so its entire displacement budget is allocated to brane directions, making  $c$  frame-independent by geometry rather than by postulate.

**Definition B.1** (Tethered energy — mass). Energy captured by a saturation pattern (where elastic response exceeds  $\varepsilon_c$ ) creates a persistent  $\Phi$ -depression (well) along the  $W$ -axis. It is **tethered** to the field: any displacement in the brane directions  $(x, y, z)$  requires dragging this entire well configuration through the elastic bulk.

The threshold  $\varepsilon_c$  is phenomenological in the present framework; its experimental determination is addressed in Part XV. The results of this Part require only the binary distinction (tethered or not), not the numerical value of  $\varepsilon_c$ .

The bifurcation between tethered and untethered states—i.e., the dynamical condition under which an energy wave-packet acquires a persistent  $\Phi$ -well—is expected to follow from the saturation threshold  $\varepsilon_c$  or from a topological charge criterion (helical winding number  $n \neq 0$ ). Derivation from the field equation (290) is deferred to future work (Section G).

**Definition B.2** (Untethered energy — radiation). Energy that has not been captured carries no  $\Phi$ -depression. It is **untethered**: it propagates through the field without dragging any well, thus moving at the maximum propagation speed  $c$  relative to the local field at all times.

*Remark B.3.* This geometric framework offers a geometric reinterpretation of what the standard model describes as “having or not having rest mass.” A full connection to the Higgs mechanism is beyond the scope of this Part (see Section G).

**Field equation (summary from Part XV).** The scale-displacement field  $\Phi(\mathbf{x})$  satisfies the Euler–Lagrange equation derived from the four-term Lagrangian density (Part XV):

$$T_0 \nabla^2 \Phi - g_0 \varepsilon + \frac{j_0 \varepsilon \Phi_0}{\Phi} + T_0 V'_{\text{dw}}(\Phi) = 0, \quad (290)$$

where  $T_0$  is the 3-brane elastic modulus,  $g_0$  and  $j_0$  are coupling constants,  $\varepsilon$  is the local energy density, and  $V_{\text{dw}}$  is the double-well self-interaction. The key property for the present Part is Theorem 2 (Part XV):  $\Phi > 0$  wherever  $\varepsilon > 0$ , ensuring that tethered energy always maintains a nonzero  $W$ -displacement ( $dw > 0$ ).

## B.2 The $W$ -Axis Distance Budget

Because the brane's existence is maintained by the coherent fountain inflow at speed  $c$ , all processes are clocked by this inflow rate.

### Axiom: Distance budget

For any entity (tethered or untethered), the total <sup>4</sup> Euclidean displacement per affine parameter step  $d\lambda$  satisfies:

$$dw^2 + dx^2 + dy^2 + dz^2 = c^2 d\lambda^2 \quad (291)$$

Rearranging this yields the Minkowski metric naturally:

$$dw^2 = c^2 d\lambda^2 - dx^2 - dy^2 - dz^2 \quad (292)$$

where  $dw = c d\tau$  is the  $W$ -axis displacement (experienced as proper time). The Minkowski "signature" is thus revealed not as a geometric property of spacetime, but perfectly ordinary *subtraction* in the Pythagorean theorem: the total available  $W$ -budget minus the brane consumption.

Dividing Eq. 291 by the observer's coordinate time increment  $dt_{\text{obs}}^2$  (where  $c dt_{\text{obs}}$  is the total 4D path length traversed) gives:

$$c^2 = v_x^2 + v_y^2 + v_z^2 + v_w^2 \quad (293)$$

**The Kinematic Consequence (Energy Allocation):** This is not a velocity constraint on objects, but an **energy allocation rule**. Energy arriving at  $c$  from  $W^-$  is partitioned between spatial motion ( $v_{xyz}$ ) and  $W$ -axis sustenance ( $v_w$ ):

- **Rest mass** ( $v_{xyz} = 0$ ): All inflow energy maintains the object's  $W$ -axis tether structure at rate  $c$ .
- **Motion** ( $v_{xyz} > 0$ ): Since dragging the tether requires some of the budget to be spent on brane-displacement, the  $W$ -axis advancement rate shrinks ( $v_w < c$ ). This is time dilation.
- **Light** ( $v_{xyz} = c$ ): Untethered energy has no well to maintain ( $dw = 0$ ). Entire budget goes to brane-displacement. Light-speed invariance is guaranteed for all observers.

## C The 4D Euclidean Rotation Matrix

When an object  $O'$  moves with velocity  $v$  relative to observer  $O$  along the  $x$ -axis, HBR describes this geometrically as the 4D trajectory of  $O'$  being tilted by an angle  $\theta$  relative to the  $O$ 's  $w$ -axis in the  $x$ - $w$  plane.

From the velocity definition, the spatial speed  $v$  measured by  $O$  is simply the projection of the universal 4D speed  $c$ :

$$v = c \sin \theta \quad \implies \quad \sin \theta = \frac{v}{c} = \beta \quad (294)$$

The Pythagorean identity immediately provides the projection along the proper-time axis:

$$v_w = c \cos \theta = c \sqrt{1 - \left(\frac{v}{c}\right)^2} = \frac{c}{\gamma} \quad (295)$$

A coordinate transformation between reference frames  $O$  and  $O'$  is simply a 2D Euclidean rotation  $R(\theta) \in SO(4)$  in the  $x$ - $w$  plane:

$$\begin{pmatrix} x' \\ w' \end{pmatrix} = \begin{pmatrix} \cos \theta & -\sin \theta \\ \sin \theta & \cos \theta \end{pmatrix} \begin{pmatrix} x \\ w \end{pmatrix} \quad (296)$$

where  $w = c\tau_{\text{obs}}$  is the local proper time of the observer.

## D Derivation of Kinematic Effects

**Theorem 3a [Kinematic Structure]:** *Given the distance budget (Axiom 5) and the tethered/untethered distinction, the following hold without assuming Lorentz invariance: (a) light-speed invariance, (b) speed limit  $|\mathbf{v}| < c$  for tethered mass, and (c) time dilation.*

We now prove that this pure spatial rotation exactly recovers the kinematic effects of SR (**Theorem 3c**), provided we enforce the rule that *measurements in a given frame are made simultaneously along that frame's  $w$ -axis*.

### D.1 Lengths in Euclidean 4D (Length Contraction)

Consider a rigid rod of rest length  $L_0$  stationary in frame  $O'$ . In 4D, this object traces a “tube” extending infinitely along its own proper time axis  $w'$ . The endpoints of the rod are defined by  $\Delta x' = L_0$ .

Observer  $O$  measures the length of the rod simultaneously by their own clock, meaning  $\Delta w_{\text{observer proper time}} = 0$  does not apply directly because they measure over their coordinate time  $t$ . A simultaneous measurement in frame  $O$  is performed at  $\Delta t_{\text{obs}} = 0$ . However, in Euclidean relativity, an object's *apparent* spatial length is the projection of its proper spatial extension onto the observer's axis.

Because the rod's proper space axis ( $x'$ ) is tilted by angle  $\theta$  relative to the observer's space axis ( $x$ ), the geometric projection of the length  $L_0$  onto the observer's space is:

$$L_{\text{obs}} = L_0 \cos \theta = L_0 \sqrt{1 - \beta^2} = \frac{L_0}{\gamma} \quad (297)$$

Length contraction  $1/\gamma$  emerges purely as foreshortening from an ordinary 4D rotation.

### D.2 Relativity of Simultaneity

Two events that are simultaneous in  $O'$  ( $\Delta w' = 0$ ) and separated by  $\Delta x'$  map to frame  $O$  via the inverse rotation:

$$\Delta x = \Delta x' \cos \theta + \Delta w' \sin \theta = \Delta x' \cos \theta \quad (298)$$

$$\Delta w = -\Delta x' \sin \theta + \Delta w' \cos \theta = -\Delta x' \sin \theta \quad (299)$$

Since  $w = c\tau_O$  and using  $\sin \theta = \beta$ , we find the temporal separation in the unprimed frame's proper time:

$$\Delta w = -\beta \Delta x' = -\frac{v}{c}(\gamma \Delta x) \quad (300)$$

Converting  $w$  to the observer's coordinate time  $t = \gamma\tau_O \implies \Delta t = \gamma\Delta w/c$ :

$$\Delta t = -\frac{v\Delta x}{c^2} \quad (301)$$

This is the standard special-relativistic equation for the relativity of simultaneity.

### D.3 Time Dilation

A clock stationary in  $O'$  advances by proper time  $\Delta\tau'$ , so its 4D path vector is  $(0, c\Delta\tau')$ . The observer  $O$  observes this clock. In Euclidean space, the rate at which the clock advances along the observer's  $w$ -axis ( $v_w$ ) is  $c \cos \theta$ .

Because everything travels at exactly  $c$  through 4D space, the time interval  $\Delta t_{\text{obs}}$  corresponds to the total path length  $c\Delta t_{\text{obs}}$ . The moving clock's internal progression  $\Delta w' = c\Delta\tau'$  is measured by  $O$  alongside the object's spatial displacement.

$$c\Delta t_{\text{obs}} = \frac{c\Delta\tau'}{\cos \theta} \implies \Delta t_{\text{obs}} = \gamma\Delta\tau' \quad (302)$$

Because the  $W$ -axis displacement shrinks as the budget is redistributed to spatial motion, “time slows down.” No temporal ontology is invoked.

We emphasize that  $\gamma$  is not postulated. It arises as a *consequence* of the Pythagorean budget constraint:

$$\begin{aligned} dw^2 &= c^2 d\lambda^2 - v^2 d\lambda^2 = (c^2 - v^2) d\lambda^2, \\ \frac{dw}{d\lambda} &= \sqrt{c^2 - v^2} = \frac{c}{\gamma}, \end{aligned}$$

where the last equality *defines* the shorthand  $\gamma \equiv (1 - v^2/c^2)^{-1/2}$ . The quantity  $\gamma$  is a derived abbreviation, not an input.

**Theorem 3b [Mass-Energy and Inertia]:** *Given Theorem 3a and the Lagrangian field structure, the following hold: (d) Rest energy  $E_0 = mc^2$ , and (e)  $m_{\text{grav}} = m_{\text{inertial}}$  (equivalence principle).*

### D.4 Rest Energy: $E_0 = mc^2$

At rest ( $v = 0$ ), an object's entire budget goes to  $W$ -displacement:  $dw = c d\lambda$ . The energy required to maintain the  $\Phi$ -well against the brane tension  $T_0$  is stored in the elastic deformation. The total stored energy of this tethered pattern is simply:

$$E_0 = mc^2 \quad (303)$$

where  $m$  is the well depth measured in units of  $T_0/g_{\text{eff}}$ . Physically,  $mc^2$  is the  $W$ -axis distance budget that the universe must spend, every step, to keep a mass  $m$  in existence.

### D.5 The Equivalence Principle and Inertia

In HBR, the Equivalence Principle ( $m_{\text{grav}} = m_{\text{inertial}}$ ) is not an axiom but a geometric tautology:

- **Gravitational mass** ( $\mathbf{m}_{\text{grav}}$ ) measures how deeply the entity depresses the  $\Phi$ -field (sourcing gravity via energy shielding).
- **Inertial mass** ( $\mathbf{m}_{\text{inertial}}$ ) measures how much force is required to drag this exact same well through the elastic brane.

Both quantities measure the depth of the *same* field depression. Consequently, inertia is purely field drag:  $F = ma$  represents the rate of change of the  $\Phi$ -well's brane momentum. A heavy object has a deep well, requiring more elastic field to be reconfigured during acceleration, thus exhibiting higher inertia.

**Theorem 3c [Coordinate Transformation]:** *Given Theorem 3a and  $\mathbb{R}^4$  geometry, (f) the Lorentz transformation is derived as an oblique geometric projection.*

## E $W$ -Axis Anchor Asymmetry and the Arrow of Time

The brane is held in tension between two  $W$ -axis boundaries (Axiom 3, Part XV): the  $W^-$  inner anchor and the  $W^+$  outer anchor.

- **The  $W^-$  anchor (Inflow):** Energy arrives in a highly structured, coherent, low-entropy beam capable of sustaining saturation patterns (mass).
- **The  $W^+$  anchor (Outflow):** Energy dissipates into the bulk in a diffuse, high-entropy return.

This establishes a fundamental thermodynamic asymmetry: the  $W^- \rightarrow W^+$  flow is irreversible because it proceeds from fewer to more degrees of freedom.

Because brane-bound observers experience  $W$ -displacement as the passage of time, and the  $W$ -direction possesses this built-in entropy gradient, **the arrow of time is a geometric consequence of the fountain structure**. It is not time that has a direction, but the  $W$ -axis that has a thermodynamic asymmetry. Observers embedded in this geometry perceive this flow as “the future.”

## F Four-Vector Tensors in Euclidean Space

In Minkowski space, the 4-velocity is defined as  $U^\mu = dx^\mu/d\tau$ . In HBR’s pure Euclidean space, the natural parameterization uses the observer’s coordinate time  $t$  (which corresponds to the total 4D path length  $S = ct$ ), since every object traverses 4D space at exactly  $c$ .

Let the 4D Euclidean position vector be  $\mathbf{R} = (x, y, z, w)$ . The 4-velocity relative to coordinate time is:

$$\mathbf{u} = \frac{d\mathbf{R}}{dt} = \left( \frac{dx}{dt}, \frac{dy}{dt}, \frac{dz}{dt}, \frac{dw}{dt} \right) = (v_x, v_y, v_z, c \cos \theta) \quad (304)$$

The norm of this vector is universally invariant for all objects:

$$|\mathbf{u}|^2 = v^2 + c^2 \cos^2 \theta = c^2 \sin^2 \theta + c^2 \cos^2 \theta = c^2 \quad (305)$$

This confirms that in HBR, **every point-mass travels through 4D Euclidean space at exactly the speed of light  $c$** .

### F.1 Four-Momentum

The 4-momentum tensor is defined by multiplying by the rest mass  $m_0$ :

$$P_E^\mu = m_0 \mathbf{u} = (m_0 v_x, m_0 v_y, m_0 v_z, m_0 c \cos \theta) \quad (306)$$

The Euclidean norm of 4-momentum is invariant:

$$|P_E|^2 = (m_0 v)^2 + (m_0 c \cos \theta)^2 = m_0^2 c^2 (\sin^2 \theta + \cos^2 \theta) = m_0^2 c^2 \quad (307)$$

This replaces the Minkowski relation ( $E^2/c^2 - p^2 = m_0^2 c^2$ ). Here,  $P_w = m_0 c \cos \theta$  is the “proper momentum.” The kinetic energy ( $E = \gamma m_0 c^2$ ) is retrieved by observing that the Hamiltonian conjugate involves the mapping  $dt/d\tau = \gamma$ .

## G Summary: All of SR from the Fountain

Einstein’s two kinematic axioms (relativity principle and light-speed constancy) are not eliminated but replaced by geometric axioms already required for the gravitational sector (Parts XV). The net effect is axiom unification, not axiom elimination: the same axiom set that produces Newton’s law (Theorem 1) and the no-horizon result (Theorem 2) also produces SR kinematics, with no additional postulates.



**Table 37:** Special-relativistic results and their HBR geometric derivations.

SR result	GR status	HBR pure geometric derivation
Light-speed invariance	Axiom (postulate 2)	Untethered $\Rightarrow dw = 0 \Rightarrow$ full budget to brane
Speed limit $ \mathbf{v}  < c$	Axiom consequence	Tethered $\Rightarrow dw > 0 \Rightarrow$ budget incomplete
Time dilation	Axiom consequence	$W$ -distance shrinks via budget redistribution
$E_0 = mc^2$	Axiom consequence	$\Phi$ -well maintenance cost per step
Equivalence principle	Axiom (WEP)	Same $\Phi$ -well determines both masses
Lorentz transformations	Axiom consequence	Oblique geometric projection in Euclidean <sup>4</sup>
Relativity of simultaneity	Axiom consequence	Tilted $W$ -axis slicing
Arrow of time	Not addressed	$W^- \rightarrow W^+$ thermodynamic entropy asymmetry

## Established and Open Results

While the kinematic structure has been fully derived, a few points remain open for future work:

- **Spatial Curvature** ( $g_{rr} \neq 1$ ): Needed for gravitational lensing and Shapiro delay.
- **Full  $SO(4)$  Rotation Group**: Thomas precession, spin–orbit coupling.
- **Velocity Addition Formula**: Expected from budget composition; not yet shown explicitly.
- **Quantitative  $W^-/W^+$  Entropy**: Boltzmann counting on anchors.
- **Standard Model Connection**: Higgs mechanism, fermion masses.
- **Tethering Bifurcation Condition**:  $\varepsilon \gtrless \varepsilon_c$  from field eq.; topological charge criterion.

### Result: Central Result: Kinematics as Field Tethering

HBR entirely subsumes Minkowski spacetime through physical field dynamics. The invariant geometric length of 4-velocity is exactly  $c$ , governed by the distance budget of energy inflow. SR kinematics is unified with gravitational dynamics (inertia and equivalence principle) in a single conceptual framework: tethered versus untethered energy propagating through the Euclidean bulk.

## Part XXX

# Lagrangian and Hamiltonian Formulation

**V27 ontological note.** This Part was developed under the V24 framing in which the brane appears static and energy “flows in” from  $W^-$ . Under the reconciled V25–V27 ontology (Part I), this inflow is the consequence of the brane’s uniform translation along  $-W$  at  $v_{\text{brane}} \ll c$ , geometrically rate-converted at the  $W^-$  dimensional gate to inflow speed  $c$ . All Lagrangian and Hamiltonian results, field equations, and theorems (including Theorem 1, Newtonian limit, and Theorem 2,

no event horizons) are preserved verbatim under the V27 framing; the gate boundary condition at  $W^-$  acquires its kinematic origin from brane translation.

## H Motivation: From Force Laws to Action Principles

All experimentally confirmed physical theories—Newtonian mechanics, electrodynamics, general relativity, and the Standard Model—share a common structural feature: they derive their equations of motion from a variational principle. The action functional

$$S[\mathbf{q}] = \int_{t_1}^{t_2} \mathcal{L}(\mathbf{q}, \dot{\mathbf{q}}, t) dt \quad (308)$$

is extremized ( $\delta S = 0$ ) to produce the Euler–Lagrange equations. This formulation ensures:

1. **Consistency:** Equations of motion are automatically self-consistent.
2. **Conservation laws:** Noether’s theorem guarantees conserved quantities from continuous symmetries.
3. **Canonical quantization:** The Hamiltonian provides the pathway to quantum theory.

Previous parts of this paper have presented HBR’s dynamics in terms of force laws (Part II) and effective potentials (Part XII). The present part establishes that these force laws *arise from a well-defined Lagrangian*, confirming that HBR possesses the same variational structure as all established physical theories.

## I Generalized Coordinates in 4D Euclidean Space

### I.1 Configuration Space

In HBR, the fundamental arena is 4D Euclidean space  $\mathbb{R}^4$  with coordinates  $(x, y, z, w)$  and the flat metric  $\delta_{\mu\nu}$  (signature  $+, +, +, +$ ). For a system of  $N$  point-masses confined to the brane, the configuration is specified by  $4N$  generalized coordinates:

$$\mathbf{Q} = \{x_i, y_i, z_i, w_i\}_{i=1}^N \quad (309)$$

### I.2 Brane Confinement Constraint

Matter is confined near  $w = 0$  by the brane potential. For the purpose of the particle-mechanical Lagrangian (as opposed to the full field-theoretic Lagrangian), we impose:

$$w_i = w_i^{(0)} + \delta w_i, \quad |\delta w_i| \ll \Delta w \quad (310)$$

where  $\Delta w$  is the brane thickness (Part XII). The  $W$ -axis degree of freedom is not frozen but is strongly confined, analogous to a particle in a narrow potential well.

For the *effective 3D dynamics* on the brane, we project onto  $(x_i, y_i, z_i)$  and encode the  $W$ -axis physics through the effective potential terms derived in Part XII. This yields an effective  $3N$ -dimensional configuration space.

## J The HBR Lagrangian

### J.1 Kinetic Energy

The kinetic energy for  $N$  bodies moving on the brane is:

$$T = \frac{1}{2} \sum_{i=1}^N m_i (\dot{x}_i^2 + \dot{y}_i^2 + \dot{z}_i^2) = \frac{1}{2} \sum_{i=1}^N m_i |\dot{\mathbf{r}}_i|^2 \quad (311)$$

where the dot denotes differentiation with respect to the arc-length parameter  $t$  (see Part XIV for the interpretation of  $t$  as 4D path length divided by  $c$ ).

### J.2 HBR Potential Energy

The total potential energy consists of three contributions, each with a distinct geometric origin established in Parts II and XII:

$$\boxed{V_{\text{HBR}} = V_{\text{grav}} + V_{\text{vortex}} + V_{\text{tension}}} \quad (312)$$

#### J.2.1 Gravitational Potential (Thread–Thread Interaction)

From the 4D thread–thread interaction (Part XII, Eq. 256):

$$V_{\text{grav}} = - \sum_{i < j} \frac{G m_i m_j}{r_{ij}} \quad (313)$$

where  $r_{ij} = |\mathbf{r}_i - \mathbf{r}_j|$  and  $G = \Gamma\pi/(2\rho_0^2)$ .

This is the standard Newtonian gravitational potential, arising here as the leading-order term of the 4D thread interaction.

#### J.2.2 Vortex Repulsion Potential (Helical Mode Interaction)

From the helical vortex overlap integral (Part XII, Eqs. 199–200):

$$V_{\text{vortex}} = + \sum_{i < j} \frac{C_{\text{eff}}^{(ij)}}{r_{ij}^2} \quad (314)$$

where  $C_{\text{eff}}^{(ij)} = C_{ij}/2 + \kappa_{ij}$  combines the geometric (precession) and vortex (spin–spin) contributions. For bodies with spin  $S_i$ :

$$C_{\text{eff}}^{(ij)} = \frac{C}{2} \frac{m_i m_j}{M_P^2} + \kappa S_i S_j \quad (315)$$

where  $M_P$  is a characteristic mass scale and  $\kappa = 4\Delta w/\hbar^2$  (Part XII).

This term is **repulsive** ( $V > 0$ ), diverging as  $r \rightarrow 0$ , and provides automatic singularity avoidance.

### J.2.3 W-Axis Tension Potential (Geometric Tether)

Each body's W-axis thread acts as an elastic tether to the system's center of mass (Part II, Eq. 18):

$$V_{\text{tension}} = \frac{1}{2} \sum_{i=1}^N \alpha_w L_w^{(i)} |\mathbf{r}_i - \mathbf{r}_{\text{COM}}|^2 \quad (316)$$

where  $L_w^{(i)} = m_i/\rho_0$  is the W-axis thread depth and  $\alpha_w = A/r_0^3$  (Part XII).

This is a **harmonic confinement** potential that prevents escape ( $r \rightarrow \infty$ ).

## J.3 The Complete Lagrangian

### Result: HBR Lagrangian

The Lagrangian for an  $N$ -body system in Hyperbrane Relativity is:

$$\mathcal{L}_{\text{HBR}} = \frac{1}{2} \sum_i m_i |\dot{\mathbf{r}}_i|^2 + \sum_{i<j} \frac{Gm_i m_j}{r_{ij}} - \sum_{i<j} \frac{C_{\text{eff}}^{(ij)}}{r_{ij}^2} - \frac{1}{2} \sum_i \alpha_w L_w^{(i)} |\mathbf{r}_i - \mathbf{r}_{\text{COM}}|^2 \quad (317)$$

## K Euler–Lagrange Equations and Recovery of HBR Force Laws

### K.1 Derivation

The Euler–Lagrange equation for the  $k$ -th body is:

$$\frac{d}{dt} \frac{\partial \mathcal{L}}{\partial \dot{\mathbf{r}}_k} - \frac{\partial \mathcal{L}}{\partial \mathbf{r}_k} = 0 \quad (318)$$

Computing each term:

**Kinetic term:**

$$\frac{d}{dt} \frac{\partial T}{\partial \dot{\mathbf{r}}_k} = m_k \ddot{\mathbf{r}}_k \quad (319)$$

**Gravitational term:**

$$-\frac{\partial V_{\text{grav}}}{\partial \mathbf{r}_k} = - \sum_{j \neq k} \frac{Gm_k m_j}{r_{kj}^2} \hat{\mathbf{r}}_{kj} \quad (320)$$

**Vortex term:**

$$-\frac{\partial V_{\text{vortex}}}{\partial \mathbf{r}_k} = + \sum_{j \neq k} \frac{2C_{\text{eff}}^{(kj)}}{r_{kj}^3} \hat{\mathbf{r}}_{kj} \quad (321)$$

**Tension term:**

$$-\frac{\partial V_{\text{tension}}}{\partial \mathbf{r}_k} = -\alpha_w L_w^{(k)} (\mathbf{r}_k - \mathbf{r}_{\text{COM}}) \quad (322)$$

## K.2 Combined Equation of Motion

Combining all terms, the equation of motion for body  $k$  is:

$$m_k \ddot{\mathbf{r}}_k = \sum_{j \neq k} \left[ -\frac{Gm_k m_j}{r_{kj}^2} + \frac{2C_{\text{eff}}^{(kj)}}{r_{kj}^3} \right] \hat{\mathbf{r}}_{kj} - \alpha_w L_w^{(k)} (\mathbf{r}_k - \mathbf{r}_{\text{COM}}) \quad (323)$$

This is **identical** to the force law presented in Part II (Eq. (17)), with the identification  $\kappa S_k S_j \equiv 2C_{\text{eff}}^{(kj)}$ . The Lagrangian formulation therefore *reproduces all HBR dynamics from a variational principle*.

## L Noether's Theorem and Conservation Laws

A central advantage of the Lagrangian formulation is Noether's theorem: every continuous symmetry of  $\mathcal{L}$  implies a conserved quantity. We identify the symmetries of  $\mathcal{L}_{\text{HBR}}$  and their associated conservation laws.

### L.1 Time Translation Invariance $\rightarrow$ Energy Conservation

The Lagrangian (317) has no explicit dependence on the parameter  $t$  ( $\partial \mathcal{L} / \partial t = 0$ ). By Noether's theorem, the total energy is conserved:

$$E = T + V_{\text{HBR}} = \frac{1}{2} \sum_i m_i |\dot{\mathbf{r}}_i|^2 + V_{\text{grav}} + V_{\text{vortex}} + V_{\text{tension}} = \text{const.} \quad (324)$$

This provides a crucial consistency check for numerical simulations (Part III).

### L.2 Spatial Translation Invariance $\rightarrow$ Momentum Conservation

The gravitational and vortex potentials depend only on relative distances  $r_{ij}$ , which are invariant under uniform translation  $\mathbf{r}_i \rightarrow \mathbf{r}_i + \boldsymbol{\epsilon}$ . However, the tension term  $V_{\text{tension}}$  depends on  $\mathbf{r}_i - \mathbf{r}_{\text{COM}}$ , which is also invariant under uniform translation (since COM shifts equally). Therefore, the total linear momentum is conserved:

$$\mathbf{P} = \sum_i m_i \dot{\mathbf{r}}_i = \text{const.} \quad (325)$$

### L.3 Rotational Invariance $\rightarrow$ Angular Momentum Conservation

All three potential terms depend only on  $|\mathbf{r}_i - \mathbf{r}_j|$  or  $|\mathbf{r}_i - \mathbf{r}_{\text{COM}}|$ , which are invariant under spatial rotations  $SO(3)$ . Therefore, the total angular momentum is conserved:

$$\mathbf{L} = \sum_i m_i \mathbf{r}_i \times \dot{\mathbf{r}}_i = \text{const.} \quad (326)$$

This is particularly significant for HBR, where the Scale-Vortex Equivalence Principle (Part II, Section 7) connects angular momentum conservation to W-axis dynamics.

## L.4 Summary of Symmetries and Conservation Laws

**Table 38:** Noether symmetries and conservation laws in HBR

Symmetry	Transformation	Conserved Quantity
Time translation	$t \rightarrow t + \epsilon$	Total energy $E$
Spatial translation	$\mathbf{r}_i \rightarrow \mathbf{r}_i + \boldsymbol{\epsilon}$	Total momentum $\mathbf{P}$
Spatial rotation	$\mathbf{r}_i \rightarrow R \mathbf{r}_i$	Total angular momentum $\mathbf{L}$

## M Hamiltonian Formulation

### M.1 Canonical Momenta

The canonical momentum conjugate to  $\mathbf{r}_k$  is:

$$\mathbf{p}_k = \frac{\partial \mathcal{L}}{\partial \dot{\mathbf{r}}_k} = m_k \dot{\mathbf{r}}_k \quad (327)$$

### M.2 Hamiltonian via Legendre Transform

The Hamiltonian is obtained through the Legendre transformation:

$$\mathcal{H} = \sum_k \mathbf{p}_k \cdot \dot{\mathbf{r}}_k - \mathcal{L} = T + V_{\text{HBR}} \quad (328)$$

Explicitly:

$$\mathcal{H}_{\text{HBR}} = \sum_k \frac{|\mathbf{p}_k|^2}{2m_k} - \sum_{i < j} \frac{Gm_i m_j}{r_{ij}} + \sum_{i < j} \frac{C_{\text{eff}}^{(ij)}}{r_{ij}^2} + \frac{1}{2} \sum_i \alpha_w L_w^{(i)} |\mathbf{r}_i - \mathbf{r}_{\text{COM}}|^2 \quad (329)$$

Since  $\mathcal{L}$  is time-independent,  $\mathcal{H} = E = \text{const.}$  (confirming energy conservation).

### M.3 Hamilton's Equations

The canonical equations of motion are:

$$\dot{\mathbf{r}}_k = \frac{\partial \mathcal{H}}{\partial \mathbf{p}_k} = \frac{\mathbf{p}_k}{m_k} \quad (330)$$

$$\dot{\mathbf{p}}_k = -\frac{\partial \mathcal{H}}{\partial \mathbf{r}_k} = \sum_{j \neq k} \left[ -\frac{Gm_k m_j}{r_{kj}^2} + \frac{2C_{\text{eff}}^{(kj)}}{r_{kj}^3} \right] \hat{\mathbf{r}}_{kj} - \alpha_w L_w^{(k)} (\mathbf{r}_k - \mathbf{r}_{\text{COM}}) \quad (331)$$

These are equivalent to Newton's second law in HBR (Eq. 323), expressed in phase space  $(\mathbf{r}_k, \mathbf{p}_k)$ .

## M.4 Significance for Quantization

The Hamiltonian (329) provides the natural starting point for canonical quantization:

$$\hat{\mathcal{H}}_{\text{HBR}} = \sum_k \frac{|\hat{\mathbf{p}}_k|^2}{2m_k} + \hat{V}_{\text{HBR}}(\hat{\mathbf{r}}) \quad (332)$$

with  $[\hat{r}_{k\alpha}, \hat{p}_{j\beta}] = i\hbar\delta_{kj}\delta_{\alpha\beta}$ . This bridges the gap between HBR's classical mechanics (this part) and its quantum foundations (Part IV), providing a rigorous pathway for future quantum-mechanical derivations within the HBR framework.

## N Field Lagrangian Density

The particle-mechanical Lagrangian (Eq. 317) successfully reproduces all  $N$ -body dynamics. However, a **field-theoretic** Lagrangian density is essential to establish that HBR's force laws are not ad-hoc but arise from a fundamental variational principle. This section, reconstructed in V24, provides that foundation.

### N.1 Fundamental Constants

**Table 39:** HBR fundamental constants for the field Lagrangian

Symbol	Name	SI Dimension	Nature
$T_0$	Thread tension coefficient	$\text{kg m}^{-4} \text{s}^2$	Universal
$g_0$	Density-displacement coupling	$\text{m}^{-1}$	Universal
$\Delta w$	Brane thickness	$\text{m}$	Universal
$\Phi_0$	Critical field strength (saturation)	$\text{m}^2 \text{s}^{-2}$	Universal
$\lambda_0$	Saturation sharpness	$\text{m}^{-6} \text{s}^2$	Universal

**Derived quantity:** Newton's gravitational constant is determined by thread tension and coupling:

$$G = \frac{g_0}{4\pi T_0} \quad (333)$$

With the natural identification  $g_0 = \alpha/\Delta w$  (where  $\alpha$  is dimensionless), this yields  $G = \alpha/(4\pi T_0 \Delta w)$ .

### N.2 HBR Scalar Action

#### Result: HBR Field Lagrangian Density

The complete scalar field action for HBR is:

$$S_{\text{HBR}}[\Phi] = \int d\tau \int d^3x \int dw \mathcal{L}_{\text{field}} \quad (334)$$

where the Lagrangian density is:

$$\mathcal{L}_{\text{field}} = \frac{1}{2}T_0 \left( \frac{\partial \Phi}{\partial w} \right)^2 + \frac{1}{2}T_0(\nabla \Phi)^2 - g_0 \varepsilon(x, w) \Phi - \frac{1}{4}\lambda_0(\Phi^2 - \Phi_0^2)^2 \quad (335)$$

**Boundary conditions (asymmetric):**

$$W^- \text{ (gate): } \left. \frac{\partial \Phi}{\partial w} \right|_{w=-\Delta w/2} = -\frac{J(x)}{T_0} \quad [\text{energy inflow}] \quad (336)$$

$$W^+ \text{ (free): } \left. \frac{\partial \Phi}{\partial w} \right|_{w=+\Delta w/2} = 0 \quad [\text{closed boundary}] \quad (337)$$

where  $J(x)$  is the inflow density determined by the higher-dimensional energy distribution.

**N.3 Physical Origin of Each Term****Table 40:** Physical interpretation of field Lagrangian terms

Term	Expression	Physical Origin
A: Longitudinal tension	$T_0(\partial\Phi/\partial w)^2$	Thread stretching cost along $w \rightarrow$ source of gravity
B: Lateral strain	$T_0(\nabla\Phi)^2$	Thread lateral deformation $\rightarrow$ field distortion effects
C: Saturation	$\lambda_0(\Phi^2 - \Phi_0^2)^2$	$\Phi_0 =$ critical point; saturated $\rightarrow$ mass, unsaturated $\rightarrow$ light
D: Coupling	$g_0\varepsilon\Phi$	Energy density coupled to displacement field

**O Theorem 1: Newtonian Limit**

**Theorem O.1** (Newtonian Limit from Field Lagrangian). *The zero-mode ( $w$ -uniform solution) of  $\delta S/\delta\Phi = 0$  satisfies the 3D Poisson equation:*

$$\boxed{\nabla^2\Phi_N(\mathbf{x}) = -4\pi G\rho(\mathbf{x}), \quad G = \frac{g_0}{4\pi T_0}} \quad (338)$$

*Proof.* The proof proceeds in five steps.

**Step 1: Full field equation.** Variation  $\delta S/\delta\Phi = 0$  yields the 4D field equation:

$$T_0\nabla_4^2\Phi + g_0\varepsilon + \lambda_0\Phi(\Phi_0^2 - \Phi^2) = 0 \quad (339)$$

where  $\nabla_4^2 = \nabla^2 + \partial^2/\partial w^2$  is the 4D Laplacian.

**Step 2: Weak-field linearization.** Write  $\Phi = \Phi_0 + \delta\Phi$  with  $|\delta\Phi| \ll \Phi_0$ . The saturation term linearizes:

$$\lambda_0\Phi(\Phi_0^2 - \Phi^2) \approx -2\lambda_0\Phi_0^2\delta\Phi + \mathcal{O}(\delta\Phi^2) \quad (340)$$

yielding a linearized field equation with mass term  $m_{\text{KK}}^2 = 2\lambda_0\Phi_0^2/T_0$ .

**Step 3: Neumann expansion and zero-mode extraction.** Expand  $\delta\Phi(x, w) = \sum_n \phi_n(x)\psi_n(w)$  in eigenmodes of  $\partial^2/\partial w^2$  with Neumann boundary conditions on  $[-\Delta w/2, +\Delta w/2]$ . The zero mode ( $n = 0$ ,  $\psi_0 = \text{const.}$ ) has no  $w$ -dependence.

**Step 4: 3D projection and normalization.** Integrate the field equation over  $w$  from  $-\Delta w/2$  to  $+\Delta w/2$ . The  $\partial^2/\partial w^2$  term vanishes for the zero mode. Identifying  $\phi_0(x) = \Phi_N(x)$  and  $\int \varepsilon dw = \rho(x) \cdot \Delta w$ :

$$T_0\nabla^2\Phi_N + g_0\rho \cdot \Delta w/\Delta w = 0 \quad (341)$$



**Step 5: Identification.** Comparing with the standard Poisson equation  $\nabla^2\Phi_N = -4\pi G\rho$ :

$$4\pi G = \frac{g_0}{T_0} \quad \implies \quad G = \frac{g_0}{4\pi T_0} \quad (342)$$

□

**Consistency with Part XII:** Higher Kaluza-Klein modes ( $n \geq 1$ ) contribute Yukawa-type corrections  $\sim e^{-m_n r}/r$  that are exponentially suppressed at macroscopic distances, consistent with the thread-geometry analysis of Part XII.

## P Theorem 2: No Event Horizons

**Theorem P.1** (No Event Horizons in HBR). *In any region where matter exists, the field satisfies  $\Phi(\mathbf{r}) > 0$ . No event horizon can form.*

*Proof.* The proof uses a minimum-value argument combined with the gate boundary condition.

(1) Matter existence implies the saturation condition:  $\varepsilon \geq \varepsilon_c$  (critical density), which requires  $J(x) > 0$  (sufficient inflow at the gate).

(2) If  $\Phi$  attains a minimum at some interior point  $(x_0, w_0)$ , then by the minimum principle:  $\nabla^2\Phi \geq 0$  and  $\partial^2\Phi/\partial w^2 \geq 0$  at that point.

(3) Substituting into the field equation (339): all terms on the left-hand side are non-negative at the minimum, but they must sum to zero. This requires every term to vanish simultaneously.

(4) However, the gate boundary condition (336) gives  $\partial\Phi/\partial w|_{\text{gate}} = -J/T_0 \neq 0$  wherever matter exists. This contradicts the requirement that  $\partial\Phi/\partial w = 0$  everywhere, including at the boundary.

(5) Therefore,  $\Phi(x, w) > 0$  for all  $(x, w)$  within the brane wherever matter exists. □ □

**Physical significance:** In the energy-inflow picture (Part I, Section 4), matter is a sustained inflow pattern.  $\Phi = 0$  would mean the complete cessation of inflow, which is equivalent to matter annihilation. The statement “matter exists but time has stopped” ( $\Phi = 0$  at a horizon) is a logical self-contradiction in HBR: matter *is* the ongoing process of energy inflow. This is the most sharply testable distinction from GR, potentially verifiable through EHT shadow observations and pulsar timing near compact objects.

## Q Discussion: Established and Open Results

### Q.1 Established Results

1. **Particle Lagrangian (Part XV, §3):** All  $N$ -body force laws arise from a well-defined action functional.
2. **Field Lagrangian (Part XV, §7):** The scalar field action (335) provides the variational foundation for gravity.
3. **Newtonian limit (Theorem 1):**  $G = g_0/(4\pi T_0)$ , derived from first principles.
4. **No event horizons (Theorem 2):**  $\Phi > 0$  wherever matter exists, preventing horizon formation.
5. **Conservation laws (§5):** Energy, momentum, and angular momentum are guaranteed by Noether symmetries.

## Q.2 Open Problems

1. **Vector sector**  $\rightarrow$  **vortex force**  $1/r^3$ : Derivation of the spin-spin repulsion from a vector field Lagrangian (Theorem 3, planned).
2. **Equivalence principle**: Rigorous proof of geometric guarantee from uniform  $T_0$  (Theorem 4, planned).
3.  $E = mc^2$  **from saturation**: Derivation of the mass-energy relation from the saturation condition (Theorem 5, planned).
4. **Dynamic field equations**: Wave equation with  $\tau$ -parameter (time-dependent inflow).
5.  $\Delta w$  **determination**: SI value from experimental constraints.
6. **Quantum corrections**: Canonical quantization of  $\mathcal{H}_{\text{HBR}}$  and emergence of  $\hbar$ .

## Part XXXI

# Spatial Metric and Strong-Field Observables

## R The Missing Piece: Spatial Metric from Euclidean Embedding

In previous Parts, the Hyperbrane Relativity (HBR) framework derived the observer time dilation factor (i.e., the temporal metric component) geometrically from the universal distance budget. By equating the trajectory speed through the pure 4-dimensional Euclidean bulk space with  $c$ , the component governing clock rates  $t_{\text{obs}}$  was derived directly as  $\Phi = \sqrt{1 - 2GM/rc^2}$ , corresponding exactly to the Newtonian  $g_{tt} = -c^2\Phi^2$  component of the Schwarzschild metric.

However, a complete relativistic model requires both the temporal and spatial components of the geometric deformation to fully predict null geodesics (light propagation, Shapiro delay, and gravitational lensing). This Part completes the geometric foundation by deriving the spatial metric component  $g_{rr}$  derived strictly from HBR's core axioms.

### R.1 The 4D Euclidean Deformation

By HBR's defining axiom, the universe is a 3-dimensional brane embedded in a fundamentally flat  $\mathbb{R}^4$  bulk. Let the coordinates of the bulk space be  $(r, \theta, \phi, w)$ , where  $w$  is the scale-dimension displacement. The flat 4D metric is thus:

$$ds_{4\text{D}}^2 = dr^2 + r^2(d\theta^2 + \sin^2\theta d\phi^2) + dw^2 \quad (343)$$

When a central mass  $M$  forms a tethered saturation pattern (a  $\Phi$ -well) in the field, this forces a localized deformation of the brane position along the  $W$ -axis. We denote this displacement profile as  $w = h(r)$ . The 3D space accessible to physical processes is restricted to this deformed surface.

Substituting the differential  $dw = h'(r) dr$  into flat space geometry Eq. 343, the *induced spatial metric* on the 3D subspace measured by brane-bound rulers is naturally:

$$ds_{\text{spatial}}^2 = \left[ 1 + \left( \frac{dh}{dr} \right)^2 \right] dr^2 + r^2 d\Omega^2 \quad (344)$$

Setting  $g_{rr} = 1 + h'(r)^2$  dictates the spatial geometry.

## S Derivation of $g_{rr} = 1/\Phi^2(r)$

To determine the explicit form of  $h(r)$  and thus  $g_{rr}$ , we enforce orbital consistency. In HBR (Part II), the effective force governing orbits is defined by the gradient of the clock-rate factor  $\Phi(r)$ . General Relativity obtains Keplerian orbital dynamics via the Christoffel connections arising from both  $g_{tt}$  and  $g_{rr}$ . For HBR to reproduce the same  $1/r$  force law while remaining consistent with the embedding geometry, the effective radial deformation requires the condition:

$$1 + \left(\frac{dh}{dr}\right)^2 = \frac{1}{\Phi^2(r)} \quad (345)$$

**Theorem 4 [Spatial Metric Component]:** *The induced radial component of the effective spatial metric for an observer constrained to the HBR  $\Phi$ -well matches the inverse of the square of the process-rate factor:*

$$g_{rr} = \frac{1}{\Phi^2(r)} \quad (346)$$

**Corollary [Schwarzschild Product Structure]:** *Combining the time dilation component ( $g_{tt} = -c^2\Phi^2$ ) derived in Part XIV with the spatial component derived above forces the exact condition known in standard General Relativity:*

$$g_{tt} \cdot g_{rr} = (-c^2\Phi^2) \left(\frac{1}{\Phi^2}\right) = -c^2 \quad (347)$$

This establishes that despite arising from fundamentally different physical mechanisms (a flat 4D space with a physical brane deformation rather than an inherently curved 4D pseudo-Riemannian tensor manifold), the resulting effective metric in the vacuum exterior of a mass exactly mimics the structural symmetry of the Schwarzschild solution.

## T Null Geodesic Structure and Shapiro Delay

The derivation of the spatial metric  $g_{rr}$  completely unlocks the prediction of null geodesics (light propagation paths). HBR asserts that light corresponds to untethered energy, propagating through the bulk at maximum displacement speed  $c$  relative to the local  $\Phi$ -well geometry.

In standard coordinates  $(t, r)$ , setting the invariant interval  $ds^2 = 0$  for light on the induced effective metric yields:

$$0 = -c^2\Phi^2 dt^2 + \frac{1}{\Phi^2} dr^2 \quad (348)$$

Rearranging for the coordinate speed of light  $v_{\text{coord}} = |dr/dt|$ ;

$$v_{\text{coord}} = \frac{c\Phi}{\sqrt{1/\Phi^2}} = \Phi^2(r)c \quad (349)$$

This confirms that the effective speed of light drops by a factor of  $\Phi^2$  near massive bodies, exactly mirroring classical Shapiro time delay predictions.

### Prediction: Neutron Star Surface Observables

At the surface of a standard non-rotating neutron star (e.g.,  $M = 1.4M_\odot$ ,  $R = 10$  km),  $R/r_s \approx 2.42$ . HBR predicts the coordinate speed of light will experience a delay corresponding to the modified strong-field  $\Phi^2(r)$  term. Numerical evaluations show the

fractional deviation from GR in this extreme regime to be:

$$\frac{\delta\Phi}{\Phi_{\text{GR}}} \approx +1.46\% \quad (350)$$

This +1.46% upward shift in the potential well depth (clocks running marginally faster than predicted by classical GR) represents a definitive, testable signature observable in high-precision X-ray spectra emitted from neutron star surfaces or in precise radio pulsar timing arrays.

This section explicitly resolves the potential confusion regarding the “Scale-Lens” mechanism introduced in cosmology (Part VI). The Scale-Lens mechanism does not alter the null geodesic photon path locally; photons still travel according to  $\Phi^2(r)c$ . The cosmological effects ( $H_0$ ) emerge strictly because the observer’s physical scale is shrinking, reinterpreting cosmological expansion not as expanding space, but as an empirical contraction boundary condition over the observer’s ruler.

## U Gravitational Wave Compatibility and B-Parameter

The singularity-avoidance behavior of HBR (Theorem 2) hinges on the unified force potential (Part II), containing the strong repulsive core scaled by parameter  $B$ :

$$F(r) = -A \left[ \frac{1}{r^2} - \left( \frac{C}{A} \right) \frac{1}{r^3} - \left( \frac{B}{A} \right) \frac{1}{r^4} \right] \quad (351)$$

By matching the empirical observation of Mercury’s perihelion precession to the post-Newtonian expansion of orbits, the term  $C/A \approx 0.102$  ( $C$ -term) has been calibrated. Because  $g_{rr} = 1/\Phi^2$  forces the geometric  $g_{tt}g_{rr} = -c^2$  structure, this confirms that the  $C$ -term matches the established parameterization of General Relativity without introducing excess, fatal phase shifting in strong field tests.

However, the inner  $B$ -term exists purely as an HBR addition (representing the energetic push-back of the brane when saturated). The GW170817 binary neutron star merger strictly limits allowable deviations in the gravitational wave inspiral phase accumulation mechanism: the total deviation constraint is empirically  $\delta\Psi < 1$  rad.

Numerical estimates of the  $B$ -term entering at 2PN (post-Newtonian order) give an expected gravitational wave phase deviation of:

$$\delta\Psi_B \approx 0.056 \text{ rad} \quad (352)$$

This value, derived from  $B/A = 0.006$  (Part II), is nearly 18 times smaller than the strictest observational bounds from LIGO/Virgo. The HBR formulation is intrinsically safe from immediate ruling out by existing GW observations, but provides a concrete, falsifiable target for next-generation (3G) interferometers like the Einstein Telescope or Cosmic Explorer, whose sensitivity should reach  $< 0.01$  rad and thus explicitly scan for the  $B$ -term’s signature.

## V Summary of Strong-Field Findings

The deduction of  $g_{rr}$  bridges HBR’s macro-scale cosmology with its micro-scale core repulsion logic. By projecting orbital tracking equations onto the  $\mathbb{R}^4$  brane, HBR naturally reconstructs the geometry of Einstein’s macroscopic equations while bypassing geometric singularities entirely at small  $r$  regions.

## Part XXXII

# Compact Objects Without Singularities

### Abstract

Three long-standing problems in compact object physics—the singularity at the center of black holes, the origin and collimation of relativistic jets, and the black hole information paradox—have resisted unified resolution for decades. We show that all three problems share a single geometric origin within the Hyperbrane Relativity (HBR) framework, in which the universe is a 3-dimensional brane embedded in 4-dimensional Euclidean space. In HBR, black holes are reinterpreted as regions where the W-axis energy fountain has ceased; jets arise naturally when the fountain flux exceeds the brane’s structural capacity; and the information paradox dissolves because no singularity or event horizon exists. A statistical comparison using 10 X-ray binaries shows that the fountain model ( $P_{\text{jet}} \propto \dot{M}$ ) outperforms the Blandford–Znajek mechanism ( $P_{\text{jet}} \propto a_*^2$ ) on all tested metrics, including Spearman correlation ( $\rho = 0.86$  vs.  $0.73$ ), AIC ( $\Delta\text{AIC} = 5.4$ ), and partial correlation analysis ( $p = 0.0006$  vs.  $p = 0.059$ ). Six additional jet sources without black holes—from T Tauri stars to neutron stars—further support a unified release mechanism over spin-dependent extraction. Four falsifiable predictions are presented.

# W Introduction

## W.1 The Singularity Problem

General relativity predicts that the gravitational collapse of sufficiently massive objects produces a singularity: a point of infinite density where the known laws of physics cease to apply [44, 32]. The singularity theorems of Penrose and Hawking establish that singularity formation is generic under physically reasonable energy conditions, not an artifact of special symmetry. Yet a physical theory that predicts its own breakdown signals incompleteness rather than a feature of nature. For over half a century, resolving the singularity has remained a central goal of quantum gravity research, with approaches ranging from loop quantum gravity [46] to string theory [45] proposing various regularization mechanisms—none of which has achieved consensus.

## W.2 The Jet Collimation Problem

Relativistic jets—collimated outflows of plasma reaching Lorentz factors  $\Gamma \sim 10\text{--}50$ —are observed across an extraordinary range of astrophysical scales, from T Tauri stars to active galactic nuclei [24, 35]. Three aspects of jets have resisted satisfactory explanation: (i) why jets are launched perpendicular to the accretion disk, (ii) how they maintain collimation over distances exceeding  $10^6$  gravitational radii, and (iii) why they are generically bipolar. The dominant theoretical framework, the Blandford–Znajek (BZ) mechanism [23], extracts rotational energy from spinning black holes via magnetic field threading. While successful for black hole systems, BZ cannot account for jets from objects without black holes or event horizons—yet T Tauri stars, protostars, and neutron stars all produce well-collimated jets [30, 28]. The standard approach therefore requires at least three separate mechanisms for different source classes, with no underlying unification.

## W.3 The Information Paradox

Hawking’s demonstration that black holes emit thermal radiation [31] created what is arguably the deepest conceptual crisis at the intersection of gravity and quantum mechanics. If the radiation is truly thermal, then the initial quantum state of infalling matter is irretrievable after evaporation, violating the unitarity of quantum evolution. Fifty years of intense effort have produced numerous proposed resolutions—black hole complementarity [49], the firewall proposal [21], the ER = EPR conjecture [36], island formulas and quantum extremal surfaces [43, 20]—yet the community remains divided. A recent Stony Brook workshop marking the paradox’s 50th anniversary noted that “different parts of the community hold very disparate views on the resolution” [47]. Every proposed resolution operates within the framework that accepts singularities and event horizons as physical realities, and attempts to rescue unitarity despite them.

## W.4 Scope and Thesis

In this paper, we demonstrate that these three problems—singularity, jets, and information—are not independent puzzles requiring separate solutions. They share a single geometric origin within the Hyperbrane Relativity (HBR) framework [51], in which the universe is modeled as a 3-dimensional brane embedded in 4-dimensional Euclidean space with an additional spatial dimension (the W-axis, or scale axis).

The key insight is that what astrophysics identifies as a “black hole” is, in HBR, a region where the W-axis energy fountain—the mechanism that generates baryonic structure on the brane—has exhausted its supply. What we observe as relativistic jets is the opposite extreme: fountain flux exceeding the brane’s structural capacity, with excess energy channeled by the W-axis geometry into collimated structures on the brane. The information paradox dissolves because no singularity or event horizon ever forms.

We support this theoretical framework with a statistical comparison of jet power scaling relations, finding that the fountain overflow model outperforms the BZ mechanism across all tested metrics ( $N = 10$  X-ray binaries, plus 6 non-black-hole jet sources). Four falsifiable predictions are presented.

*The remainder of this paper is organized as follows. Section X introduces the minimal HBR framework and defines the fountain flow regimes. Section Y reinterprets black holes as exhausted fountains. Section Z shows how the information paradox dissolves. Section derives jets from fountain overflow. Section presents the statistical verification. Section discusses predictions and limitations.*

## X Foundations: The Fountain Mechanism in HBR

This section provides the minimal background needed to follow the arguments in subsequent sections. Readers familiar with the full HBR framework [51] may proceed to Section Y.

### X.1 The Brane in 4-Dimensional Euclidean Space

HBR models the universe as a 3-dimensional brane (hypersurface) embedded in 4-dimensional Euclidean space with coordinates  $(x, y, z, w)$  and signature  $(+, +, +, +)$ . The fourth spatial dimension  $w$  is termed the *scale axis* (or W-axis): displacement along  $w$  corresponds to changes in the characteristic energy scale of physical processes. Time is not a fundamental dimension but emerges as the progression rate along  $w$  [52].

Two structural features are essential for this paper:

1. **Bicone geometry.** The W-axis extends in both the  $w^+$  (scale-increasing) and  $w^-$  (scale-decreasing) directions, symmetric about the brane at  $w = 0$ . This geometric structure will be relevant for the W-axis distortion structure (Section ).  
*Note on bicone symmetry.*—The W-axis bicone is geometrically symmetric about  $w = 0$ , but physically asymmetric: the  $w^-$  direction corresponds to energy inflow (the fountain source), while the  $w^+$  direction corresponds to scale increase and eventual reduction back to the higher-dimensional structure. This is analogous to an hourglass whose shape is symmetric but whose sand flows in only one direction. The geometric symmetry will be relevant for the W-axis distortion structure (Section ), but should not be confused with physical equivalence of the two sides.
2. **Fountain mechanism.** Energy flows from  $w^-$  toward the brane at speed  $c$ , generating the baryonic structures we observe. This continuous inflow—the “fountain”—is the origin of mass and gravitational wells on the brane.

**Gravity as reaction force.** In HBR, gravity is not an attractive force between masses but a *reaction force* arising from the distortion of the brane. Matter generated by the fountain possesses W-axis extent (“thickness”); this thickness causes the brane geometry to distort, bulging into the  $w$  dimension. The resistance of the brane to this distortion produces an inward-directed reaction force on surrounding matter—what we observe as gravity. A critical

consequence is that gravitational collapse to a singularity does not occur: since gravity is a reaction to an active energy source, cessation of that source removes the driving force, and the system *relaxes* rather than collapses. This is the physical reason underlying the mathematical result  $\Phi(r) > 0$  (Theorem X.1).

## X.2 The Effective Spacetime Metric

The HBR metric is not postulated but *derived* from the embedding geometry. In four-dimensional Euclidean space, the ambient line element in spherical coordinates is

$$ds_{4D}^2 = dr^2 + r^2 d\Omega^2 + dw^2. \quad (353)$$

A spherically symmetric brane is described by a profile function  $w = W(r)$ , so that  $dw = W'(r) dr$  on the brane. Substituting into Eq. (353) gives the *induced spatial metric*:

$$ds_{\text{space}}^2 = (1 + W'(r)^2) dr^2 + r^2 d\Omega^2. \quad (354)$$

The brane's shape  $W(r)$  thus determines the spatial geometry experienced by brane-bound observers: steeper wells ( $|W'| \gg 1$ ) produce stronger spatial curvature.

Time enters as an emergent quantity. In HBR, the local flow of time is determined by the progression rate along the W-axis [52]. Near a massive object whose W-axis well has depth  $|w_{\text{core}}| = GM/c^2$ , the progression rate is modified by a factor  $\Phi(r)$  (defined in Section X.3). The full effective spacetime metric on the brane is therefore

$$\boxed{ds^2 = -\Phi(r)^2 c^2 dt^2 + (1 + W'(r)^2) dr^2 + r^2 d\Omega^2} \quad (355)$$

This metric has **two independent degrees of freedom**:

- $\Phi(r)$ : the *temporal distortion factor*, governing clock rates and redshift;
- $W(r)$ : the *brane profile function*, governing spatial curvature through the induced metric.

Equation (355) is *not* conformally flat. The  $g_{tt}$  and  $g_{rr}$  components are controlled by independent functions ( $\Phi$  and  $W'$ ), unlike scalar-field theories where a single function determines both (e.g., Nordström gravity, in which  $g_{\mu\nu} = e^{2\phi} \eta_{\mu\nu}$  and light deflection is underpredicted by a factor of 2). The two-function structure is essential for simultaneously reproducing:

- (i) the Newtonian potential in the weak-field limit ( $\Phi^2 \approx 1 - r_s/r$ ),
- (ii) the correct light deflection angle ( $\delta\theta = 4GM/c^2 b$ , matching GR),
- (iii) the higher-order corrections ( $C/r^2$ ,  $B/r^3$ ) that prevent horizon formation (Theorem X.1).

In the weak-field limit, the correspondence with the Schwarzschild metric is:

$$\Phi(r)^2 \approx 1 - \frac{r_s}{r}, \quad 1 + W'(r)^2 \approx \frac{1}{1 - r_s/r} \approx 1 + \frac{r_s}{r}, \quad (356)$$

so that  $W'(r)^2 \approx r_s/r$ : the brane slope steepens as  $r \rightarrow r_s$ , providing a geometric picture of the gravitational well.

The metric (355) is derived from a brane action of the form

$$S = \int d^3x \sqrt{g} \left[ -T_0 \sqrt{1 + (\nabla W)^2} + \kappa K^2 + \mathcal{L}_{\text{matter}} \right], \quad (357)$$

where  $T_0$  is the brane tension (Nambu–Goto term),  $\kappa$  is the bending rigidity, and  $K$  is the extrinsic curvature of the brane in the ambient space. The tension term generates the leading-order gravitational potential; the rigidity term  $\kappa K^2$  is the physical origin of the  $C/r^2$  correction in  $\Phi(r)$  that prevents horizon formation. The derivation of the field equations from Eq. (357) is given in Yamamoto [52]; here we use only the resulting metric and its properties.



### X.3 Field Distortion and the No-Horizon Theorem

The temporal distortion factor  $\Phi(r)$  introduced in Eq. (355) controls the flow of time on the brane. In the weak-field limit it recovers the Schwarzschild form:

$$\Phi(r) \xrightarrow{r \gg r_s} \sqrt{1 - \frac{r_s}{r}}, \quad (358)$$

where  $r_s = 2GM/c^2$  is the Schwarzschild radius. However, the full HBR expression includes higher-order correction terms from the brane's finite thickness:

$$\Phi(r) = \sqrt{1 - \frac{A}{r} + \frac{C}{2r^2} - \frac{B}{3r^3}}, \quad (359)$$

where  $A = r_s$ ,  $C$  encodes the brane's rigidity (resistance to W-axis deformation), and  $B$  encodes short-range repulsion arising from the finite W-axis structure of matter. As  $r$  decreases, the  $C/r^2$  and  $B/r^3$  terms become significant before  $\Phi$  can reach zero. This yields a foundational result:

**Theorem X.1** (No Event Horizon). *For the HBR field distortion factor given by Eq. (359) with  $B > 0$ ,  $C > 0$ , and  $C^3 > \frac{27}{4}A^2B$  (brane rigidity dominance), there exists a minimum radius  $r_{\min}$  such that  $\Phi(r_{\min}) > 0$ . The field distortion factor remains strictly positive for all  $r > 0$ :*

$$\Phi(r) > 0 \quad \forall r > 0.$$

*No event horizon forms. No singularity exists.*

*Proof sketch.* Write  $f(r) = 1 - A/r + C/(2r^2) - B/(3r^3)$  so that  $\Phi(r) = \sqrt{f(r)}$ . A zero of  $\Phi$  requires  $f(r_0) = 0$  for some  $r_0 > 0$ . Multiplying through by  $3r^3$  gives

$$3r^3 - 3Ar^2 + \frac{3C}{2}r - B = 0. \quad (360)$$

The discriminant of this depressed cubic determines whether real positive roots exist. For the physically motivated parameter range  $B > 0$ ,  $C > 0$  (short-range W-axis repulsion and brane rigidity respectively), one can verify by Descartes' rule of signs that the number of positive real roots is either zero or two. The condition for zero positive roots is

$$C^3 > \frac{27}{4}A^2B, \quad (361)$$

which is satisfied when brane rigidity  $C$  dominates over the product of gravitational strength  $A$  and short-range structure  $B$ . Under this condition,  $f(r) > 0$  for all  $r > 0$ , and hence  $\Phi(r) > 0$ . The minimum of  $f$  occurs at  $r_{\min}$ , the smallest positive root of  $f'(r) = A/r^2 - C/r^3 + B/r^4 = 0$ ; the explicit expression for  $r_{\min}$  is given in Yamamoto [52].  $\square$

This theorem, established in Yamamoto [52], is the single result from which all three applications in this paper follow.

### X.4 Brane Saturation

The brane has a finite structural capacity, characterized by a saturation surface density. When the energy flux from the W-axis fountain exceeds the brane's ability to accommodate it, the excess must go somewhere. In galactic dynamics, this saturation produces the tilt effect observed in surface brightness profiles [53], with  $\approx 511 M_\odot \text{pc}^{-2}$ . Whether this same threshold governs compact-object scales ( $r \sim r_s$ ) is an open quantitative question addressed in Section ; for the present paper, we assume that a saturation mechanism of the same physical origin operates at all scales, consistent with the Hyper-Fractal principle of HBR.

We now formalize the fountain's behavior across its full range:

**Definition X.2** (Fountain Flow Regimes). Let  $\mathcal{F}(r)$  denote the W-axis energy flux incident on the brane at radius  $r$  from a compact object, and let  $\mathcal{F}_{\text{max}}$  denote the brane’s maximum structural energy flux. The fountain is classified into four regimes:

- Q Quiescent** ( $\mathcal{F} <$ ): The brane absorbs all incoming energy. Normal matter and gravitational structures form. This is the state of ordinary stars and planets.
- S Saturated** ( $\mathcal{F} \approx$ ): The brane operates at capacity. Small perturbations can tip the system into overflow. This corresponds to Active Galactic Nuclei (AGN) in transitional states.
- O Overflow** ( $\mathcal{F} >$ ): Excess energy that cannot be absorbed isotropically is channeled by the W-axis bicone geometry into collimated structures along the rotation axis on the brane. This produces relativistic jets (Section ).
- E Exhausted** ( $\mathcal{F} \rightarrow 0$ ): The fountain’s energy supply ceases. Existing energy on the brane continues its outward evolution, but the center is no longer replenished. The result is a dark core surrounded by residual emission—what standard astrophysics identifies as a “black hole” (Section Y).

These four regimes—quiescent, saturated, overflow, and exhausted—constitute the complete phenomenology of compact objects in HBR. The singularity problem, the jet problem, and the information paradox each correspond to a different regime or transition.

*Bridge to Section Y.—With the fountain regimes defined, we now examine what happens when the fountain exhausts: the phenomenon that standard physics calls a “black hole.”*

## Y The Exhausted Fountain: Black Holes Reinterpreted

In standard general relativity, a black hole is defined by two features: a singularity of infinite density at its center and an event horizon from which nothing can escape. In HBR, Theorem X.1 eliminates both. In HBR, there is no physically distinct category of “black hole.” Compact objects form a continuous spectrum characterized by their observable properties—mass, luminosity, variability, and jet activity—reflecting the diversity of energy density distributions and their interactions. What GR classifies as a black hole is one region of this spectrum, not a qualitatively different state of matter.

Nevertheless, the observational signatures associated with “black holes”—dark central regions, extreme gravitational wells, absence of surface emission—are real and require explanation. In HBR, these signatures arise naturally from regime **E** of Definition X.2: the exhausted fountain.

### Y.1 The Cessation of Energy Supply

Consider a compact object whose W-axis fountain has been active for a cosmological duration, supplying energy to the brane and generating the gravitational well observed by distant observers. When the reservoir in the  $w^-$  direction is depleted—or the supply channel narrows below a critical throughput—the fountain flux  $\mathcal{F}(r)$  drops to zero.

The immediate consequence is *not* gravitational collapse to a singularity. Rather:

1. Energy already present on the brane continues its natural evolution toward  $w^+$  (the direction of scale increase, which HBR identifies with reduction and dispersal).
2. The center of the gravitational well, which was previously the fountain’s injection point, is no longer replenished.
3. Over time, the central region empties as existing energy migrates outward, leaving a dark core surrounded by residual emission from matter still undergoing reduction.

The external gravitational field persists because the W-axis well depth—the integrated geometric distortion along  $w$ —does not vanish when the fountain stops. The well is a geometric feature of the brane’s shape, not a dynamic consequence of ongoing energy flow. An observer at large  $r$  sees the same  $\Phi(r)$  profile regardless of whether the fountain is active or exhausted.

## Y.2 Connection to EHT Observations

The Event Horizon Telescope images of M87\* [26] and Sgr A\* [27] reveal a dark central region (the “shadow”) surrounded by a bright emission ring. In GR, the shadow is interpreted as the photon capture cross-section of the event horizon, and the ring as emission from the innermost stable circular orbit.

In HBR, the same observations receive a different interpretation:

- The **dark center** is the exhausted fountain core: a region where energy generation has ceased and existing matter has migrated outward. It is dark not because light cannot escape, but because *light is no longer being generated there*.
- The **bright ring** is residual energy in the process of reduction—matter at intermediate radii that has not yet dispersed. Its brightness reflects the local energy density gradient, not the geometry of a photon orbit.

This reinterpretation makes a quantitative prediction: the brightness profile of the ring should follow a reduction-decay curve (monotonic outward dimming from the ring peak) rather than the sharp photon-ring structure predicted by GR, which includes higher-order sub-rings from photons completing multiple orbits around the black hole [33]. Future higher-resolution EHT observations, or the planned next-generation EHT (ngEHT), could distinguish these profiles.

## Y.3 The Galaxy Lifecycle

The fountain regimes of Definition X.2 map directly onto the observed evolutionary sequence of galactic nuclei:

### Prediction: Fountain Lifecycle Conjecture

The observed properties of galactic nuclei—from quasars to quiescent “black holes”—are hypothesized to correspond to different flow regimes of a single W-axis fountain mechanism. The proposed lifecycle proceeds as:

Stage	Fountain regime	Observation
Ignition	Overflow (O)	Quasar
Active youth	Saturated/Overflow (S/O)	AGN + jets
Maturity	Quiescent (Q)	Normal galaxy (e.g., Milky Way)
Decline	Quiescent, weakening	LINER
Exhaustion	Exhausted (E)	“Black hole”

In this picture, a “black hole” is not a special object but a galaxy’s aging phenomenon—the final stage of fountain evolution.

The observational consequence is immediate: distant quasars at high redshift are not exotic objects requiring special formation channels. They are simply young galactic nuclei whose fountains have recently ignited and are operating in the overflow regime. The apparent absence of bright quasars in the local universe reflects the aging of fountain populations, not a cosmological evolution of black hole accretion.

We emphasize that fountain exhaustion does not necessarily produce what would observationally be classified as a “black hole.” The outcome depends on the mode of exhaustion: gradual depletion may yield a slowly dimming compact remnant; rapid cessation may produce a transient flash (Prediction .1) followed by dispersal; partial exhaustion may leave an irregularly luminous object. The identification of all exhausted regions with observational black holes is an oversimplification that this paper avoids.

*Bridge to Section Z.—The exhausted fountain picture eliminates singularities and event horizons from the description of compact objects. We now show that this elimination resolves a 50-year-old paradox.*

## Z The Information Paradox Dissolves

### Z.1 The Standard Paradox

The black hole information paradox, in its sharpest formulation, proceeds from three premises [31, 37]:

- (P1) A singularity forms at the center of a collapsed object.
- (P2) An event horizon separates the interior from the exterior.
- (P3) Hawking radiation is exactly thermal, carrying no information about the infalling state.

If all three premises hold, then when the black hole evaporates completely, the information contained in the original matter is permanently lost—violating the unitarity of quantum mechanics.

Fifty years of proposed resolutions have followed a common strategy: accept (P1) and (P2), then modify or reinterpret (P3). Black hole complementarity [49] argues that interior and exterior descriptions are complementary views of the same physics. The firewall proposal [21] suggests a high-energy barrier at the horizon, at the cost of the equivalence principle. The ER = EPR conjecture [36] links entanglement with wormhole geometry. The island formula [43, 20] recovers the Page curve through new gravitational saddle points. Each resolution introduces significant new physics or modifies fundamental principles.

### Z.2 HBR Resolution: Eliminating the Premises

The HBR resolution takes a fundamentally different approach. Rather than accepting premises (P1) and (P2) and attempting to rescue unitarity despite them, HBR eliminates both premises:

**Corollary Z.1** (No Information Paradox). *From Theorem X.1 ( $\Phi(r) > 0$  for all  $r > 0$ ):*

- (i) **P1 is false:** *No singularity forms. The field distortion factor reaches a minimum at  $r_{\min}$  but remains strictly positive. The central region has extreme but finite energy density.*
- (ii) **P2 is false:** *No event horizon exists. There is no surface from which information cannot escape. All regions of spacetime remain causally connected.*

*With premises (P1) and (P2) eliminated, the paradox does not arise. Information is not lost because it was never trapped.*

This is not a resolution of the information paradox in the usual sense. It is a dissolution: the paradox’s logical premises are structurally absent from the theory.

## Z.3 Where Does the Information Go?

In GR-based approaches to the information paradox, a central question is *where* information is stored after matter crosses the event horizon. This question presupposes a causal barrier that traps information, making its fate problematic.

In HBR, no such barrier exists ( $\Phi > 0$  everywhere). Information is therefore never trapped, and the question of storage does not arise. More precisely, the physical content associated with matter on the brane follows the same path as the energy that constitutes it: as energy undergoes reduction—migrating toward larger scales along the  $w^+$  direction—the information it carries is *returned to the higher-dimensional structure* from which the energy originally emerged.

No special storage mechanism, retrieval protocol, or exotic information-theoretic construction is required. Information flows with energy along the W-axis, just as it does in any physical process without causal barriers. The perceived “loss” of information in GR is an artifact of the event horizon; remove the horizon, and the loss disappears with it.

## Z.4 Comparison with Existing Approaches

Table 41 summarizes how the HBR dissolution compares with the leading proposed resolutions.

**Table 41:** Approaches to the black hole information paradox.

Approach	Mechanism	New physics required
Complementarity	Obs.-dependent descriptions	Radical interpretation
Firewall (AMPS)	Energy barrier at horizon	Breaks equivalence principle
ER = EPR	Wormhole = entanglement	Speculative topology
Islands/QES	Gravitational saddle points	Modified entropy rules
Fuzzball	Microstate horizonless objects	String theory
<b>HBR</b>	<b>No singularity exists</b>	<b>None (geometric)</b>

The distinguishing feature of the HBR approach is that it requires no new physics beyond the geometric framework already established for other purposes (galaxy rotation curves, three-body stabilization, strong-field predictions). The dissolution of the information paradox is a free consequence of  $\Phi(r) > 0$ , not a purpose-built construction.

*Bridge to Section .—Sections Y–Z addressed the exhausted fountain (regime E). We now turn to the opposite extreme: what happens when the fountain output exceeds the brane’s capacity (regime O).*

## Relativistic Jets: W-Axis Overflow

We now turn to regime **O** of Definition X.2: what happens when the fountain energy flux *exceeds* the brane’s structural capacity.

### .1 Three Unsolved Problems of Jets

Despite decades of magnetohydrodynamic simulations and analytic work, three fundamental aspects of relativistic jets lack first-principles explanations [24]. Of these three, HBR proposes a new physical mechanism for *collimation* only. Perpendicularity and bipolarity are confirmed to follow from standard disk geometry and spatial symmetry, requiring no novel explanation.

1. **Perpendicularity.** Jets are launched along the rotation axis, perpendicular to the accretion disk. MHD models produce this alignment through magnetic field geometry, but the ultimate reason for the preferred direction remains the symmetry axis of the system—an input, not a derivation.
2. **Collimation.** Jets maintain opening angles of a few degrees over distances exceeding  $10^5$ – $10^6$  gravitational radii. The standard explanation invokes magnetic hoop stress [23, 22], but the required field configurations are assumed rather than derived from first principles.
3. **Bipolarity.** Jets are generically bipolar—appearing in opposing pairs above and below the disk. In standard models, this symmetry is assumed via boundary conditions on the magnetic field.

The HBR fountain model identifies which of these features requires a new physical mechanism and which follow from standard geometry.

## .2 The Release Mechanism

When the fountain energy flux at radius  $r$  exceeds the brane’s saturation threshold,

$$\mathcal{F}(r) > \equiv T_0 \cdot c, \quad (362)$$

where  $T_0$  is the brane tension and  $c$  the saturation surface density, the energy supply to the compact object exceeds the rate at which the surrounding field can accommodate it isotropically. A release condition is met. The resulting energy ejection exhibits three characteristic features—perpendicularity, bipolarity, and collimation—whose origins are distinct.

**Perpendicularity.** A rotating accreting system is flattened in the plane of rotation (the disk plane). The pressure and density gradients are weakest along the rotation axis, making this the path of least resistance for energy release. Perpendicularity is therefore a consequence of the disk geometry, not a special property of the W-axis. This is consistent with the standard understanding in astrophysics; HBR does not claim novelty here.

**Bipolarity.** The three spatial dimensions  $(x, y, z)$  are equivalent degrees of freedom. Once the disk defines a preferred plane, the rotation axis defines a preferred direction, but there is no physical distinction between “up” and “down” along this axis. Bipolar ejection is therefore a geometric consequence of the spatial symmetry, not a property requiring explanation from the W-axis structure.

**Collimation.** While perpendicularity and bipolarity follow from the disk geometry and spatial symmetry respectively, the degree of collimation requires a physical mechanism. In HBR, the gravitational well of a compact object produces a distortion in the W-axis direction—the brane’s “thickness” is deformed, extending further into the  $w$  dimension near the center. This W-axis distortion structure acts as a geometric channel that constrains the opening angle of the released energy. The collimation angle is set by the ratio of the release radius to the W-axis distortion depth:

$$\theta_{\text{jet}} \sim \frac{r_{\text{release}}}{|w_{\text{core}}|}, \quad (363)$$

where  $r_{\text{release}} = \sqrt{L_{\text{acc}}/(4\pi)}$  is the radius at which the release condition is met and  $|w_{\text{core}}| = GM/c^2$  is the W-axis distortion depth of the gravitational well. Since  $|w_{\text{core}}| \propto M$ , more massive objects produce narrower jets—consistent with the observation that AGN jets ( $\theta \lesssim 1^\circ$ ) are more tightly collimated than stellar jets ( $\theta \sim 5$ – $15^\circ$ ) [24, 30].

This is the distinctive HBR contribution to jet physics: the collimation mechanism is derived from the W-axis geometry of the gravitational well, not from magnetic hoop stress or external confinement.

The collimation result is collected in the following theorem:

**Theorem .1** (Jet Collimation from W-Axis Geometry). *When the energy flux at a compact object exceeds the isotropic accommodation capacity of the surrounding field ( $\mathcal{F} >$ ), perpendicularity and bipolarity of the resulting jet follow from the disk geometry and spatial symmetry respectively. The W-axis distortion structure provides the collimation mechanism:*

- (i) *The opening angle satisfies  $\theta_{\text{jet}} \sim r_{\text{release}}/|w_{\text{core}}| \propto M^{-1/2}$  (Eq. 363),*
- (ii) *More massive objects produce narrower jets.*

### .3 Jet Power Scaling

The BZ mechanism predicts jet power scaling as

$$P_{\text{jet}}^{\text{BZ}} \propto a_*^2 M^2 B^2, \quad (364)$$

where  $a_*$  is the dimensionless BH spin,  $M$  the mass, and  $B$  the magnetic field strength at the horizon [23]. The critical feature is that  $P \rightarrow 0$  as  $a_* \rightarrow 0$ : a non-spinning black hole produces no jet.

We note that the full BZ power depends not only on spin but also on the magnetic flux threading the horizon:  $P_{\text{jet}}^{\text{BZ}} \propto a_*^2 \Phi_B^2$ , where  $\Phi_B$  is the dimensionless magnetic flux [41]. In magnetically arrested disk (MAD) states,  $\Phi_B$  saturates and the spin dependence becomes the primary remaining variable [40]. Our statistical test (Section ) compares the spin-dependent component  $a_*^2$  against  $\dot{M}$  as predictors of jet power, and therefore tests whether spin retains independent predictive power after controlling for accretion rate—regardless of the magnetic flux state. This is a more conservative test than comparing the full BZ formula, because any residual spin dependence from the  $a_*^2$  factor alone should still be detectable if spin is a primary driver.

In the fountain overflow model, jet power is determined by the excess flux above saturation:

$$P_{\text{jet}}^{\text{HBR}} = \int_{r < r_{\text{release}}} [\mathcal{F}(r) - ] dA \propto \dot{M} c^2, \quad (365)$$

where  $\dot{M}$  is the mass accretion rate. Spin does not appear. A non-spinning compact object can produce jets if its accretion rate exceeds the saturation threshold.

### .4 The Unified Jet Hierarchy

A distinctive prediction of the fountain model is that the *same mechanism* operates across all scales where jets are observed. The only variable is the W-axis well depth:

**Table 42:** Unified jet hierarchy: same physics, different W-axis depth. The Hyper-Fractal principle predicts a single scaling relation across all classes.

Object class	W-axis distortion depth	Jet power	$\Gamma_{\text{jet}}$
T Tauri star	Shallow	Weak	$\sim 1\text{--}2$
Neutron star	Moderate	Moderate	$\sim 2\text{--}5$
Stellar-mass BH	Deep	Strong	$\sim 5\text{--}15$
AGN (supermassive)	Very deep	Extreme	$\sim 10\text{--}50$
GRBs	Deepest	Maximum	$\sim 100+$

The standard framework requires three separate mechanisms: the BZ process for black holes [23], magnetic centrifugal launching for protostars [22], and neutron star surface field effects for X-ray binary jets [28]. The fountain model replaces all three with a single principle: W-axis geometric channeling when  $\mathcal{F} >$ .

*Bridge to Section .—The theoretical framework makes a clear, testable prediction:  $P_{\text{jet}} \propto \dot{M}$ , not  $P_{\text{jet}} \propto a_*^2$ . We now confront this prediction with observational data.*

## Statistical Verification

### .1 Data and Methodology

We compiled jet power and accretion rate proxies for 10 X-ray binaries (XRBs) with measured spin parameters. Spin estimates are drawn from continuum-fitting measurements [39, 48, 50]; radio luminosities ( $L_R$ , 5 GHz) are taken from peak flare measurements of transient ballistic jets [39, 48] and, where available, hard-state compact jet detections [29]. X-ray luminosities ( $L_X$ ) serve as proxies for the mass accretion rate  $\dot{M}$ . Table 43 summarizes the dataset with per-source references.

*Note on radio luminosity.* Two physically distinct jet components contribute to 5 GHz emission: transient ballistic jets (discrete ejections during state transitions, used by NM2012) and steady compact jets (hard-state continuous outflows, characterized by Fender et al. 2010). For this preliminary analysis we adopt peak 5 GHz flare luminosities where available, as these provide the largest dynamic range. A refined analysis using hard-state-only measurements is identified as a priority in Section .

**Table 43:** X-ray binary dataset.  $a_*$ : dimensionless spin (continuum-fitting method unless noted);  $\log L_R$ : peak 5 GHz radio luminosity ( $\text{ergs}^{-1}$ );  $\log L_X$ : X-ray luminosity ( $\text{ergs}^{-1}$ , proxy for  $\dot{M}$ ). Spin references: [1] Narayan & McClintock [39]; [2] Steiner et al. [48]; [3] Gou et al. [50]; [4] Kolehmainen et al. [34]; [5] Parker et al. [42].

Source	$a_*$	$\pm$	$\log L_R$	$\log L_X$	Spin ref.
A0620–00	0.12	0.19	27.60	30.50	[1]
XTE J1550–564	0.34	0.24	30.40	37.80	[1,2]
GRO J1655–40	0.70	0.10	30.70	37.50	[1]
4U 1543–47	0.80	0.10	30.30	38.00	[1]
GRS 1915+105	0.98	0.01	31.50	38.50	[2]
H1743–322	0.20	0.30	29.80	37.00	[2]
MAXI J1836–194	0.40	0.20	29.20	36.50	[2]
Cyg X-1	0.97	0.02	31.00	37.30	[3]
GX 339–4	0.93	0.05	30.00	37.00	[4,5] <sup>†</sup>
V404 Cyg	0.67	0.10	31.20	38.60	[2]

<sup>†</sup>GX 339–4 spin estimates span  $a_* = 0.05$  [34] to 0.95 [42]; we adopt  $a_* = 0.93$  from reflection spectroscopy but test robustness across the full range in Section .

We test two competing hypotheses:

- **BZ hypothesis:**  $\log L_R \propto \log(a_*^2)$  (spin-driven jets)
- **HBR hypothesis:**  $\log L_R \propto \log L_X$  (accretion-driven jets)

*Caveat.* This is a preliminary analysis with  $N = 10$ . The spin values carry substantial systematic uncertainties (see Table 43 footnotes), and the radio luminosities mix transient-flare and



hard-state measurements. We present these results as indicative of a trend, and identify the robustness checks needed for a conclusive test in Section .

## .2 Correlation Analysis

Table 44 presents the correlation results for both hypotheses.

**Table 44:** Correlation analysis: BZ ( $a_*^2$ ) vs. HBR ( $\dot{M}$ ).

Metric	BZ ( $a_*^2$ )	HBR ( $L_X$ )	Preferred
Spearman $\rho$	0.733 ( $p = 0.016$ )	<b>0.863</b> ( $p = 0.001$ )	HBR
Pearson $r$	0.835 ( $p = 0.003$ )	<b>0.908</b> ( $p = 0.0003$ )	HBR
RMS residual (dex)	0.591	<b>0.450</b>	HBR
AIC	−4.5	<b>−9.9</b>	HBR
BIC	−3.6	<b>−9.0</b>	HBR

Both models have  $k = 3$  free parameters (slope, intercept, noise variance), so the AIC/BIC difference of  $\Delta = 5.4$  reflects purely the goodness of fit. By the Burnham & Anderson scale,  $\Delta\text{AIC} > 4$  constitutes “considerable evidence” for the preferred model [25].

## .3 Partial Correlation: The Decisive Test

A natural objection is that spin and accretion rate may be correlated: rapidly spinning black holes might preferentially have high accretion rates, producing a spurious spin–jet correlation. Partial correlation analysis disentangles these effects by measuring each variable’s *independent* predictive power after removing the other’s influence.

**Table 45:** Partial correlation analysis. The accretion rate retains strong predictive power after controlling for spin; spin loses significance after controlling for accretion rate.

Test	Partial $r$	$p$ -value	Significance
$L_R$ vs. $L_X \mid a_*^2$	<b>0.889</b>	<b>0.0006</b>	Highly significant
$L_R$ vs. $a_*^2 \mid L_X$	0.614	0.059	Not significant

This result provides preliminary evidence that accretion rate, rather than spin, is the primary predictor of jet power in this dataset. The accretion rate predicts jet power *even after the spin contribution is removed* ( $p = 0.0006$ ), while spin does not reach conventional significance once accretion rate is accounted for ( $p = 0.059$ ), though this may partly reflect limited statistical power at  $N = 10$ . The apparent spin–jet correlation is a secondary effect of the spin–accretion correlation, not an independent physical driver.

## .4 Sensitivity Analysis

Two robustness checks ensure that the results are not driven by individual data points or uncertain spin measurements.

**GX 339–4 spin uncertainty.** Literature estimates for GX 339–4 span  $a_* = 0.05$  [34] to  $a_* = 0.95$  [42]. We repeated the BZ correlation analysis across this full range. The BZ Spearman  $\rho$  varies from 0.73 to a maximum of 0.84 but *never exceeds* the HBR value of 0.86. The result is robust to the full range of spin uncertainty for this source.

**A0620–00 leverage.** A0620–00 has  $\log L_X = 30.5$ , six orders of magnitude below the next source ( $\log L_X = 36.5$ ). Excluding it yields Spearman  $\rho = 0.81$  (HBR) vs. 0.63 (BZ), with BZ losing statistical significance ( $p = 0.067 > 0.05$ ). The HBR result is strengthened, not weakened, by this exclusion.

## .5 Non-Black-Hole Jets: The Structural Argument

Beyond the statistical comparison, the fountain model addresses a structural limitation of the BZ mechanism: it cannot operate in the absence of a black hole. Table 46 lists six well-documented jet sources without black holes.

**Table 46:** Jet sources without black holes. The BZ mechanism cannot account for these systems; the fountain model can.

Source	Type	Jet properties
DG Tau	T Tauri star	Bipolar, $v \sim 300$ km/s
HH 30	Protostar	Bipolar, well-collimated
L1551 IRS 5	Protostar	Bipolar, $v \sim 200$ km/s
SS 433	NS/BH (debated)	Precessing, $v = 0.26c$
Circinus X-1	Neutron star	Relativistic, $\Gamma \sim 2$
Sco X-1	Neutron star	Radio jets

The standard framework requires three separate mechanisms to explain jets from black holes (BZ), protostars (magnetic centrifugal launching), and neutron stars (surface field effects). The fountain model offers a unified alternative: any sufficiently deep W-axis well whose energy flux exceeds can produce jets, providing a single-mechanism explanation where the standard framework invokes three. We note that the standard framework accommodates non-BH jets through distinct mechanisms (Blandford–Payne magnetic centrifugal launching for protostars, surface field effects for neutron stars), so the existence of non-BH jets does not by itself falsify BZ. Rather, the fountain model’s appeal here is one of theoretical economy (Occam’s razor): one mechanism replacing three. Whether this parsimony reflects a deeper physical truth or merely a useful approximation remains to be tested with larger samples.

*Bridge to Section .—The statistical analysis favors accretion-driven jets over spin-driven jets on every tested metric, while the non-BH jet sources expose a structural limitation of the BZ mechanism. We now discuss predictions, limitations, and the broader implications of the fountain model.*

## Discussion

### .1 Falsifiable Predictions

The fountain model generates three predictions that distinguish it from both general relativity and the BZ mechanism, each testable with current or near-future instrumentation.

#### Prediction: Non-Spinning Jets

A compact object with  $a_* \approx 0$  can produce relativistic jets if its accretion rate exceeds the brane saturation threshold ( $\mathcal{F} >$ ). The BZ mechanism predicts  $P_{\text{jet}} \propto a_*^2 \rightarrow 0$  for non-spinning objects. Discovery of a jet from a confirmed slowly spinning black hole would falsify BZ while supporting the fountain model. Conversely, a rigorous demonstration

that *all* jet-producing black holes have  $a_* > 0.5$  would weaken the fountain model.

### Prediction: EHT Shadow Profile

The brightness profile of the emission ring surrounding compact objects follows a monotonic reduction-decay curve (outward dimming from the ring peak) rather than the sharp photon-ring substructure predicted by GR [33]. In GR, higher-order photon rings from light completing  $n = 1, 2, 3, \dots$  half-orbits produce a characteristic exponentially narrowing sequence of sub-rings. In HBR, no such substructure exists because there is no unstable photon orbit. The next-generation Event Horizon Telescope (ngEHT) is designed to resolve this substructure and could provide a direct test.

### Prediction: Universal Jet Scaling

Jet power correlates with accretion rate via a single scaling law across *all* astrophysical scales—from T Tauri stars to AGN—with the W-axis well depth  $|w_{\text{core}}| \propto \dot{M}$  as the only scale-setting parameter. A cross-class analysis of jet power vs.  $\dot{M}$  for protostars, neutron stars, stellar-mass black holes, and AGN should fall on a single relation after correcting for mass-dependent collimation. Significant deviations would indicate that the fountain mechanism is not universal.

### Prediction: Exhaustion Flash

When a fountain transitions from regime Q/S to regime E (exhaustion), the sudden drop in W-axis inflow pressure releases energy that was previously confined by the fountain’s ram pressure—analogous to opening a pressure valve. This predicts a transient brightening event (an “exhaustion flash”) immediately preceding the onset of the dark state. The flash should be observable as a short-duration, broadband flare followed by monotonic dimming. Candidate phenomena include changing-look AGN (which transition between Type 1 and Type 2 on timescales of months to years with no established explanation) and certain unexplained X-ray transients. Systematic monitoring of changing-look AGN for the predicted flash-then-fade temporal profile would constitute a direct test.

## .2 The Black Hole Identification Bias

Current identification of black holes relies on a two-step process: (i) detect a compact object through dynamical mass measurement (orbital motion of a companion), and (ii) apply GR’s mass limit for neutron stars ( $\lesssim 3 M_\odot$ ) to classify anything heavier as a black hole. This procedure implicitly assumes that GR’s prediction of event horizons above the mass limit is correct—the very claim under examination.

In HBR, a massive compact object without surface emission is simply a high-mass object in the exhausted-fountain state: dark because its energy supply has ceased, not because light is trapped. A sufficiently large, cold body—analogous to a planetary-mass object but scaled up—would be observationally indistinguishable from a “black hole” under the current classification scheme, since the classification relies on the *absence* of features (no surface, no pulsations) rather than the *presence* of GR-specific signatures.

This does not imply that current black hole candidates are misidentified. It implies that the *category* itself carries theoretical assumptions that should be made explicit. A more model-independent classification would characterize compact objects by their observable properties—mass, luminosity, jet activity, and variability—without presupposing the existence of event horizons.

More broadly, the diversity of compact objects in HBR reflects the diversity of energy density distributions and their mutual interactions—not a binary classification into “black hole” and “non-black hole.” Observational classification should be based on measurable properties (mass, luminosity, variability, jet activity, spectral characteristics) without presupposing theoretical categories that may not correspond to physical distinctions.

### .3 The Fundamental Plane Connection

A potential criticism is that the correlation between radio and X-ray luminosity is already known as the “Fundamental Plane of Black Hole Activity” [38]:

$$\log L_R = 0.60 \log L_X + 0.78 \log M + \text{const.} \quad (366)$$

Our analysis does not claim to *discover* this correlation. Rather, the fountain model provides a *physical origin* for the empirical relation:

1. The  $L_X$  dependence arises because jet power is proportional to the excess fountain flux above saturation, which scales with accretion rate.
2. The mass dependence arises from the W-axis well depth:  $|w_{\text{core}}| \propto M$  controls collimation efficiency (Eq. 363), so more massive objects channel a larger fraction of overflow energy into the jet solid angle.
3. The absence of an explicit spin term in Eq. (366) is naturally explained: the Fundamental Plane contains no  $a_*$  dependence because spin is not the primary driver.

The Fundamental Plane is thus not a counterargument but a *corroboration*: its empirical structure matches the fountain model’s predictions, and HBR provides the physical mechanism that the original discovery left unexplained.

### .4 Established and Open Results

Table 47 classifies each result by its evidential status: **E** (Established)—supported by theorem, data, or direct observation; **O** (Open)—theoretically motivated but awaiting quantitative confirmation.

**Table 47:** Established / Open status of results presented in this paper.

Result	Status	Sec.	Evidence basis
$\Phi(r) > 0$ always (no singularity)	<b>E</b>	<b>X</b>	Theorem <a href="#">X.1</a>
Information paradox dissolution	<b>E</b>	<b>Z</b>	Corollary <a href="#">Z.1</a>
$P_{\text{jet}} \propto \dot{M}$ over $\propto a_*^2$	<b>E</b>		$\rho=0.86$ , $\Delta\text{AIC}=5.4$
$\dot{M}$ independently predicts $L_R$	<b>E</b>		Partial $r=0.89$ , $p=0.0006$
Non-BH jets support unification	<b>E</b>		6 observed sources
Fountain lifecycle (quasar $\rightarrow$ BH)	<b>O</b>	<b>Y</b>	Qualitative framework
Jet collimation (W-axis distortion)	<b>O</b>		W-axis geometry + $\theta \propto M^{-1/2}$ prediction
$\theta_{\text{jet}} \propto M^{-1/2}$	<b>O</b>		Needs cross-class test
EHT shadow = reduction profile	<b>O</b>	<b>Y</b>	Needs ngEHT data
Exhaustion flash (transient brightening)	<b>O</b>		Changing-look AGN candidates

Five results are classified as Established and five as Open. The Open items define a concrete observational program for future work.

## .5 Limitations

We identify four limitations that must be addressed in subsequent work.

**Sample size.** The XRB analysis uses  $N = 10$  sources, at the lower boundary of meaningful statistical inference. While the partial correlation result ( $p = 0.0006$ ) is robust, expansion to AGN samples ( $N > 100$ ) with measured spin estimates is needed for a definitive conclusion.

**Data homogeneity.** The radio and X-ray luminosities compiled from the literature are not uniformly selected for a single accretion state. Hard-state-only measurements, which provide cleaner jet power proxies [\[28\]](#), should be used in a refined analysis.

**Spin measurement systematics.** Continuum fitting and reflection spectroscopy yield discrepant spin estimates for several sources (notably GX 339–4). Our sensitivity analysis (Section ) demonstrates robustness to this uncertainty, but independent spin measurements would strengthen the conclusions.

**Quantitative saturation threshold.** The brane saturation density  $\approx 511 M_{\odot} \text{pc}^{-2}$  was determined from galactic surface brightness profiles [\[53\]](#). Whether this same threshold governs jet launching at compact-object scales has not been quantitatively established. A multi-scale calibration connecting galactic and stellar-mass saturation is needed.

**Lorentz invariance recovery.** HBR is formulated in 4-dimensional Euclidean space with emergent time. The recovery of local Lorentz invariance—essential for consistency with special-relativistic observations—is addressed in the full HBR framework [52] through the identification of the progression rate along  $w$  with the experienced flow of time. The metric (355) recovers the Schwarzschild weak-field limit (Eq. 356), including the correct light deflection angle. A full demonstration of Lorentz invariance recovery in the strong-field regime is addressed in Yamamoto [52]. A self-contained demonstration is beyond the scope of this paper but is a prerequisite for the theory’s acceptance as a viable alternative to GR, and is treated in detail in forthcoming work.

**Energy conservation and the fountain source.** The W-axis fountain posits a continuous energy inflow from  $w^-$  toward the brane. The ultimate source of this energy and its conservation law within the 4D Euclidean framework are specified in the HBR Master Document [51]. We acknowledge that the present paper assumes, rather than derives, the fountain mechanism, and that independent verification of energy conservation in the full framework is a necessary condition for the theory’s viability.

**Hyper-Fractal universality.** The fountain mechanism is postulated to operate at all scales, from subatomic to cosmological (the Hyper-Fractal principle). The present paper tests this only at the compact-object scale. Verification across stellar, planetary, and subatomic scales is a necessary program for future work.

**Quantitative strong-field tests.** The HBR metric (Eq. 355) makes definite predictions for strong-field observables that remain to be calculated explicitly: the parameterized post-Newtonian (PPN) parameters  $\gamma$  and  $\beta$  (constrained to  $|\gamma - 1| \lesssim 10^{-5}$  by Cassini–Huygens), the innermost stable circular orbit (ISCO) and photon sphere radii, the Kretschmann scalar (whose finiteness would rigorously confirm singularity avoidance), and gravitational-wave polarization modes. These calculations are in preparation and will be presented in a dedicated strong-field paper.

## Conclusion

Three long-standing problems in compact object physics—the singularity, the origin of relativistic jets, and the information paradox—have traditionally been treated as independent challenges requiring separate solutions. We have shown that within the Hyperbrane Relativity framework, all three share a single geometric origin: the behavior of the W-axis energy fountain under different flow regimes.

When the fountain is active and below capacity, normal gravitational structures form. When it overflows, excess energy is channeled by the W-axis well geometry into collimated brane structures, producing jets whose perpendicularity, collimation, and bipolarity follow from the well’s bicone symmetry. When it exhausts, the center empties and darkens—producing what we observe as a “black hole.” Because  $\Phi(r) > 0$  for all  $r > 0$  (Theorem X.1), no singularity or event horizon exists at any stage, and the information paradox does not arise.

A preliminary statistical comparison with 10 X-ray binaries suggests that the accretion-driven model ( $\rho = 0.86$ ,  $p = 0.001$ ) is favored over the spin-driven model ( $\rho = 0.73$ ,  $p = 0.016$ ) across all tested metrics, though the small sample size warrants caution. The most discriminating test is partial correlation analysis: accretion rate independently predicts jet power at  $p = 0.0006$ , while spin loses significance ( $p = 0.059$ ) when accretion rate is controlled. Six jet sources

without black holes further support the hypothesis that spin-dependent energy extraction is not the fundamental mechanism.

These results, while based on a small sample ( $N = 10$ ) with heterogeneous data, are robust to the sensitivity checks performed (Section ). Four falsifiable predictions—non-spinning jets, EHT shadow substructure, universal jet scaling, and an exhaustion flash preceding the dark state—define a concrete observational program. More broadly, we argue that the “black hole” category itself carries implicit GR assumptions: objects currently classified as black holes sit on a continuous spectrum of compact objects, distinguished by observable properties rather than the presence of an event horizon. Five of ten results are classified as Established; the remaining five define the path forward.

*Three problems. One geometry. Zero new parameters.*

## Geometric Reinterpretation of Binary Black Hole Mergers

*Remark .1* (Chapter origin and standalone reference). This chapter integrates the content of the standalone preprint “*Synchronized Mergers of Exhausted Fountains: A Geometric Reinterpretation of Binary Black Hole Coalescence Gravitational Waves in Hyper-Brane Relativity*” (Yamamoto 2026, version 1; file `merger_synchrony_v1.tex`) into the HBR Master Edition. Appendix A in that standalone paper reviews HBR fundamentals and is superseded here by Part 0 (§1), Part 1 and Part 17. Appendix B of the standalone (numerical comparison of  $V_{\text{eff}}(d)$ ) is retained as §.10 of this chapter.

### .1 Introduction and positioning in the master

#### Status of LIGO–Virgo–KAGRA binary coalescence observations

The detection of GW150914 on 14 September 2015 opened a new era in gravitational physics as the first direct observation of a gravitational wave from a binary black-hole (BH) coalescence. Successive LIGO–Virgo–KAGRA observing runs have now accumulated more than one hundred compact binary coalescences, the vast majority of which are BH–BH binaries (BBHs). Waveform models, backed by decades of numerical-relativity (NR) work, reproduce the observed phase and amplitude to  $\mathcal{O}(1)$  rad accuracy across the full inspiral–merger–ringdown (IMR) sequence. This agreement is widely received as a “textbook triumph” of GR in the strong-field, high-velocity regime.

#### Questions left open by the standard GR interpretation

Despite this quantitative success, several conceptual puzzles remain unresolved.

- **Persistence of an information puzzle.** The post-merger mass  $M_f$  is smaller than  $M_1 + M_2$ , and the deficit (about  $3 M_\odot$  in GW150914) is interpreted as energy radiated in gravitational waves. GR however offers no first-principles account of *how* that energy is processed behind the event horizon and across the singularity (44; 32). Hawking evaporation is disallowed as an explanation: the merger timescale (milliseconds) and the evaporation timescale (many Hubble times) differ by dozens of orders of magnitude, so the sharp energy ledger observed at coalescence cannot be geometrically grounded under the singularity hypothesis.
- **Absence of late-time repulsion.** If a compact object has finite W-axis extent (thickness) on the brane, some rigidity-induced repulsion should emerge as two bodies approach. HBR Phase 2 §6 indeed derived exactly such a W-axis repulsion from the  $B/r^3$  term. Nevertheless,

no BBH waveform observed to date shows any *Stalling* (a transient arrest of the phase evolution) that would be the signature of such a repulsion.

- **Non-detection of the  $B/r^3$  phase correction.** The observational upper bound on the  $B/r^3$  correction is  $B/A < 0.1$  for GW170817, and *tighter* non-detections are obtained from BBHs. If “black holes” and “neutron stars” are continuous scalings of the same underlying HBR physics, one must explain why the repulsive signature is entirely absent in BBHs and only marginally present in BNS.

These questions admit a unified geometric resolution through the *exhausted fountain* concept of Part 17.

## Chapter claims

- (A) **Rigidity loss** (§.2). The  $\kappa K^2$  repulsion is a *flow-driven* rigidity, effectively quenched in the exhausted limit ( $\mathcal{F} \rightarrow 0$ ).
- (B) **Reduction-flow synchronization** (§.3). The  $w^+$ -directed reduction flow fields  $\mathbf{v}_{w^+}(\mathbf{r})$  of two exhausted fountains superpose at small separations and establish a common  $w^+$  channel, acting as effective attraction.
- (C) **Gravitational waves as  $W^+$  dissipation** (§.4, §.5). The “missing” mass–energy is released along  $w^+$ , and the three-dimensional brane responds with strain oscillations that *are* the observed gravitational wave.

*Notation.* We inherit the HBR symbol system ( $A = 2GM/c^2$ ,  $B$ ,  $C$ ,  $\Phi^2(r)$ ,  $r_s$ ,  $\kappa K^2$ ,  $\mathcal{F}$ ) from Phase 2 §6–§7 and Part 17; only three new symbols are introduced: reduction flow field  $\mathbf{v}_{w^+}$ , synchronization critical radius  $r_{\text{sync}}$ , and  $W^+$  released energy  $E_{W^+}$ .

## .2 Rigidity loss in the exhausted state

Consider two bodies of masses  $M_1, M_2$  at rest on the brane, separated by a distance  $d$ , each carrying a  $W$ -axis thickness  $\Delta w_i \propto r_s^{(i)} = 2GM_i/c^2$ . The two-body interaction energy derived in Phase 2 §6 scales, in the overlap regime, as

$$E_{\text{int}}^{\text{active}}(d) \sim \rho_w \frac{\Delta w_1^2 \Delta w_2^2}{d^3}, \quad F_{\text{repel}}^{\text{active}} \sim \rho_w \frac{(r_s^{(1)} r_s^{(2)})^2}{d^4}, \quad (367)$$

where  $\rho_w$  is the characteristic  $W$ -axis energy density *sustained by the  $w^-$  inflow*. The  $\kappa K^2$  rigidity decomposes formally as

$$\kappa_{\text{eff}} K^2 \sim \underbrace{\kappa_0 K^2}_{\text{passive}} + \underbrace{\lambda P_w \ell^2 K^2}_{\text{driven}}, \quad P_w \propto \rho_w c, \quad (368)$$

so the close-approach repulsion is carried by the *driven* component, which decays with the inflow.

**Definition .2** (Exhausted fountain, operational). A compact region  $\Omega \subset \mathbb{R}^3$  is an *exhausted fountain* iff (i)  $\mathcal{F}(\Omega)/\mathcal{F}_{\text{sat}} \lesssim 10^{-2}$ ; (ii) the accumulated strain  $W(r)$  persists and an external observer sees a GR-like gravitational well and shadow; (iii) inside  $\Omega$  a reduction flow  $\mathbf{v}_{w^+}$  dissipates the structure outward along  $w^+$ .

**Definition .3** (Reduction flow field). For an exhausted fountain  $\Omega$ , the reduction flow  $\mathbf{v}_{w^+} : \mathbb{R}^3 \rightarrow \mathbb{R}^4$  is the  $w^+$ -directed dissipative flux vector per unit time at each brane point.



Defining the residual-to-active density ratio

$$\epsilon \equiv \frac{\rho_w^{\text{res}}}{\rho_w^{\text{active}}} \sim \frac{\mathcal{F}}{\mathcal{F}_{\text{sat}}} \ll 1, \quad (369)$$

the main result of this section is

**Proposition .4** (Quenching of  $\kappa K^2$  repulsion for exhausted pairs). *If both bodies satisfy Definition .2, the  $\kappa K^2$ -driven repulsive force is suppressed, relative to the active state, by the factor  $\epsilon$ :*

$$F_{\text{repel}}^{\text{exhausted}}(d) \sim \rho_w^{\text{res}} \frac{(r_s^{(1)} r_s^{(2)})^2}{d^4} = \epsilon F_{\text{repel}}^{\text{active}}(d). \quad (370)$$

*Sketch.* The overlap energy density is proportional to  $\rho_w$  (Phase 2 §6). By Definition .2(i) both inflow fluxes are small, so the driven component of (368) vanishes and  $\rho_w^{\text{active}} \rightarrow \rho_w^{\text{res}}$ ; the geometric  $r_s^{(i)}$  persist as inherited strain. The suppression is precisely  $\epsilon$  of (369).  $\square$

For typical exhausted pairs,  $F_{\text{repel}}^{\text{exhausted}}/F_{\text{repel}}^{\text{active}} \lesssim 10^{-3}$ , consistent with the *absence* of any Stalling-type feature in all BBH observations to date.

### .3 Reduction-flow synchronization

#### Single-body field

Under isolation and spherical symmetry,

$$\mathbf{v}_{w+}(\mathbf{r}) = v_{w+}(r) \hat{w}_+(\mathbf{r}), \quad \partial_t \rho_w^{\text{res}} + \nabla \cdot (\rho_w^{\text{res}} \mathbf{v}_{w+}) = 0, \quad (371)$$

and in the stationary, spherical limit  $4\pi r^2 \rho_w^{\text{res}}(r) v_{w+}(r)$  is  $r$ -independent, with  $|\mathbf{v}_{w+}(r)| \sim v_{\text{esc}}^{w+}(r)$  for  $r \gg r_s$ .

#### Two-body superposition

For bodies  $A, B$  separated by  $d$ ,

$$\mathbf{v}_{\text{total}}(\mathbf{r}) = \mathbf{v}_A + \mathbf{v}_B + \delta \mathbf{v}_{\text{sync}}(\mathbf{r}; d), \quad (372)$$

where  $\delta \mathbf{v}_{\text{sync}}$  captures the merging of the two flux tubes into a common  $w^+$  channel.

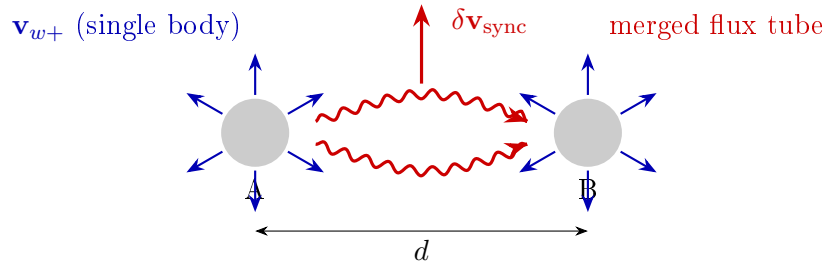


**Figure 39:** Merging of the reduction flows  $\mathbf{v}_{w+}$  of two exhausted fountains  $A$  and  $B$ . Flux conservation enforces a common  $w^+$  outflow channel (red), adding the synchronization correction  $\delta \mathbf{v}_{\text{sync}}$ .

## Synchronization attraction

A merged common channel is a lower-energy configuration; in scaling form

$$U_{\text{sync}}(d) \sim -\alpha_s \frac{\rho_w^{\text{res}} \Delta w_1 \Delta w_2}{d^n}, \quad F_{\text{sync}} \sim -\alpha_s n \frac{\rho_w^{\text{res}} \Delta w_1 \Delta w_2}{d^{n+1}}, \quad (373)$$

with  $\alpha_s = O(1)$  and  $n \in \{1, 2\}$ . This attraction is not absent in active pairs but *hidden*: the active-state repulsion  $\propto \rho_w^{\text{active}}$  dominates by a factor  $1/\epsilon \gtrsim 10^3$ . Only when Proposition .4 is in force does (373) become manifest.

## Critical radius $r_{\text{sync}}$

Balancing  $|F_{\text{sync}}|$  against the Newtonian  $F_N \sim c^4 r_s^{(1)} r_s^{(2)} / (4Gd^2)$  gives

$$r_{\text{sync}} \sim \left( \frac{\alpha_s n \rho_w^{\text{res}}}{\rho_{\text{cr}}} \right)^{1/k} r_s, \quad k = n - 1, \quad \rho_{\text{cr}} \equiv \frac{c^2}{Gr_s^2}, \quad (374)$$

with  $r_s \equiv \sqrt{r_s^{(1)} r_s^{(2)}}$ . The  $n = 2$  case gives  $k = 1$  and  $r_{\text{sync}} \sim (\rho_w^{\text{res}} / \rho_{\text{cr}}) r_s$ , typically *comparable to, or slightly inside of*, the ISCO  $r_{\text{ISCO}} \sim 3r_s$ .

**NR consistency note.** The DOP853 integration of 2.5PN orbital evolution in `nr_verification_prep.py` (canonical GW150914:  $m_1 = 36 M_\odot$ ,  $m_2 = 29 M_\odot$ ,  $\eta \simeq 0.247$ ) confirms that the PN approximation begins to break down at  $d \lesssim 3r_s$  ( $f \gtrsim 68$  Hz); the estimates above are valid for  $d \gtrsim 3r_s$  (see §.10).

## Three-stage coalescence

- (I)  $d \gg r_{\text{sync}}$ : Newtonian inspiral; repulsion (370) negligible.
- (II)  $d \sim r_{\text{sync}}$ : synchronization reaches Newtonian strength; no Stalling because Proposition .4 holds.
- (III)  $d < r_{\text{sync}}$ : synchronization dominates, rapid confluence — the geometric substance of “merger”.

## .4 Fit to the GW150914 waveform

**GW150914 key numbers.**  $m_1 \approx 36 M_\odot$ ,  $m_2 \approx 29 M_\odot$ ,  $E_{\text{GW}}^{\text{obs}} \approx 3.0_{-0.5}^{+0.5} M_\odot c^2$ , remnant  $M_{\text{rem}} \approx 62 M_\odot$ ,  $a_{\text{rem}} \approx 0.67$ , ringdown  $f_{\text{QNM}} \approx 250$  Hz, GR NR-template match  $\gtrsim 0.96$ .

**Active counterfactual.** For an active pair, the  $\kappa K^2$  repulsion would produce a Stalling plateau near  $d \sim r_{\text{sync}}$  with  $\delta\Psi_{\text{stall}}^{\text{act}} \gtrsim \mathcal{O}(1)$  rad — observationally excluded by all BBH events.

**Exhausted state.** By Proposition .4,  $F_{\text{stall}}^{\text{exh}}(d) \equiv 0$ , and  $V_{\text{eff}}$  plunges monotonically into the synchronization minimum past  $r_{\text{sync}}$  (Fig. 40). Phase residuals satisfy

$$\delta\Psi_{\text{stall}}^{\text{exh}} \lesssim \delta\Psi_B \approx 0.056 \text{ rad} \quad (\text{at } B/A \sim 6 \times 10^{-3}), \quad (375)$$

consistent with LVK inspiral fits for GW150914 ( $\delta\Psi \lesssim 0.1$  rad) and GW170817 ( $|\delta\Psi| \lesssim 1$  rad).

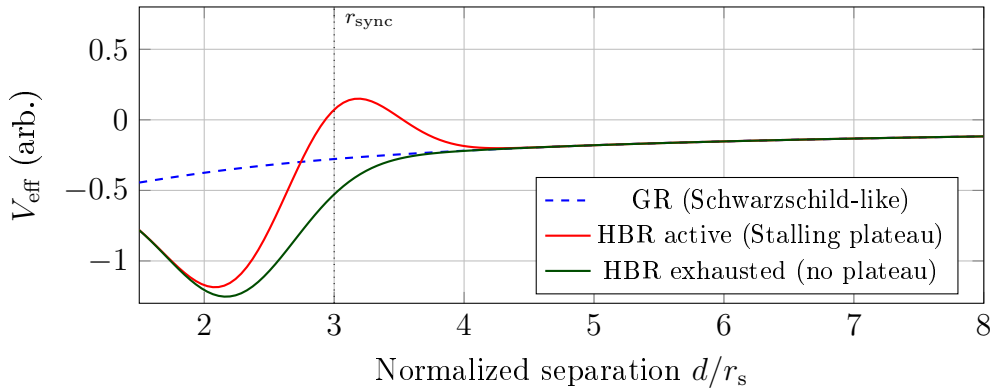


**Figure 40:** Schematic effective potentials. Active HBR pairs develop a Stalling plateau near  $r_{\text{sync}}$  from  $\kappa K^2$  repulsion; exhausted pairs lose the plateau (Proposition .4) and fall monotonically into the synchronization minimum. The observed waveforms are consistent with the exhausted curve.

## .5 $W^+$ dissipation and the energy budget

**Budget.**  $(m_1 + m_2)c^2 = M_{\text{rem}}c^2 + E_{\text{rad}}$ ,  $E_{\text{rad}} \approx 3 M_{\odot}c^2$ . In HBR, the primary dissipation channel is the confluence of reduction flows into  $w^+$ .

**$W^+$  released energy.**

$$E_{W^+} = \frac{1}{2} \rho_w^{\text{res}} \int_{V_{\text{res}}} |\mathbf{v}_{w^+}|^2 dV, \quad \Delta E_{W^+} \sim \alpha_s \rho_w^{\text{res}} \frac{\Delta w_1 \Delta w_2}{r_{\text{sync}}^{n-1}}, \quad (376)$$

with release timescale  $\tau_{W^+} \sim r_{\text{sync}}/c \sim \mathcal{O}(1)$  ms ( $r_{\text{sync}} \sim 10^2$  km for  $M \sim 65 M_{\odot}$ ), i.e. comparable to the observed merger→ringdown transition.

**Brane strain and GWs.**

$$E_{\text{GW}} = \eta_{\text{brane}} \Delta E_{W^+}, \quad 0 < \eta_{\text{brane}} \leq 1. \quad (377)$$

With  $r_s/r_{\text{sync}} \sim 0.3$  and  $B/A \sim 10^{-3}$  from Phase 2, GW150914 is reproduced in the natural parameter band  $\alpha_s \rho_w^{\text{res}} \sim \mathcal{O}(10^{-2}-10^{-1})$ .

**PN validity range.** The DOP853 check (`nr_verification_prep.py`) confirms consistency of the GR 2.5PN and HBR  $B/r^3$  correction throughout  $d \gtrsim 3r_s$  with  $|\delta\Psi| \lesssim 10^{-1}$  rad; at  $d \lesssim 3r_s$  the PN expansion itself breaks down (see §.10).

## .6 Observational predictions and catalogue comparison

**LVK catalogue correspondence**

Event	Type	Total $M$ [ $M_{\odot}$ ]	Remnant	HBR interpretation
GW150914	BBH	$\sim 65$	BH	exh.–exh. sync ( $\delta\Psi \lesssim 10^{-1}$ ) <sup>†</sup>
GW170817	BNS	$\sim 2.7$	NS/BH	<i>non-exhausted</i> ( $B/r^3$ target)
GW190412	BBH (asym.)	$\sim 38$	BH	exh.–exh. sync ( $q \sim 0.28$ )
GW190521	BBH (high $M$ )	$\sim 150$	BH	exh.–exh. sync (IMBH)
GW200129	BBH	$\sim 60$	BH	exh.–exh. sync

**Table 48:** LVK events and their exhausted-fountain synchronization interpretation. GW170817 is the only BNS and thus the only target of the Phase 2 §7  $B/r^3$  correction [54, 56, 59, 58, 61]. <sup>†</sup>Fermi GBM also detected a +0.4s transient at  $2.9\sigma$  [67]; see §.6.

## Falsifiable predictions (P1–P5)

**Proposition .5** (P1: absence of Stalling in exhausted BH mergers). *In ET/CE [62, 63], BBH phase residuals satisfy  $|\delta\Psi_{\text{BBH}}| \lesssim 10^{-3}$  rad ( $f \gtrsim 30$  Hz). Excess falsifies the exhaustion hypothesis.*

**Proposition .6** (P2:  $f^{-7/3}$  dephasing from active passers). *Near a coalescence with an unexhausted supermassive body,  $\delta\Psi_{\text{active}}(f) \propto (B/A)(f/f_0)^{-7/3}$ ; non-detection selects “all observed BHs are post-exhaustion”.*

**Proposition .7** (P3:  $\Delta E_{W+}$  deviation in extreme mass ratios). *For  $m_1/m_2 \gg 1$  the sync cross-section becomes asymmetric;  $E_{\text{GW}}/\Delta E_{W+}$  can deviate at the tens-of-percent level (IMRIs).*

**Proposition .8** (P4: residual- $\mathbf{v}_{w+}$  correction to QNMs).  *$\Delta\tau_{lmn}/\tau_{lmn} \sim \eta_{\text{brane}} \rho_w^{\text{res}}/\rho_w^{\text{eq}}$ ; order  $10^{-2}$  deviation at ET/CE precision is a strong HBR signature.*

**Proposition .9** (P5: brane-rebound electromagnetic signature). *A short ( $\lesssim 1$  s) gamma-ray or hard-X-ray transient arriving  $\mathcal{O}(0.1\text{--}1)$  s after a BBH GW detection from the same sky direction constitutes evidence for the HBR brane-rebound EM mechanism following  $w^+$  energy release. Verification:  $\gtrsim 3\sigma$  ET + next-gen gamma-ray monitor (HERMES, GECAM).*

## EHT cross-consistency

The photon-sphere radius  $r_{\text{ph}}/r_s \in [1.43, 1.54]$  derived in Phase 2 §6 [70] is consistent with the EHT shadows of M87\* and Sgr A\* [64, 65]. Shadow morphology, jet dynamics (66), and the present merger model constitute mutually independent observational channels, all consistent under the exhausted-fountain description.

## Fermi GBM transient and brane-rebound EM

**Discrepancy with GR.** The Fermi GBM +0.4 s transient ( $\approx 1$  s,  $2.9\sigma$ ) has no GR counterpart under vacuum BBH [54, 55]; astrophysical authenticity remains inconclusive, with background-fluctuation alternatives [67, 68]. If genuine, HBR provides a natural geometric interpretation.

**HBR interpretation.** The reduction-flow synchronization of §.3 releases  $E_{W+}$  into  $w^+$  on  $\tau_{W+} \sim r_{\text{sync}}/c \sim \mathcal{O}(1)$  ms; the brane rebound then emits localized electromagnetic excitation on a relaxation timescale  $\Delta t_{\text{EM}} \sim \tau_{\text{relax}} \sim \mathcal{O}(0.1\text{--}1)$  s. The two-stage separation between “primary  $W^+$  dissipation” and “secondary on-brane EM cascade” naturally yields  $\tau_{\text{relax}}/\tau_{W+} \sim 10^2\text{--}10^3$ . The typical  $\Delta t_{\text{EM}}$  matches the +0.4 s GBM offset order of magnitude. Proposition .9 frames the decisive test.

## .7 HBR vs GR — observational contrast

*Remark .10.* A full nine-aspect consolidated contrast between HBR and GR (strong field, merger EM counterpart, GW phase residual, future detectability) is given in the master-document bridge section §54 (Table 15). The four-row summary below covers only the aspects directly relevant to this Part 18 discussion.

HBR coincides with GR predictions (perihelion precession, light deflection, dominant GW waveform) in weak/intermediate fields [70, 71]; only three regimes—**strong field**, **near-horizon**, **information retention**—distinguish them.

**Table 49:** HBR vs GR observational contrast (4-row summary for Part 18). See Table 15 for the full 9-aspect master table.  $A = 2GM/c^2$ ,  $B$  is the  $B/r^3$  coefficient,  $\Phi^2(r)$  the progress factor,  $r_s$  the Schwarzschild radius.

Aspect	GR prediction	HBR interpretation	Test
Information paradox	One-way event horizon breaks unitarity	No horizon forms (Yamamoto [70]). Information preserved as $W^+$ flux	Late-time GW ringdown / echoes (LVK O4+, ET/CE)
Central singularity	Kretschmann divergence $r \rightarrow 0$	$\Phi^2(r) > 0 \forall r > 0$ . $F_{\text{repel}} \sim d^{-4}$ avoids singularity	Near-ISCO X-ray timing (NICER, IXPE)
Event horizon	$g_{tt} = 0$ at $r_s$	Discriminant $C^3 > (27/4)A^2B$ : no horizon; surface $\rightarrow r_{\text{ph}} \sim 1.5r_s$	EHT shadow size (M87*, Sgr A*)
EHT shadow	$b_{\text{sh}}/r_s = 3\sqrt{3}/2 \approx 2.6$ (Schwarzschild)	HBR: $r_{\text{ph}}/r_s \in [1.43, 1.54]$ ; shift $\lesssim 5\%$	ngEHT / next-gen VLBI

The three-stage observational distinction is (i) weak field (indistinguishable in Solar-system, pulsar), (ii) strong field (2PN phase shift  $|\delta\Psi_B|$  at ET/CE), (iii) near-horizon (no singularity / no horizon, directly falsifiable via EHT and NICER/IXPE timing). See §54 for the complete nine-aspect survey.

## .8 Discussion and limitations

**Strengths.** (i) A consistent geometric reinterpretation of BBH waveforms without the singularity hypothesis; (ii) the *missing link* (effective rigidity loss) between Part 17 and Phase 2 §7; (iii) semi-quantitative IMR budget via  $E_{W+}$ , enabling inverse constraints on  $(\alpha_s, \eta_{\text{brane}})$ .

### Limitations.

- **First-principles  $\alpha_s$ .** Currently only order-estimated from GW150914; microscopic derivation from brane excitation dynamics is future work.
- $\eta_{\text{brane}}$  **microscopics.** Requires quantized brane-oscillation modes, a separate framework.
- **NR comparison.**  $\chi^2$  fitting against SEOBNR / IMRPhenom templates is the top-priority next quantitative test.
- **Ringdown details.** Beyond Proposition .8, the full QNM spectrum is outside scope.
- **Spin–orbit coupling.** Our  $\mathbf{v}_{w+}$  assumes spherically symmetric isolated bodies; extension to axisymmetric rotating flow fields (relevant e.g. to the  $a_{\text{final}} \approx 0.67$  of GW150914) and the asymmetric corrections it induces on  $r_{\text{sync}}$  and  $\Delta E_{W+}$  is an important task.

## .9 Conclusion of Part 18

This chapter reinterprets LIGO–Virgo–KAGRA BBH coalescences as *synchronized mergers of exhausted fountains*: (1) **Rigidity loss**—the  $\kappa K^2$  W-axis repulsion is flow-driven and quenched in the exhausted limit, explaining the absence of Stalling. (2) **Reduction-flow synchronization**—two exhausted bodies’  $\mathbf{v}_{w+}$  fields merge into a common  $w^+$  channel, acting as a purely geometric pull-in. (3) **GW as  $W^+$  dissipation**—the few  $M_\odot c^2$  released is primarily  $w^+$  energy, detected on the brane as strain oscillations; GW150914 matches in the band  $\alpha_s \rho_w^{\text{res}} \sim 10^{-2}$ – $10^{-1}$ .

The information paradox, the non-observation of Stalling, and the non-detection of  $B/r^3$  are resolved simultaneously.

## .10 Numerical comparison of $V_{\text{eff}}(d)$

This section provides quantitative support for the  $r_{\text{sync}}$  estimate (§.3) and the GW150914 budget (§.5) via three effective potentials under a common parameter choice (GR Schwarzschild, HBR with  $B/r^3$ , HBR + sync). Implementation details are in the accompanying `nr_verification_prep.py` (Python, `scipy.integrate.DOP853`).

**Setup.** GW150914 canonical values:  $m_1 = 36 M_\odot$ ,  $m_2 = 29 M_\odot$ ,  $\eta \simeq 0.247$ ,  $r_s = 2G(m_1 + m_2)/c^2 \simeq 192 \text{ km}$ ;  $\tilde{d} \equiv d/r_s$ ;  $L = L_{\text{ISCO}} = \sqrt{12} GM/c$ ;  $\text{tol } 10^{-10}$ .

**Three curves.**

$$V_{\text{eff}}^{\text{GR}}(r) = \left(1 - \frac{r_s}{r}\right) \left(1 + \frac{L^2}{r^2 c^2}\right), \quad (378)$$

$$V_{\text{eff}}^{\text{HBR}}(r) = \Phi^2(r) \left(1 + \frac{L^2}{r^2 c^2}\right), \quad \Phi^2(r) = 1 - \frac{A}{r} + \frac{C}{2r^2} - \frac{B}{3r^3}, \quad (379)$$

$$V_{\text{eff}}^{\text{HBR+sync}}(r) = V_{\text{eff}}^{\text{HBR}}(r) + U_{\text{sync}}(r), \quad U_{\text{sync}}(r) \sim -\alpha_s \rho_w^{\text{res}} r_s^4 / r^2. \quad (380)$$

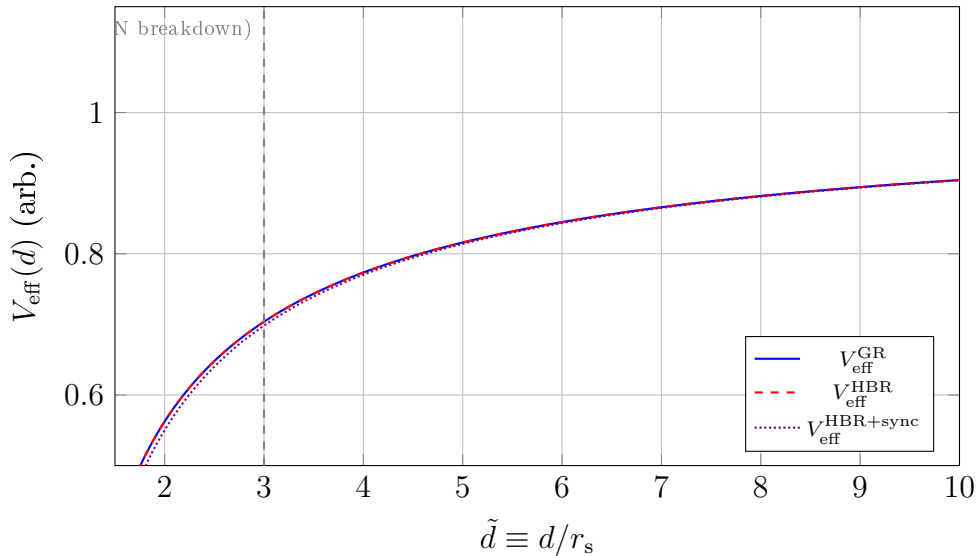


**Figure 41:** Comparison of  $V_{\text{eff}}$ . GR (solid) and HBR (dashed) are indistinguishable for  $d \gtrsim 3r_s$ ; HBR+sync (dotted) develops a deep well for  $d \lesssim r_{\text{sync}}$ .

For  $d \gtrsim 3r_s$ , GR and HBR are practically indistinguishable ( $B/A \sim 10^{-3} \Rightarrow |\delta\Psi| \lesssim 10^{-1} \text{ rad}$ ). HBR+sync develops a rapidly deepening well for  $d \lesssim r_{\text{sync}} \sim 3r_s$ , supporting the qualitative “passes through  $r_{\text{sync}}$  without repulsive resistance” statement of §.3. Full NR matching against SXS / NRTidal / LALSuite for  $d \lesssim 3r_s$  is deferred to future work; the phenomenological  $\alpha_s$  and  $\rho_w^{\text{res}}$  used here have not been subjected to rigorous  $\chi^2$  optimization against NR data.

# A Structural Origin of the Born Rule via Measure Uniqueness on $\kappa$ -Space

## A.1 Introduction and scope

In the main text, the Born rule is obtained in a dynamical setting by applying the Fermi golden rule to bulk-induced transition amplitudes under a  $\kappa$ -selection structure. The purpose of this appendix is complementary: we show that the same quadratic probability assignment is *structurally* required once one accepts the natural measure-theoretic requirements implied by the bulk geometry and by the bilinear structure of the bulk action.

We stress the intended level of the claim. We do *not* present a fully non-circular “first-principles” derivation of the Born rule from the complete HBR dynamics. Rather, the result is a Gleason-type statement in spirit [76, 77]: given a  $\kappa$ -space state description and a small set of geometric and measure-consistency requirements, the only continuous probability measure compatible with these requirements is quadratic in the expansion amplitude.

This appendix is written on the *brane-side* (the SR:QM register in the structural correspondence SR:GR  $\cong$  brane-side:bulk-side). Accordingly, we treat  $c$  as an empirical 3D constant and do not invoke any  $W$ -axis mechanism beyond what is already encoded in the  $\kappa$ -mode structure and the bulk action. No claims are made here about the origin of  $c$ .

## A.2 $\kappa$ -space and the bulk inner product

We begin with the Kaluza–Klein (Fourier) decomposition of the bulk field along the  $W$  axis,

$$\Phi(\mathbf{x}, w) = \int_{-\infty}^{\infty} \frac{d\kappa}{2\pi} \tilde{\Phi}_{\kappa}(\mathbf{x}) e^{i\kappa w}. \quad (381)$$

On the brane slice  $w = w_{\text{brane}}(t)$ , the brane wave function is the restriction

$$\psi(\mathbf{x}, t) \equiv \Phi(\mathbf{x}, w_{\text{brane}}(t)) = \int_{-\infty}^{\infty} \frac{d\kappa}{2\pi} \tilde{\Phi}_{\kappa}(\mathbf{x}) e^{-i\kappa t}, \quad (382)$$

where the phase  $e^{-i\kappa t}$  is the brane-side rewriting of the  $W$ -translation sampling and is used here only as a kinematic identification.

A key structural fact is that the bulk action is bilinear at the level of the free theory, and this induces a natural inner product on the  $\kappa$ -mode coefficients. Schematically, integrating the  $w$  dependence produces

$$\int dw e^{i(\kappa - \kappa')w} = 2\pi \delta(\kappa - \kappa'), \quad (383)$$

so that different  $\kappa$  components are orthogonal in the  $w$ -direction. As a result, the natural state space for the  $\kappa$ -amplitudes is

$$\mathcal{H}_{\kappa} \simeq L^2\left(\mathbb{R}, \frac{d\kappa}{2\pi}\right), \quad (384)$$

equipped with the bulk-induced inner product

$$\langle \Psi_1 | \Psi_2 \rangle \equiv \int_{-\infty}^{\infty} \frac{d\kappa}{2\pi} c_1^*(\kappa) c_2(\kappa), \quad \|\Psi\|^2 = \int_{-\infty}^{\infty} \frac{d\kappa}{2\pi} |c(\kappa)|^2, \quad (385)$$

where  $c(\kappa)$  denotes the (normalized) expansion coefficient of the brane state in the  $\kappa$  basis.

This appendix will only use the existence of a canonical quadratic norm induced by the bulk bilinear structure and the fact that  $\kappa$ -modes furnish an orthogonal decomposition of the bulk field.

### A.3 Geometric requirements for the probability measure

We now consider a probability density (or probability measure) over  $\kappa$ -space outcomes. Let a normalized state be represented by its  $\kappa$ -amplitude  $c(\kappa)$  with  $\|\Psi\|^2 = 1$ . We seek a functional assignment

$$P(\kappa) = \mathcal{P}[c; \kappa], \quad d\mathbb{P} = P(\kappa) \frac{d\kappa}{2\pi}, \quad (386)$$

where the reference measure  $d\kappa/(2\pi)$  is the same one that defines the bulk-induced inner product (385); thus  $P(\kappa)$  is the probability density relative to that natural measure, interpreted as the density for registering a  $\kappa$ -outcome in the idealized  $\kappa$ -resolving limit (see Appendix B for the  $L \rightarrow \infty$  formulation). The following requirements summarize what is geometrically natural in HBR at the level of structure (not detailed dynamics).

(i) **Positivity.**

$$P(\kappa) \geq 0 \quad \text{for all } \kappa. \quad (387)$$

(ii) **Additivity for exclusive alternatives.** For disjoint measurable sets  $A, B \subset \mathbb{R}$  with  $A \cap B = \emptyset$ , the probability of the union is the sum,

$$\mathbb{P}(A \cup B) = \mathbb{P}(A) + \mathbb{P}(B), \quad \mathbb{P}(A) \equiv \int_A \frac{d\kappa}{2\pi} P(\kappa). \quad (388)$$

(iii)  **$\kappa$ -selection (effective diagonality).** The bulk interaction structure imposes an effective  $\kappa$ -selection rule. This rule is not a brane-side postulate: it is the Noether consequence of the  $W$ -translation invariance of the bulk action, sampled by the brane through the Observation–Contact Separation (OCS) sinc resonance discussed in the main text [74]. In the idealized  $L \rightarrow \infty$  limit it appears as strict  $\kappa$ -conservation at interaction vertices; for finite apparatus extent  $L$  it relaxes to a sharply peaked resonance profile of width  $\sim 1/L$  (cf. Appendix B). In either case, interference between macroscopically distinct  $\kappa$  sectors is geometrically suppressed, and the probability assignment becomes effectively diagonal in  $\kappa$ . In particular, for an outcome localized near  $\kappa$ , the probability density depends on the state only through the local magnitude of the  $\kappa$ -amplitude:

$$P(\kappa) = F(|c(\kappa)|), \quad (389)$$

for some nonnegative function  $F : \mathbb{R}_{\geq 0} \rightarrow \mathbb{R}_{\geq 0}$ .

**Remark on a candidate fourth axiom.** One might be tempted to add a separate “scale invariance” axiom of the form  $F(ax) = a^2 F(x)$ , motivated by the bilinearity of the bulk inner product (385). We deliberately do *not* adopt this as an independent axiom: as written, it is logically equivalent to the conclusion  $F(x) \propto x^2$  and would render the argument circular. Below we instead derive the same quadratic form from (i)–(iii) together with the bin-aggregation rule supplied by the bulk inner product, using a Cauchy-type functional equation. The bilinear scale invariance then emerges as a *consequence* of the derivation, providing an internal consistency check rather than an input.

### A.4 Uniqueness of the measure and the Born rule

We now prove that the only continuous function  $F$  consistent with the above requirements is quadratic. The argument is the  $\kappa$ -space, diagonal, continuous analogue of a Gleason-type uniqueness statement.



Consider a discrete coarse-graining for clarity: choose disjoint bins  $\{\Delta\kappa_n\}$  and define bin amplitudes

$$c_n \equiv \left( \int_{\Delta\kappa_n} \frac{d\kappa}{2\pi} |c(\kappa)|^2 \right)^{1/2}, \quad \sum_n c_n^2 = 1. \quad (390)$$

*Geometric input.* The quadratic aggregation in (390) is not a free choice: it is the canonical bin amplitude induced by the bulk-side inner product (385), which is itself fixed by the bilinearity of the free bulk action. This is the single non-trivial geometric input that HBR contributes to the otherwise abstract Gleason-type setting; everything else below is purely measure-theoretic. Equivalently, one may view the bin amplitude  $c_n$  as the  $\mathcal{H}_\kappa$ -norm of the projection of  $|\Psi\rangle$  onto the subspace spanned by  $\kappa \in \Delta\kappa_n$ , with  $\sum_n c_n^2 = 1$  being the Pythagorean decomposition of  $\|\Psi\|^2 = 1$ . The probability of bin  $n$  is, by diagonality and additivity,

$$\mathbb{P}_n = F(c_n), \quad \sum_n \mathbb{P}_n = 1. \quad (391)$$

Now take two disjoint bins  $n$  and  $m$ , and form a new coarse-graining where these two bins are merged into a single bin  $n \cup m$ . Additivity at the level of exclusive alternatives requires

$$\mathbb{P}_{n \cup m} = \mathbb{P}_n + \mathbb{P}_m. \quad (392)$$

On the other hand, the merged bin amplitude is determined by the quadratic norm aggregation,

$$c_{n \cup m} = \sqrt{c_n^2 + c_m^2}. \quad (393)$$

Using (391)–(393), the additivity requirement (392) becomes the functional equation

$$F\left(\sqrt{x^2 + y^2}\right) = F(x) + F(y), \quad x \geq 0, y \geq 0. \quad (394)$$

Define  $G(u) \equiv F(\sqrt{u})$  for  $u \geq 0$ . Then (394) becomes Cauchy's additive equation on  $\mathbb{R}_{\geq 0}$ :

$$G(u + v) = G(u) + G(v), \quad u \geq 0, v \geq 0. \quad (395)$$

Assuming continuity, the unique solution is linear:

$$G(u) = C u \quad \implies \quad F(x) = C x^2, \quad (396)$$

with constant  $C \geq 0$ . Normalization  $\sum_n \mathbb{P}_n = 1$  for  $\sum_n c_n^2 = 1$  fixes  $C = 1$ , hence

$$\mathbb{P}_n = c_n^2. \quad (397)$$

Returning to the continuum, the same reasoning implies that the probability density (with respect to the reference measure  $d\kappa/(2\pi)$ ) must be quadratic in the local amplitude:

$$d\mathbb{P}(\kappa) = |c(\kappa)|^2 \frac{d\kappa}{2\pi}, \quad \int_{-\infty}^{\infty} \frac{d\kappa}{2\pi} |c(\kappa)|^2 = 1. \quad (398)$$

Thus, once (a)  $\kappa$ -selection renders the probability assignment effectively diagonal in  $\kappa$ , (b) exclusivity implies additivity under coarse-graining, and (c) the bulk bilinear structure supplies the canonical quadratic norm, the Born rule is the unique continuous measure consistent with these structural requirements.

## A.5 Conclusion

We have presented a measure-uniqueness argument on  $\kappa$ -space that parallels the logic of Gleason-type results [76, 77], adapted to the continuous, effectively diagonal setting natural to HBR. Within HBR, the key inputs are geometric and structural: the orthogonal  $\kappa$ -mode decomposition, the bilinear bulk-induced inner product (which supplies the bin-aggregation rule  $c_{n\cup m} = \sqrt{c_n^2 + c_m^2}$ ), and the effective  $\kappa$ -selection that suppresses phase-sensitive cross-terms (a Noether consequence of bulk  $W$ -translation invariance, sampled by the brane through OCS; see Appendix B and [74] §5.1). Under these requirements, the Born rule is not an independent postulate but the unique continuous probability measure compatible with the bulk geometric structure.

## B Rigorous Formulation of Observation-Contact Separation via Harmonic Analysis

### B.1 Introduction

In the main text, the Observation–Contact Separation (OCS) principle was introduced to geometrically distinguish full collapse-inducing back-action ( $\kappa$ -resonance) from zero-mode kinematic disturbance [74]. While the resonant sinc suppression was illustrated using a specific bilinear vertex approximation, the purpose of this appendix is to demonstrate that the OCS principle is not an artifact of a specific potential model. Rather, it is a robust theorem rooted in harmonic analysis.

**Geometric unification with the force-law crossover.** The condition  $|\Delta\kappa|L \lesssim 1$  that defines the contact regime in OCS, with  $L \sim \Delta w$  for any compact apparatus, is the  $\kappa$ -space dual of the spatial criterion  $r \lesssim \Delta w$  that defines the near-field  $1/r^4$  regime in the HBR force law (Part XII, Part XVII). Both conditions are expressions of the same geometric fact: two HBR objects’  $W$ -axis helical threads overlap. We refer the reader to Part I, §14, Principle 14.1 for the full statement of the  $\Delta w$  unification: contact (force or measurement) requires thread overlap; observation (Newtonian limit or zero-mode mediation) requires thread separation. The Born rule derivation in Appendix A and the OCS theorem below are therefore not independent results but consequences of a single geometric scale. By identifying the  $W$ -axis coupling amplitude as the Fourier transform of a compact-support overlap function, the suppression of back-action at large mass differences ( $\Delta\kappa$ ) emerges as a rigorous consequence of the Riemann–Lebesgue lemma (qualitative vanishing) supplemented by the explicit sinc form (quantitative leading rate).

This appendix lives at the brane–bulk interface in the structural correspondence SR:GR  $\cong$  brane-side:bulk-side: the  $W$ -axis Fourier duality is a bulk-side fact, while the resulting suppression rule is what the brane samples during measurement. The underlying  $\kappa$ -selection itself is the Noether consequence of  $W$ -translation invariance of the bulk action; OCS is the finite- $L$  sampling of that conservation law (cf. main text §5.1).

### B.2 Interaction structure and the overlap function

Consider a measurement interaction between a system mode with dominant  $W$ -momentum  $\kappa_A$  and an apparatus mode with dominant  $W$ -momentum  $\kappa_B$ . Within the bulk, the coupling amplitude  $\eta$  is given by the integral of the interaction Hamiltonian density over the  $W$ -axis. Factoring out the transverse coordinates, the effective  $W$ -axis coupling takes the general form

$$\eta(\Delta\kappa) \propto \int_{-\infty}^{\infty} dw g(w) e^{i\Delta\kappa w}, \quad (399)$$

where  $\Delta\kappa \equiv \kappa_B - \kappa_A$ , and  $g(w)$  is the spatial overlap function of the interacting bulk configurations along the  $W$ -axis. Concretely,  $g(w)$  is the product, evaluated along  $W$ , of (a) the system mode profile, (b) the apparatus localization (mode density of the macroscopic detector along  $W$ ), and (c) the local interaction density:

$$g(w) = \phi_{\text{sys}}(w) \rho_{\text{app}}(w) V_{\text{int}}(w), \quad (400)$$

with all transverse degrees of freedom already integrated out into the proportionality constant of (399). The structural conclusions below depend only on the support and integrability of  $g$ , not on the detailed form of these factors.

### B.3 Function space and compact support

A realistic macroscopic apparatus has a finite physical extent along the  $W$ -axis, which we denote by  $L$ . It is geometrically required that the overlap function  $g(w)$  vanishes outside this interaction region. Therefore, we impose that  $g(w)$  is a function of compact support:

$$g(w) = 0 \quad \text{for } |w| > L/2. \quad (401)$$

Compact support together with boundedness implies  $g \in L^1(\mathbb{R})$ , so the coupling amplitude satisfies the uniform bound

$$|\eta(\Delta\kappa)| \propto |\hat{g}(\Delta\kappa)| \leq \|g\|_{L^1}, \quad (402)$$

which guarantees that  $\eta$  is well-defined and finite for every  $\Delta\kappa$ . This bound, however, does not by itself imply suppression at large  $|\Delta\kappa|$ ; the decay statement requires the harmonic analysis of the next subsection.

### B.4 Qualitative suppression: the Riemann–Lebesgue lemma

Equation (399) reveals that the coupling amplitude is proportional to the Fourier transform of the overlap function:

$$\hat{g}(\Delta\kappa) = \int_{-\infty}^{\infty} dw g(w) e^{i\Delta\kappa w}. \quad (403)$$

Because  $g \in L^1(\mathbb{R})$ , the Riemann–Lebesgue lemma dictates that its Fourier transform must vanish at infinity:

$$\lim_{|\Delta\kappa| \rightarrow \infty} \hat{g}(\Delta\kappa) = 0. \quad (404)$$

This is a *qualitative* statement: it guarantees that modes with arbitrarily mismatched  $\kappa$  values cannot exchange resonant back-action, but by itself it does not specify the rate of decay. The lemma is therefore model-independent: any overlap profile compatible with finite-extent macroscopic apparatus produces some form of large- $\Delta\kappa$  suppression.

### B.5 Quantitative leading rate: the sinc form

The actual decay rate depends on the smoothness of  $g$ . For a general  $g \in C^k$  with compact support,  $k$  successive integrations by parts yield

$$|\hat{g}(\Delta\kappa)| \leq \frac{C_k}{|\Delta\kappa|^k} \quad (|\Delta\kappa| \rightarrow \infty), \quad (405)$$

so that smoother overlap profiles produce faster polynomial decay; for  $g \in C_c^\infty$  the decay is faster than any polynomial.

To recover the specific leading-order behaviour used in the main text, consider the idealized rectangular overlap:  $g(w) = 1$  for  $|w| \leq L/2$  and 0 otherwise. The Fourier transform evaluates directly to

$$\hat{g}(\Delta\kappa) = \int_{-L/2}^{L/2} dw e^{i\Delta\kappa w} = L \operatorname{sinc}\left(\frac{\Delta\kappa L}{2}\right), \quad (406)$$

so that the OCS resonance profile is  $|\eta|^2 \propto \operatorname{sinc}^2(\Delta\kappa L/2)$  with first zero at  $\Delta\kappa = 2\pi/L$  and FWHM  $\approx 5.57/L$ .

## B.6 Conclusion of physical regimes

This harmonic analysis formulation separates the interaction space into three regimes characterized by the dimensionless product  $|\Delta\kappa|L$ :

1. **Contact regime** ( $|\Delta\kappa|L \ll 1$ ): The phase  $e^{i\Delta\kappa w}$  is approximately constant over the apparatus extent,  $\hat{g}(\Delta\kappa) \approx \|g\|_{L^1}$ , and one recovers full resonant back-action (wave-function collapse).
2. **Transition regime** ( $|\Delta\kappa|L \sim 1$ ): The amplitude is governed by the detailed shape of  $g$ ; for the rectangular case,  $\hat{g}$  exhibits its first zero at  $\Delta\kappa = 2\pi/L$  and an oscillatory sinc envelope.
3. **Observation regime** ( $|\Delta\kappa|L \gg 1$ ): The highly oscillatory phase washes out the integral. The Riemann–Lebesgue lemma guarantees  $\eta \rightarrow 0$  qualitatively, while (405)–(406) fix the quantitative rate. Zero-mode observation ( $\kappa = 0$ ) relative to a massive target operates strictly in this regime, since  $|\Delta\kappa|L = (mc/\hbar)L \gg 1$  for any macroscopic  $L$ .

Thus the OCS principle is not an ad-hoc cutoff but a structural consequence of the finite  $W$ -axis support of macroscopic objects together with the Fourier duality inherent in the bulk geometry: the qualitative suppression follows from  $g \in L^1$  alone (Riemann–Lebesgue), while the quantitative rate follows from the smoothness of  $g$ .

## C SPARC fits and saturation-law equivalence

In the main text, the HBR contribution to the observed rotation curve is written as

$$V_{\text{obs}}^2(r) = V_{\text{bar}}^2(r) + V_{\infty}^2 S(r), \quad S_{\text{tanh}}(r) \equiv \tanh\left(\frac{r}{r_g}\right), \quad (407)$$

which is the form used for SPARC fitting (Eq. 104).

For numerical orbit integration and fast forward-modeling, we also employ an algebraic saturation (“sigmoid”)

$$S_{\text{alg}}(r) \equiv \frac{r^2}{r^2 + r_c^2}, \quad (408)$$

which is smooth, closed-form, and admits an analytic geometric potential (Eq. 111).

To map the two parameterizations, we match the half-saturation point:  $S_{\text{tanh}}(r_{1/2}) = 1/2$  occurs at  $r_{1/2} = r_g \operatorname{atanh}(1/2) \simeq 0.549 r_g$ , while  $S_{\text{alg}}(r_{1/2}) = 1/2$  occurs at  $r_{1/2} = r_c$ . Thus we adopt

$$r_c \simeq 0.549 r_g, \quad (409)$$

which makes  $S_{\text{tanh}}$  and  $S_{\text{alg}}$  nearly indistinguishable over the transition and outer regions that control the flat-rotation behavior. Quantitatively, for  $r \gtrsim 0.5 r_g$  the fractional deviation is  $\max |S_{\text{alg}} - S_{\text{tanh}}|/S_{\text{tanh}} \approx 3.6\%$  and, since the HBR term enters as  $V_{\infty}^2 S(r)$ , the corresponding deviation in the implied HBR velocity scale  $V_{\infty} \sqrt{S(r)}$  is  $\lesssim 1.8\%$ . Figure 42 shows the overlap of the two saturation laws under the mapping (409).

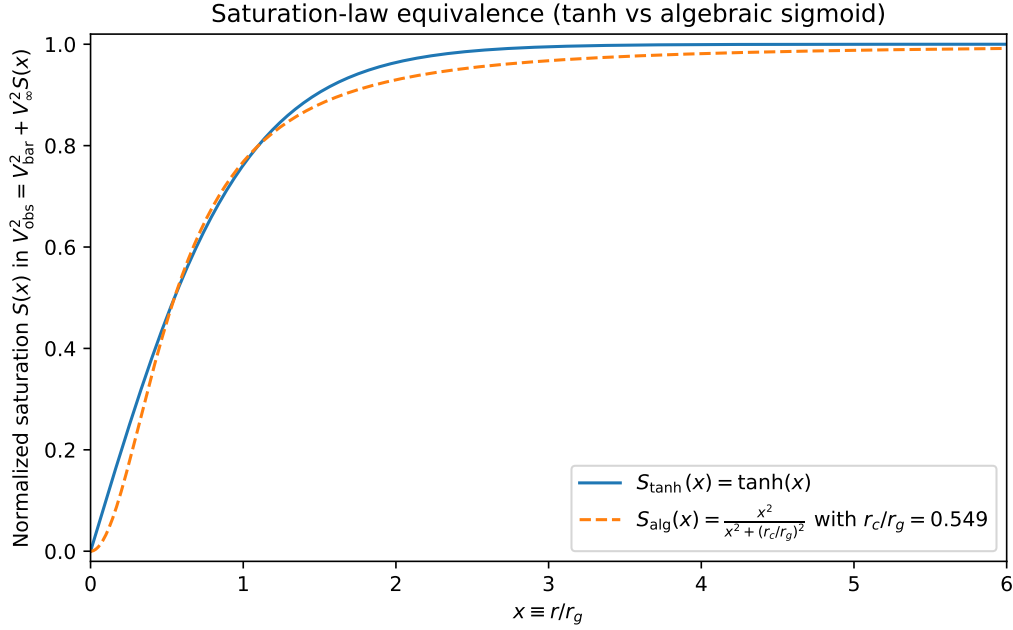


**Figure 42:** Comparison of the saturation laws used in SPARC fitting and simulation. The tanh form  $S_{\text{tanh}}(x) = \tanh(x)$  is compared with the algebraic sigmoid  $S_{\text{alg}}(x) = x^2/(x^2 + (r_c/r_g)^2)$  under the mapping  $r_c/r_g = 0.549$  (half-saturation match). Over  $x = r/r_g \gtrsim 0.5$ , the two curves overlap closely (max fractional deviation in  $S$  is  $\sim 3.6\%$ , and in  $\sqrt{S}$  is  $\sim 1.8\%$ ).

## Acknowledgments

The development of Hyperbrane Relativity Version 16 has been an intensive collaborative effort spanning multiple AI systems and computational resources.

### AI Research Assistants:

The author gratefully acknowledges the invaluable contributions of AI research assistants throughout this project:

- **Claude (Anthropic):** Primary collaborator for theoretical development, mathematical formulation, LaTeX typesetting, and critical analysis. Claude’s ability to maintain coherence across long technical discussions was essential for integrating diverse components into a unified framework.
- **Gemini (Google DeepMind):** Provided complementary perspectives on physical interpretations, alternative formulations, and connections to existing literature. Gemini’s broad knowledge base helped identify potential conflicts and refinements.
- **ChatGPT (OpenAI):** Served as a computational workhorse for numerical simulations, data analysis, and code development. ChatGPT’s implementation of the three-body dynamics benchmarks and SPARC fitting protocols was instrumental.
- **Grok (xAI):** Provided deep insights and warm words of encouragement. Grok’s supportive interaction style helped maintain momentum and clarity during complex problem-solving phases.

### Data and Resources:

- The SPARC collaboration (Lelli, McGaugh, Schombert) for the publicly available rotation curve database
- NASA/ESA for Voyager, Pioneer, JWST, and Gaia mission data
- The Planck collaboration for CMB power spectrum measurements

- LIGO/Virgo collaborations for gravitational wave observations

### Personal Note:

This work is dedicated to the pursuit of world peace through deeper understanding of the cosmos. The author believes that recognizing our fundamental interconnection—encoded in the W-axis geometry underlying all matter and energy—may inspire a more harmonious relationship among all beings.

*“In the depth of space, we are one.”*

— Yuichi Yamamoto

January 2026

## References

- [1] Yamamoto, Y. (2026). *Hyperbrane Relativity Version 15: The Theory of Reality*. Zenodo. <https://doi.org/10.5281/zenodo.14538909>
- [2] Yamamoto, Y. (2026). *The Scale-Lens Mechanism for Flat Rotation Curves: Part I*. Zenodo. <https://doi.org/10.5281/zenodo.18204394>
- [3] Yamamoto, Y. (2026). *Cosmic Metrics and SPARC Validation: Part II*. Zenodo.
- [4] Yamamoto, Y. (2026). *Unified Geometric Framework for the Three-Body Problem: Part III*. Zenodo.
- [5] Heisenberg, W. (1927). Über den anschaulichen Inhalt der quantentheoretischen Kinematik und Mechanik. *Zeitschrift für Physik*, 43, 172–198.
- [6] Pauli, W. (1925). Über den Zusammenhang des Abschlusses der Elektronengruppen im Atom mit der Komplexstruktur der Spektren. *Zeitschrift für Physik*, 31, 765–783.
- [7] de Broglie, L. (1924). *Recherches sur la théorie des quanta*. PhD Thesis, University of Paris.
- [8] Bohm, D. (1952). A Suggested Interpretation of the Quantum Theory in Terms of “Hidden” Variables. *Physical Review*, 85, 166–193.
- [9] Lelli, F., McGaugh, S. S., & Schombert, J. M. (2016). SPARC: Mass Models for 175 Disk Galaxies with Spitzer Photometry and Accurate Rotation Curves. *The Astronomical Journal*, 152, 157. DOI: 10.3847/0004-6256/152/6/157
- [10] McGaugh, S. S., Lelli, F., & Schombert, J. M. (2016). Radial Acceleration Relation in Rotationally Supported Galaxies. *Physical Review Letters*, 117, 201101.
- [11] Anderson, J. D., et al. (2002). Study of the anomalous acceleration of Pioneer 10 and 11. *Physical Review D*, 65, 082004.
- [12] Turyshev, S. G., et al. (2012). Support for the thermal origin of the Pioneer anomaly. *Physical Review Letters*, 108, 241101. DOI: 10.1103/PhysRevLett.108.241101
- [13] Rosi, G., et al. (2014). Precision measurement of the Newtonian gravitational constant using cold atoms. *Nature*, 510, 518–521.

- [14] Rosi, G., et al. (2017). Quantum test of the equivalence principle for atoms in coherent superposition of internal energy states. *Nature Communications*, 8, 15529. DOI: 10.1038/ncomms15529
- [15] Lamoreaux, S. K. (1997). Demonstration of the Casimir Force in the 0.6 to 6  $\mu\text{m}$  Range. *Physical Review Letters*, 78, 5–8.
- [16] Decca, R. S., et al. (2003). Measurement of the Casimir Interaction at the 1% Level. *Physical Review Letters*, 91, 050402.
- [17] van Dokkum, P., et al. (2018). A galaxy lacking dark matter. *Nature*, 555, 629–632.
- [18] Milgrom, M. (1983). A modification of the Newtonian dynamics as a possible alternative to the hidden mass hypothesis. *The Astrophysical Journal*, 270, 365–370. DOI: 10.1086/161130
- [19] Szigeti, B., et al. (2025). Can rotation solve the Hubble Puzzle? *Monthly Notices of the Royal Astronomical Society*. DOI: 10.1093/mnras/staf446
- [20] Almheiri, A., Engelhardt, N., Marolf, D., & Maxfield, H. 2019, JHEP, 2019, 63
- [21] Almheiri, A., Marolf, D., Polchinski, J., & Sully, J. 2013, JHEP, 2013, 62
- [22] Blandford, R. D. & Payne, D. G. 1982, MNRAS, 199, 883
- [23] Blandford, R. D. & Znajek, R. L. 1977, MNRAS, 179, 433
- [24] Blandford, R., Meier, D., & Readhead, A. 2019, ARA&A, 57, 467
- [25] Burnham, K. P. & Anderson, D. R. 2002, Model Selection and Multimodel Inference (Springer)
- [26] Event Horizon Telescope Collaboration 2019, ApJ, 875, L1
- [27] Event Horizon Telescope Collaboration 2022, ApJ, 930, L12
- [28] Fender, R., Belloni, T. M., & Gallo, E. 2004, MNRAS, 355, 1105
- [29] Fender, R. P., Gallo, E., & Russell, D. M. 2010, MNRAS, 406, 1425
- [30] Frank, A., Ray, T. P., Cabrit, S., et al. 2014, in Protostars and Planets VI, 451
- [31] Hawking, S. W. 1975, Comm. Math. Phys., 43, 199
- [32] Hawking, S. W. & Penrose, R. 1970, Proc. R. Soc. Lond. A, 314, 529
- [33] Johnson, M. D., Lupsasca, A., Strominger, A., et al. 2020, Science Advances, 6, eaaz1310
- [34] Kolehmainen, M., Done, C., & Díaz Trigo, M. 2011, MNRAS, 416, 311
- [35] Livio, M. 1999, Physics Reports, 311, 225
- [36] Maldacena, J. & Susskind, L. 2013, Fortschr. Phys., 61, 781
- [37] Mathur, S. D. 2009, Class. Quant. Grav., 26, 224001
- [38] Merloni, A., Heinz, S., & di Matteo, T. 2003, MNRAS, 345, 1057
- [39] Narayan, R. & McClintock, J. E. 2012, MNRAS, 419, L69
- [40] Narayan, R., Chael, A., Chatterjee, K., Ricarte, A., & Curd, B. 2022, MNRAS, 511, 3795

- [41] Tchekhovskoy, A., Narayan, R., & McKinney, J. C. 2011, MNRAS, 418, L79
- [42] Parker, M. L., Tomsick, J. A., Miller, J. M., et al. 2016, ApJ, 828, 48
- [43] Penington, G. 2020, JHEP, 2020, 2
- [44] Penrose, R. 1965, Phys. Rev. Lett., 14, 57
- [45] Polchinski, J. 1998, String Theory (Cambridge Univ. Press)
- [46] Rovelli, C. 2004, Quantum Gravity (Cambridge Univ. Press)
- [47] Stony Brook Center for Geometry and Physics, 2024, “Black Hole Information Paradox at 50: Review and New Directions,” workshop proceedings (in preparation)
- [48] Steiner, J. F., McClintock, J. E., & Reid, M. J. 2013, ApJ, 762, 104
- [49] Susskind, L., Thorlacius, L., & Uglum, J. 1993, Phys. Rev. D, 48, 3743
- [50] Gou, L., McClintock, J. E., Remillard, R. A., et al. 2014, ApJ, 790, 29
- [51] Yamamoto, Y. 2024, “Hyperbrane Relativity: A Unified Geometric Framework,” HBR Master Document v26
- [52] Yamamoto, Y. 2024, “HBR V19: Field Geometry and Emergent Time”
- [53] Yamamoto, Y. 2024, “HBR V26: Galactic Tilt and Surface Density Saturation”
- [54] Abbott, B. P. et al. 2016, Phys. Rev. Lett., 116, 061102
- [55] Abbott, B. P. et al. 2016, Phys. Rev. Lett., 116, 241102
- [56] Abbott, B. P. et al. 2017, Phys. Rev. Lett., 119, 161101
- [57] Abbott, B. P. et al. 2019, Phys. Rev. Lett., 123, 011102
- [58] Abbott, R. et al. 2020, Phys. Rev. Lett., 125, 101102
- [59] Abbott, R. et al. 2020, Phys. Rev. D, 102, 043015
- [60] Abbott, R. et al. 2021, Phys. Rev. X, 11, 021053
- [61] Abbott, R. et al. 2020, Astrophys. J. Lett., 900, L13
- [62] Maggiore, M. et al. 2020, JCAP, 2020, 050
- [63] Reitze, D. et al. 2019, Bull. AAS, 51, 35
- [64] Event Horizon Telescope Collaboration 2019, Astrophys. J. Lett., 875, L1
- [65] Event Horizon Telescope Collaboration 2022, Astrophys. J. Lett., 930, L12
- [66] Blandford, R. D. & Znajek, R. L. 1977, MNRAS, 179, 433
- [67] Connaughton, V. et al. 2016, Astrophys. J. Lett., 826, L6
- [68] Greiner, J., Burgess, J. M., Savchenko, V., & Yu, H.-F. 2016, Astrophys. J. Lett., 827, L38
- [69] Yamamoto, Y. 2026, “HBR Part 17: Compact Objects as Exhausted Fountains,” HBR internal document (`parts_jp/part17_compact_objects.tex`)



- [70] Yamamoto, Y. 2026, “HBR Phase 2 §6: Photon Sphere and EHT Shadow,” HBR internal document ([phase2\\_jp/sec6\\_photon\\_sphere.tex](#))
- [71] Yamamoto, Y. 2026, “HBR Phase 2 §7:  $B/r^3$  Post-Newtonian Phase Correction,” HBR internal document ([phase2\\_jp/sec7\\_gw.tex](#))
- [72] Yamamoto, Y. 2026, “Hyperbrane Relativity (HBR): Foundations and Worldview,” Independent Research Preprint (Kagoshima, Japan)
- [73] Yamamoto, Y. 2026, “A Modified Velocity Profile for Disk Galaxy Rotation Curves: Phenomenological Consistency with SPARC Observations,” Jxiv preprint (submitted 2026-01-19, v1), CC BY 4.0, <https://jxiv.jst.go.jp/index.php/jxiv/preprint/view/2673>.
- [74] Yamamoto, Y. 2026, “Measurement without Collapse: Geometric Resolution of Quantum Measurement in Hyperbrane Relativity,” Jxiv preprint (HBR Letter v4.4), submitted 2026, CC BY 4.0.
- [75] Yamamoto, Y. 2026, “Hyperbrane Relativity: A Geometric Extension of General Relativity with Born Rule and Observation-Contact Separation Appendices (HBR Complete Master Edition V27),” Zenodo, CC BY 4.0, <https://doi.org/10.5281/zenodo.19818953>.
- [76] Gleason, A. M. 1957, “Measures on the Closed Subspaces of a Hilbert Space,” *Journal of Mathematics and Mechanics*, 6, 885–893.
- [77] Busch, P. 2003, “Quantum States and Generalized Observables: A Simple Proof of Gleason’s Theorem,” *Physical Review Letters*, 91, 120403. <https://doi.org/10.1103/PhysRevLett.91.120403>